Ventricular Function Under LVAD Support

Matthew McCormick[†]

Primary Advisors

Prof. Nicolas Smith[†,‡] Dr. David Kay[†]

[†] *Department of Computer Science, University of Oxford*
Parks RD, OX1 3JP, UK
[‡] *Department of Imaging Sciences and Biomedical Engineering, King's College London*
St Thomas Hospital, SE1 7EH, UK

Overview

This thesis presents a finite element methodology for simulating fluid–solid interactions in the left ventricle (LV) under LVAD support. The developed model was utilised to study the passive and active characteristics of ventricular function in anatomically accurate LV geometries constructed from normal and patient image data.

A non–conforming ALE Navier–Stokes/finite–elasticity fluid–solid coupling system formed the core of the numerical scheme, onto which several novel numerical additions were made. These included a fictitious domain (FD) Lagrange multiplier method to capture the interactions between immersed rigid bodies and encasing elastic solids (required for the LVAD cannula), as well as modifications to the Newton–Raphson/line search algorithm (which provided a 2 to 10 fold reduction in simulation time). Additional developments involved methods for extending the model to ventricular simulations. This required the creation of coupling methods, for both fluid and solid problems, to enable the integration of a lumped parameter representation of the systemic and pulmonary circulatory networks; the implementation and tuning of models of passive and active myocardial behaviour; as well as the testing of appropriate element types for coupling non–conforming fluid–solid finite element models under high interface tractions (finding that curvilinear spatial interpolations of the fluid geometry perform best). The behaviour of the resulting numerical scheme was investigated in a series of canonical test problems and found to be convergent and stable. The FD convergence studies also found that discontinuous pressure elements were better at capturing pressure gradients across FD boundaries.

The ventricular simulations focused firstly on studying the passive diastolic behaviour of the LV both with and without LVAD support. Substantially different vortical flow features were observed when LVAD outflow was included. Additionally, a study of LVAD cannula lengths, using a particle tracking algorithm to determine recirculation rates of blood within the LV, found that shorter cannulas improved the recirculation of blood from the LV apex. Incorporating myocardial contraction, the model was extended to simulate the full cardiac cycle, converging on a repeating pressure–volume loop over 2 heart beats. Studies on the normal LV geometry found that LVAD implementation restricts the recirculation of early diastolic inflow, and that fluid–solid coupled models introduce greater heterogeneity of myocardial work than was observed in equivalent solid only models.

A patient study was undertaken using a myocardial geometry constructed using image data from an LVAD implant recipient. A series of different LVAD flow regimes were tested. It was found that the opening of the aortic valve had a homogenising effect on the spatial variation of work, indicating that the synchronisation of LVAD outflow with the cardiac cycle is more important if the valve remains shut. Additionally, increasing LVAD outflow during systole and decreasing it during diastole led to improved mixing of blood in the ventricular cavity – compared with either the inverse, or holding outflow constant. Validation of these findings has the potential to impact the treatment protocols of LVAD patients.

Acknowledgements

This thesis is the culmination of four years hard work to which many people have contributed. In these pages, I hope to acknowlege my gratitude for all the assistance and support I have received along the way.

To my supervisors – Professor Nic Smith and Dr Dave Kay

Nic Smith, for taking me on as a student at Oxford, giving me the opportunity to work on such an exciting project and for supporting me and guiding me as I struggled to find the direction I wanted to take this work. It was a difficult process bringing this project together and he gave me the freedom and assistance to make it a project I could be proud of.

Dave Kay, for his assistance and advice on the numerics and implementation of finite element techniques in this project. Additionally, for the many helpful discussions that ensured I knew what I was doing and that it would be appropriate for the problems I faced.

To David Nordsletten

This thesis would not have been possible without the invaluable contribution of David Nordsletten. His advice and assistance were formative in establishing the direction the thesis took, as well as in overcoming the many challenges I faced along the way. Additionally, his patience and friendship made the collaboration an absolute pleasure. Thank you.

To my parents

For giving me the love and support to go out and follow my dreams. Without them none of this would have been possible and I do not think there is any way I can thank them enough.

The Woolf Fisher Trust

In 2006, on a rainy day in Auckland, they gave me the opportunity to fullfil my ambitions at Oxford. For this I am extremely grateful. Also, to *Dr Nigel Evans*, secretary of the trust, for his continued interest in my progress and yearly visits. I know myself and the other Woolf Fisher scholars appreciated these greatly.

Special Acknowledgements

First of all I would like to acknowlege my colleagues in both the Oxford and KCL labs, it has been an exciting and fun place to work and it is the people who have made it that. Additionally, several people and groups deserve to be singled out for either their friendship, assistance or both.

Jack Lee, for being a good friend and colleague, always ready to help me out, or just for a chat.

Eoin Hyde, for the regular coffee breaks that kept me sane while writing up.

Steven Niederer, for the helpful discussions and advice that assisted me with many of the problems I faced.

Pablo Lamata, who helped me construct the patient mesh used for the final study in this thesis.

Berlin Heart, for providing the industrial support on this project and for the regular meetings on where we should focus our investigations.

Philips Research, for segmenting the patient data.

Oxford University Supercomputing Centre, for ensuring the clusters kept on running and that my code was linked in to the optimal set of libraries on their machines.

Jon Whitely, for helping point me in the right track with my transfer report and examining my confirmation of status.

Peter Hunter and the Auckland Bioengineering Institute, for giving me a grounding through my undergraduate years, helping me with my transition to Oxford and maintaining a continued interest in my progress.

Finally, I cannot complete this section without thanking all the amazing people at Oxford who have made the last four years a fantastic experience. There have been countless dinners, lunches and evenings which could not have been possible at any other location or with other groups of people. While the work has been hard, I cannot think of a better place to have done it in. The memories and experiences I have had will stay with me forever.

Publications

The following publications are associated with this thesis.

Journal Papers

M. McCormick, D. Nordsletten, D. Kay and N. Smith, 2011, Modelling left ventricular function under assist device support. *International Journal for Numerical Methods in Biomedical Engineering*, 27, 1073–1095.

M. McCormick, D. Nordsletten, D. Kay and N. Smith, 2012, Simulating left ventricular function under assist device support. *Journal of Computational Physics*, submitted, in review.

M. McCormick, D. Nordsletten, P. Lamata, D. Kay and N. Smith, 2012, The importance of aortic valve opening in myocardial energetics and blood hemodynamics in an LVAD supported LV. *PLoS Computational Biology*, submitted, in review.

D. Nordsletten, M. McCormick, P. Kilner, D. Kay and N. Smith, 2011, Fluid–solid coupling for the investigation of diastolic and systolic human left ventricular function. *International Journal for Numerical Methods in Biomedical Engineering*, 27, 1017–1039.

Conference Papers

M. McCormick, D. Nordsletten, A. de Vecchi, D. Kay and N. Smith, 2010, Fluid–mechanics simulations of ventricular function under LVAD support. *World Congress on Medical Physics and Biomedical Engineering, September 7–12, Munich, Germany*, DOI: 10.1007/978–3–642–03882–2-417.

- This paper won a Diploma in the Young Investigator competition, placing 3rd overall out of more than 600 entries.

M. McCormick, D. Nordsletten, D. Kay and N. Smith, 2011, Modelling ventricular function under LVAD support. *Mathematical and Computational Biomedical Engineering, March 30 – April 1, Washington D.C., USA.*

D. Nordsletten, M. McCormick, D. Kay and N. Smith, 2011, Tissue length dependence and left ventricular blood flow in the human heart. *Mathematical and Computational Biomedical Engineering, March 30 – April 1, Washington D.C., USA.*

Media Publications

M. McCormick, D. Nordsletten, N. Smith, 2011, How to mend a broken heart, *Video contribution, BBC Horizon*, http://www.bbc.co.uk/programmes/b00ysh81.

M. McCormick, D. Nordsletten, N. Smith, 2011, Under Pressure, *Finalist, British heart Foundation Image Competition*, www.guardian.co.uk/science/gallery/2011/jun/15/medical-research-heart-disease-images.

Contents

For Alisa

1 Introduction

In western society there is a 1 in 5 life–time risk of Heart Failure with a 50% one year survival rate. Including both acute and long term hospital stays, heart failure consumes 2% of the total European healthcare budget[20]. Orthotropic heart transplantation is recognised as the best therapy for end-stage heart failure[168]. However, approximately 20-30% of potential recipients will die while waiting for a donor heart[188]. Due to this shortage, left ventricular assist devices (LVADs) are often used as a bridge to transplant[1].

LVADs are pumps that reduce the mechanical load on the heart by pumping blood from the left ventricular (LV) apex directly to the aorta, see figure 1.1. The implantation of these devices significantly reduces both LV pressure and volume[82]. This reduces the stress on the myocardium and, additionally, reduces the stress produced by the myocardium due to the Frank-Starling effect[141]. As a result of this unloading, the myocardial architecture is restructured in a process called reverse remodelling which, in a small subset of patients, can lead to a recovery of cardiac function, enabling the device to be explanted[107, 10]. While the mechanisms behind reverse remodelling remain poorly understood, the optimal degree of unloading to assist patient recovery is also unknown[21].

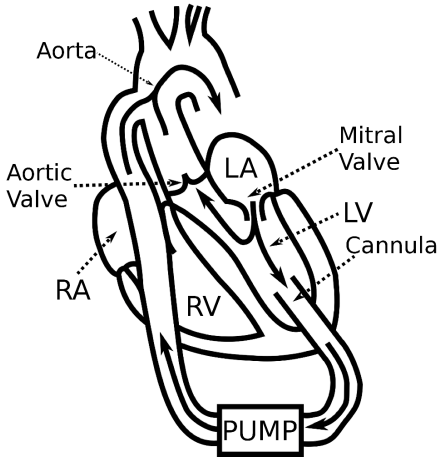

FIGURE 1.1. *Schematic of an LVAD assisted heart. Blood is pumped via the cannula, through the LVAD pump, to the aorta. Labeled on the diagram are the LV valves along with the left and right atria (LA and RA) and the right ventricle (RV). The arrows show possible flow paths from the LA to the aorta.*

At present patient selection for LVAD implantation is based on relatively simple, qualitatively based, clinical metrics combined with some standard hemodynamic variables[205]. Additionally, once implanted there is little customisation to the patient nor tuning to the cardiac cycle. It is in this context that the ability to optimise LVAD use, via patient specific customisation, to benefit cardiac function has the potential to provide substantial clinical gains[21]. However, due to metallic components in the pump, implanted LVADs cannot be directly observed using standard medical image modalities such as MRI. This provides a niche for mathematical

modelling techniques to be used as an investigative tool for studying the behaviour of the ventricle under LVAD support and analysing its efficacy as a pump.

Cardiac modelling has progressed significantly in recent decades from early models that focused on the relationship between blood pressure and cavity volume[186, 70] to biophysically based models that span a range of both emphasis and spatial scales. Such models include studies on cellular and subcellular behaviour[67, 125, 38], electrophysiology[126], mechanical function[68, 123] and blood flow[169, 3, 140]. Recent developments have seen the integration of models that combine these various functions and behaviours to study pathophysiological problems, where changes in one mechanism are linked to changes in another[138].

To address the question of how LVAD support impacts cardiac function, the interaction at the core of cardiac behaviour needs to investigated - i.e. the interaction between blood flow within the heart chambers and the passive and active behaviour of the myocardium. Therefore, coupled fluid–solid mechanics models of the heart are required. Several coupled fluid-solid mechanical cardiac models exist in the literature, ranging from the pioneering work of Peskin and McQueen[151, 117] through to more recent models incorporating greater degrees of physical realism, in particular in their descriptions of myocardial behaviour[137]. These models have been used to investigate blood flow within the ventricular cavities and the efficiency of the heart as a pump from diastole[24] through to systole[88, 137].

To capture the impact of LVADs on ventricular behaviour, coupled fluid-solid mechanics models of a supported LV must be able to describe the full range of ventricular behaviour under LVAD support. This includes the capability to simulate the full cardiac cycle and the interaction between the LVAD cannula and the myocardial wall, see figure 1.2. This interaction occurs either intermittently, during systole, or, if cannula outflow is high, continuously as the myocardium is sucked onto the cannula[163]. Incorporating such interactions requires the integration of cardiac fluid-solid modelling techniques with methods developed to deal with interacting bodies immersed in fluids. Additionally, for such a model to provide useful information on the efficacy of the pump function of the heart under support, feedback must exist between cardiac output, the systemic circulatory system and venous return. This involves the coupling of the simulation to models of the systemic circulatory network[178]. Finally, the complexities involved in large coupled biophysical schemes can make them inherently unstable and difficult to solve[136]. Therefore, the numerical scheme developed to simulate supported ventricular behaviour must be verified against relevant test problems to ensure both convergence and that the relevant physics within the problem are being accurately resolved.

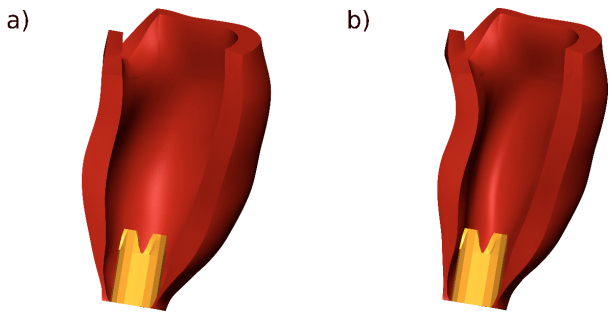

FIGURE 1.2. *a) the LVAD cannula positioned in the ventricle. b) contact or suction between the LVAD cannula and the myocardial wall, this occurs either during systole or if the LVAD pump rate is too high.*

The primary aim of this thesis is to develop an anatomical coupled fluid-solid mechanical model of the left ventricle under LVAD support. Additionally, this model should be able to simulate multiple cardiac beats and be capable of being customised to individual patients. Building on the significant advances in both mathematics and the modelling of heart mechanics, the objective of this work is to provide – to our knowledge – the first anatomically accurate model of the left ventricle that:

1. Incorporates physiologically based models of the myocardium, ventricular blood flow and their interactions.
2. Can simulate the complex interactions between the LVAD cannula and the myocardial wall.
3. Is capable of resolving multiple cardiac beats to converge on a repeating pressure-volume loop.
4. Simulates cardiac function in a patient customised, coupled fluid–solid mechanics ventricular model of an LVAD supported LV.

In developing a model that meets these goals, this work provides both an extension of existing coupled fluid-solid cardiac modelling techniques and a fundamental first step towards applying these models to patient treatment.

With these objectives in mind, the rest of this chapter discusses relevant aspects of cardiac anatomy and function, along with previous modelling efforts. Section 1.1 contains an overview of heart structure and function while section 1.2 provides an outline of the effects and treatment options for heart disease, focusing on the current state of knowledge on the impact of LVADs on the heart. Section 1.3 reviews the substantial body of existing work in the fields of heart tissue mechanics, blood flow modelling and their coupled interaction. As much of this thesis involves the implementation of various mathematical models, the numerical schemes developed for solving the relevant equations are also discussed. Finally, section 1.4 presents a brief outline of the thesis structure.

1.1 Cardiac Anatomy and Physiology

> *The heart, with the veins and arteries and the blood they contain, is to be regarded as the beginning and the author, the fountain and original of all things in the body, the primary cause of life.*
>
> William Harvey, 1628

The human heart is an electromechanical pump that delivers blood to the body via a network of blood vessels of varying size. In order to develop mathematical models of its function, an understanding of the relationship between its structure and function is required along with its electro-physiological behaviour through the entire cardiac cycle. This section outlines the basics of cardiac anatomy and physiology focusing on aspects of critical importance to developing anatomical, biophysically based models of ventricular function. For a more detailed review of cardiac physiology see Opie[141].

1.1.1 The Heart and the Cardiovascular System

The heart is the central organ of the cardiovascular system, a network of vessels tasked with delivering blood to the bodies tissues and organs. The heart pumps blood, a colloidal suspension consisting of hemoglobin rich erythrocytes, electrolytes, amino acids and leukocytes, through this network. As a result, it is responsible for delivering nutrients to the body and transferring oxygen from the lungs to the tissue and the waste product carbon dioxide from the tissue to the lungs where it is expelled. Additionally, the cardiovascular system acts as a conduit for many of the bodies hormonal regulatory pathways, helps the body fight disease and assists in stabilising body temperature and pH to maintain homeostasis.

The cardiovascular system consists of two circulatory networks, the pulmonary and systemic. The pulmonary arterial network delivers deoxygenated blood from the heart to the alveolar sacs in the lungs where carbon dioxide is expelled from the body and the hemoglobin within the erythrocytes is replenished with oxygen. The oxygenated blood is then returned to the heart via the pulmonary venous network. The systemic arterial network delivers oxygenated blood from the heart to the bodies tissues and organs, while the systemic venous network returns the now deoxygenated blood to the heart.

This division of the cardiovascular system into two circulatory networks is reflected in the structure of the heart, which is divided into two halves, the right and the left. The right half drives the pulmonary network, while the left half pumps blood through the systemic network. Each half is divided into two chambers, called atria and ventricles, that differ both structurally and functionally. The atria (left and right, LA and RA) act as thin walled reservoirs, pooling blood that has been returned from the circulatory networks and assisting in ventricular filling. The ventricles (left and right, LV and RV), in contrast, are thick walled muscular pumps that eject blood from the heart, powering the cardiovascular system.

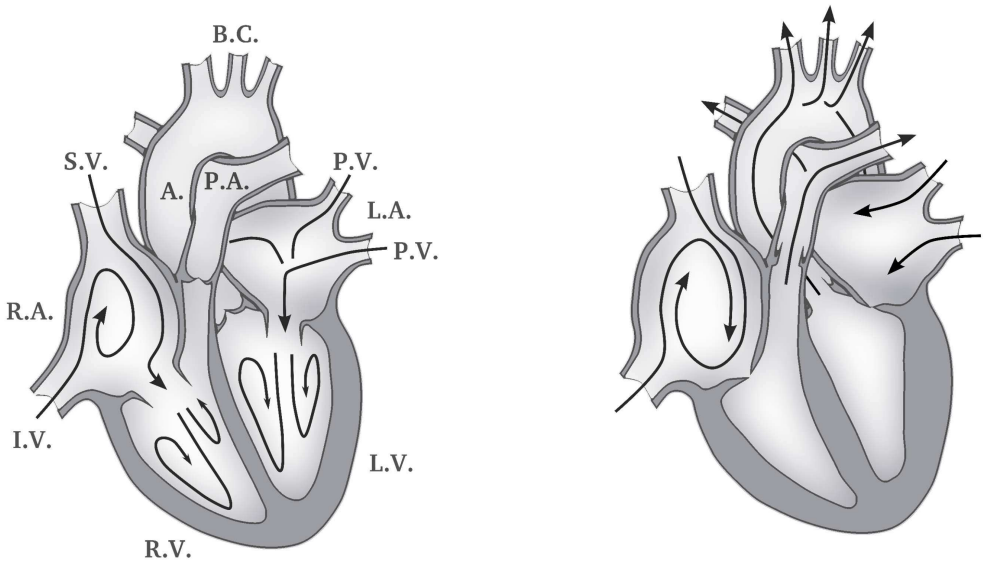

Figure 1.3. *Schematic of the heart during diastole (left) and systole (right)*[134]*. The arrows show the dominant patterns of flow observed experimentally in Kilner* et al.[76, 78]*. The vessels and chambers labeled are: S.V superior vena cava, I.V. inferior vena cava, P.V. pulmonary vein, A. aorta, B.C. brachiocephalic arteries, P.A. pulmonary artery, L.A. left atrium, L.V. left ventricle, R.A. right atrium, and R.V. right ventricle.*

Blood is transported from the circulatory systems through the cardiac chambers via a succession of major vessels and one way valves. Blood returning from the systemic system enters the RA from the superior and inferior vena cava, passing through the semilunar and coronary sinus valves. From the RA, blood enters the RV through the tricuspid valve that separates the two chambers. Blood then exits the right side of the heart via the pulmonary valve into the pulmonary arteries. Similarly, blood enters the LA via the pulmonary veins, however, unlike the RA, there are no valves separating the chamber from the returning venous vessels. Blood then passes into the LV through the mitral valve. Blood is expelled from the LV via the aortic valve into the aorta. Figure 1.3 presents the arrangement of the vessels, valves and chambers along with the direction of blood flow through the heart.

The left and right sides of the heart operate under significantly different conditions. Due to lower resistance in the pulmonary network, pulmonary arterial pressures are significantly lower than in their systemic counterparts. As a result the afterload, that is the resistance to the expulsion of blood from the ventricles, is substantially lower for the right side of the heart than the left (typically less than 30mmHg for the right side compared with greater than 100mmHg on the left). This dichotomy in output pressures between the left and right sides is reflected in the structure of the muscular walls of the left and right ventricles. In order to generate the force required to work against the greater systemic afterload, the LV wall is substantially thicker than that of the RV. In contrast, the preload, that is the load, or pressure, provided by venous return, varies minimally between the left and right sides (approximately 5mmHg in normal subjects).

1.1.1.1 Myocardial Laminar Structure

The myocardium is the muscular wall of the heart. The inner surface of the myocardium is called the endocardium while its exterior surface is called the epicardium. The epicardium is encased by the pericardium, a thin, fibrous bag like structure within which the heart lies. The endocardium has a large surface area due to the many papillary muscles and the irregular pattern of the inner wall of the LV.

The arrangement of cardiac muscle cells, or myocytes, within the myocardium is a major determinant of both the passive and contractile behaviour of myocardial tissue[123, 175]. Early understanding of myocardial tissue structure held that the ventricles were made up of nested muscle bundles, each characterised by a well defined helical fibre path running from apex to base[102, 105, 166]. However, later quantitative studies, including the work of Streeter[184, 185] and Fox[46], did not confirm this arrangement. By analysing the transmural variation in the orientation of myocardial fibres they determined a simple model of fibre orientation where the fibre angle, measured from the base, varied from $+60^\circ$ at the endocardium to -60° at the epicardium. This model remains the standard framework applied in many mathematical models[123].

Further work, including the detailed anatomical studies of canine and rat hearts by LeGrice *et al.*[96], quantifiably characterised myocardial laminar structure showing that the ventricular myocardium should not be viewed as a uniformly continuous structure. Instead, they revealed that cardiac tissue is a composite of discrete layers of myocardial muscle fibres tightly bound by endomysial collagen. These myocardial sheets, or *laminae*, are loosely constrained by perimysial collagen and have the ability to slide over each other with relative ease. Laminae are on average four to six cells thick and continuously branch throughout the ventricular walls. Figure 1.4 shows a stylised representation of myocardial laminar structure. The quantification of sheet orientation, along with

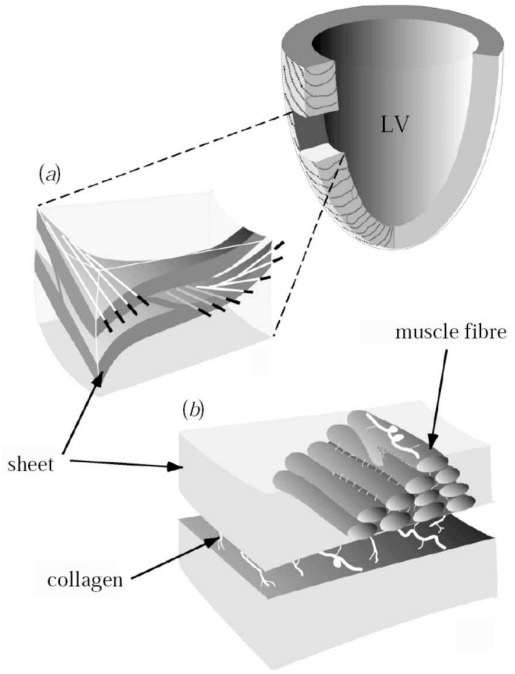

FIGURE 1.4. *Diagram showing the laminar structure of the myocardium[96]. a) cross section from the LV myocardial wall showing the through wall sheet structure. b) the layered myocyte structure of the laminar sheets. Perimysial collagen (white) is visible between the sheets, endomysial collagen is shown surrounding the fibres.*

the earlier work on fibres, was incorporated into finite element models by Nielsen *et al.*[131]. More recent work by LeGrice, Sands *et al.*[95, 171] has utilised advances in confocal microscopy to provide data at greater spatial resolution. This has further enhanced the understanding of myocardial microstructure.

With the exception of Fox's early study[47], data on the myocardial fibre architecture in humans has been limited. However, recent advances in diffusion tensor magnetic resonance imagine (DTMRI) have made the direct imaging of human fibres along with laminar structures possible. Rohmer *et al.*[167] have performed detailed qualitative analysis of fibre and laminar structures from ex vivo human DTMRI data. Their work found similar transmural variations in fibre angles to those seen in earlier animal studies. However, without quantitative analysis, these results remain challenging to embed within biophysically based models.

For modelling purposes, it is convenient to consider the myocardium to have three principle coordinate axes. The fibre axis, aligned with the myocardial fibres; the sheet axis, orthogonal to the fibre axis, in the plane of the laminar sheets; and the normal axis, orthogonal to both the fibre and sheet axes. The axes rotate with the myocardial fibres and sheets as they vary transmurally[174].

1.1.1.2 Myocardial Activation and Contraction

The contraction of the heart is initiated by the spontaneous depolarisation of the pacemaker cells in the sinoatrial (SA) node. This generates an electrical impulse which is rapidly conducted through the atria to

the atrioventricular (AV) node, where it undergoes filtration and delay. The AV node then stimulates the His bundle and the Purkinje fibre network, which rapidly depolarise through the endocardial walls of the heart. Subsequently, a wave of depolarisation spreads transmurally through to the epicardium.

Depolarisation, in the form of an influx of calcium ions (Ca^{2+}) across the myocyte cellular membrane, triggers calcium induced calcium release from stores within the sarcoplasmic reticulum (SR) of the cell. This leads to an increase in cytosolic calcium levels sufficient to initiate the myocyte's contractile machinery – a contractile unit composed of the proteins myosin, actin, troponin, tropomyosin and titin. The binding of Ca^{2+} to troponin-C enables the repetitive binding of myosin to actin, the 'cross bridge cycle', generating force at the expense of the phosphorylation of adenosine triphosphate (ATP) - the molecular unit of energy within the cell. The return of Ca^{2+} to the SR via sodium-calcium exchangers gradually switches off this process, ending contraction leading to the relaxation of the myocardium.

The synchronous activation of myocytes throughout the myocardium in both the atria and the ventricles generates the force responsible for the expulsion of blood from the cardiac chambers.

1.1.1.3 The Cardiac Cycle

The cardiac cycle is the intermittent filling and ejection of blood from the ventricular chambers caused by the contraction and relaxation of the myocardium.

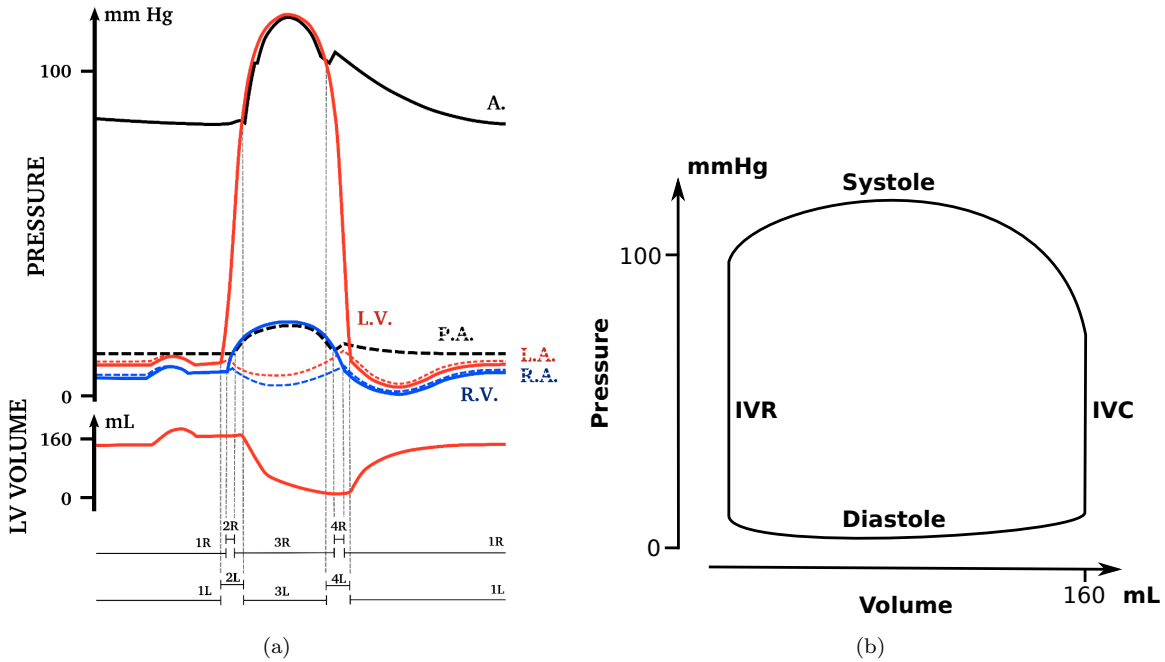

(a) (b)

FIGURE 1.5. *(a) Wigger's plot of normal heart function*[134]*. The curves show the pressures in the cardiac chambers and the aorta as well as LV volume. The periods of cardiac cycle are numbered, (1) is diastole, (2) is isovolumetric contraction, (3) is systole and (4) is isovolumetric relaxation. The letters L and R refer to left and right hearts respectively. (b) LV pressure volume loop for normal heart function.*

The cardiac cycle can be divided into four distinct phases, diastole (filling), isovolumetric contraction (IVC), isovolumetric relaxation (IVR) and systole (ejection). The repetition of these phases generates the rhythmical pumping action of the heart. Figure 1.5 shows an idealised Wigger plot and LV pressure volume loop for normal heart function, these summarise the changes in cavity blood pressures and LV volume during the cardiac cycle.

Diastole:

Blood flows continuously into the left and right atria from the pulmonary and systemic networks. Diastole occurs when atrial pressure exceeds ventricular pressure, causing the mitral and tricuspid valves to open and blood to flow into the ventricles. This only occurs when the pressure in the left ventricle is low, i.e. when the ventricular myocardium is relaxing. Diastole can be divided into three filling phases, early, mid (diastasis) and end (atrial systole).

Early Diastole: During early diastole, the relaxing ventricular myocardium continues to decrease ventricular pressure, increasing the pressure gradient between the atria and the ventricles, effectively sucking blood into the ventricles[164]. The atrial valve annuli recoil due to the relaxation of the myocardium, further increasing net inward flux. Blood flow into the ventricles is predominantly uniaxial with peak velocities reaching between 0.4 and $0.7ms^{-1}$ in healthy hearts at rest[76]. Vortical flows develop in the ventricle chambers, predominantly due to the geometric shape of the ventricles, but also due to the valves themselves[78, 134].

Diastasis: The suction force due to the relaxation of the myocardium diminishes as the rate of myocardial relaxation slows. The increasing ventricular volume causes ventricular pressure to begin to rise. This drop in the pressure gradient between the atria and ventricles leads to a reduction in the blood flow rate across the mitral and tricuspid valves. The extent of this reduction depends on both the physiology of the individual and their exercise state - during exercise diastasis is not observed[76]. Blood inflow becomes more sporadic but remains largely uniaxial and there are marginal increases in vortex size in both ventricles[138].

Atrial systole: The electrical activation of the heart at the SA node occurs during end–diastole, inducing atrial systole. This increases atrial pressure, creating additional force to drive blood into the ventricle chambers. Atrial pressure peaks at this time and there is a second, smaller, peak in mitral valve flow. Pulmonary venous flow is reversed as the LA contracts, however the semilunar and coronary sinus valves prevent a similar effect occurring in the RA[138].

Isovolumetric contraction:

On reaching the AV node the activation wave pauses during end–diastole before spreading, via the Purkinje fibre network, across the ventricular myocardium inducing ventricular contraction. Isovolumetric contraction is the period where ventricular pressure, increasing due to myocardial contraction, is below that of the circulatory networks and is therefore insufficient to open the aortic and pulmonary valves. Diastole ends at this point since the build up in pressure closes the mitral and tricuspid valves. Blood flow within the ventricles follows a spiral pattern with rapidly diminishing momentum[138].

Systole:

Systole begins once the pressures built up during IVC exceed those of the circulatory networks. This leads to the opening of the aortic and pulmonary valves and the expulsion of blood from the ventricles. Like diastole,

systole can be considered to consist of three phases, early, mid and end.

Early–systole: Early systole is characterised by the rapid acceleration of blood from the ventricles into the aortic and pulmonary arteries. The remnants of vortical flow are replaced by a uniaxial flow through the aortic and pulmonary valves. From the LV, outflow favours the proximal ventricular wall due to the curvature of the aorta, while outflow from the RV is relatively symmetric. Myocardial contraction draws the mitral valve annulus towards the apex, elongating the atria and inducing a low pressure gradient. This leads to the commencement of atrial filling from the left and right pulmonary veins and vena cava. Atrial filling sees vortical flows develop in the LA and RA[78].

Mid–systole: Peak aortic outflow occurs during the initial stages of mid–systole with velocities around 0.8–1.2m/s[81]. LV outflow gradually decreases from this peak and the flow profile shifts from favouring the inner to the outer curvature of the aorta. Flow within the ventricles peaks and slowly declines as the myocardial tissue reaches maximum contraction. In the LV, flow converges on the outlet while flow in the RV is thought to be slightly more complex, probably due to geometric asymmetries[134]. Vortical flows develop at the aortic and pulmonary roots, a lobular region between the valve flaps and the vascular wall.

End–systole: Rapid decline in ventricular outflow results in end–systole. As the outflow valves close retrograde flows occur within both ventricles. The closure of the valves prevents the regurgitation of blood back into the ventricles. The rapidity of valve closure has been shown experimentally to be due in part to vortical flow patterns within the aortic and pulmonary roots exerting a centripetal pressure gradient on the valve leaflets[77]

Isovolumetric relaxation:

The end of contraction sees the myocardium begin to relax. As with IVC, during IVR the inflow and outflow valves in both ventricular chambers are closed. As a result, the release of the elastic potential energy, built up during contraction, of the ventricular myocardium is limited by the constraint of constant ventricular volume. As a consequence, ventricular cavity pressure rapidly falls. IVR ends when ventricular blood pressure falls below atrial pressure, opening the mitral and tricuspid valves, restarting the cardiac cycle.

1.1.1.4 Regulation of Cardiac Function

Regulation of the cardiac cycle is primarily achieved through three main mechanisms: the Frank–Starling law of the heart, the force–frequency relationship and the sympathetic and parasympathetic systems.

Frank–Starling Law of the Heart: First postulated in 1915, the law states that, within physiological limits, the larger the volume of the heart, the greater the force of its contraction. The force–length relationship of cardiac muscle is the mechanism behind this law. An increase in end diastolic volume is, at the microstructural level, observed as lengthening of cardiac myocytes. This leads to a greater contractile force, resulting in increased stroke volume.

Force–Frequency Relationship: As heart rate increases there is a positive inotropic response and vice versa. As heart rate increases, more sodium and calcium ions enter the myocardial cells than are be removed by

the sodium pump. The increase in sodium concentration leads to an increase in cytosolic calcium via the sodium–calcium exchanger, resulting in greater force of contraction[141].

Sympathetic and parasympathetic systems: The sympathetic and parasympathetic systems work in tandem to regulate the cardiac cycle in response to various states of excitation. The system is regulated by the autonomic nervous system and the heart responds to these signals via two main types of receptors. Sympathetic signals either stimulate heart rate and contractility (β–adrenergic receptors), or increase arteriole tone (α–adrenergic receptors). In general parasympathetic signals have the opposite effect of adrenergic stimulation and are received by muscarinic receptors.

1.2 Heart Failure and Left Ventricular Assist devices

Heart failure is the physiological state where cardiac output is insufficient to meet the bodies needs. It is often called congestive heart failure, or CHF, since one of the manifestations of the condition is that the body becomes congested with fluid. There are three main myocardial mechanisms that lead to heart failure: pressure overload, volume overload and cardiomyopathy. A fourth common cause is coronary artery disease with post–infarction remodelling[141]. In each case, while different mechanisms may be responsible for causing the condition, the myocardium attempts to compensate for the primary defect before the stage of overt myocardial failure develops.

This section details the impact of heart failure on cardiac function; the current treatments used to ameliorate the symptoms of end-stage heart failure; and the use of LVADs as a bridge to both transplant and recovery.

1.2.1 The Impact of Heart Failure on Cardiac Function

It is convenient to consider heart failure as a combination of three separate components: diastolic failure, systolic failure and neurohumoral changes[179]. Diastolic failure is the imperfect emptying of the LA and filling of the LV. This results in pulmonary congestion and increased venous pressure. Systolic failure is due to impaired contractile behaviour in the heart leading to a reduction in peripheral perfusion and arterial blood pressure. Diastolic failure can exist in isolation, however systolic failure is always accompanied by diastolic failure. Finally, there are neurohumoral changes that occur in response to the changes in cardiac performance. These changes increase peripheral vascular resistance and afterload resulting in fluid retention, peripheral congestion and edema, leading to a further increase in preload on the heart.

Both systolic and diastolic failure significantly affect cardiac function. In systolic failure, the increase in afterload due to neurohumoral effects, combined with the already reduced contractile efficiency, further reduces cardiac stroke volume. Meanwhile, the increase in preload results in a greater volume of blood being returned to the heart, increasing cavity volume. These combined effects result in the pressure volume curve being pushed to the right, see figure 1.6. In diastolic failure, the impairment of LV filling results in the pooling of blood in the pulmonary circulatory network. This continues until pulmonary pressures are sufficiently high to adequately fill the LV. As a result, diastolic failure manifests itself in elevated diastolic pressures despite essentially normal

end diastolic volumes[179], see figure 1.6. The combined effect of both diastolic and systolic failure is to increase ventricular volume and pressure while reducing cardiac output.

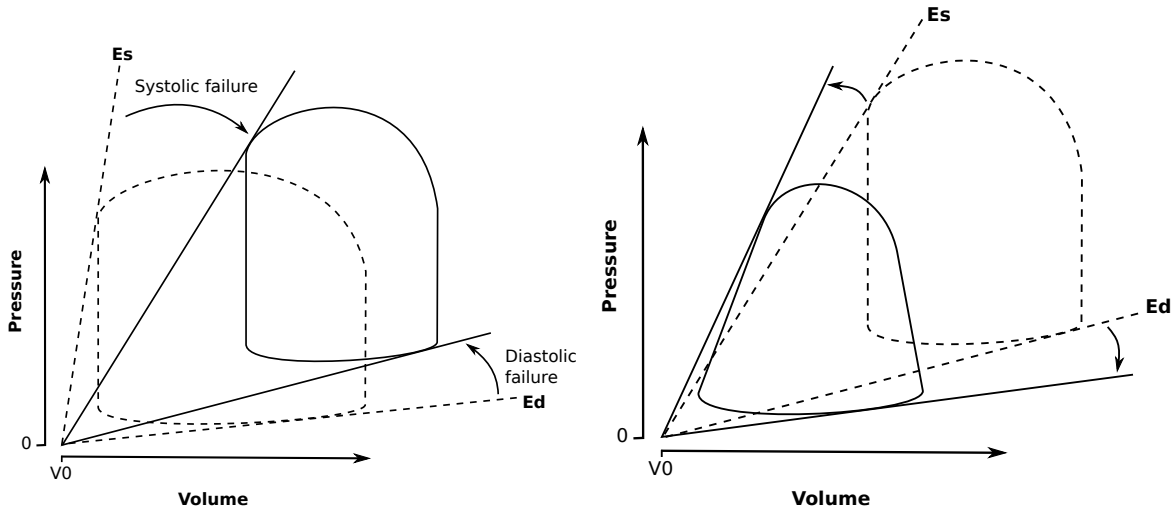

(a) Heart Failure (b) LVAD Support

FIGURE 1.6. *(a) The effect of diastolic and systolic heart failure on the LV pressure volume loop. Dashed line shows the normal relationship. (b) Effect of LVAD support on the LV pressure volume loop. Dashed line shows the heart failure relationship prior to LVAD implantation. Note that there is volume change during both IVC and IVR due to continual outflow from the LVAD.*

At the structural level, hearts with CHF often exhibit organ dilation and increased ventricular wall thickness. Dilation is followed by increased ventricular wall stress resulting in decreased coronary blood flow and impaired pump function. These effects are reflected through diminished cardiac output[207]. At a microstructural level, changes are observed in parallel fashion, for example, increases in cardiac mass and the increase in relative wall thickness are linked to increases in myocyte volume and relative elongation[108]. These changes have been termed 'ventricular remodeling'[21].

1.2.1.1 Standard Treatments

Since the 1980s heart transplantation has been recognised as the most effective therapy for end–stage heart disease, including CHF, with 10 year survival rates approaching 50%. However, due to a chronic shortage of donor hearts, up to 30% of potential recipients die before receiving a transplant operation[168, 53, 188].

Standard therapeutic interventions for end-stage heart failure range from the use of positive inotropic agents to increase the force of myocyte contraction[26, 192] through to more invasive treatments such as cardiac resynchronisation therapy (CRT)[23], for patients with both CHF and left ventricular dyssynchrony, and LVADs.

Inotropic treatments have the advantage of being largely non-invasive. Unfortunately, not all patients demonstrate a positive response to these therapies. Additionally, prolonged inotrope use has been associated with increased mortality in patients with advanced heart failure[192, 161]. CRT involves the placing of pacing leads on the heart to improve contractile synchrony. CRT has proven to be effective in treating a significant percentage of patients with both CHF and LV dyssynchrony - evidenced by a prolonged QRS duration on an

echo–cardiogram[25] - however, not only does this represent merely a subset of heart failure patients, around 30% of patients do not respond to the treatment[14].

LVAD implantation, like CRT, is an extremely invasive procedure. While there can be significant complications, by mechanically unloading the heart cardiac output is automatically improved. The rest of this section discusses LVAD implantation and its effect on cardiac performance.

1.2.2 Left Ventricular Assist Devices

LVADs are surgically implanted in the thoracic cavity to reduce ventricular load by pumping blood from the apex of the LV directly into the aorta. This directly leads to the unloading of both LV volume and pressure. The increase in cardiac output reverses many of the neurohumoral changes discussed above resulting in reductions in systemic arterial resistance, pulmonary venous and arterial pressures and reduced pulmonary vascular resistance. As a result, both LV preload and afterload are reduced. The reduction in pulmonary arterial pressure means LVADs reduce the loading on the RV as well[98]. Figure 1.6 shows the impact of LVAD implantation on the ventricular pressure volume relationship.

The decrease in left ventricular volume and pressure lead to significant reductions in stress in the myocardial wall. Additionally, the continual removal of blood from the apex decreases the rate of pressure build up during contraction. This means that the opening of the aortic valve is no longer guaranteed and, if LVAD flow is sufficiently high, may not happen at all. The impact of this myocardial unloading on the short and long term functionality of the heart is unknown[107, 21].

1.2.2.1 Reverse Remodelling

LVAD support changes nearly every aspect, both structural and systemic, that is pathologically altered by heart failure. By normalising blood pressure and cardiac output, LVAD support improves perfusion to all body organs. As heart failure is considered a systemic disease, LVAD implantation has the effect of promoting system wide recovery[21].

It was initially thought that the changes associated with ventricular remodeling were permanent and no therapy could meaningfully reverse the process. This led to the idea of irreversible, end–stage cardiomyopathy. However, experiments on hearts explanted from LVAD supported patients prior to orthotropic heart transplants showed that the pressure volume relationship had nearly returned to normal[98]. This shift can be defined as 'reverse remodeling'[21]. Furthermore, at a cellular level, significant decreases in cardiomyocyte diameter are observed along with improved contractile responses to both increased frequency of stimulation, i.e. a normalised force frequency relationship, and to β–adrenergic stimulation[207]. The effect of LVAD implantation on the extracellular matrix is less clear, with conflicting studies showing either increases[103, 111] or decreases[19] in collagen content.

In a small subset of patients these changes are significant enough to enable the device to be explanted without the need for transplantation. However, the incidence of this permanent reverse remodelling is low. In one

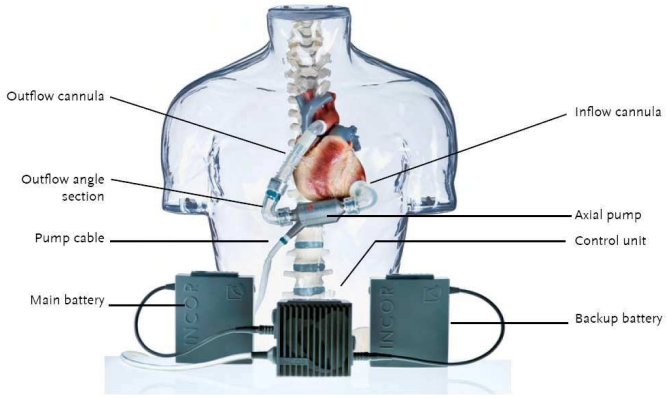

FIGURE 1.7. *Model showing an axial flow LVAD implanted in the thoracic cavity along with the external power source and leads, source Berlin Heart*[209].

study, 5 from 111 LVAD patients showed sufficient improvement to enable LVAD removal. Of these 5, 2 required a second LVAD to be implanted at a later date and the remaining 3 died of progressive heart failure[107]. Other studies show similar poor success rates for LVAD explantation[21, 75]. Exercise stress testing, including exercise hemodynamics, echocardiography and oxygen consumption, can be used to identify potentially recovered patients[107]. However, difficulties still arise in determining when a patient has demonstrated sufficient remodeling to enable the explantation of the device.

The use of LVADs as a bridge to recovery is still poorly understood. Without greater knowledge of the impact of LVADs on cardiac function and the mechanisms that underpin reverse remodelling, it is unlikely LVADs will be considered specifically for such a role in the near future.

1.2.2.2 Continuous versus Pulsatile Flow LVADs

LVADs can provide either pulsatile or continuous support to ventricular function. Pulsatile flow LVADs are pneumatically driven and can be implanted either intra or extra-corporal. While they can dynamically alter stroke volume and pump rate, and hence provide a physiological pulse profile, they are relatively large and are very susceptible to infection[173]. Maximum cardiac output is generally around 10L per minute with an ejection fraction of approximately 90%[54]. Axial flow devices, in contrast, are electromagnetically actuated and fully implantable. The axial flow motor is small and contains rotary blades that spin at 7500 to 12500rpm and can pump approximately 5 to 6L per minute against 100mmHg pressure[173]. In both device types, the electrical power cable is tunneled subcutaneously to an external power source[146], see figure 1.7.

The degree of LV pressure unloading is similar among patients supported by axial flow pump and a pulsatile device, owing to a similar reduction of mean pulmonary pressure. Left ventricular volume unloading is more pronounced with a pulsatile device owing to a statistically significant higher pump output with a pulsatile device[82]. However, the optimal degree of LV unloading during device support remains unknown. There are limited studies comparing outcome rates in patients with continuous and pulsatile flow LVADs. Studies exploring the impact of both device types on biochemical markers for brain-injury[155] and activation of the inflammatory system[100] found no differences in the early phase after LVAD surgery. Additionally, the impact

on patients suffering various medical conditions, such as medically unresponsive pulmonary hypertension and acute cardiogenic shock was found to be comparable with both device types[84].

The primary advantage of continuous flow LVADs is that they are significantly smaller and do not require venting or extra corporal cannulas. This significantly reduces the risk of infection associated with LVAD implantation[10]. As a result, continuous flow LVADs have become more prevalent in recent years[21]. Thus, for the purposes of this DPhil, we will focus on continuous axial flow LVADs due to our collaboration with Berlin Heart[209] as part of the European Union framework 7 grant euHeart[211].

1.3 Previous work

The construction of coupled fluid–solid mechanical simulations of an LVAD supported LV requires an understanding of the previous work in cardiac modelling, in particular focusing on tissue mechanics, blood flow and existing coupled fluid–solid models. Equally important is a knowledge of the solution methods used to accurately resolve the problems. This section reviews the current state of cardiac modelling along with the numerical schemes used in their solution.

1.3.1 Modelling Cardiac Mechanics

One of the first mathematical models of cardiac wall mechanics was the analytical work of Woods[208], who modelled the heart as a thin walled spherical shell. More physiologically relevant geometry was incorporated in later analytical models[120, 50], where the LV was modelled as an ellipsoid. By the 1970s, improved computational resources led to early attempts at incorporating greater complexity in geometric and material approximations. A series of finite element models were published examining the influence of more realistic model conditions. Studies found that geometry[49, 55], fibre orientation[144, 145] and constitutive behaviour[121, 71] (in particular the use of non–linear elasticity) were significant in modelling the mechanics of the heart.

Following on from the work of Hunter[67], finite element cardiac models progressed with advances in both geometric realism and the constitutive description of the non–linear tissue behaviour (see section 1.3.1.2). Subsequent models incorporated higher order finite element methods as well as descriptions of both ventricles[69, 115, 116]. The detailed quantification of the fibre and laminar structure by LeGrice *et al.*[93, 96] (outlined in section 1.1.1.1) enabled further advances in cardiac tissue modelling and was incorporated into the models of Nash[122, 123] and Stevens *et al.*[181, 182].

Much of the progression in early finite element cardiac models focused on the constitutive behaviour of the passive myocardium. Many models also considered contraction[58, 181], based on simple models that described physiological concepts such as the force–length relationship and the calcium transient[68]. The coupling of these models to models of cardiac electrophysiology[206] represented the next advance in this field. The preliminary work of Nickerson *et al.*[125, 126], developed the mechanism for coupling the electrical and mechanical aspects of heart function. These methods have been subsequently extended by Whiteley *et al.*[203] and Niederer and Smith[130]. Applying these techniques to human models has seen the field begin to address clinical problems in

patient cases[128].

The work of Nash and Hunter[69, 122, 123], along with the constitutive model developed by Costa *et al.*[27], forms the basis for the tissue model of the left ventricle used in this thesis. In their formulation, high order curvilinear finite elements are used to describe the ventricular geometry, within which a fibre architecture may be embedded.

1.3.1.1 Tissue Mechanics

Models of myocardial deformation are derived from the finite–elasticity theory for the deformation of solids, see Malvern[106]. Using the continuum hypothesis, the mechanics of solids can be described by the equations for the conservation of mass and Cauchy's first law, which expresses locally the balance of linear momentum. The standard difficulty in modelling any solid is the definition of the stress strain relationship contained within the equations. In myocardial mechanics this is generally more complex due to challenges in quantifying both the complex structure, as outlined in section 1.1.1.1, and the stress strain relationship of a tissue in vivo[177]. As such, the constitutive properties for most mechanical models are derived from histological studies[174, 175] and subsequently fitted to match clinical data[137].

In cardiac mechanics, these models are solved almost exclusively using the Galerkin Finite Element Method[123, 27, 126, 182]. By enabling the representation of continuous fields, the finite element method has enabled the incorporation of fibre architecture and tissue variation within the mathematical representation of the model.

1.3.1.2 Constitutive Laws

Due to complexities in the underlying architecture, myocardial tissue exhibits complex constitutive behaviour under deformation. Biaxial tension tests on thin sections of the ventricular myocardium show non–linear, anisotropic stress–strain behaviour. Additionally, the stress–strain relationships along each of the microstructurally relevant directions are quite different, reflecting the organisation of collagen relative to these axes[122, 123]. Constitutive laws have been developed to either reflect observed behaviour, e.g. the Costa law[27] and the Pole–zero law[68], or derived based on assumptions of the underlying micro–structure, e.g. the Langevin eight chain law[11].

Schmid *et al.*[174, 175] performed a study of three commonly used constitutive laws as well as two modified laws. The standard laws were the Costa, Pole–zero and Langevin eight chain laws, while the modified laws were a Fung–type law and the tangent law. By comparing with experimental results[36] he found that the Costa law was the most suitable to model passive myocardial mechanics in both homogeneous and non–homogeneous simple shear as well as uniaxial extension.

Parameterising cardiac constitutive relationships is complicated not only by the tissue structure, but also due to a combination of population heterogeneity and, particularly in human models, the paucity of histological samples. This has led to the development of methods to tune constitutive models to in vivo medical image data. Due to the large number of parameters present in most cardiac constitutive laws, it is not possible

find a unique fit from image data alone[214]. However, by holding the ratios between the various isotropic constants fixed and varying their magnitude, the constitutive law can be tuned to a desired pressure volume relationship[137]. Additional methods, including using data assimilation techniques to estimate local contractility from given displacements[177], have also been developed.

1.3.2 Blood Flow Modelling Techniques

Blood flow, at the macro–scale – of which the ventricular chambers can be considered – has typically been modelled using the Navier–Stokes equations. First postulated by Claude Navier (1822) and George Stokes (1845), the equations describe the motion of a Newtonian (linear) fluid which conserves mass and momentum. The equations are based on the continuum approximation whereby the particulate nature of a fluid is homogenised by bulk properties represented by continuous fields. In the Navier–Stokes equations, the stress is Newtonian, or linearly related to the rate of strain[106]. In the case of blood flow, non–Newtonian behaviour is observed at small scales, such as within blood vessels. However, for larger scale blood flow modelling the Newtonian approximation is valid[157, 204].

A wide variety of numerical techniques have been advanced for solving the Navier–stokes equations. The main methods used for problems relating to blood flow in the heart and in the great vessels include: the finite difference method[150, 151], the finite volume method[217, 172] and the Galerkin finite element method[198, 135]. Alternative methods have been attempted, including an aortic valve flow model solved using the Lattice Boltzmann method[87] and, more recently, a level-set solution of flow through the cardiac chambers[119]. These methods have not been widely used in cardiac studies therefore they will not be reviewed here.

Blood flow in the heart and great vessels is typically characterised by relatively high Reynold's numbers, as well as complex flow patterns due to their interaction with anatomical geometries. Therefore a methods applicability to a given problem rests with its capacity to efficiently resolve these two factors.

The finite difference method was used in some of the first studies of ventricular blood flow, conducted by Peskin[150, 151] and McQueen[117]. This method involves breaking the fluid domain into a lattice of points over which the operators in the Navier–Stokes equations (i.e. the gradient, divergence *etc*) may be approximated as stencils derived from a given order of Taylor series expansion[165]. This method has the advantage of being highly tractable, computationally efficient and it allows for high order approximations through increasing stencil size[104]. The method is most efficient on regular grids therefore resolving complex, anatomical, geometries is challenging. Peskin and McQueen bypassed this issue by developing the immersed boundary method[153], discussed further in section 1.3.3. This method enabled the imposition of complex geometries by superimposing boundaries over a regular computational grid. Additional studies have extended these methods to more complex problems, including simulations of diastole[97] and systole[216, 189].

Along with difficulties in describing complex geometries, finite difference methods have been criticised[200] for not fully imposing conservation due to their stencil based approach. Additionally, the application of boundary conditions in finite difference methods are problematic, particular in higher order schemes when increases in stencil size are not easily accommodated on the boundary. The finite volume method[32, 33, 40] alleviates the conservation concern by using the integral form of the Navier–Stokes equations to conserve flux between

adjacent cells, or control volumes. In three–dimensions, the fluid domain is divided into non–overlapping polyhedral graphs[101]. The Navier–Stokes operators are still approximated using a Taylor series expansion, however, this expansion now estimates facial integrals on the polyhedrons rather than point values[32, 33]. The integral form makes it easier to approximate complex geometries in low order schemes. However, for high orders, the irregularity of their cell structure inhibits large stencils. Furthermore, while the finite volume method provides improvements through volume interpolation, many of the boundary condition problems from the finite difference method remain.

The finite volume method has been used extensively in blood flow simulations, including ventricular models[24, 89, 88, 140, 169, 170, 172] (discussed further in sections 1.3.2.1 and 1.3.3) and simulations of vascular flow[72, 217, 8]. These models all involve the use of commercial CFD codes in their simulations.

The finite element method, in contrast to finite volumes and finite differences, solves for a continuous approximation of the solution over the domain of interest. Taking the weak form of the Navier–Stokes equations, the solution space is approximated by test functions which, if correctly chosen over a geometric tessellation, or mesh, approximate both the spatial and solution spaces continuously[106]. Finite element methods benefit from being able to accommodate a large range of geometrically complex domains. Additionally, boundary conditions arise naturally within this formulation, allowing more precise adherence to known boundary data. Unfortunately, finite elements are the most computationally intensive of the methods discussed here due to the complexity of integral calculations and, in some cases, the construction of large matrix systems. Additionally, unlike the finite volume method, which seeks local and global conservation, the finite element method only provides weak conservation – i.e. conservation is not sought discretely, rather continuously across an element.

The most common application of finite elements to blood flow modelling has been in simulations of flow through large vessels[198, 158] and aneurysms[48, 64]. Additionally, both Watanabe *et al.*[201, 202] and Nordsletten *et al.*[135, 137] has used this method in their LV simulations.

Building on the foundations developed by Nordsletten *et al.*[135, 134, 136], ventricular flows in this thesis are solved using the finite element method. From the work reviewed, no one method stands out as most appropriate for simulations of cardiac ventricular blood flow. The finite element model was chosen, in part, due to the wealth of mathematical theory available[190, 191, 159, 16], which enabled the robust theoretical analyses outlined in Nordsletten's work. Additionally, as shown in section 1.3.1, myocardial solid mechanics has been developed using the finite element method, as such, for a monolithic coupled scheme (see section 1.3.3.3) solving both problems using the finite element method presents a natural interface.

1.3.2.1 The Arbitrary Lagrange Eulerian Form of the Navier Stokes Equations

Simulations of blood flow within the ventricular chambers must take into account the motion of the endocardial walls of the myocardium. The models of Peskin, McQueen and colleagues (discussed above) achieve this by allowing the structural boundary to move over the computational fluid domain. However, this approach does not rigorously enforce the boundary due to its reliance on a delta function[153] to approximate the influence of the solid structure on the fluid domain. As a result, the boundaries are not clearly defined and volume conservation is not ensured close to the boundaries, i.e. leakage occurs across them.

The arbitrary Lagrange Eulerian (ALE) formulation of the Navier–Stokes equations was developed by Hirt[63] to enable Navier–Stokes problems to be solved independent of the frame of reference, i.e. it spans the reference frames from Lagrangian to Eulerian. Initially developed for finite volumes it was subsequently adapted to finite elements as well[37, 66]. The strength of this formulation is that it enables the fluid domain to move, allowing the boundaries to be dynamic. The problems with immersed boundary models no longer occur as boundary motion can be directly applied.

Using this approach, modelling blood flow within the cardiac chambers based on prescribed wall motion has become relatively common in recent years[24, 140, 172, 169, 170]. Taking myocardial motion directly from image data, these models have been used to simulate ventricular flow through the full cardiac cycle. However, due to limitations in the ability of imaging modalities to capture the full three dimensional motion of the myocardium, for example movement normal to the image plane, it is difficult to accurately prescribe boundary motion. Additionally, the absence of a myocardial model, means this approach lacks both a predictive capacity and the ability to analyse the interaction between blood flow and the myocardium. As such they are insufficient for understanding the mechanisms of heart function and therefore provide limited value to the study of heart function and disease.

1.3.2.2 Coupling Lumped Parameter Models to 3D Blood Flow Problems

One of the principle challenges in modelling fluid flow in three dimensional systems is defining boundary conditions, particularly in instances where flow enters or leaves the system (*i.e.* inflow/outflow boundaries). In blood flow modelling, the classical approach has been to obtain boundary conditions by estimations or measurements of the physical boundaries of interest[142, 149]. While this approach provides a good approximation of flow behaviour on the boundaries, it is not responsive to changes in the modelled region. As a result, it is often desirable to couple the three dimensional model to lumped parameter (typically 0D or 1D) representations of the upstream and downstream systems. In the case of blood flow modelling, these representations typically represent aspects of the systemic and pulmonary networks. However, given that the physical system is by nature three dimensional, lumped parameter representations can only provide averaged values for the quantities of interest (such as flow rate and pressure). As a result, the interface between the 3D model and the lumped parameter system represents a non–physical discontinuity, whereby flow and pressure are completely described on one side of the interface, while on the other only partial representations exist. Due to this discontinuity, modelling the interface between lumped parameter and 3D models creates specific numerical challenges.

If the mean lumped parameter values are directly applied as boundary conditions (*i.e.* Neumann tractions) on the lumped parameter/3D interface, numerical instabilities arise since the mean quantities lack the spatial resolution of the 3D boundary. In effect the problem is poorly constrained. Various methods have been developed to solve this issue[43, 79, 158, 198]. These broadly fall into two categories, prescribed flow rate[158], where the flux across the boundary is imposed as a constraint, and mean pressures[80, 79], where the flux is a consequence of the pressure difference over the 3D/lumped parameter interface. In both cases, to ensure the well posedness of the numerical scheme, either constraints need to be applied that govern the shape of the flow profile[80], or inflow/outflow cannulas are required to regularise boundary flow[158]. Alternative constraints do exist, for example Formaggia *et al.*[44] proposed a total pressure based boundary condition based on energy flux, however these typically require alternative formulations of the governing equations and are therefore complex

to implement.

In a practical sense, it has been shown by Blanco *et al.*[12] that by iteratively updating the lumped parameter system based on changes in the 3D model in response to flux across the boundary, the two categories (boundary flow rate and mean pressures) are effectively the same. However, their relative equivalence is dependent on the realism (compared with the 3D system) of the lumped parameter approximations of pressure and/or flow rate. As a result, due to the limited spatial information provided by lumped parameter models, no reliable solutions in regions near the lumped parameter/3D interface can be expected. Therefore the choice of coupling method should be chosen based on the problem of interest and the complexities of computational implementation[12]. Additionally, it should be noted that *a priori* knowledge is often required if constraints are made on the shape of the flow profile. As this information is normally not available, it is preferable to distance the lumped parameter/3D interface from the region of interest.

1.3.3 Coupling Fluid-Solid Mechanics in the Heart

The coupling of fluid solid problems requires the conservation of both kinematic and force transduction across the common interface of the fluid and solid. While these mechanisms are straightforward, their numerical implementation is often more complex. This section reviews the various approaches to fluid–solid coupling used in cardiac problems.

As with fluid flow, the pioneering work in coupled fluid–solid models in the ventricles was performed by Peskin and McQueen[117, 118, 154, 152]. Their immersed boundary method – which imposes fibre-like constraints within a fluid – uses feedback between the force acting on the fluid and the fibres to mimic solid response, effectively modelling the myocardium as a series of 1D fibres. Models using this method incorporated many of the gross structural features of the heart including, in their most complex form, all four chambers of the heart, the inflow and outflow valves for both ventricles as well as the ascending aorta and main pulmonary artery. No subsequent model has attempted to include as many geometric features.

Unfortunately, using this method to simulate the coupled fluid–solid mechanical function of the heart has both mathematical and physiological drawbacks. Along with the volume conservation issue discussed in section 1.3.2.1, the method provides non-standard discretisations of surfaces, making it challenging to address the convergence and estimation properties of the method (along with its stability). Additionally, the accuracy of modelling materials as collections of fibres has not been addressed, bringing into question the efficacy of the method for simulating the mechanical behaviour of solids. Furthermore, as part of the method, the myocardial model is immersed in a fluid box. As such, forces act not just on the endocardium but also on the epicardial surface. Momentum effects due to interactions between the exterior wall and the encasing fluid produce unknown effects on the material response of their model.

1.3.3.1 Coupled Fluid–Solid Ventricular Simulations

Considering finite volume and finite element methods, a substantial body of work exists on numerical schemes designed to couple fluid and solid problems. A variety of approaches exist both in terms of mesh conformity[31] –

i.e. whether fluid and solid degrees of freedom 'match' on the interface – and solution methods, including both partitioned and monolithic schemes, section 1.3.3.3 discusses their relative merits. In all of these approaches, the solid can be approximated using complex constitutive laws and the other issues associated with the Peskin and McQueen model are not present.

Due to the substantial differences in the behaviour of fluid and solid problems, for numerical reasons it is desirable to use non–conforming schemes in problems of blood flow coupled to tissue mechanics. Otherwise, one of the domains will be either over or under refined, affecting either computational cost or solution accuracy.

The predominant cardiovascular application of these standard coupled fluid–solid methods has been in vascular modelling. Coupled models have been developed to analyse flow features and wall stress in problems including arterial flow[22, 42], cerebral[7] and aortic aneurysms[109] and vascular stents[99, 127].

In ventricular modelling, Watanabe *et al.*[201, 202] constructed the first 3D coupled finite element model of the LV. They incorporated simple models of electrophysiology, mechanics and blood flow into a single monolithic modelling scheme. The model, however, requires complete conformity of fluid–solid components, limiting the size of the model for numerical purposes. As such, while most individual models require upwards of 50,000 elements for the fluid domain[134], the most refined Watanabe model has less that 10,000. In addition to the lack of spatial resolution, their method relies on low order finite elements which, in general, fail theoretical requirements[17] and affect solution convergence and accuracy.

A more numerically rigorous coupled ventricular model was developed by Cheng *et al.*[24] and subsequently improved upon by Krittian *et al.*[88] and Shenkel *et al.*[172]. They developed a coupled finite volume (fluid)/finite element (solid) non–conforming approach enabling appropriate numerical resolution for resolving both the fluid and solid components. Of note, is Krittian's pressure driven phantom validation study[89] which demonstrated good agreement between their model and the physical system. However, due to methodological constraints (discussed in section 1.3.3.3), they could not easily incorporate modern developments in myocardial constitutive laws. Instead they modelled the myocardium as either a thin shelled hyperelastic material (Cheng) or approximated the laminar structure using a layered composite approach (Krittian).

Finally, Nordsletten *et al.*[135, 134, 136] developed a finite element fluid–solid non–conforming monolithic coupling scheme using a Lagrange multiplier approach to equate tractions on the coupling interface. They performed rigorous theoretical and numerical analysis on their methods, ensuring solution accuracy and stability and convergence. The scheme enables the optimisation of element types as well as spatial resolution for both fluid and solid sub problems. Incorporating complex constitutive laws, they have performed simulations of LV function in diastole and systole[137].

1.3.3.2 Fluid–solid coupling using Fictitious Domain

An alternative coupling approach, of particular interest to this thesis due to their capacity to resolve rigid bodies immersed in fluids (of which the LVAD cannula can be considered), are fictitious domain (FD) methods. These have been used most notably in valve modelling[60, 183, 197]. Effectively the integral form of the immersed boundary method, they define surfaces immersed in fluid and therefore can be directly applied as boundaries onto three dimensional solids, avoiding the constitutive limitations of immersed boundary methods.

Additionally, unlike the immersed methods, FD methods have been thoroughly analysed for fluid mechanical problems by Girault *et al.*[51] and Babuska *et al.*[2]. Through this work, the solutions using FD were proven stable and convergent. The primary challenge for fictitious domain methods is defining the integral of the immersed surface and the intersecting fluid elements. This is particularly difficult for higher order spatial discretisations.

1.3.3.3 Partitioned versus Monolithic schemes

There are two broad approaches for solving coupled fluid–solid mechanical schemes, partitioned and monolithic. In partitioned schemes, each problem is solved separately using individually tailored solvers. Monolithic schemes, in contrast, solve both problems as a single system. The optimal method depends strongly on problem type.

Partitioned schemes take either a strong or weak coupling approach. Strong coupling involves fixed–point methods[35] that iterate towards minimisation. Weak coupling, in contrast, approximates the coupled condition through time using staggered or augmented time stepping[39]. Weakly coupled methods tend to be more computationally efficient and less stable than strong schemes. For systems with strong fluid–solid interactions, more robust, strongly coupled systems are often necessary.

In cardiovascular modelling, most partitioned approaches have involved combining multiple commercial software packages. These are often highly optimised for their respective problems. However, their use limits the ability to generate bespoke simulations – for example in the choice of constitutive law. This is evidenced in the constitutive limitations in the Cheng, Krittian and Schenkel models (section 1.3.3). Additionally, implementation of new numerical schemes within these packages is difficult.

In monolithic schemes, the fluid and solid subproblems are typically coupled either directly or using Lagrange multipliers[194]. In general, this makes monolithic coupling techniques more stable[4, 5]. However, due to often different problem behaviours, solvers cannot be optimised to the individual problems. Additionally, as these methods produce one large global system, computational efficiency is limited by the efficiency of the linear solver used. Furthermore, these methods are typically employed for coupling problems that have consistent numerical methods – e.g. both problems are solved using finite elements/volumes etc.

Due to the lack of dominance of either the fluid or solid sub problem in coupled fluid–solid ventricular simulations, monolithic solvers represent a more reliable, stable numerical scheme[61, 136].

1.3.4 Computational LVAD Models

LVADs have been the subject of multiple numerical studies. Much work has focused on simulating flow through the LVAD pump. These simulations have addressed a wide range of quantitative questions relating to pump function including optimal pump design[193] and estimating rates of cell damage using statistical models[180].

Away from simulations of blood flow through the pump, there have been simulations performed on the effect of LVAD implantation on blood flow in the aorta[110, 73]. Recent studies include Bazilevs *et al.*[6] who used a

fluid–structure interaction model to analyse the LVADs impact on Aortic wall stress and Brown *et al.*[18] who evaluated aortic flow fields at different anastomosis locations within a patient specific aortic geometry.

To our knowledge, this work represents the first computational study on the impact of LVADs on blood flow within the ventricles.

1.4 Thesis Overview

Chapter 2: Beginning with the conservation laws that underpin the finite element methods used in this thesis, chapter 2 presents the models and numerical methods that were developed to solve fluid–solid interaction problems in an LVAD supported LV. The methods outlined in this chapter underpin all the results presented in the thesis. Novel contributions included incorporating a fictitious domain method within an ALE fluid mechanics scheme and modifications to the Newton–Raphson/line search numerical scheme.

Chapter 3: Several new numerical schemes and methods were implemented as part of this thesis. Chapter 3 outlines a series of canonical test problems designed to investigate their impact on system convergence and performance. These problems test the convergence behaviour of the fictitious domain scheme, along with the impact of the implemented numerical methods on overall computational performance. Additionally, this chapter presents a study on the impact of basis functions on problems with high tension solids (relevant with respect to myocardial contraction) and an investigation into coupling with lumped parameter models.

Chapter 4: The object of this thesis is to investigate left ventricular function under left ventricular assist device support. Chapter 4 introduces the left ventricular model, outlining a novel mesh structure and geometric fitting procedure, a particle tracking algorithm, and a method developed for fitting passive myocardial parameters. This chapter also presents the results of several studies, including a comparison of diastolic filling in normal and LVAD supported hearts, an investigation into the impact of using a fictitious domain to prescribe the LVAD cannula on ventricular flow, and a study of the importance of LVAD cannula length on residence times in the LV.

Chapter 5: To fully understand the impact of LVAD support on ventricular function, simulations of the full cardiac cycle are required. To accomplish this, a biophysically based model of cardiac contraction, along with a lumped parameter representation of the circulatory networks, are introduced in chapter 5. These were coupled to a simulation of the cardiac cycle under LVAD support which was solved through 3 heart beats, converging on a repeating pressure volume loop. Two analyses were performed on these results, the first comparing the residence times of blood at different seed points during diastole, and the second investigating the impact of fluid on the energy relationships in myocardial models, performing a comparison with an equivalent solid only model.

Chapter 6: This chapter introduces a patient LV model constructed from CT images taken from an LVAD implant patient. A study of the impact of different LVAD flow regimes was performed, investigating the impact of both constant and variable flow on ventricular hemodynamics and myocardial behaviour. Analyses were performed examining the impact of LVAD flow on energy transfer in the myocardium, along with residence times of fluid in the ventricle. This study represents the first fluid–solid coupled study of a failing LV under

LVAD support.

Chapter 7: In this thesis, novel numerical methods and computational models were developed to solve fluid–solid interaction problems in an LVAD supported ventricle. The framework developed presents numerous methodological and physiological opportunities for future investigation. Chapter 7 discusses both model limitations and directions for future reseach. Extension of the methodology developed in this thesis, along with greater clinical data, will extend the models physiological realism and applicability to patient specific problems.

Part I

Model Development and Verification

2 Finite Element Models for Simulating Cardiac Function

To provide a physiological description of the myocardium and ventricular blood flow, a model must be derived from the physical laws that govern the behaviour of each system along with the conditions that describe their interaction. Based on the mathematical laws of mass and momentum conservation, combined with constitutive laws based on empirical data, continuum mechanics provides a framework for developing this model.

In this chapter, a continuum model, solved using the Galerkin finite element method[52], is derived to describe the behaviour of blood flow and myocardial deformation, as well as their interaction. To enable the maximum range of cardiac motion in the presence of the LVAD cannula, the model must be capable of representing the interaction of fluid immersed rigid bodies and elastic solid boundaries. A fictitious domain (FD) approach is developed to address this issue. While the model was developed to solve a specific problem, this chapter presents the derivation and implementation of a general model describing the behaviour and interactions of quasi–static hyperelastic solids and incompressible Navier–Poisson fluids.

This chapter, firstly, outlines the mathematical definitions and laws that underpin the model (section 2.1). Secondly, it presents the model problems (section 2.2), before defining the discrete forms of these problems (section 2.3) and the global system within which they are solved (section 2.4). Finally, the solution methods used to build and solve the global system are discussed (section 2.5), along with the software package, cHeart, within which the model is solved (section 2.6). Additional descriptions of the methods are outlined in Nordsletten *et al.*[136], McCormick *et al.*[113] and McCormick *et al.*[114].

2.1 Problem Foundations

Before defining the model problems, it is necessary to outline some standard mathematical definitions, as well as the conservation laws from which the continuum models in this thesis are derived. This section introduces the mathematical notation (section 2.1.1), the conservation laws of mass and momentum (section 2.1.2) and defines the constitutive laws that govern the behaviour of Navier–Poisson fluids and hyperelastic solids (section 2.1.3).

2.1.1 Definitions

Both the solid and fluid problems can be represented geometrically by moving domains, $\Omega_i \subset \mathbb{R}^d \times I$, that alter shape through the time interval $I = [0, T]$ with a coordinate system $\mathbf{x}$ (note $i = [f, s]$ and d is the dimension

of Ω_i). The boundary of each domain is treated as continuous and is partitioned so that $\Gamma_i = \Gamma_i^N \oplus \Gamma_i^D \oplus \Gamma_i^C$, where N, D and C refer to the Neumann, Dirichlet and coupling subdomains of the boundary respectively. The domain, Γ_c, represents the coupling interface, where $\Gamma_c := \Gamma_f^C = \Gamma_s^C$. The fictitious domain problem is posed on the domain Γ_{Fd}, where Γ_{Fd} is an interior manifold in Ω_f, see figure 2.1. For the problems presented in this thesis, the coupling is normally performed between solid and fluid problems. However, the methods outlined in this chapter are general and can equally apply to the coupling of two fluid or two solid domains, in which case, $\Gamma_c := \Gamma_{f_1}^C = \Gamma_{f_2}^C$ or $\Gamma_c := \Gamma_{s_1}^C = \Gamma_{s_2}^C$.

2.1.1.1 Reference Frames

Considering a particle within Ω, different reference frames can be used to define the velocity of the particle at time t. The two most commonly used reference frames are the Eulerian, where the material velocity $\mathbf{v}$ is defined with respect to a fixed coordinate, and the Lagrangian, where the reference frame moves with the motion of the particle. Both the Eulerian and Lagrangian descriptions are effectively subsets of the Arbitrary Lagrange–Eulerian (ALE) reference frame in which the motion of the particle and the motion of the reference frame are independent of each other[134].

Due to their different material behaviours, solid mechanics problems are typically solved using a purely Lagrangian material description, while fluid problems on a moving domain are normally solved within the more general ALE framework.

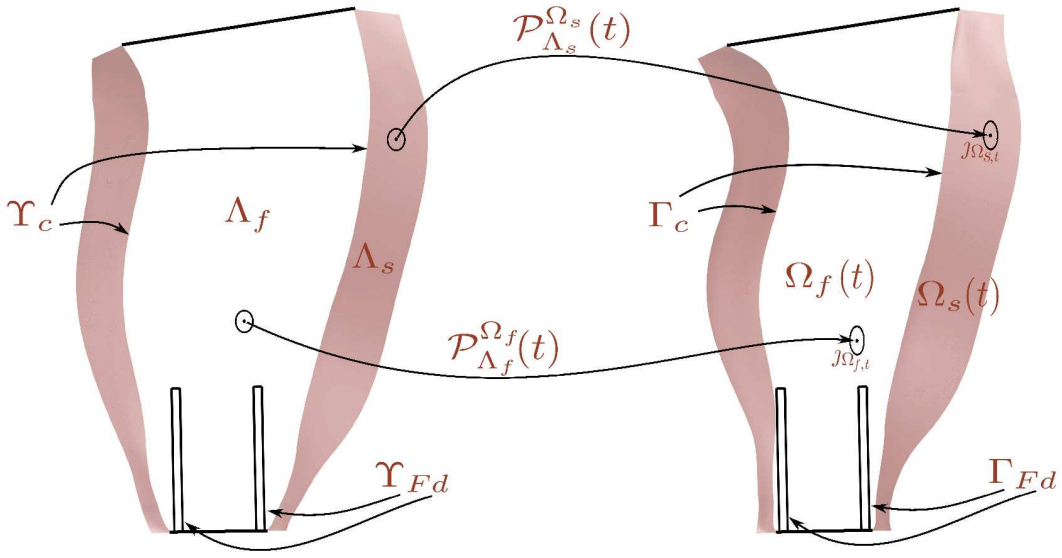

Figure 2.1. *The reference domains, Λ, left, physical domains, Ω, right. The mappings $\mathcal{P}^{\Omega}_{\Lambda}$ take a point in Λ and map it to Ω. The mapping Jacobians, $\jmath_{\Omega,t}$, represent the local volume change induced by the mappings.*

2.1.1.2 Preliminary notation

It is convenient to pose the Lagrangian (solid) and ALE (fluid) problems on a static reference domain Λ ($\Lambda = [\Lambda_f, \Lambda_s]$ depending on the problem), with the boundary Υ and coordinate system $\boldsymbol{\eta}$[114, 113, 136], see figure 2.1. For each transient physical domain, $\Omega(t)$, a bijective mapping to Λ is defined as $\mathcal{P}^{\Lambda}_{\Omega} : \Omega(t) \rightarrow \Lambda$. The mapping transforms all points $\mathbf{x} \in \Omega(t)$ to points $\boldsymbol{\eta} \in \Lambda$, simplifying the problem description – *i.e.*

$$\mathcal{P}^{\Lambda}_{\Omega} : \Omega(t) \rightarrow \Lambda\,, \quad \boldsymbol{\eta} = \mathcal{P}^{\Lambda}_{\Omega}(\mathbf{x}, t)\,, \;\; \forall \mathbf{x} \in \Omega(t)\,, \;\; \forall \boldsymbol{\eta} \in \Lambda, \;\; \forall t \in I. \tag{2.1}$$

The inverse, $\mathcal{P}^{\Omega}_{\Lambda}$, performs the reverse mapping. Additionally, $\mathcal{P}^{\Lambda}_{\Omega}$ is defined so that regions on the physical boundary, Γ, map to regions on the reference boundary Υ.

A function, $\mathbf{f}$, defined on Λ, can be represented on Ω as $\hat{\mathbf{f}}$,

$$\hat{\mathbf{f}}(\mathbf{x}, t) := \mathbf{f}(\boldsymbol{\eta}, t)\,, \quad \mathbf{x} = \mathcal{P}^{\Omega}_{\Lambda}(\boldsymbol{\eta}, t)\,, \;\; \forall \mathbf{x} \in \Omega\,, \;\; t \in I. \tag{2.2}$$

Considering its temporal rate of change, $\partial_t \hat{\mathbf{f}}$ represents the change in the field $\mathbf{f}$ along some trajectory in Ω. $\partial_t \hat{\mathbf{f}}$ is defined at any fixed coordinate $\boldsymbol{\eta} \in \Lambda$ as,

$$\partial_t \hat{\mathbf{f}}(\mathbf{x}, t) := \lim_{\delta \rightarrow 0} \frac{\mathbf{f}(\boldsymbol{\eta}, t + \delta) - \mathbf{f}(\boldsymbol{\eta}, t)}{\delta}, \;\; \boldsymbol{\eta} \in \Lambda. \tag{2.3}$$

This ALE derivative is related to the Lagrangian (D/Dt) and Eulerian ($\partial/\partial t$) derivatives by,

$$\frac{D}{Dt}\bar{\mathbf{f}} = \frac{\partial}{\partial t}\hat{\mathbf{f}} + \mathbf{v} \cdot \nabla_{\mathbf{x}} \hat{\mathbf{f}} = \partial_t \mathbf{f} + (\mathbf{v} - \mathbf{w}) \cdot \nabla_{\mathbf{x}} \hat{\mathbf{f}}, \tag{2.4}$$

where $\bar{\mathbf{f}}$ represents the Lagrangian projection of $\mathbf{f}$, $\mathbf{w} = \partial_t \mathcal{P}^{\Omega}_{\Lambda}$ is the domain velocity and $\mathbf{v}$ is equivalent to the fluid/solid material velocity. Note that when $\mathbf{v} = \mathbf{w}$, ∂_t is simply the Lagrangian time derivative, D/Dt.

The gradients, $\nabla_{\mathbf{x}}$ and $\nabla_{\boldsymbol{\eta}}$, on Ω and Λ respectively, are related by the deformation gradient tensor, $\mathbf{F}_t$, where[1],

$$\nabla_{\mathbf{x}} = \mathbf{F}_t^{-T} \nabla_{\boldsymbol{\eta}}, \;\; \mathbf{F}_t = \nabla_{\boldsymbol{\eta}} \mathcal{P}^{\Omega}_{\Lambda}(\boldsymbol{\eta}, t), \tag{2.5}$$

so that, the gradient of $\hat{\mathbf{f}}$ on Ω is,

$$\nabla_{\mathbf{x}} \hat{\mathbf{f}} = (\mathbf{F}_t^{-T} \nabla_{\boldsymbol{\eta}}) \mathbf{f}. \tag{2.6}$$

Finally, using the framework defined in this section, an integral on $\Omega(t)$ at some time t can be defined on Λ in terms of the weighted integral,

$$\int_{\Omega(t)} \hat{\mathbf{f}} \mathbf{dx} = \int_{\Lambda} \mathbf{f} \jmath_{\Omega,t} \mathbf{d}\boldsymbol{\eta}\,, \quad \jmath_{\Omega,t} = det\,|\mathbf{F}_t|\,. \tag{2.7}$$

[1]Note that for any two vectors $\mathbf{v}, \mathbf{w} \in \mathbb{R}^d$, $\mathbf{vw}$ denotes the dyadic product, *i.e.* $\mathbf{vw} \in \mathbb{R}^{d \times d}$ where, $(\mathbf{vw})_{ij} = \mathbf{v}_j \mathbf{w}_i$.

2.1.2 Conservation Laws

Conservation laws define mathematically the physical laws that govern the behaviour of material bodies. These laws define the transfer of physical quantities within a closed system. The continuum equations governing the motion/deformation of a fluid/solid are derived from the conservation laws for mass and momentum. In addition, the space conservation law is required to ensure that the volume induced on Λ by $\jmath_{\Omega,t}$ is preserved. This section outlines the relevant conservation laws required to formulate the equations of fluid and solid mechanics. The space conservation law is given in equation 2.8, while the ALE formulations of the conservation of mass and momentum equations are defined in equations 2.9 (mass) and 2.13 (momentum).

2.1.2.1 Space Conservation Law

The space conservation law (SCL) is independent of the physical system and material body, sometimes referred to as the Euler Expansion formula[132], it is an inherent property of the mapping $\mathcal{P}^{\Lambda}_{\Omega}$. As a differential conservation law, it is defined as,

$$\partial_t \jmath - \jmath \nabla_{\mathbf{x}} \cdot \mathbf{w} = 0, \quad \text{on } \Lambda. \tag{2.8}$$

This equation holds for any map for which the mapping Jacobian, $\jmath = \jmath_{\Omega,t}$, and rate of change ($\mathbf{w}$) are well defined[134].

2.1.2.2 Conservation of Mass

The mass conservation law is a balance law for the mass per unit volume (or density), ρ. For the problems outlined in this thesis, mass can neither be created or destroyed. Rather, it is transferred throughout the domain by either physical advection (*i.e.* due to the material velocity $\mathbf{v}$), or through domain movement. As a differential conservation law, the ALE form of mass conservation is defined as,

$$\partial_t(\rho\jmath) + \jmath \nabla_{\mathbf{x}} \cdot \rho(\mathbf{v} - \mathbf{w}) = 0 \quad \text{on } \Lambda. \tag{2.9}$$

Incorporating the space conservation law, equation 2.8, enables the ALE form of the law, if ρ is constant in space, to be simplified to,

$$\partial_t(\rho) + \rho \nabla_{\mathbf{x}} \cdot \mathbf{v} = 0 \quad \text{on } \Lambda. \tag{2.10}$$

Note that this is identical to posing the law in the Eulerian coordinate frame as, in that case, the Jacobian of the mapping, $\partial_t \jmath$, and the domain velocity, $\mathbf{w}$, equal zero. Alternatively, considering a Lagrangian definition of Ω, where the domain and material velocities are equal, the law can be rewritten as,

$$\partial_t(\rho\jmath) = 0 \quad \text{on } \Lambda. \tag{2.11}$$

For incompressible problems, including those solved in this thesis, ρ is defined as a spatiotemporal constant. This simplifies equations 2.11 and 2.10 to the standard Lagrangian and ALE/Eulerian incompressibility constraints,

$$\partial_t \jmath = 0, \qquad \nabla_{\mathbf{x}} \cdot \mathbf{v} = 0. \tag{2.12}$$

2.1.2.3 Conservation of Linear Momentum

The conservation of linear momentum, or Cauchy's first Law[106], governs nearly all systems in continuum mechanics. Momentum may be physically advected by underlying motion or induced by surface traction, or stress. Additionally, momentum can be created within a body by forces such as gravity. As a differential conservation law, the ALE formulation is defined as,

$$\partial_t(\rho \mathbf{v} \jmath) + \jmath \nabla_{\mathbf{x}} \cdot [\rho(\mathbf{v} - \mathbf{w})\mathbf{v} - \boldsymbol{\sigma}] - \mathbf{f}\jmath = 0 \quad \text{on} \quad \Lambda, \tag{2.13}$$

where $\mathbf{f}$ represents a force responsible for the generation of momentum and $\boldsymbol{\sigma}$ is a $d \times d$ tensor typically referred to as the Cauchy stress tensor[106]. As in section 2.1.2.2, defining 2.13 in the Lagrangian frame, the law may be written as,

$$\partial_t(\rho \mathbf{v} \jmath) - \jmath \nabla_{\mathbf{x}} \cdot \boldsymbol{\sigma} - \mathbf{f}\jmath = 0 \quad \text{on} \quad \Lambda. \tag{2.14}$$

For incompressible problems, the advective term in equation 2.13 ($\nabla_{\mathbf{x}} \cdot (\rho(\mathbf{v} - \mathbf{w})\mathbf{v})$) can be reduced. Including the SCL, equation 2.8, and the ALE incompressibility constraint, equation 2.12,

$$\nabla_{\mathbf{x}} \cdot (\rho(\mathbf{v} - \mathbf{w})\mathbf{v}) = \rho(\mathbf{v} - \mathbf{w}) \cdot \nabla_{\mathbf{x}}\mathbf{v} + \rho\mathbf{v} \left(\nabla_{\mathbf{x}} \cdot (\mathbf{v} - \mathbf{w})\right) \tag{2.15}$$

$$= \rho(\mathbf{v} - \mathbf{w}) \cdot \nabla_{\mathbf{x}}\mathbf{v} - \frac{\rho\mathbf{v}}{\jmath}\partial_t \jmath. \tag{2.16}$$

Consequently, equation 2.13 can be redefined as,

$$\rho\partial_t(\mathbf{v}) + \rho(\mathbf{v} - \mathbf{w}) \cdot \nabla_{\mathbf{x}}\mathbf{v} - \nabla_{\mathbf{x}} \cdot \boldsymbol{\sigma} - \mathbf{f} = 0 \quad \text{on} \quad \Lambda. \tag{2.17}$$

This is the non–conservative form of the ALE momentum conservation equation (as opposed to the conservative form in equation 2.13) and will be used for the remainder of this section. For an analysis of the two forms in ALE Navier–Stokes problems see Nordsletten *et al.*[135, 134].

2.1.2.4 Conservation of Angular Momentum

An additional requirement of the laws governing the behaviour of physical systems, is the conservation of angular momentum. If linear momentum is conserved, angular momentum depends solely on the symmetry of the Cauchy stress tensor[106], *i.e.*

$$\boldsymbol{\sigma} = \boldsymbol{\sigma}^T. \tag{2.18}$$

While the stress tensor is often experimentally defined, the functional form is constructed by restricting it to forms that guarantee symmetry of Cauchy stress, see section 2.1.3. As a result, angular momentum is conserved via the conservation of linear momentum.

2.1.3 Constitutive Relationships

An adequate definition of stress is required in order to use the conservation laws to model the mechanics of materials. Constitutive laws describe the behaviour of a material in response to different loading conditions.

Characterising this behaviour is inherently empirical, therefore, defining its functional form (the Cauchy stress tensor) is complex. For the mechanics of bodies at steady temperature/pressure, the definition of stress is usually simplified through dependence on kinematic quantities, such as strain or rate of deformation. The mathematical descriptions of these relationships are referred to as constitutive equations.

In many cases it is experimentally challenging to measure Cauchy stress, particularly with respect to hyperelastic materials where the body deforms under load. As a result, it is often necessary to define the constitutive law with respect to the undeformed configuration – the first and second Piola Kirchoff stress tensors – and use the deformation gradient tensor, $\mathbf{F}$, to map the resulting stresses back to the deformed state, *i.e.* the Cauchy stress tensor.

This thesis focuses on both fluid and solid problems. Fluid problems will be defined using the Navier–Poisson constitutive law. For solid problems, a number of constitutive laws are used and will be defined as the models arise. A generic form is provided in section 2.1.3.2

2.1.3.1 Navier–Poisson Fluids

The ALE Navier–Stokes equations for an incompressible, Newtonian fluid are derived from equations 2.12 and 2.13 incorporating the Navier–Poisson law for a Newtonian fluid[106]. The law defines the Cauchy stress tensor as,

$$\boldsymbol{\sigma}_f = -p\mathbf{I} + \mu\mathcal{D}_{\mathbf{x}}\mathbf{v}, \tag{2.19}$$

where μ is viscosity (considered constant in space and time for this thesis), $\mathbf{I}_{jk} := \delta_{jk}$, and the operator, $\mathcal{D}_{\mathbf{x}}\mathbf{v} = \nabla_{\mathbf{x}}\mathbf{v} + \mathbf{v}\nabla_{\mathbf{x}}$. Using this, the ALE Navier–Stokes problem can be defined.

The law is the most widely applied fluid model. In addition to experimental results suggesting the appropriateness of the model for a large class of fluids[92], equation 2.19 satisfies the symmetry requirement of angular momentum (see section 2.1.2.4).

2.1.3.2 Hyperelastic Incompressible Solids

For hyperelastic solids the stress tensor is defined from an isochoric strain energy function, W, specific to the material. W is related to the Cauchy stress tensor by the relation,

$$\boldsymbol{\sigma}_s = -p\mathbf{I} + \frac{1}{2}\mathbf{F}\left(\frac{\partial W}{\partial \mathbf{E}} + \left(\frac{\partial W}{\partial \mathbf{E}}\right)^T\right)\mathbf{F}^T, \tag{2.20}$$

where

$$\mathbf{E} = \frac{1}{2}\left(\mathbf{F}^T\mathbf{F} - \mathbf{I}\right) \tag{2.21}$$

is the Green strain tensor[106].

Different solids exhibit vastly different strain energy relationships, therefore, there is no generic functional form of the stress equation. As a result, in this thesis, the strain energy functions will be defined on a problem specific basis. Taking this into consideration, the finite elasticity problem can be defined.

2.2 Problems

In this section the model problems and weak forms of the ALE Navier Stokes and quasi–static finite elasticity equations are defined based on the foundations outlined in section 2.1. Additionally, two further problems are defined: a Lagrange multiplier coupling constraint (defining the conditions on the interface, Γ_c, between two coupled domains) and a fictitious domain constraint describing fluid immersed rigid bodies.

2.2.1 Model Problems

Using the definitions outlined in section 2.1.1 and the conservation laws and constitutive relationships outlined in sections 2.1.2 and 2.1.3, the model problems can be derived. Four problems are defined, ALE Navier–Stokes, finite elasticity, fluid–solid coupling and fictitious domain.

2.2.1.1 ALE Navier-Stokes Equations

Taking the Navier–Poisson stress relationship, equation 2.19, the ALE Navier–Stokes problem can be defined. The bijective ALE mapping, $\mathcal{P}^{\Omega_f}_{\Lambda_f}$, is arbitrary as long as it adheres to movement on the coupled boundary, see section 2.3.1.4.

Let $\mathbf{v}$ and p be the velocity and pressure state variables, which satisfy,

$$\rho\partial_t(\mathbf{v}) + \rho(\mathbf{v}-\mathbf{w})\cdot\nabla_{\mathbf{x}}\mathbf{v} + \nabla_{\mathbf{x}}p - \mu\nabla_{\mathbf{x}}\cdot\mathcal{D}_{\mathbf{x}}\mathbf{v} = \mathbf{f}_f \text{ in } \Omega_f, \tag{2.22a}$$

$$\nabla_{\mathbf{x}}\cdot\mathbf{v} = 0 \text{ in } \Omega_f, \tag{2.22b}$$

$$\mathbf{v} = \mathbf{g}_f^D \text{ on } \Gamma_f^D, \tag{2.22c}$$

$$(\mu\mathcal{D}_{\mathbf{x}}\mathbf{v} - p\mathbf{I})\cdot\mathbf{n} = \mathbf{g}_f^N \text{ on } \Gamma_f^N, \tag{2.22d}$$

$$\mathbf{v}(\cdot, t=0) = \mathbf{g}_f^0 \text{ on } \Omega_f, \tag{2.22e}$$

where $\mathbf{n}$ is the outward boundary normal, $\mathbf{f}_f$ is the contribution to momentum of body forces, $\mathbf{g}_f^D = \mathbf{g}_f^D(\mathbf{x}, t)$ and $\mathbf{g}_f^N = \mathbf{g}_f^N(\mathbf{x}, t)$ are the given Dirichlet and Neumann boundary conditions and $\mathbf{g}_f^0(\mathbf{x}, 0)$ are the initial conditions.

2.2.1.2 Finite-Elasticity Equations

Hyperelastic, incompressible solids, particularly in cardiac modelling[123], are usually modelled using the quasi–static assumption whereby momentum effects (*i.e.* $\partial_t(\rho\mathbf{v}\jmath)$) are ignored. Taking the Lagrangian formulation – where $\mathbf{v} = \mathbf{w}$ and $\mathbf{v}$ describes the rate of change of the material displacement $\mathbf{u}$ – the reference domain, Λ_s, is chosen to be the undeformed state of the solid. In this case, the mapping $\mathcal{P}^{\Omega_s}_{\Lambda_s}(t) := \mathbf{u}(\boldsymbol{\eta}, t) + \boldsymbol{\eta}$. From these assumptions, the finite–elasticity problem can be defined.

Let $\mathbf{u}$ and p be the displacement and pressure state variables, which satisfy,

$$\nabla_{\mathbf{x}} \cdot (\hat{\boldsymbol{\sigma}}_s(\mathbf{u}) - p\mathbf{I}) = \mathbf{f}_s \text{ in } \Omega_s, \tag{2.23a}$$

$$\partial_t J = 0 \text{ in } \Omega_s, \tag{2.23b}$$

$$\mathbf{u} = \mathbf{g}_s^D \text{on } \Gamma_s^D, \tag{2.23c}$$

$$(\hat{\boldsymbol{\sigma}}_s(\mathbf{u}) - p\mathbf{I}) \cdot \mathbf{n} = \mathbf{g}_s^N \text{on } \Gamma_s^N, \tag{2.23d}$$

$$\mathbf{u}(\cdot, t = 0) = \mathbf{g}_s^0 \text{on } \Omega_s, \tag{2.23e}$$

where $\boldsymbol{\sigma}_s = \hat{\boldsymbol{\sigma}}_s - p\mathbf{I}$, $\mathbf{n}$ is the outward boundary normal, $\mathbf{f}_s$ is the contribution to momentum of body forces, $\mathbf{g}_s^D = \mathbf{g}_s^D(\mathbf{x}, t)$ and $\mathbf{g}_s^N = \mathbf{g}_s^N(\mathbf{x}, t)$ are the given Dirichlet and Neumann boundary conditions and $\mathbf{g}_s^0(\mathbf{x}, 0)$ are the initial conditions.

2.2.1.3 Fluid-Solid Coupling

To couple any two physical domains on Γ_c, conditions need to be applied to ensure that the interacting domains do not detach or overlap during motion and that stresses are continuous across the boundary. These conditions are met in a basic sense by equating velocities across Γ_c, while the condition of stress continuity is satisfied by equating normal stresses, or traction vectors ($\mathbf{t}$), between the interacting domains, such that:

$$(\mathbf{v} - \partial_t \mathbf{u}) = 0 \text{ on } \Upsilon_c, \tag{2.24a}$$

$$\mathbf{t}_f = -\mathbf{t}_s \text{ on } \Upsilon_c, \tag{2.24b}$$

where $\mathbf{t}_f = (\mu \mathcal{D}_{\mathbf{x}} \mathbf{v} - p\mathbf{I}) \cdot \mathbf{n}$ and $\mathbf{t}_s = (\hat{\boldsymbol{\sigma}}_s(\mathbf{u}) - p\mathbf{I}) \cdot \mathbf{n}$, $\mathbf{n}$ is the outward boundary normal on Γ_f^C and Γ_s^C. For clarity in the following sections, $\mathbf{t}_i = \mathbf{t}_i^C$ on Υ_c. Equation 2.24b ensures that the fluid and solid domains provides equal and opposite tractions at the interface, while equation 2.24a enforces the no slip condition at the interface.

2.2.1.4 Fictitious Domain

To define a rigid body immersed within Ω_f, conditions need to be applied to enforce the boundary conditions, *i.e.* no slip, on the rigid body in Ω_f. In the fictitious domain method the rigid body is prescribed as Γ_{Fd}, which is embedded in Ω_f. The boundary is applied by enforcing the continuity of $\mathbf{v}$ with Γ_{Fd} such that:

$$\mathbf{v} = \mathbf{v}_{Fd} \text{ on } \Upsilon_{Fd}, \tag{2.25}$$

where $\mathbf{v}_{Fd}$ is the velocity of Γ_{Fd}. This constraint has the effect of applying a traction on the fluid,

$$\mathbf{t}_{Fd} = (\mu \mathcal{D}_{\mathbf{x}} \mathbf{v} - p\mathbf{I}) \cdot \mathbf{n} \text{ on } \Upsilon_{Fd}, \tag{2.26}$$

where $\mathbf{n}$ is the direction of the outward boundary normal on Γ_{Fd}.

2.2.2 Weak Forms of the Model Problems

The weak form, required for the finite element formulation of the model problems, is constructed by multiplying the equations by suitable test functions[218] and integrating over the domain. Defining the inner product as,

$$(\mathbf{a}, \mathbf{b})_\Omega = \int_\Omega \mathbf{a} \cdot \mathbf{b} \, \mathbf{dx}, \tag{2.27}$$

this section presents the weak forms of the problems outlined in section 2.2.1.

2.2.2.1 Divergence of Cauchy Stress

The weak form of the divergence of Cauchy stress terms, $\nabla_\mathbf{x} \cdot \boldsymbol{\sigma}_i$, in equations 2.22 and 2.23 can, using integration by parts, be broken down into a combination of internal stress and boundary tractions, $\mathbf{t}_i$,

$$(\nabla_\mathbf{x} \cdot \boldsymbol{\sigma}_i, \mathbf{y})_{\Omega_i} = (\mathbf{t}_i, \mathbf{y})_{\Gamma_i} - (\boldsymbol{\sigma}_i, \nabla_\mathbf{x} \mathbf{y})_{\Omega_i}, \tag{2.28}$$

where $\mathbf{y}$ is an appropriate test function. The tractions, $\mathbf{t}_i$, can be further broken down depending on whether they arise on Neumann ($\mathbf{t}_i = \mathbf{g}_i^N$), coupling interface ($\mathbf{t}_i = \mathbf{t}_i^C$), or FD ($\mathbf{t}_i = \mathbf{t}_{Fd}$) boundaries.

With respect to the Navier–Stokes problem, the divergence of the stress tensor in equation 2.22a can be reduced to the standard Laplacian operator for viscous stress, since,

$$\nabla_\mathbf{x} \cdot \mathcal{D}_\mathbf{x} \mathbf{v} = \nabla_\mathbf{x} (\nabla_\mathbf{x} \cdot \mathbf{v}) + (\nabla_\mathbf{x} \cdot \nabla_\mathbf{x}) \mathbf{v} \tag{2.29}$$

$$= (\nabla_\mathbf{x} \cdot \nabla_\mathbf{x}) \mathbf{v}. \tag{2.30}$$

However, from equation 2.28 the tractions that arise naturally on the boundaries through integration by parts are not equivalent between these two definitions, *i.e.* the tractions resulting from,

$$((\nabla_\mathbf{x} \cdot \nabla_\mathbf{x} \mathbf{v}), \mathbf{y})_{\Omega_i} = (\nabla_\mathbf{x} \mathbf{v} \cdot \mathbf{n}, \mathbf{y})_{\Gamma_i} - (\nabla_\mathbf{x} \mathbf{v}, \nabla_\mathbf{x} \mathbf{y})_{\Omega_i},$$

are not equivalent to those calculated using the symmetric Cauchy stress operator, $\mathcal{D}_\mathbf{x} \mathbf{v}$,

$$((\nabla_\mathbf{x} \cdot \mathcal{D}_\mathbf{x} \mathbf{v}), \mathbf{y})_{\Omega_i} = (\mathcal{D}_\mathbf{x} \mathbf{v} \cdot \mathbf{n}, \mathbf{y})_{\Gamma_i} - (\mathcal{D}_\mathbf{x} \mathbf{v}, \nabla_\mathbf{x} \mathbf{y})_{\Omega_i}.$$

This variance in form has been shown to be significant for coupled problems[132], therefore the symmetric Cauchy stress tensor is used to formulate the Navier–Stokes weak form.

2.2.2.2 Weak Form of the Navier-Stokes Equations

Integrating over Ω_f (note the equivalence defined in equation 2.7), equations 2.22 become,

$$\begin{aligned} &\rho \left(\partial_t(\mathbf{v}), \mathbf{y}\right)_{\Omega_f} + \rho \left((\mathbf{v} - \mathbf{w}) \cdot \nabla_\mathbf{x} \mathbf{v}, \mathbf{y}\right)_{\Omega_f} + \mu \left(\mathcal{D}_\mathbf{x} \mathbf{v}, \nabla_\mathbf{x} \mathbf{y}\right)_{\Omega_f} \\ &+ \left(\mathbf{t}_f^C, \mathbf{y}\right)_{\Gamma_c} + \left(\mathbf{t}_f^{Fd}, \mathbf{y}\right)_{\Gamma_{Fd}} - \left(p, \nabla_\mathbf{x} \cdot \mathbf{y}\right)_{\Omega_f} = \left(\mathbf{f}_f, \mathbf{y}\right)_{\Omega_f} + \left(\mathbf{g}_f^N, \mathbf{y}\right)_{\Gamma_f^N}, \end{aligned} \tag{2.31a}$$

$$(\nabla_\mathbf{x} \cdot \mathbf{v}, q)_{\Omega_f} = 0, \tag{2.31b}$$

for all suitable test functions $\mathbf{y}$ and q. Note that the tractions, $\mathbf{t}_f^C$ and $\mathbf{t}_f^{Fd}$, which represent the forces applied by the coupling condition and the fictitious domain respectively, are applied on the left hand side to enable their solution using a Lagrange multiplier method.

2.2.2.3 Weak Form of the Finite Elasticity Equations

Integrating over Ω_s, the weak form of the finite–elasticity equations may be written as,

$$(\hat{\boldsymbol{\sigma}}_s(\mathbf{u}), \nabla_{\mathbf{x}}\mathbf{y})_{\Omega_s} - (p, \nabla_{\mathbf{x}} \cdot \mathbf{y})_{\Omega_s} + \left(\mathbf{t}_s^C, \mathbf{y}\right)_{\Gamma_c} = (\mathbf{f}_s, \mathbf{y})_{\Omega_s} + \left(\mathbf{g}_s^N, \mathbf{y}\right)_{\Gamma_s^N}, \tag{2.32a}$$

$$(\partial_t \jmath, q)_{\Omega_s} = 0, \tag{2.32b}$$

for all suitable test functions $\mathbf{y}$ and q. Again, note that the traction $\mathbf{t}_s^C$, which represents the force applied on Γ_c due to the coupling condition, is applied on the left hand side to enable its solution using a Lagrange multiplier method.

2.2.2.4 Weak Form of the Coupling Constraint

The constraint, posed by equations 2.24, requires the stresses and velocities to be mapped between Ω_s and Ω_f, across the coupling interface, Γ_c. In both the fluid and solid problems, the traction forces, $\mathbf{t}_f$ and $\mathbf{t}_s$, arise naturally on all Γ_f^N and Γ_s^N through integration by parts. Considering equation 2.24b, it is therefore logical to introduce a Lagrange multiplier, $\boldsymbol{\lambda_c}$, which, after summing equations 2.31a and 2.32a, may be defined such that:

$$(\boldsymbol{\lambda}_c, (\mathbf{y}_s - \mathbf{y}_f))_{\Upsilon_c} = \left(\jmath_{\Gamma_c,t}\mathbf{t}_s^C, \mathbf{y}_s\right)_{\Upsilon_c} - \left(\jmath_{\Gamma_c,t}\mathbf{t}_f^C, \mathbf{y}_f\right)_{\Upsilon_c}, \tag{2.33}$$

for the given fluid, $\mathbf{y}_f$, and solid, $\mathbf{y}_s$, test functions[136]. Note that $\boldsymbol{\lambda}_c$ is defined on the reference frame, therefore $\boldsymbol{\lambda}_c = \jmath_{\Gamma_c,t}\mathbf{t}_s^C = -\jmath_{\Gamma_c,t}\mathbf{t}_f^C$.

The weak form of equation 2.24a, also integrating over Υ_c, after multiplying by any suitable test function $\mathbf{q}$ is weakly equal to,

$$\left((\partial_t \mathbf{u} - \mathbf{v}), \mathbf{q}\right)_{\Upsilon_c} = 0. \tag{2.34}$$

2.2.2.5 Weak Form of the Fictitious Domain Constraint

In a similar manner to the coupling constraint, stress and velocity continuity must be mapped between Ω_f and Γ_{Fd}. Taking the traction force $\mathbf{t}_f$ on Γ_{Fd} and considering equations 2.26 and 2.31a, a Lagrange multiplier, $\boldsymbol{\lambda}_{Fd}$, is introduced to be weakly equivalent to $\mathbf{t}_{Fd}$ on Γ_{Fd} such that:

$$(\boldsymbol{\lambda}_{Fd}, \mathbf{y})_{\Gamma_{Fd}} = \left(\mathbf{t}_f^{Fd}, \mathbf{y}\right)_{\Gamma_{Fd}}. \tag{2.35}$$

Note that since the intersection between the FD and Ω_f varies if either the fluid or fictitious domains are moving, it is more convenient to define the weak form on Γ_{Fd} rather than Υ_{Fd}.

The weak form of equation 2.25, after multiplying by any suitable test function $\mathbf{q}$, is weakly equal to:

$$(\mathbf{v}, \mathbf{q})_{\Gamma_{Fd}} = (\mathbf{v}_{Fd}, \mathbf{q})_{\Gamma_{Fd}}. \tag{2.36}$$

2.2.2.6 Weak Form Operators

For notational clarity, a series of operators are introduced to simplify equations 2.31 through 2.36. The operators are defined as,

$$\mathbf{m}_t\left(\mathbf{v},\mathbf{y}\right)_{\Omega} = \left(\mathbf{v},\mathbf{y}\right)_{\Omega}, \tag{2.37a}$$

$$\mathbf{a}_t\left(\mathbf{v},\mathbf{y}\right)_{\Omega} = \left(\mathcal{D}_{\mathbf{x}}\mathbf{v},\nabla_{\mathbf{x}}\mathbf{y}\right)_{\Omega}, \tag{2.37b}$$

$$\mathbf{b}_t\left(p,\mathbf{y}\right)_{\Omega} = \left(p,\nabla_{\mathbf{x}}\cdot\mathbf{y}\right)_{\Omega}, \tag{2.37c}$$

$$\mathbf{c}_t\left(\mathbf{z};\mathbf{v},\mathbf{y}\right)_{\Omega} = \left(\mathbf{z}\cdot\nabla_{\mathbf{x}}\mathbf{v},\mathbf{y}\right)_{\Omega}, \tag{2.37d}$$

$$\mathbf{s}_t\left(\mathbf{u},\mathbf{y}\right)_{\Omega} = \left(\boldsymbol{\sigma}_s(\mathbf{u}),\nabla_{\mathbf{x}}\mathbf{y}\right)_{\Omega}. \tag{2.37e}$$

2.2.2.7 Integral Weak Forms

Incorporating the weak form operators and integrating over the time interval $I = [a, b]$, the integral weak forms are derived. These forms are the basis for constructing the discrete equations outlined in section 2.3.

Integral Weak form of the ALE Navier–Stokes Equations:

$$\begin{aligned}\rho\,\mathbf{m}_b\left(\mathbf{v},\mathbf{y}\right)_{\Omega_f} - \rho\,\mathbf{m}_a\left(\mathbf{v},\mathbf{y}\right)_{\Omega_f} + \rho\int_a^b \mathbf{c}_t\left(\mathbf{v}-\mathbf{w};\mathbf{v},\mathbf{y}\right)_{\Omega_f}\,dt + \mu\int_a^b \mathbf{a}_t\left(\mathbf{v},\mathbf{y}\right)_{\Omega_f}\,dt \\ -\int_a^b \left(\boldsymbol{\lambda}_c,\mathbf{y}\right)_{\Gamma_c}\,dt + \int_a^b \left(\boldsymbol{\lambda}_{Fd},\mathbf{y}\right)_{\Gamma_{Fd}}\,dt - \int_a^b \mathbf{b}_t\left(p,\mathbf{y}\right)_{\Omega_f}\,dt \\ = \int_a^b \left(\mathbf{f}_f,\mathbf{y}\right)_{\Omega_f}\,dt + \int_a^b \left(\mathbf{g}_f^N,\mathbf{y}\right)_{\Gamma_f^N}\,dt,\end{aligned} \tag{2.38a}$$

$$\int_a^b \mathbf{b}_t\left(q,\mathbf{v}\right)_{\Omega_f}\,dt = 0. \tag{2.38b}$$

Integral Weak form of the Finite Elasticity Equations:

$$\begin{aligned}\int_a^b \mathbf{s}_t\left(\hat{\boldsymbol{\sigma}}_s(\mathbf{u}),\mathbf{y}\right)_{\Omega_s}\,dt - \int_a^b \mathbf{b}_t\left(p,\mathbf{y}\right)_{\Omega_s}\,dt + \int_a^b \left(\boldsymbol{\lambda}_c,\mathbf{y}\right)_{\Gamma_c}\,dt \\ = \int_a^b \left(\mathbf{f}_s,\mathbf{y}\right)_{\Omega_s}\,dt + \int_a^b \left(\mathbf{g}_s^N,\mathbf{y}\right)_{\Gamma_s^N}\,dt,\end{aligned} \tag{2.39a}$$

$$\mathbf{m}_b\left(q,1\right)_{\Omega_s} - \mathbf{m}_a\left(q,1\right)_{\Omega_s} = 0. \tag{2.39b}$$

By induction $\mathbf{m}_b\left(q,1\right)_{\Omega_s} = \mathbf{m}_\alpha\left(q,1\right)_{\Omega_s}\ \forall\,\alpha$, therefore, given that at $t = 0$ the solid is in the undeformed state, the incompressibility constraint for the finite elasticity equations can be defined as,

$$\mathbf{m}_b\left(q,1\right)_{\Omega_s} - \left(q,1\right)_{\Lambda_s} = 0. \tag{2.40}$$

Integral Weak form of the Coupling Constraint:

$$\mathbf{m}_b\left(\mathbf{u},\mathbf{q}\right)_{\Upsilon_c} - \mathbf{m}_a\left(\mathbf{u},\mathbf{q}\right)_{\Upsilon_c} - \int_a^b \left(\mathbf{v},\mathbf{q}\right)_{\Upsilon_c}\, dt = 0. \tag{2.41}$$

Integral Weak form of the Fictitious Domain Constraint:

$$\int_a^b \left(\mathbf{v},\mathbf{q}\right)_{\Gamma_{Fd}}\, dt = \int_a^b \left(\mathbf{v}_{Fd},\mathbf{q}\right)_{\Gamma_{Fd}}\, dt. \tag{2.42}$$

2.2.2.8 Global System

Combining the integral weak forms, a global system can be formulated. Identifying the state variables (velocity, displacement, fluid/solid pressure and coupling/FD Lagrange multipliers) as either kinematic $\Theta = (\mathbf{v}, \mathbf{u})$, or Lagrange multipliers $Z = (p_f, p_s, \boldsymbol{\lambda}_c, \boldsymbol{\lambda}_{Fd})$,

$$\mathscr{A}_I(\Theta, Y) := \rho\,\mathbf{m}_b\left(\mathbf{v},\mathbf{y}_f\right)_{\Omega_f} + \int_a^b \rho\mathbf{c}_t\left(\mathbf{v}-\mathbf{w};\mathbf{v},\mathbf{y}_f\right)_{\Omega_f} + \mu\mathbf{a}_t\left(\mathbf{v},\mathbf{y}_f\right)_{\Omega_f} + \mathbf{s}_t\left(\boldsymbol{\sigma}_s(\mathbf{u}),\mathbf{y}_s\right)_{\Omega_s} dt, \tag{2.43a}$$

$$\mathscr{B}_I(Z, Y) := \int_a^b \left(\boldsymbol{\lambda}_c,\mathbf{y}_s-\mathbf{y}_f\right)_{\Gamma_c} - \mathbf{b}_t\left(p,\mathbf{y}_f\right)_{\Omega_f} - \mathbf{b}_t\left(p,\mathbf{y}_s\right)_{\Omega_s} + \left(\boldsymbol{\lambda}_{Fd},\mathbf{y}_f\right)_{\Gamma_{Fd}} dt, \tag{2.43b}$$

$$\mathscr{C}_I(\Theta, Q) := \mathbf{m}_b\left(\mathbf{u},\mathbf{q}_c\right)_{\Upsilon_c} + \mathbf{m}_b\left(q_s,1\right)_{\Omega_s} + \int_a^b \mathbf{b}_t\left(q_f,\mathbf{v}\right)_{\Omega_f} - \left(\mathbf{v},\mathbf{q}_c\right)_{\Upsilon_c} + \left(\mathbf{v},\mathbf{q}_{Fd}\right)_{\Gamma_{Fd}} dt, \tag{2.43c}$$

$$\mathscr{F}_I(Y) := \rho\,\mathbf{m}_a\left(\mathbf{v},\mathbf{y}_f\right)_{\Omega_f} + \int_a^b \left(\mathbf{f}_f,\mathbf{y}_f\right)_{\Omega_f} + \left(\mathbf{g}_f^N,\mathbf{y}_f\right)_{\Gamma_f^N} + \left(\mathbf{f}_s,\mathbf{y}_s\right)_{\Omega_s} + \left(\mathbf{g}_s^N,\mathbf{y}_s\right)_{\Gamma_s^N}\, dt, \tag{2.43d}$$

$$\mathscr{G}_I(Q) = \int_a^b \left(\mathbf{v}_{Fd},\mathbf{q}_{Fd}\right)_{\Gamma_{Fd}}\, dt - \left(q,1\right)_{\Lambda_s} + \mathbf{m}_a\left(\mathbf{u},\mathbf{q}_c\right)_{\Upsilon_c}, \tag{2.43e}$$

for the test functions $Y = [\mathbf{y}_f,\, \mathbf{y}_s]$ and $Q = [q_f,\, q_s,\, \mathbf{q}_c,\, \mathbf{q}_{Fd}]$. Therefore the Global system can be constructed as,

$$\mathscr{A}_I(\Theta, Y) + \mathscr{B}_I(Z, Y) = \mathscr{F}_I(Y) \tag{2.44a}$$

$$\mathscr{C}_I(\Theta, Q) = \mathscr{G}_I(Q). \tag{2.44b}$$

2.3 Discrete Weak System

The previous section presented the weak formulations of the ALE Navier–Stokes and Finite Elasticity problems, along with the coupling and fictitious domain constraints. In this section, the system is reduced to a finite

dimensional problem, where the continuous test functions defining the weak problems are approximated by finite dimensional variants forming the discrete weak system.

2.3.1 Discretisation

To construct the discrete weak forms of the governing equations, the system is discretised using Galerkin finite elements and implicit Euler time stepping. The reference domains, Λ_i, $i = [f, s]$, are divided into non–overlapping elements, e, which assemble to form the mesh $\mathcal{T}_h(\Lambda_i)$, *i.e.*

$$\mathcal{T}_h(\Lambda_i) = \{e_1, ..., e_{n_i}\}, \;\; h_i = \max diam(e), \tag{2.45}$$

where h_i can be considered to be the mesh characteristic length (CL) and n_i is the number of elements constructed on Λ_i.

2.3.1.1 Temporal Discretisation

The time domain, I, is divided into n_I non–overlapping intervals,

$$(t^0, t^1, ..., t^{m-1}, t^m),$$
$$t^{m-1} < t^m, \;\; t^0 = 0, \;\; t^{n_I} = T. \tag{2.46}$$

Over each time interval, $t \in [t^{m-1}, t^m]$, the velocity, pressure, Lagrange multiplier and domain velocity are taken as constants in time, while solid displacement is necessarily piecewise linear to satisfy the kinematic equality condition at the coupled interface.

2.3.1.2 Spatial Discretisation

On the elements in $\mathcal{T}_h(\Lambda_i)$, continuous piecewise polynomial functions can be constructed, defined by a series of node points. Discrete approximations on $\mathcal{T}_h(\Lambda_i)$ may be written as weighted sums of basis functions, $\mathbf{\Psi}_j$[57, 159], j indexes the state and spatial variables θ_j, $\theta = [\mathbf{v}, \mathbf{u}, p_f, p_s, \lambda_c, \lambda_{Fd}, \mathbf{w}, \mathbf{x}_f, \mathbf{x}_s]$, note $\mathbf{x}_i$ is used to define the finite element geometric approximation of Ω_i. The dimension of the subspaces of the state/spatial variables, $\mathcal{V}_j$, is $N_j = d \times \mathbb{N}_j$ or $\mathbb{N}_j$ for vector and scalar variables respectively, $\mathbb{N}_j$ is the number of nodes used for the approximation, across Ω_i, of the variable θ_j. Thus, the finite element approximations, denoted by superscript h, of the variables and spatial geometry are defined for any time t^m as,

$$\begin{aligned}
&\mathbf{v}^{h,m} = V^m \cdot \mathbf{\Psi}_{\mathbf{v}}, \quad \mathbf{u}^{h,m} = U^m \cdot \mathbf{\Psi}_{\mathbf{u}}, \\
&p_f^{h,m} = P_f^m \cdot \mathbf{\Psi}_{p_f}, \quad p_s^{h,m} = P_s^m \cdot \mathbf{\Psi}_{p_s}, \\
&\boldsymbol{\lambda}_c^{h,m} = \lambda_c^m \cdot \mathbf{\Psi}_{\boldsymbol{\lambda}_c}, \quad \boldsymbol{\lambda}_{Fd}^{h,m} = \lambda_{Fd}^m \cdot \mathbf{\Psi}_{\boldsymbol{\lambda}_{Fd}}, \\
&\mathbf{w}^{h,m} = W^m \cdot \mathbf{\Psi}_{\mathbf{w}},
\end{aligned} \tag{2.47a}$$

$$\mathbf{x}_f^{h,m} = X_f^m \cdot \mathbf{\Psi}_{\mathbf{x}_f}, \quad \mathbf{x}_s^{h,m} = X_s^m \cdot \mathbf{\Psi}_{\mathbf{x}_s}, \tag{2.47b}$$

where the weightings, V^m, U^m, P_f^m, P_s^m, λ_c^m, λ_{Fd}^m, W^m, X_f^m, X_s^m, are constant vectors with N_j components defining the variables θ_j at each node.

Using the finite element approximation for the variables θ_j, the discrete form of equation 2.44 is,

$$\mathscr{A}_I^m(\Theta^{h,m}, Y^h) + \mathscr{B}_I^m(Z^{h,m}, Y^h) = \mathscr{F}_I^m(Y^h) \tag{2.48a}$$

$$\mathscr{C}_I^m(\Theta^{h,m}, Q^h) = \mathscr{G}_I^m(Q^h). \tag{2.48b}$$

Where $\Theta^{h,m} = [\mathbf{v}^{h,m}, \mathbf{u}^{h,m}, \mathbf{w}^{h,m}]$, $Z^{h,m} = [p_f^{h,m}, p_s^{h,m}, \boldsymbol{\lambda}_c^{h,m}, \boldsymbol{\lambda}_{Fd}^{h,m}]$, $Y^h = [\mathbf{y}_f^h, \mathbf{y}_s^h]$ and $Q^h = [q_f^h, q_s^h, \mathbf{q}_c^h, \mathbf{q}_{Fd}^h]$. In the Galerkin Finite element approximation, the test functions Y^h and Q^h are chosen to be the same as the basis functions $\boldsymbol{\Psi}_j$[218].

The basis functions, $\boldsymbol{\Psi}_j$, are defined by the order and type of element used to construct $\mathcal{T}_h(\Lambda_i)$. Many different element types can be used[218] and often there are stability requirements on the order of that used to approximate the various state variables. These are discussed in detail in section 2.5.1.

2.3.1.3 Basis Functions

The nodal Lagrange basis functions $\boldsymbol{\Psi}_j$ may be represented as the piece–wise continuous functions ψ_j,

$$\boldsymbol{\Psi}_j = \left\{ \psi_j^1 \mathbf{e}_1, ..., \psi_j^1 \mathbf{e}_d, ..., \psi_j^{\mathbb{N}_j} \mathbf{e}_d \right\}, \tag{2.49}$$

where $\{\mathbf{e}_1, ..., \mathbf{e}_d\}$ are the unit basis vectors of $\mathbb{R}^d$. Any function, for example $\mathbf{w} \in \mathcal{V}_j$, may then be expressed as a linear combination of the weighted basis functions, *i.e.*

$$\mathbf{w}(\boldsymbol{\eta}) = \sum_{i=1}^{d} \sum_{k=1}^{\mathbb{N}_j} \mathbf{e}_i w_i^k \psi_j^k(\boldsymbol{\eta}), \;\; \boldsymbol{\eta} \in \mathcal{T}_h(\Lambda), \tag{2.50}$$

where w_i^k is the weight for the k^{th} basis in the i^{th} component of $\mathbf{w} = (w_1, ...w_d)$. This notation can be simplified assuming summation over shared indices. It is convenient to define the basis functions, ψ, with respect to a reference element, $\hat{e}(\boldsymbol{\phi})$, on which local basis functions, $\varphi(\boldsymbol{\phi})$, are defined ($\boldsymbol{\phi}$ represents the local coordinates on $\hat{e}$). These are discussed further in appendix A.

2.3.1.4 Lagrangian/ALE Mapping Discretisations

The fluid and solid problems are defined on moving domains (ALE or Lagrangian), which vary in time. As stated in section 2.1.1, the problems are defined on static reference domains, Λ_i, that map to the physical domain, Ω_i, via the mapping $\mathcal{P}_{\Lambda_i}^{\Omega_i}$. For the discrete system the mapping $\mathcal{P}_{\Lambda_i}^{h,\Omega_i} := \mathcal{P}_{\mathcal{T}_h(\Lambda_i)}^{\mathcal{T}_h(\Omega_i)}$ is defined. A continuous piecewise linear interpolation of the mapping is used through time, so that at any time t^m, $m \in [0, T]$,

$$\mathcal{P}_{\Lambda_i}^{h,\Omega_i}(\cdot, t) := \frac{t^m - t}{\triangle_t^m} \mathcal{P}_{\Lambda_i}^{h,\Omega_i}(\cdot, t^{m-1}) + \frac{t - t^{m-1}}{\triangle_t^m} \mathcal{P}_{\Lambda_i}^{h,\Omega_i}(\cdot, t^m), \;\; t \in (t^{m-1}, t^m), \;\; \triangle_t^m = t^m - t^{m-1}. \tag{2.51}$$

This results in continuous piecewise linear displacements (solid) and piecewise constant domain velocities (fluid) on Γ_c, through the interval $I = [t^{m-1}, t^m]$.

Due to the coupling constraints, the domain movements of Ω_f and Ω_s are linked on the boundary Γ_c. While the solid map is defined by the displacement $\mathbf{u}$, the fluid map is arbitrary as long as it adheres to movement on the coupled boundary. To satisfy this constraint, the weak Laplacian problem was selected to define the fluid map. For the displacement variable $\mathbf{d}$ and any suitable test function $\mathbf{y}$,

$$\mathbf{a}_t\left(\mathbf{d}^h, \mathbf{y}^h\right)_{\Omega_f(t^{m-1})} = 0, \text{ in } \Omega_f(t^{m-1}), \tag{2.52a}$$

$$\mathbf{d}^h = \triangle_t^m \mathbf{v}^{h,m}, \text{ on } \Gamma_f(t^{m-1}). \tag{2.52b}$$

Note that due to the no slip condition $\mathbf{w} = \mathbf{v}$ on Γ_f^C and the fluid map problem is calculated on Ω from the previous time step. The discrete mesh velocity $\mathbf{w}^{h,m} = \frac{\mathbf{d}^h}{\triangle_t^m}$. The ALE map is updated as,

$$\mathcal{P}_{\Lambda_f}^{h,\Omega_f}(t^m) = \mathbf{d}^h + \mathcal{P}_{\Lambda_f}^{h,\Omega_f}(t^{m-1}), \tag{2.53}$$

where $\mathcal{P}_{\Lambda_f}^{h,\Omega_f}(0) = \mathcal{T}_h(\Lambda_f)$. As this problem needs to be solved for each residual evaluation (see section 2.4), it is not solved as part of the global system. The solution methods used are discussed in section 2.5.4.

For solid problems the computation of stress is dependent on deformation from the reference configuration, Λ_s. For this reason, the solid map is defined from Λ_s where, in the discrete form,

$$\mathcal{P}_{\Lambda_s}^{h,\Omega_s}(t^m) = \mathbf{u}^{h,m} + \mathcal{P}_{\Lambda_s}^{h,\Omega_s}(0),\ \mathcal{P}_{\Lambda_s}^{h,\Omega_s}(0) = \mathcal{T}_h(\Lambda_s). \tag{2.54}$$

2.3.2 Coupling Lagrange Multiplier Subspace

Different problem types can exhibit unique behaviour, often requiring different degrees of refinement of $\mathcal{T}_h(\Lambda_i)$ to adequately approximate the solution in Ω_i. Additionally, it is often preferable to use different state and spatial interpolation functions to describe the different domains due to both geometric and problem considerations. As a result, when coupling problems together the discretised domains are not necessarily equivalent across $\mathcal{T}_h(\Upsilon_c)$. To cope with this lack of congruence in $\mathcal{T}_h(\Lambda_i)$, an additional domain, $\Xi \subset \mathbb{R}^{d-1}$, with local coordinates ξ, is introduced to apply the weak constraint across each approximation of Υ_c. Ξ is mapped to $\mathcal{T}_h(\Upsilon_f^C)$ and $\mathcal{T}_h(\Upsilon_s^C)$ by $\mathcal{P}_\Xi^{\Upsilon_i^c}$. $\boldsymbol{\lambda}_c$ is redefined such that $\boldsymbol{\lambda}_c = (\jmath_{\Gamma_c,t})(\jmath_{\Upsilon_c,t})\mathbf{t}_s = -(\jmath_{\Gamma_c,t})(\jmath_{\Upsilon_c,t})\mathbf{t}_f$. The discrete form of equation 2.33 becomes,

$$\left(\boldsymbol{\lambda}_c^h, (\hat{\mathbf{y}}_s^h - \hat{\mathbf{y}}_f^h)\right)_\Xi = \left(\mathbf{t}_s^h \jmath_{\Gamma_c,t}, \mathbf{y}_s^h\right)_{\Upsilon_c} - \left(\mathbf{t}_f^h \jmath_{\Gamma_c,t}, \mathbf{y}_f^h\right)_{\Upsilon_c}, \tag{2.55}$$

where $\mathbf{t}_i^h$ are the tractions resulting from the discrete approximations. $\hat{\mathbf{y}}_i^h$ refer to the projections of $\mathbf{y}_i^h$ onto Ξ such that, $\hat{\mathbf{y}}_i^h(\xi) = \mathbf{y}_i^h(\eta)$. Figure 2.2 shows a schematic representation of the relationship between Ξ, Γ_f^C and Γ_s^C.

For all problems presented in this thesis, Ξ is embedded in the most refined of $\mathcal{T}_h(\Upsilon_f)$ and $\mathcal{T}_h(\Upsilon_s)$, which was shown in Nordsletten *et al.*[136] to provide optimal results when one domain is dominant.

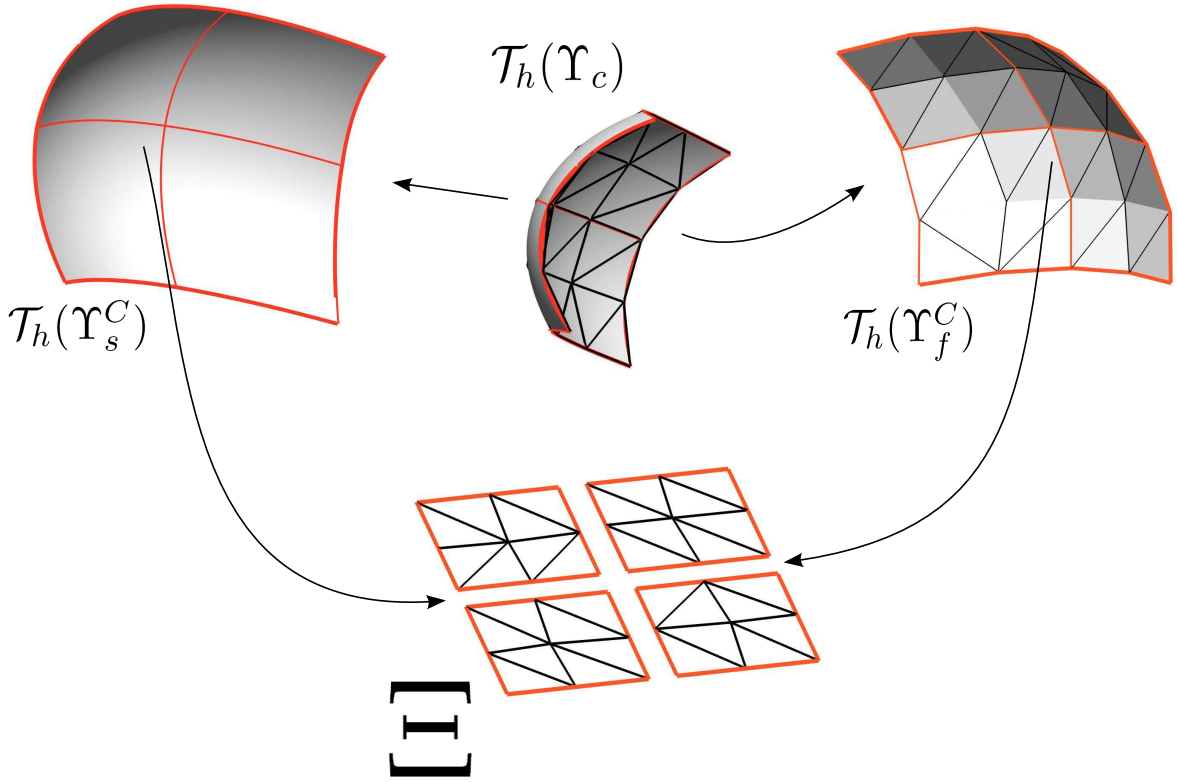

FIGURE 2.2. *Relationship between the coupling interface, $\mathcal{T}_h(\Upsilon_c)$, the respective fluid and solid boundaries, Γ_f^C and Γ_s^C, and the coupling Lagrange multiplier subspace Ξ. Note how each Ξ region,* i.e. *the red squares, is nested within the larger of the two interface domains. On these regions, the local coordinates ξ relate to the projection of a point on Γ_f^C onto Γ_s^C on the reference element (see section 2.3.1.3).*

2.3.3 Discretised Fictitious Domain Constraint and Contact Enforcement

The discrete forms of the fictitious domain constraint are defined from equations 2.35 and 2.36 as,

$$(\boldsymbol{\lambda}_{Fd}^h, \mathbf{y}^h)_{\Gamma_{Fd}} = (\mathbf{t}_f^h, \mathbf{y}^h)_{\Gamma_{Fd}}, \tag{2.56a}$$

$$(\mathbf{v}^h, \mathbf{q}^h)_{\Gamma_{Fd}} = (\mathbf{v}_{Fd}^h, \mathbf{q}^h)_{\Gamma_{Fd}}. \tag{2.56b}$$

Of critical importance when computing the weak forms in the finite element method is an accurate evaluation of the integral over the domain of interest. In the FD method this is complicated as $\mathcal{T}_h(\Upsilon_{Fd})$ will not necessarily be congruous with the fluid mesh $\mathcal{T}_h(\Lambda_f)$. The methods used to perform this integration are defined in section 2.5.2.

The two Lagrange multiplier constraints within the global system have an interesting impact on coupled fluid–solid problems with an immersed FD body. The action of the these Lagrange multipliers, $\boldsymbol{\lambda}_{Fd}$ enforcing the fluid velocity on Γ_{Fd} to be equivalent to $\mathbf{v}_{Fd}$ and $\boldsymbol{\lambda}_c$ enforcing equivalence of the solid and fluid velocities on

Γ_c, implicitly resolves the contact problem of an immersed rigid body. As a rigid body, prescribed by a FD, approaches Γ_c, the velocity of Γ_c approaches $\mathbf{v}_{Fd}$ which, for adequate mesh and time step refinement, prevents penetration of the elastic solid by the immersed rigid body. Additionally, the FD prevents compaction of the fluid mesh, $\mathcal{T}_h(\Lambda_f)$, by allowing $\mathcal{T}_h(\Lambda_f)$ to move through Γ_{Fd} while still maintaining the constraint.

2.4 Solving the Global System

The discrete weak form is solved using the Newton–Raphson method[15] whereby the non–linear system is formulated as a matrix of linear equations. The solution of the state variables, $\mathbf{X}^m$, $\mathbf{X}^m = [\Theta^{h,m}, Z^{h,m}]$, is calculated by iteratively updating the linear system until a convergence criteria has been satisfied. This section outlines the formulation of the matrix system built to solve the global system for $\mathbf{X}^m$.

2.4.1 Newton–Raphson Method

Considering the discrete global system, a functional $\mathbf{f}$ can be defined at time step m, where $\mathbf{f}$ is the subtraction of equations 2.48,

$$\mathbf{f}(\mathbf{X}^m, \mathbf{Y}) = \mathscr{A}_I^m(\Theta^{h,m}, Y^h) + \mathscr{B}_I^m(Z^{h,m}, Y^h) - \mathscr{C}_I^m(\Theta^{h,m}, Q^h) - \mathscr{F}_I^m(Y^h) + \mathscr{G}_I^m(Q^h) = 0, \tag{2.57}$$

for the test functions $\mathbf{Y} = [Y^h, Q^h]$. Due to the linear dependence of $\mathbf{f}$ on $\mathbf{Y}$, the constraint can be satisfied by ensuring $\mathbf{f} = 0$ for each basis function $\mathbf{\Psi}_j^k$, $k \in [1, \cdots, N_j]$, associated with the state variables $\mathbf{X}^m$. The resulting vector of constraints, or residual vector, $\mathscr{R}^m(\mathbf{X}^m)$, of length $N = \sum_{j=1}^{n_s} N_j$, where n_s is the number of kinematic and constraint variables, satisfies,

$$\mathscr{R}^m(\mathbf{X}^m) = 0. \tag{2.58}$$

From equation 2.47, $\mathbf{X}^m$ is defined as the weighted sum of all basis functions for all state variables, *i.e.*

$$\mathbf{X}^m = \mathcal{X}^m \cdot \mathbf{\Psi}_{\mathbf{X}} = \begin{pmatrix} \mathbf{v}^{h,m} \\ \mathbf{u}^{h,m} \\ p_f^{h,m} \\ p_s^{h,m} \\ \boldsymbol{\lambda}_c^{h,m} \\ \boldsymbol{\lambda}_{Fd}^{h,m} \\ \mathbf{w}^{h,m} \end{pmatrix}, \ \mathcal{X}^m = \begin{pmatrix} V^m \\ U^m \\ P_f^m \\ P_s^m \\ \lambda_c^m \\ \lambda_{Fd}^m \\ W^m \end{pmatrix}, \ \mathbf{\Psi}_{\mathbf{X}} = \begin{pmatrix} \mathbf{\Psi}_{\mathbf{v}} \\ \mathbf{\Psi}_{\mathbf{u}} \\ \mathbf{\Psi}_{p_f} \\ \mathbf{\Psi}_{p_s} \\ \mathbf{\Psi}_{\boldsymbol{\lambda}_c} \\ \mathbf{\Psi}_{\boldsymbol{\lambda}_{Fd}} \\ \mathbf{\Psi}_{\mathbf{w}} \end{pmatrix}. \tag{2.59}$$

The Newton–Raphson method involves iteratively updating the coefficient vector $\mathcal{X}^m$. Given an initial guess, $\mathcal{X}^{m,0}$, the approximate solution $\mathbf{X}^m$ at the m^{th} time step is,

$$\mathbf{X}^m = \lim_{k\to\infty} \mathcal{X}^{m,k} \cdot \mathbf{\Psi}_{\mathbf{X}}, \ \ \mathcal{X}^{m,k} := \mathcal{X}^{m,k-1} + \alpha^k \delta\mathcal{X}^{m,k}, \tag{2.60}$$

where the vector $\delta\mathcal{X}^{m,k}$ is the Newton update, chosen as the solution to equation 2.61, k is the iteration number and α^k is a scalar parameter. Taking the gradient, $\nabla_{\mathcal{X}^{m,k-1}}$, with respect to each scalar coefficient of $\mathcal{X}^{m,k-1}$,

of $\mathscr{R}^m(\mathbf{X}^{m,k-1})$, the Jacobian system can be formulated as,

$$\nabla_{\mathcal{X}^{m,k-1}}\mathscr{R}^m(\mathbf{X}^{m,k-1})\cdot\delta\mathcal{X}^{m,k} = -\mathscr{R}^m(\mathbf{X}^{m,k-1}). \tag{2.61}$$

The scalar parameter $\alpha^k \in [0,1]$ is chosen to ensure a monotonic decrease in the l_2-norm of the residual vector, $|\mathscr{R}^m(\mathbf{X}^{m,k})|_{l2}$, using a line search based algorithm, see section 2.5.3.1.

2.4.2 Matrix System

Each Newton iteration requires the solution of the linear Jacobian system given in equation 2.61. This is achieved by defining the Jacobian as a block matrix $\mathcal{A}^{m,k}$,

$$\nabla_{\mathcal{X}^{m,k-1}}\mathscr{R}^m(\mathbf{X}^{m,k-1}) = \mathcal{A}^{m,k} := \begin{bmatrix} \mathbf{A}^{m,k} & \mathbf{B}^{m,k} & \mathbf{W}_1^{m,k} \\ \mathbf{C}^{m,k} & \mathbf{0} & \mathbf{W}_2^{m,k} \\ \mathbf{P}^{m,k} & \mathbf{0} & \mathbf{M}^{m,k} \end{bmatrix}, \tag{2.62}$$

where $\mathbf{W}_{1,2}^{m,k}$ are the contributions from gradients with respect to the discrete domain velocities $W^{h,m}$, $\mathbf{P}^{m,k}$ represents the projection of the velocity solution on Γ_f^C and is otherwise zero (noting $\mathbf{v} = \mathbf{w}$ on the fluid–solid interface), and $\mathbf{M}^{m,k}$ is the matrix form of the ALE mapping problem defined in equation 2.52. The other matrix blocks, $\mathbf{A}^{m,k}$, $\mathbf{B}^{m,k}$ and $\mathbf{C}^{m,k}$ are the matrix form of the continuous operators $\mathscr{A}_I$, $\mathscr{B}_I$ and $\mathscr{C}_I$.

Using a fixed point iterative scheme for $\mathbf{w}^{h,m}$ (where the solution to the ALE mapping problem is calculated using $\mathbf{v}^{h,m,k-1}$ on Γ_f), $\mathbf{w}^{h,m}$ is equal to,

$$\mathbf{w}^{h,m} = \left(\mathbf{M}^{m,k}\right)^{-1}\mathbf{P}^{m,k}\mathbf{v}^{h,m,k-1} \tag{2.63}$$

and can be solved for independently. Assuming $\mathbf{A}^{m,k}$, $\mathbf{B}^{m,k}$ and $\mathbf{C}^{m,k}$ are dominant, $\mathcal{A}^{m,k}$ can be redefined as the system,

$$\mathcal{A}^{m,k} := \begin{bmatrix} \mathbf{A}^{m,k} & \mathbf{B}^{m,k} \\ \mathbf{C}^{m,k} & \mathbf{0} \end{bmatrix}. \tag{2.64}$$

Noting that $\mathbf{X}^m$ no longer includes $\mathbf{w}^{h,m}$, the update vector is determined as,

$$\delta\mathcal{X}^{m,k} = -(\mathcal{A}^{m,k})^{-1}\mathscr{R}^m(\mathbf{X}^{m,k-1}). \tag{2.65}$$

Considering each matrix row represents a separate coefficient of the discrete state variables, the matrix blocks in equation 2.64 can individually be defined as,

$$\mathbf{A}^{m,k} = \begin{bmatrix} A_f^{m,k} & 0 \\ 0 & A_s^{m,k} \end{bmatrix}, \quad \mathbf{B}^{m,k} = \begin{bmatrix} (B_f^{m,k})^T & 0 & (C_f^{m,k})^T & (FD_f^{m,k})^T \\ 0 & \tilde{B}_s^{m,k} & (C_s^{m,k})^T & 0 \end{bmatrix},$$

$$\mathbf{C}^{m,k} = \begin{bmatrix} B_f^{m,k} & 0 \\ 0 & B_s^{m,k} \\ C_f^{m,k} & C_s^{m,k} \\ FD_f^{m,k} & 0 \end{bmatrix}. \tag{2.66}$$

Each of these matrix block subcomponents can be further divided into distinct blocks of size $\mathbb{N} \times \mathbb{N}$, where $\mathbb{N}_j$ refers to the number of nodes used to describe variable j in $\mathcal{T}_h(\Lambda)$. These blocks are individually defined as,

$$A_f^{m,k} = \begin{bmatrix} A_{f,11}^{m,k} & \cdots & A_{f,1d}^{m,k} \\ \vdots & \ddots & \vdots \\ A_{f,d1}^{m,k} & \cdots & A_{f,dd}^{m,k} \end{bmatrix} \in \mathbb{R}^{N_{\mathbf{v}} \times N_{\mathbf{v}}}, \qquad A_s^{m,k} = \begin{bmatrix} A_{s,11}^{m,k} & \cdots & A_{s,1d}^{m,k} \\ \vdots & \ddots & \vdots \\ A_{s,d1}^{m,k} & \cdots & A_{s,dd}^{m,k} \end{bmatrix} \in \mathbb{R}^{N_{\mathbf{u}} \times N_{\mathbf{u}}},$$

$$B_f^{m,k} = \begin{bmatrix} B_{f,11}^{m,k} & \cdots & B_{f,1d}^{m,k} \end{bmatrix} \in \mathbb{R}^{N_{p_f} \times N_{\mathbf{v}}}, \qquad B_s^{m,k} = \begin{bmatrix} B_{s,11}^{m,k} & \cdots & B_{s,1d}^{m,k} \end{bmatrix} \in \mathbb{R}^{N_{p_s} \times N_{\mathbf{u}}},$$

$$\tilde{B}_s^{m,k} = \begin{bmatrix} \tilde{B}_{s,11}^{m,k} & \cdots & \tilde{B}_{s,1d}^{m,k} \end{bmatrix}^T \in \mathbb{R}^{N_{\mathbf{u}} \times N_{p_s}},$$

$$C_f^{m,k} = \begin{bmatrix} C_{f,11}^{m,k} & \cdots & C_{f,1d}^{m,k} \\ \vdots & \ddots & \vdots \\ C_{f,d1}^{m,k} & \cdots & C_{f,dd}^{m,k} \end{bmatrix} \in \mathbb{R}^{N_{\lambda_c} \times N_{\mathbf{v}}}, \qquad C_s^{m,k} = \begin{bmatrix} C_{s,11}^{m,k} & \cdots & C_{s,1d}^{m,k} \\ \vdots & \ddots & \vdots \\ C_{s,d1}^{m,k} & \cdots & C_{s,dd}^{m,k} \end{bmatrix} \in \mathbb{R}^{N_{\lambda_c} \times N_{\mathbf{u}}},$$

$$FD_f^{m,k} = \begin{bmatrix} FD_{f,11}^{m,k} & \cdots & FD_{f,1d}^{m,k} \\ \vdots & \ddots & \vdots \\ FD_{f,d1}^{m,k} & \cdots & FD_{f,dd}^{m,k} \end{bmatrix} \in \mathbb{R}^{N_{\lambda_{Fd}} \times N_{\mathbf{v}}}. \tag{2.67}$$

As defined earlier, N_j is the number of degrees of freedom associated with the variable j. The indexing for each matrix block is defined as $(D_{i,ab}^{m,k})_{op}$, where $o <= \mathbb{N}_j$ and $p <= \mathbb{N}_i$, index each $d \times d$ (or $1 \times d$) component within the matrix block – note $j \neq i$ for the constraint blocks where it indexes the corresponding kinematic variable on which the constraint is applied.

2.4.3 Matrix Block Components

The components of the matrix blocks can be defined for iteration k, at time step m over the interval $I_m = [t^{m-1},\ t^m]$, incorporating the basis functions ψ_j, using the operators introduced in equations 2.37.

2.4.3.1 Fluid Matrix Block

Starting with the fluid matrix block, the contributions to $(A_{f,ab}^{m,k})_{op}$ can be determined analytically and are given as,

$$(A_{f,ab}^{m,k})_{op} = \rho \mathbf{m}_{t^m}(\psi_{\mathbf{v}}^p \mathbf{e}_b, \psi_{\mathbf{v}}^o \mathbf{e}_a)_{\Omega_f} + \int_{t^{m-1}}^{t^m} \rho \mathbf{c}_t(\mathbf{v}^{h,m,k-1} - \mathbf{w}^{h,m,k-1}; \psi_{\mathbf{v}}^p \mathbf{e}_b, \psi_{\mathbf{v}}^o \mathbf{e}_a)_{\Omega_f}$$

$$+ \rho \mathbf{c}_t(\psi_{\mathbf{v}}^p \mathbf{e}_b; \mathbf{v}^{h,m,k-1}, \psi_{\mathbf{v}}^o \mathbf{e}_a)_{\Omega_f} + \mu \mathbf{a}_t(\psi_{\mathbf{v}}^p \mathbf{e}_b, \psi_{\mathbf{v}}^o \mathbf{e}_a)_{\Omega_f} dt. \tag{2.68}$$

2.4.3.2 Solid Matrix Block

Analytic computation of the true Jacobian solid matrix block, $(A^{m,k}_{s,ab})_{op}$, is complicated by the inherent non–linearity of many hyperelastic constitutive laws. Additionally, since there is no standard formulation of the Cauchy stress, $\boldsymbol{\sigma}_s$, between different constitutive equations, a more generally applicable method is preferred. Therefore, a finite difference approximation is used to compute the components of $(A^{m,k}_{s,ab})_{op}$, where, defining the operator,

$$\mathbf{h}_t(p, \boldsymbol{\lambda}_c, \mathbf{y}) = -\mathbf{b}_t\left(p, \mathbf{y}\right)_{\Omega_s} + \left(\boldsymbol{\lambda}_c, \mathbf{y}\right)_{\Gamma_c} - \left(\mathbf{f}_s, \mathbf{y}\right)_{\Omega_s} - \left(\mathbf{g}^N_s, \mathbf{y}\right)_{\Gamma^N_s}, \tag{2.69}$$

the block contributions are given as,

$$(A^{m,k}_{s,ab})_{op} = \frac{1}{2\epsilon}\int_{t^{m-1}}^{t^m} \mathbf{s}^+_t\left(\boldsymbol{\sigma}_s(\mathbf{u}^{h,+}), \psi^o_{\mathbf{u}}\mathbf{e}_a\right)_{\Omega_s} - \mathbf{s}^-_t\left(\boldsymbol{\sigma}_s(\mathbf{u}^{h,-}), \psi^o_{\mathbf{u}}\mathbf{e}_a\right)_{\Omega_s} dt$$

$$+\frac{1}{2\epsilon}\int_{t^{m-1}}^{t^m} \mathbf{h}^+_t(p^{h,m,k-1}, \boldsymbol{\lambda}^{h,m,k-1}_c, \psi^o_{\mathbf{u}}\mathbf{e}_a) - \mathbf{h}^-_t(p^{h,m,k-1}, \boldsymbol{\lambda}^{h,m,k-1}_c, \psi^o_{\mathbf{u}}\mathbf{e}_a)dt, \tag{2.70}$$

where,

$$\mathbf{u}^{h,\pm}(t) := \mathbf{u}^{h,m,k-1}(t) \pm \epsilon\frac{(t - t^{m-1})}{\triangle^m_t}\psi^p_{\mathbf{v}}\mathbf{e}_a. \tag{2.71}$$

Here, $\epsilon \approx 10^{-4}h_s$ and the superscript $\pm$ denotes the use of the perturbed operators defined in equation 2.72. Due to the Lagrangian formulation, integrals and gradients on Ω are functions of $\mathbf{u}^h$. To estimate the Jacobian, perturbations of $\mathbf{u}^h$ must be accounted for in the gradient and mapping Jacobian functions, which become,

$$\nabla^{\pm}_{\mathbf{x}} := [\nabla_{\boldsymbol{\eta}}\mathbf{u}^{h,\pm} + \mathbf{I}]^{-T}\nabla_{\boldsymbol{\eta}}, \;\; \jmath^{\pm}_t := det|\nabla_{\boldsymbol{\eta}}\mathbf{u}^{h,\pm} + \mathbf{I}|. \tag{2.72}$$

The perturbed gradient and mapping Jacobian functions are used in the computation of the operators $\mathbf{s}^{\pm}_t\left(\boldsymbol{\sigma}_s(\mathbf{u}^{h,\pm}), \psi^o_{\mathbf{u}}\mathbf{e}_a\right)_{\Omega_s}$ and $\mathbf{h}^{\pm}_t(p^{h,m,k-1}, \boldsymbol{\lambda}^{h,m,k-1}_c, \psi^o_{\mathbf{u}}\mathbf{e}_a)$.

2.4.3.3 Pressure Matrix Blocks

The components of the fluid and solid pressure blocks, $(B^{m,k}_{f,a})_{op}$ and $(\tilde{B}^{m,k}_{s,a})_{op}$, can be determined analytically and are defined as,

$$(B^{m,k}_{f,a})_{op} = \int_{t^{m-1}}^{t^m} \mathbf{b}_t\left(\psi^o_{p_f}, \psi^p_{\mathbf{v}}\mathbf{e}_a\right)_{\Omega_f} dt, \;\; (\tilde{B}^{m,k}_{s,a})_{op} = \int_{t^{m-1}}^{t^m} \mathbf{b}_t\left(\psi^o_{p_s}, \psi^p_{\mathbf{u}}\mathbf{e}_a\right)_{\Omega_s} dt. \tag{2.73}$$

Due to non–linearities in the mapping Jacobian, $\jmath_{\Omega_s}, t$, with respect to changes in $\mathbf{u}$, the solid incompressibility constraint block, $(B^{m,k}_{s,a})_{op}$, is computed using a finite difference approximation,

$$(B^{m,k}_{s,a})_{op} = \frac{1}{2\epsilon}\left((\psi^o_{p_s}, \jmath^+_{t^m})_{\Lambda_s} - (\psi^o_{p_s}, \jmath^-_{t^m})_{\Lambda_s}\right), \tag{2.74}$$

where, $\jmath^{\pm}_{t^m}$ and ϵ are as defined in section 2.4.3.2.

2.4.3.4 Lagrange Multiplier Constraint Matrix Blocks

Lastly, the Lagrange multiplier blocks for the coupling and FD constraints are introduced. For the coupling constraint, the inputs to the $d \times d$ matrix subcomponents, $(C^m_{f,ab})_{op}$ and $(C^m_{s,ab})_{op}$, are given as,

$$(C^m_{f,ab})_{op} = -\int_{t^{m-1}}^{t^m} (\psi^o_{\boldsymbol{\lambda}_c}\mathbf{e}_a, \psi^p_{\mathbf{v}}\mathbf{e}_b)_{\Xi} dt, \quad (C^m_{s,ab})_{op} = (\psi^o_{\boldsymbol{\lambda}_c}\mathbf{e}_a, \psi^p_{\mathbf{u}}\mathbf{e}_b)_{\Xi}. \tag{2.75}$$

The integrals are performed on the reference domain Ξ and the mapping Jacobian is incorporated into the variables $\boldsymbol{\lambda}^h_c$. As a result, the inputs to $(C^m_{f,ab})_{op}$ and $(C^m_{s,ab})_{op}$ do not change with successive Newton iterations or time steps and they only need to be computed once.

The inputs to the FD $d \times d$ matrix subcomponents, $(FD^{m,k}_{f,ab})_{op}$, are,

$$(FD^m_{f,ab})_{op} = \int_{t^{m-1}}^{t^m} (\psi^o_{\boldsymbol{\lambda}_{Fd}}\mathbf{e}_a, \psi^p_{\mathbf{v}}\mathbf{e}_b)_{\Gamma_{Fd}} dt. \tag{2.76}$$

2.4.4 Populating the Jacobian Sub–Matrices

Practically, the matrix subcomponents are populated by summing the integrals over each element, $e \in \mathcal{T}_h(\Lambda)$. The basic algorithm for assembling the matrix sub–blocks is the same for all the Jacobian subcomponents. Considering the case of the fluid subcomponent, $(A^{mk}_{f,ab})$, for a mesh of n_e elements, with n_p nodes per element and n_z test functions per element, $(A^{mk}_{f,ab})$ is populated by performing the following loops,

for $i = 1 : n_e$ **do**
  for $j = 1 : n_p$ **do**
    for $l = 1 : n_z$ **do**
      $(\mathcal{Z}_{ab})_{(T_{\mathbf{v}}(i,j))(T_{\mathbf{v}}(i,l))} = (\mathcal{Z}_{ab})_{(T_{\mathbf{v}}(i,j))(T_{\mathbf{v}}(i,l))} + (A^{mk}_{f,ab})^{e_i}_{(T_{\mathbf{v}}(i,j))(T_{\mathbf{v}}(i,l))}$
    end for
  end for
end for

$(A^{mk}_{f,ab})_{(T_{\mathbf{v}}(i,j))(T_{\mathbf{v}}(i,l))} = (\mathcal{Z}_{ab})_{(T_{\mathbf{v}}(i,j))(T_{\mathbf{v}}(i,l))}$

where $(\mathcal{Z}_{ab})$ is an empty matrix block, initialised to zero, of equal size to $(A^{mk}_{f,ab})$ and $(A^{mk}_{f,ab})^{e_i}_{rs}$ is the evaluation of the operator $(A^{mk}_{f,ab})_{rs}$ integrating over the element e_i. $T_{\mathbf{v}}$ represents the node element map for $\mathcal{T}_h(\Lambda_f)$. Note that for the kinematic blocks $n_p = n_z$, while for the constraint blocks, $n_p < n_z$ and n_z is equal to the number of nodes per element in the domain on which the constraint is applied.

2.5 Solution Methods

The previous section detailed the global Jacobian matrix system, which is solved for the iterative update of the solution vector $\mathcal{X}^{m,k}$. To practically construct and solve the system, various elements need to be

addressed. This section outlines the necessary details and methods used to solve the system including, element types (section 2.5.1), numerical integration of the fictitious domain space (section 2.5.2), a modified Newton–Raphson/line search method for minimising matrix solves (section 2.5.3), the mesh update problem (section 2.5.4) and finally the methods used for coupling model boundaries to lumped parameter models (section 2.5.5).

2.5.1 Element Types

The choice of polynomial functions, ψ_j, for interpolating the spatial and state variable fields, $\mathcal{V}_j$, is important for the stability and convergence of the finite element system[13]. The element type is defined as the combination of polynomials on an element, $e \in \mathcal{T}_h(\Lambda)$, used to interpolate all spatial and state variables within Λ. The primary restriction on the element type is that it satisfies the *inf–sup* condition[134] for uniqueness of solution. In this thesis, two classes of basis functions are used, Taylor–Hood[17] and Crouzeix–Raviart[30].

Many stable element types exist[218], however, for this thesis, meshes are constructed using 3 different element types, curvilinear tetrahedrals (TET), curvilinear hexahedrals (HEX) and linear triangles (TRI). These element types were chosen due to a combination of numerical simplicity – integration schemes are equivalent on all element faces for each of these element types – and practical mesh generation reasons. Given that the kinematic and constraint variables are defined using different polynomial orders, for notational simplicity an element type, ELEM, is defined as,

$$\text{ELEM}(i, j, k),$$

for an element type of i^{th} order spatial interpolation, j^{th} order velocity/displacement interpolation and k^{th} order pressure interpolation. For example, using this notation, a mesh constructed of linear tetrahedrals, where velocity is solved using quadratic and pressure using linear polynomials is defined as $\text{TET}(1, 2, 1)$. For the Lagrange multiplier bases, only two polynomial orders are required, the first defining the geometry of the Lagrange multiplier domain and the second giving the order of approximation of the solution space. For example, a Lagrange multiplier space made from linear triangles and solved using linear basis would be defined as $\text{TRI}(1, 1)$.

2.5.1.1 Basis Function Types

To integrate over the global elements, e, it is necessary to define the composition of the basis functions, φ. Given the basis, $\varphi : \mathbb{R}^d \to \mathbb{R}$, consisting of n polynomials of order m,

$$\varphi_i = \sum_{j=1}^{m} \alpha_{ij} \prod_{k=1}^{d} \phi_k^{\beta_{kj}}, \tag{2.77}$$

α is an $n \times m$ coefficient array and β an $d \times m$ array of power terms. The determinants of the coefficients in α and β differ between Taylor–Hood (TH) and Crouzeix–Raviart (CR) basis types. Appendix A provides α and β, along with the nodal coordinates $\boldsymbol{\phi}$, for the basis functions used in this thesis.

Taylor–Hood Basis Functions:

For TH elements of order O, a cardinal basis, $\mathcal{S}(\boldsymbol{\phi})$, is constructed consisting of all possible combinations of $\prod_{i=1}^{d}\phi_i^{a_i}$, with a combined order, *i.e.* the sum of the powers, a_i, $\sum_{i=1}^{d}a_i \leq \mathcal{O}$, $a_i > 0$. The maximum combined polynomial power, $\mathcal{O}$, is defined as $\mathcal{O} = O$ for tetrahedral/triangular elements and $\mathcal{O} = d \times O$ for hexahedral/quadrilateral elements. For example, a 2^{nd} order cardinal basis is defined with respect to a triangular element as,

$$\mathcal{S} = \left\{1,\, \phi_1,\, \phi_2,\, \phi_1\phi_2,\, \phi_1^2,\, \phi_2^2\right\} \tag{2.78}$$

while for a quadrilateral,

$$\mathcal{S} = \left\{1,\, \phi_1,\, \phi_2,\, \phi_1\phi_2,\, \phi_1^2,\, \phi_2^2,\, \phi_1^2\phi_2,\, \phi_1\phi_2^2,\, \phi_1^2\phi_2^2\right\}. \tag{2.79}$$

The number of nodes, n, in $\hat{e}$ is defined from the cardinal basis as $n = \text{span}\left\{\mathcal{S}\right\}$, where node i is located at $\phi = \gamma_i$ within $\hat{e}$.

Based on the Nodal Lagrange definition in equation 1.1, the coefficient tensor α is defined as the solution to,

$$M\alpha^T = I,\;\; \alpha = M^{-T}. \tag{2.80}$$

Note that for Taylor–Hood basis functions α is an $n \times n$ tensor. M is populated by evaluating $\mathcal{S}$ at each nodal coordinate, *i.e.*

$$M(i,:) = \mathcal{S}(\gamma_i). \tag{2.81}$$

The array of power terms, β, is also defined from $\mathcal{S}$, where the power terms are equivalent to the power terms used to construct $\mathcal{S}$, *i.e.* using $\mathcal{S}$ as defined in equation 2.78,

$$\beta = \begin{bmatrix} 0 & 1 & 0 & 1 & 2 & 0 \\ 0 & 0 & 1 & 1 & 0 & 2 \end{bmatrix}. \tag{2.82}$$

Crouzeix–Raviart Basis Functions:

Crouzeix–Raviart (CR) basis functions are defined on tetrahedrons and triangles where, unlike with TH, the order of the polynomial, m, is greater than the number of polynomials, n, *i.e.* the coefficient array, α is an $n \times m$ array, $n < m$. As a result, there is no unique solution for the coefficients that satisfies,

$$M\alpha^T = I, \tag{2.83}$$

where M is defined in equation 2.81, except the cardinal basis now incorporates $m - n$ additional power terms. The additional orders arise as extra polynomial terms are incorporated to define 'bubble' functions on the faces of, and within, $\hat{e}$, see figure 2.4 for a spatial representation of the functions. The Crouzeix–Raviart coefficients of α and β for 2^{nd} order triangles and tetrahedrons are provided, based on Bertrand *et al.*[9], in appendix A.

Using CR interpolation functions for the kinematic variables enables the pressure space to be approximated by discontinuous interpolation functions (*i.e.* where the nodes defining the discrete pressure space, $\mathcal{V}_p$ are unique to each element), see section 2.5.1.2. Discontinuous pressures mean additional degrees of freedom are added to $\mathcal{V}_p$, which are balanced by an enrichment of the velocity space, $\mathcal{V}_{\mathbf{v}}$, by adding degrees of freedom corresponding to each bubble function. For example, a second order[3] CR tetrahedron has extra degrees of freedom, compared

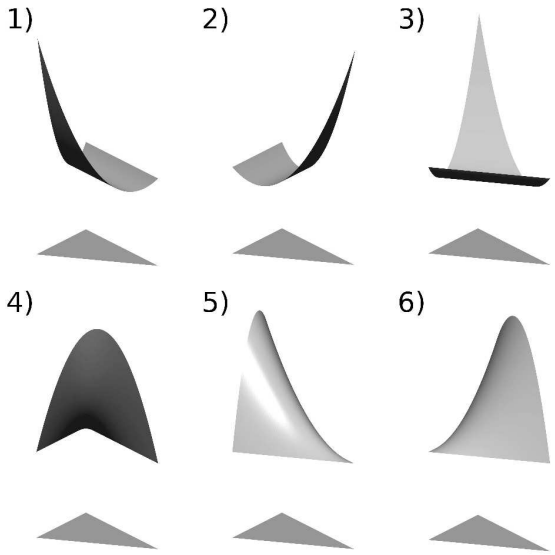

FIGURE 2.3. 2^{nd} *order triangular TH basis functions.*

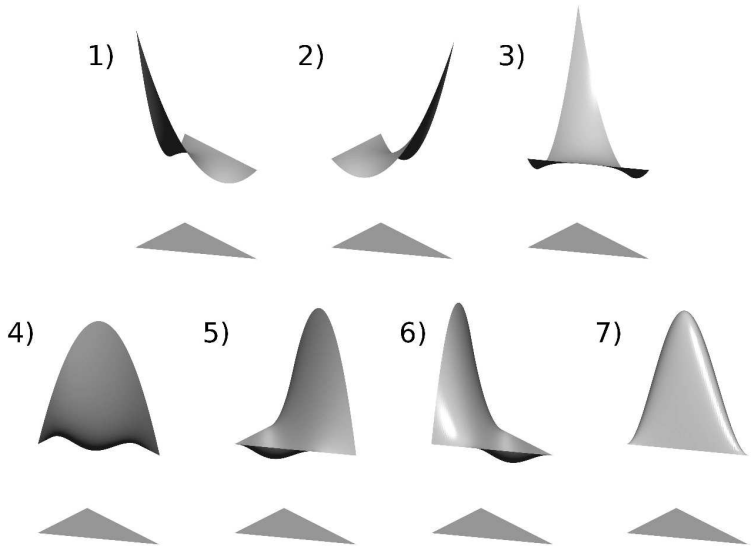

FIGURE 2.4. 2^{nd} *order triangular CR basis functions. Note the effect of the bubble function (7) on the shapes of the other interpolation functions. Equations for all basis functions used in this thesis are given in appendix A.*

with an equivalent second order TH element, added at each face and one within the tetrahedral volume. Table 1 compares the degrees of freedom associated with second order CR elements and comparable TH elements.

In this thesis, a CR element with i^{th} order spatial interpolation, j^{th} order CR spatial/velocity interpolation

[3]The extra degrees of freedom mean that a second order CR element is not strictly second order, it contains higher order terms to define the bubble functions associated with the additional element degrees of freedom. For convenience the CR elements will be referred to as having the order of an equivalent TH element, *i.e.* the CR element without the bubble functions.

	2^{nd} order TH	2^{nd} order CR	3^{rd} order TH
Triangle	6	7	10
Tetrahedron	10	15	20

TABLE 1

Comparison of the degrees of freedom associated with 2^{nd} and 3^{rd} order Taylor–Hood (TH) triangular/tetrahedral elements and equivalent CR elements. Note that the basis degrees of freedom on each CR element is between the equivalent TH elements.

and discontinuous pressure interpolation of order k, will be referred to as,

$$\text{ELEM}(i, j\,cr, k\,dc),$$

where ELEM refers to the element type (either TET or TRI for CR elements).

2.5.1.2 Restrictions on Element Type

Restrictions exist on the suitability of various element types with different problems. For incompressible fluid/solid problems, in order to satisfy the *inf–sup* condition, the test functions for the pressure Lagrange multipliers must be of lower order than those for the kinematic variables. This restricts element types for the fluid/solid problems to ELEM$(k, i, i-j)$, where $i > j \geq 0$ and $k \geq 1$.

Further restrictions arise when additional constraints are placed on the system. In particular, for FD methods to adequately characterise pressure gradients (see chapter 3), the ability to represent discontinuous pressures is required. To enable this, CR elements are used to prevent loss of accuracy when there is a pressure drop across the FD. Additionally, discontinuous elements should be used to characterise the FD Lagrange multiplier space, in this thesis FD elements are interpolated as discontinuous constants. The final restriction with respect to FD elements relates to the CL of the elements immersed in the fluid. To prevent locking from over constraining the system, the CL of the FD mesh should not be smaller than the CL of the fluid mesh in which it is immersed.

With respect to the element types for the coupling space, Nordsletten *et al.*[136] showed that the optimal weak approximation of the coupling Lagrange multiplier space, when there is clear dominance of one system over the other, is achieved by nesting the Ξ domain elements on the boundary elements of the most refined of the coupled domains. In general, this means Ξ is nested on Υ_f^C. Additionally, the interpolation order should be the same as that used to approximate the kinematic variables on the nested boundaries.

2.5.2 Integration of the Fictitious Domain Subspace

Using the finite element method, difficulties in applying FD methods arise in accurately evaluating the discrete weak form equations for the FD constraint, equations 2.56. These difficulties occur because $\mathcal{T}_h(\Upsilon_{Fd})$ will not necessarily be congruous with the fluid mesh, $\mathcal{T}_h(\Lambda_f)$ (particularly for ALE problems and/or when $\mathbf{v}_{Fd} \neq 0$). Furthermore, calculating integrals on the intersection of complex geometries is computationally costly, which makes it impractical to use curvilinear element types for either the fluid or FD meshes. To overcome this issue,

for a fluid mesh constructed of linear tetrahedral elements and a FD mesh of triangular elements, a simple triangulation algorithm was developed to accurately calculate the integrals.

The intersection of any triangle with any linear tetrahedron creates either an $n-$sided convex polygon, a line, or a point. Given that a line and a point have zero area, only the $n-$sided polygon is considered. For any element $e_i \in \mathcal{T}_h(\Gamma_{Fd})$ a set $P_i(t)$ is defined at time t, which denotes those tetrahedra intersecting with e_i, i.e.

$$P_i(t) = \{e_p \in \mathcal{T}_h(\Omega_t) |\ e_i \cap e_p \neq \emptyset\}.$$

To create the $n-$sided polygon created by the intersection between a tetrahedral element $e_p \in P_i(t)$ and e_i, a set of the n vertices of $e_p \cap e_i$ is constructed. Letting $\{F_i^j\}_{j=1}^3$ and $\{L_i^j\}_{j=1}^3$ denote the nodes and edges of the triangle, e_i, and $\{Q_p^j\}_{j=1}^4$ denote the faces of $e_p \in P_i(t)$, the vertices are defined as,

$$V_k = \{F_i^j \in F_i |\ F_i^j \in e_p\} \cup \{L_i^j,\, Q_p^o \in L_i \times Q_p | L_i^j \cap Q_p^o \text{ is a point }\}.$$

Thus the $n-$sided polygon is constructed from the convex hull of V which can be triangulated into $n-2$ triangles, see figure 2.5.

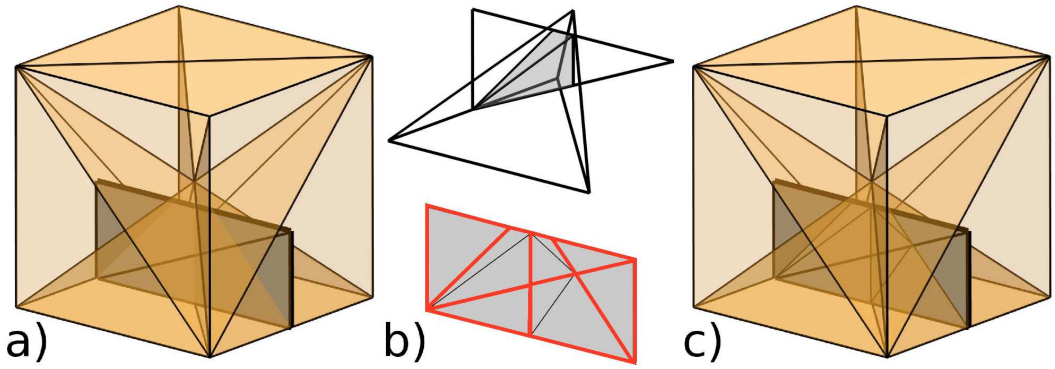

FIGURE 2.5. *a) the intersection of two FD elements with a tetrahedral mesh. b), top, the intersection of one of the FD elements with one of the tetrahedrons, the triangulated polygon is shaded gray on the face of the FD element. b), bottom, the FD elements after all intersecting polygons, outlined in red, have been triangulated, the integration subdivisions are shown on the faces of the FD elements. c) the triangulated FD elements intersecting with the tetrahedral mesh.*

The integral of a function, $f(x)$, defined on each of the intersecting tetrahedron, e_p, over e_i can be calculated as the sum of the integrals over each of the $m \times (n-2)$ triangles, where m is the number of elements e_i intersects with. Using Gaussian integration this is:

$$\int_{e_i} f \, \mathbf{dx} = \sum_{a=1}^{m} \sum_{b=1}^{n-2} \sum_{c=1}^{nGp} f(Gp(c))\, Gw(c)\, \jmath_t^a(b), \tag{2.84}$$

where $\jmath_t^a(b)$ is the area of triangle b from the polygon a, while nGp, Gp and Gw refer to the number of Gauss points, the Gauss points and the Gauss weights respectively. Note that the function is evaluated with respect to Gauss points and weights on the $m \times (n-2)$ triangles.

In an ALE problem and/or when $\mathbf{v}_{Fd} \neq 0$ the intersection of $\mathcal{T}_h(\Upsilon_{Fd})$ with $\mathcal{T}_h(\Lambda_f)$ needs to be computed at each iteration. This is performed efficiently using a nearest neighbour search method. The algorithm first

checks the elements in $P_i(t)$ from the previous iteration then, if the integration is not complete, *i.e.* $\int_{e_i} dx$ is less than the area of e_i, the algorithm searches the neighbours of the elements in $P_i(t)$, creating a new set of tetrahedra $P_i^*(t)$. This process continues until either the integration is complete or the elements in $P_i^*(t)$ are outside a bounding box encasing e_i.

2.5.3 A Modified Newton–Raphson Scheme and Line Search Algorithm

Computing the inverse, of the global Jacobian matrix, $\mathcal{A}^{m,k}$, is computationally costly and, as a result, it is desirable to minimise the number of times the inverse is calculated. This section outlines a novel approach involving reusing the Jacobian inverse from previous iterations, combined with correct selection in line search convergence criteria, for minimising calls to the matrix solver.

From equation 2.65, the k^{th} update vector, or descent direction towards the solution, $\mathbf{X}^m$, at time step m, is given as,

$$\delta\mathcal{X}^{m,k} = -(\mathcal{A}^{m,k})^{-1}\mathscr{R}^m(\mathbf{X}^{m,k-1}).$$

The update, $\delta\mathcal{X}^{m,k}$, monotonically decreases the residual, such that,

$$\max_{\alpha^k\in[0,1]} |\mathscr{R}^m(\mathbf{X}^{m,k})|_{l2} < |\mathscr{R}^m(\mathbf{X}^{m,k-1})|_{l2}, \;\; \mathbf{X}^{m,k} = \mathbf{X}^{m,k-1} + \alpha^k\delta\mathcal{X}^{m,k}. \tag{2.85}$$

Over successive iterations the update, $\delta\mathcal{X}^{m,k}$, is usually small compared with the solution, *i.e.*

$$|\delta\mathcal{X}^{m,k}|_{l2} << |\mathcal{X}^{m,k}|_{l2}.$$

As a result, the change in $\mathcal{A}^{m,k}$ is also small, therefore,

$$\mathcal{A}^{m,k} \approx \mathcal{A}^{m,k-1} \tag{2.86}$$

and the update,

$$\delta\mathcal{X}^{m,k} \approx -(\mathcal{A}^{m,k-1})^{-1}\mathscr{R}^m(\mathbf{X}^{m,k-1}). \tag{2.87}$$

This approximate equivalence means the computed inverse, $(\mathcal{A}^{m,k-1})^{-1}$, can be reused for successive iterations and time steps as long as the update continues to monotonically decrease the residual. However, the further the iterative solution, $\mathbf{X}^{m,k}$, is from the iterative solution used to compute the inverse, the worse the approximation of $\mathscr{A}^{m,k}$. Therefore, an additional convergence criteria is introduced, whereby the matrix inverse will be reused if,

$$\frac{|\mathscr{R}^m(\mathbf{X}^{m,k})|_{l2}}{|\mathscr{R}^m(\mathbf{X}^{m,k-1})|_{l2}} < \kappa, \;\; \kappa < 1 \tag{2.88}$$

otherwise the inverse, $(\mathcal{A}^{m,k})^{-1}$, will be computed at the following iteration. Each Newton iteration performed using the precomputed Jacobian inverse is termed a sub–iteration and κ the sub–iteration convergence criteria. κ is chosen based on problem characteristics and is typically between 0.5 and 0.8. The impact of this reuse of the Jacobian inverse is discussed in chapter 3.

2.5.3.1 Line Search

Due to the use of both Newton iterations and sub–iterations, depending on whether the matrix is inverted, it is necessary to modify the standard line search algorithm[156] for calculating the update scalar α_k. The line search algorithm uses previous evaluations of $\mathscr{R}^m(\mathbf{X}^{m,k-1}+\alpha_{k,i}\delta\mathcal{X}^{m,k})$ to fit a polynomial which is minimised to provide an update, $\alpha_{k,i+1}$, of the scalar coefficient. Defining the function,

$$\mathbf{g}(\alpha_k) = |\mathscr{R}^m(\mathbf{X}^{m,k-1} + \alpha_k\delta\mathcal{X}^{m,k})|_{l2}, \quad \alpha_{k,i} \in [0,1] \tag{2.89}$$

a quadratic polynomial is constructed to approximate $\mathbf{g}(\alpha_k)$, where,

$$\mathbf{g}(\alpha_k) \approx a\alpha_k^2 + b\alpha_k + \mathbf{g}(0). \tag{2.90}$$

Finding the quadratic coefficients, a and b, requires the evaluation of $\mathbf{g}(\alpha_k)$ at three points, *i.e.* $\mathbf{g}(\alpha_{k,i})$, $\mathbf{g}(\alpha_{k,i-1})$ and $\mathbf{g}(0)$. Note $\mathbf{g}(0)$ is known from the solution to the previous Newton iteration/sub–iteration. The minimum of equation 2.90 is chosen as the update $\alpha_{k,i+1}$.

Iteratively solving for α_k so that it finds the true $\min\{\mathscr{R}^m(\mathbf{X}^{m,k-1}+\alpha_k\delta\mathcal{X}^{m,k})\}$, $\alpha_k \in [0,1]$, involves numerous residual evaluations which can be computationally costly. Therefore, a criteria is set such that if,

$$0 < \upsilon < \zeta, \;\; \upsilon = \frac{|\mathscr{R}^m(\mathbf{X}^{m,k-1} + \alpha_{k,i}\delta\mathcal{X}^{m,k})|_{l2}}{|\mathscr{R}^m(\mathbf{X}^{m,k-1})|_{l2}}, \;\; \zeta \leq 1, \tag{2.91}$$

the algorithm exits and the scalar $\alpha_{k,i}$ is chosen.

Starting with an initial guess, $\alpha_{k,0} = 1$, if $\mathbf{g}(\alpha_{k,0})$ does not satisfy equation 2.91, the interval $[0,1]$ is bisected so that $\alpha_{k,1} = 0.5$. If this still does not satisfy equation 2.91, the system,

$$\begin{bmatrix} \alpha_{k,i}^2 & \alpha_{k,i} \\ \alpha_{k,i-1}^2 & \alpha_{k,i-1} \end{bmatrix} \begin{bmatrix} a \\ b \end{bmatrix} = \begin{bmatrix} \mathbf{g}(\alpha_{k,i}) - \mathbf{g}(0) \\ \mathbf{g}(\alpha_{k,i-1}) - \mathbf{g}(0) \end{bmatrix} \tag{2.92}$$

is solved for the coefficients a and b and $\alpha_{k,i+1}$ is updated as,

$$\alpha_{k,i+1} = \begin{cases} \frac{b}{2a}, & \text{if } 0 \leq \frac{b}{2a} \leq 1 \\ 0.5\alpha_{k,i}, & \text{else} \end{cases}. \tag{2.93}$$

The algorithm iterates until either equation 2.91 is satisfied, or a maximum iteration number, i_{max}, is reached.

In the standard line search algorithm $\zeta = 1$, however, if $\kappa < \upsilon < 1$ a new matrix inverse will be computed. Since it is desirable to minimise matrix inversions, $\zeta = \kappa$ is chosen, *i.e.* the line search algorithm will attempt to find an improved update $\alpha_k\delta\mathcal{X}^{m,k}$ before inverting the matrix. If, after attempting to improve the update using line search, equation 2.91 still is not satisfied, α_k is selected as that which evaluates $\min\{\mathbf{g}(0), \mathbf{g}(1), \cdots, \mathbf{g}(\alpha_{k,i_{max}})\}$ and a new matrix inverse is calculated at the subsequent Newton iteration.

2.5.4 Mesh Update for ALE Problems

The mesh update Laplacian problem for the fluid mesh, defined in equation 2.52, is solved as a separate system of linear equations for each residual evaluation, where, at time step m, the mesh update matrix is defined as,

$$M^m = \begin{bmatrix} M^m_{11} & \cdots & M^m_{1d} \\ \vdots & \ddots & \vdots \\ M^m_{d1} & \cdots & M^m_{dd} \end{bmatrix} \in \mathbb{R}^{N_{\mathbf{x}_f} \times N_{\mathbf{x}_f}}, \quad (M^m_{ab})_{op} = \mathbf{a}_t(\psi^p_{\mathbf{x}_f}\mathbf{e}_b, \psi^o_{\mathbf{x}_f}\mathbf{e}_a)_{\Omega_f(t^{m-1})} \tag{2.94}$$

As the Laplacian problem is linear, the solution does not need to be solved iteratively. A conjugate gradient method[124] is used to solve the matrix problem.

To preserve mesh regularity, particularly important in FD problems due to integration issues, the problem is modified for cases where the spatial domain is approximated by high order tetrahedrons. For these cases, internal elements are spatially interpolated using linear tetrahedra, while the boundaries are approximated using curvilinear spatial interpolation.

Let $\mathbf{x}_v \in \mathcal{T}_h(\Lambda_f)$ be the set of all nodes situated on element vertices in the curvilinear fluid tetrahedral mesh. M^m is reformulated to be a $N_{\mathbf{x}_v} \times N_{\mathbf{x}_v}$ matrix, $N_{\mathbf{x}_v} = \text{span}\{\mathbf{x}_v\}$, and the Laplacian problem is now solved for the update of $\mathbf{x}_v$ only[4]. The boundary condition on the mesh update, $\mathbf{d}^h = \triangle^m_t \mathbf{v}^{h,m}$, on $\Gamma_f(t^{m-1})$, is not altered, therefore the higher order spatial interpolation on the boundary is maintained. Internal nodes, not included in $\mathbf{x}_v$ are updated as the interpolated linearised solution.

2.5.5 Coupling to Lumped Parameter Models

Physical systems do not exist in isolation and it is often necessary to incorporate the effects of the environment surrounding the three–dimensional model as boundary conditions. Normally this is achieved by coupling the 3D model to lumped parameter models (typically 0D or 1D) representing the the response of the surrounding environment to model behaviour. In this thesis, the 3D models are coupled to 0D Windkessel models representing the systemic and pulmonary circulatory networks. As a result, it is necessary to define the methods used for coupling boundaries to 0D lumped parameter models. Here two methods will be presented, the first is a fixed point iterative scheme for coupling 0D models to boundaries on Ω_f (defined Γ^{0D}_f) and the second, a Lagrange multiplier method for coupling lumped parameter models to boundaries on Ω_s (defined Γ^{0D}_s).

2.5.5.1 Fixed–Point Scheme for 0D–Fluid Domain Coupling

As discussed in section 1.3.2.2, there are multiple methods for resolving the issues inherent in coupling fluid problems to 0D models. Lumped parameter models provide an averaged representation of pressure, P_{0D}, which,

[4]note the basis functions $\psi_{\mathbf{x}_f}$ in equation 2.94 are now $\psi_{\mathbf{x}_v}$ and are defined with respect to a linear tetrahedral.

if applied directly as a Neumann traction condition, is equivalent to,

$$\mathbf{t} = P_{0D}\mathbf{I}\cdot\mathbf{n} = (\mu\mathcal{D}_{\mathbf{x}}\mathbf{v} - p\mathbf{I})\cdot\mathbf{n}.$$

There are two main issues associated with this direct approach, firstly, unless $\mathcal{D}_{\mathbf{x}}\mathbf{v} \approx 0$, the flux across the fluid boundary will not characterise the pressure, P_{0D}. Secondly, applying the condition directly is effectively equivalent to introducing an infinite reservoir of fluid to which the boundary is attached. This can cause instabilities if there are rapid changes in P_{0D} (this instability is demonstrated in section 3.2). Other methods, for example using inflow/outflow cannula to stabilise flow on Γ_f^{0D} are computationally impractical for the large problems such as the coupled fluid–solid LV simulations presented in this thesis and can introduce flow artifacts in moving domain problems. Additionally, they do not address the problem of non–physical approximations of the 0D/3D interface. Therefore a prescribed profile/free volume flux method was developed for this thesis.

The pressure gradient, between the 0D and 3D models can be approximated as the difference between the 0D pressure and the integrated domain pressure,

$$P = \frac{1}{|\Omega_f|}\int_{\Omega_f} p \; d\Omega_f, \tag{2.95}$$

where $|\Omega_f|$ is the volume of the cavity. Volume flux (Q) across Γ_f^{0D} is subsequently calculated from the lumped parameter model, using P as a boundary condition. Q is prescribed on Γ_f^{0D} by scaling a function, $\mathbf{f}(\mathbf{x},\mathbf{t}) \in \Gamma_f^{0D}$, which describes a profile, e.g. Poiseuille, Womersley etc, representing the flow across Γ_f^{0D},

$$Q = \alpha\int_t\int_{\Gamma_f^{0D}} \mathbf{f}(\mathbf{x},\mathbf{t}) \; d\Gamma_f^{0D} \; dt. \tag{2.96}$$

The scaled function, $\alpha\mathbf{f}(\mathbf{x},\mathbf{t})$, is prescribed as the Dirichlet condition, $\alpha^h\mathbf{f}^h(\mathbf{x},t)$ on Γ_f^{0D}, where $\mathbf{f}^h(\mathbf{x},t)$ is the finite element approximation of $\mathbf{f}(\mathbf{x},\mathbf{t})$ and α^h is chosen to maintain the equivalence in equation 2.96.

Flux across Γ_f^{0D} inevitably changes the integrated domain pressure, which will lead to an updated evaluation of Q from the lumped parameter model. Therefore, the system is iteratively updated using a fixed–point scheme whereby Q, and by extension the prescribed profile, is recalculated at each residual evaluation based on the current domain pressure.

2.5.5.2 Lagrange Multiplier/Fixed–Point Method for 0D–Solid Domain Coupling

The coupling of solid problems to lumped parameter models can be accomplished by either applying the pressure calculated from the 0D model as a boundary condition, or, for cavity problems, applying the volume change evaluated from the 0D model on the cavity as a constraint. Since this thesis is focused on ventricular (*i.e.* cavity) problems, a Lagrange multiplier constraint, $\lambda_{0D} \in \Gamma_s^{0D}$, was introduced to prescribe volume change on a cavity encased by a hyperelastic solid.

Given an empty cavity encased by a hyperelastic solid, the volume change of the cavity, over the time interval $I = [a,b]$, is equivalent to,

$$\delta V = \int_a^b \int_{\Gamma_s^{0D}} \partial_t\mathbf{u}\cdot\mathbf{n} \; d\Gamma_s^{0D}, \tag{2.97}$$

where $\mathbf{n}$ is the outward normal on Γ_s^{0D}. If V is known, *i.e.* has been calculated by the lumped parameter model, this forms a constraint on the solid problem, equations 2.32. Considering the Finite Elasticity weak form, the weak form of the Lagrange multiplier volume constraint problem is given as,

$$\int_a^b \mathbf{s}_t \left(\boldsymbol{\sigma}_s(\mathbf{u}), \mathbf{y}\right)_{\Omega_s} \, dt - \int_a^b \mathbf{b}_t \left(p, \mathbf{y}\right)_{\Omega_s} \, dt + \int_a^b \left(\lambda_{0D}\mathbf{n}, \mathbf{y}\right)_{\Gamma_c} \, dt = 0,$$

$$\int_a^b \left(\partial_t \mathbf{u}, \mathbf{n}\right)_{\Gamma_s^{0D}} \, dt = \delta V, \tag{2.98a}$$

where δV is the volume change of the cavity. The Lagrange multiplier represents the normal pressure applied to Γ_s^{0D}, this equivalence is shown in chapter 3. For a solid only problem, on which this constraint is applied, the block matrix structure, defined using the methods outlined in section 2.4, at iteration k, time step m, is,

$$\begin{bmatrix} A_s^{m,k} & \tilde{B}_s^{m,k} & (LM_s^{m,k})^T \\ B_s^{m,k} & 0 & 0 \\ LM_s^{m,k} & 0 & 0 \end{bmatrix}, \tag{2.99}$$

where the Lagrange multiplier block $LM_s^{m,k}$ is defined as,

$$LM_s^{m,k} = \begin{bmatrix} LM_{s,11}^{m,k} & \cdots & LM_{s,1d}^{m,k} \end{bmatrix} \in \mathbb{R}^{1\times N_{\mathbf{u}}}, \quad (M_a^m)_{1p} = \int_{t^{m-1}}^{t^m} (\psi_{\mathbf{u}}^p \mathbf{e}_a, \mathbf{n}\mathbf{e}_a)_{\Gamma_s^{0D}} dt. \tag{2.100}$$

Additionally, the operator $\mathbf{h}_t$, equation 2.69, is updated to include $(\lambda_{0D}, \mathbf{n}\cdot\mathbf{y})_{\Gamma_c}$, *i.e.* $\mathbf{h}_t = \mathbf{h}_t + (\lambda_{0D}, \mathbf{n}\cdot\mathbf{y})_{\Gamma_c}$.

As with the 0D–fluid coupling problem, solving for the pressure, λ_{0D}, changes the volume change calculated by the lumped parameter model. Therefore, the system is iteratively updated using a fixed–point method where, as with the fluid problem, V is recalculated for each Residual evaluation based on the current applied pressure.

2.6 Computational Implementation

The numerical methods developed during this thesis were implemented in cHeart, a coupled multi–physics software programme originally developed by Nordsletten[134]. Written in FORTRAN 90, using MPI parallel computing, cHeart enables the finite element solution of the problem types outlined in this section. The major additions to cHeart made during this thesis include: implementation of FD methods within the ALE coupled fluid–solid framework; coupling cHeart to lumped parameter models for both solid and fluid problems; and various improvements to the solution methods including investigating matrix solvers, as well as the line search/Newton–Raphson modifications. Additionally, various minor schemes were implemented, such as the modifications to the mesh update scheme, as well as several techniques/methods required for cardiac simulations. These are described in the subsequent chapters.

Figure 2.6 shows a schematic of the cHeart code structure along with the core solution steps. The outline describes the process by which the code reads in problem files, constructs the matrix structure and solves the

problem at each time step. The problem types available in cHeart are fluid (Stokes/Navier–Stokes), solid, coupled, FD and lumped parameter. Where compatible, any number of these problem types can be solved for/coupled together. Tessellations are provided for each problem type, read in from separate problem files. The tessellations for each field (spatial, velocity/displacement, pressure, coupling, FD etc.) and boundary domain (*i.e.* $\mathcal{T}_h(\Upsilon^i)$, where $i = N, C, D$) are provided by the user and are constructed using preparatory routines. cHeart supports nodal Lagrange interpolation functions of an arbitrary degree, allowing a diverse range of element types to be used, see appendix A.

The core routines in cHeart are the residual and Jacobian sub–matrix evaluations. At each residual evaluation, both the FD intersections and lumped parameter model solutions are updated based on the previous solution update. The Jacobian sub–matrices, in contrast, are evaluated much less frequently and, depending on the rate of change of the global system, might not be recomputed for multiple time steps. The sparsity patterns for these matrices, with the exception of the FD matrix block, are constructed prior to entering the initial time step. For the FD problem, since the intersections can change with either FD or fluid mesh movement, the sparsity pattern is recomputed when the residual is updated.

Due to the size of the global matrices in large coupled systems, parallelisation was a necessity. The direct matrix solvers used to invert the matrix regularly use 1+GB of memory on 16+ cores, which (obviously) would not be solvable on most architectures in serial. Additionally, populating the global matrix, particularly when residual differencing is used, requires a large number of function evaluations which would be costly to perform in serial. However, various aspects, such as the mesh update algorithm, have not been optimised for parallel computing and, as a result, a future area of code development is improving such issues to improve the scalability of the code.

2.6.1 Monolithic Matrix Solver

The global Jacobian matrix, $\mathcal{A}^{m,k}$, is solved monolithically using a direct matrix solver. Direct solvers were chosen as, unlike iterative solvers, there are no preconditioner requirements. Additionally, due to the Lagrange multiplier constraints, the indefinite structure of $\mathcal{A}^{m,k}$ is complex, making the convergence of iterative solvers slow.

Two direct solvers were tested as part of this Thesis, SuperLU[29] and Mumps[56]. Their relative performance is compared in section 3.5.

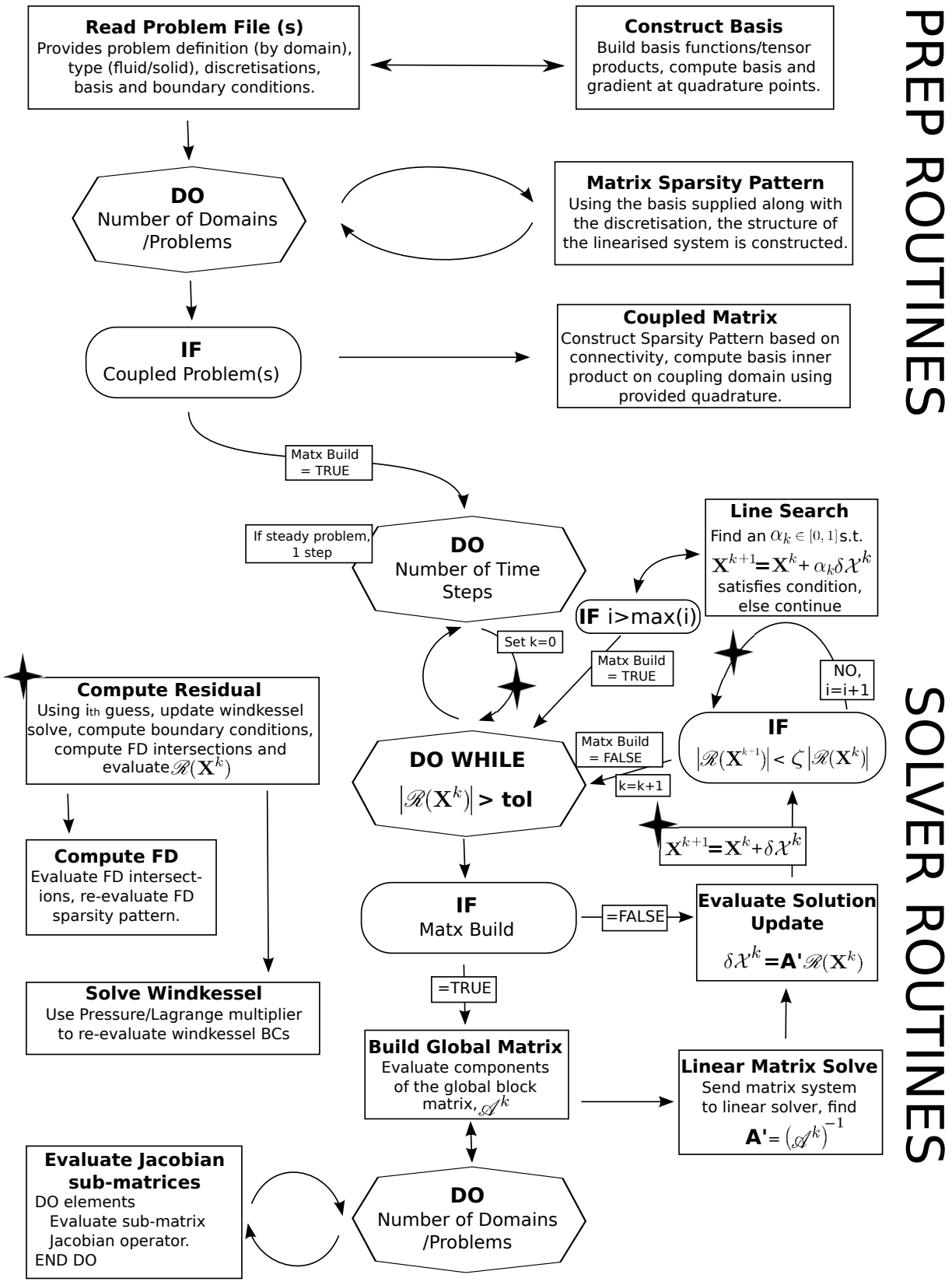

FIGURE 2.6. *Schematic of cHeart structure. Note star symbol equates to residual evaluation.*

3 Numerical Accuracy and Convergence

In this thesis, building on the fluid–solid coupling scheme developed by Nordsletten *et al.*[134, 136], novel numerical methods were implemented and applied to a range of canonical test problems and specific cardiac related simulations. As part of this work, the convergence behaviour and impact on system performance of the implemented methods was analysed in detail. To this end, specific problems were developed to test the convergence of the FD scheme (section 3.1), the 0D/3D coupling methods (section 3.2), as well as the spatial fluid element types used for coupling to high tension solids (section 3.3). Additionally, various methods were implemented to reduce the solution time at each time step. These methods include the line search/Newton Raphson modifications (section 3.4), as well as the choice of direct matrix solver (section 3.5).

Unless stated otherwise, all solid test examples use the isovolumetric neo–Hookean constitutive law, *i.e.* $\hat{\boldsymbol{\sigma}}_s = \frac{\mu}{2}(\mathbf{B} - \mathbf{I})$, where $\mathbf{B}$ is the left Cauchy–Green deformation tensor[106] ($\mathbf{F}\mathbf{F}^T$) and μ is the shear modulus.

3.1 Fictitious Domain Convergence

To analyse the performance of the fictitious domain model, test problems were performed to determine firstly, the accuracy of different element types in imposing a boundary on the fluid; secondly, the accuracy of FD techniques compared with equivalent non-FD simulations; and finally, the convergence of the the global system with mesh and time step refinement. To test the numerical properties of the FD implementation, multiple temporal and spatial refinements are required. Due to the computational expense of this analysis, the problems were implemented as thin 3D slices (two elements thick). This section presents the results of three types of problems: analytic (section 3.1.1), steady-state convergence (section 3.1.2) and transient fluid–solid coupled with FD (section 3.1.3)

3.1.1 Analytic Problems

The FD method indirectly applies boundaries on the fluid domain by imposing a constraint on the system. Before using this method in complex problems, it is important to understand the accuracy of the method in imposing this constraint. Additionally, the interaction between the FD Lagrange multiplier and the fluid domain is affected by the choice of element type for the fluid. To study these effects, two analytic problems were developed to test the accuracy of Crouzeix–Raviart/discontinuous pressure elements (CR/DP), compared with standard Taylor–hood/continuous pressure elements (TH/CP), for imposing a boundary on a fluid. The

problems, and their analytic solutions, are described in figure 3.1. For each problem, four different mesh refinements were used with characteristic lengths (CLs) of h, $h/2$, $h/4$, $h/8$, where $h = 0.08$. The TH/CP meshes were constructed using TET(1,2,1) elements, while the CR/DP meshes consisted of TET(1,2cr,1dc) elements. Problem degrees of freedom ranged from $\approx 1.8^4$ to $\approx 1.0^6$ for the TH/CP meshes; and $\approx 5.9^4$ to $\approx 3.4^6$ for the CR/DP. FD elements, TRI(1,0), were constructed so that their CL matched that of the fluid meshes, *i.e.* for a given fluid mesh $CL = h$ the FD meshes CL was also h. Meshes were constructed so that the FD boundary did not align with the fluid element faces. The results computed using these meshes are described in sections 3.1.1.1 and 3.1.1.2. An additional mesh was constructed, $CL = h$, specifically so that the FD boundary did align with the fluid element faces, results computed using this mesh are presented in section 3.1.1.3.

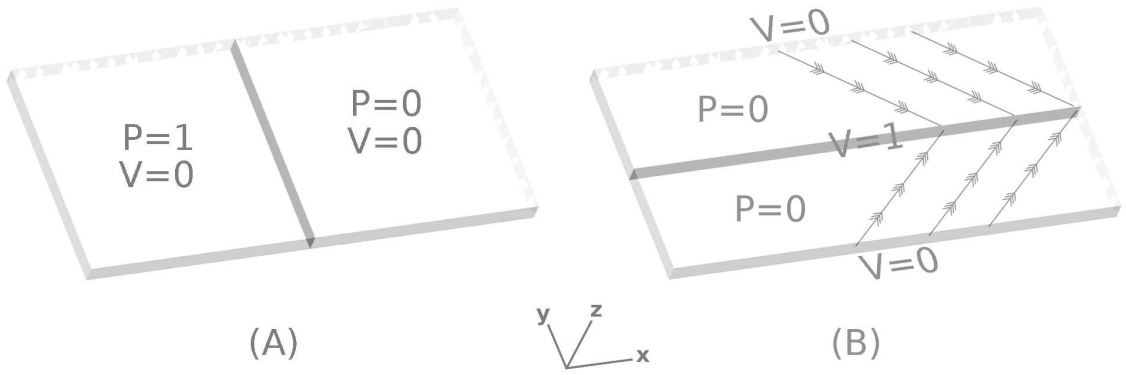

FIGURE 3.1. *Analytic problems to test the convergence of different fluid element types used in FD problems. Each box has dimensions* $2 \times 1 \times 2h$*, where* h *is the meshes* CL*. Coordinate axis,* $\mathbf{x}$, $\mathbf{y}$, $\mathbf{z}$ *are shown. For the simulations, fluid density was* 1.0 *and viscosity was* 0.1.

A) ***Pressure gradient in a blocked channel.*** *Pressure of 1 was applied on the left hand boundary while the right hand boundary was left free (*$\Gamma_f^N = 0$*). On the edges of the box* $\mathbf{v} = 0$ *and* $\mathbf{v_z} = 0$ *on the top and bottom boundaries. A FD divided the domain in two, blocking flow through the box. The analytic solution has* $p = 1$, $\mathbf{v} = 0$ *to the left of the FD and* $p = 0$, $\mathbf{v} = 0$ *to the right.*

B) ***Sliding boundary.*** *In this problem, the left and right hand boundaries were left free (*$\Gamma_f^N = 0$*) while the FD, situated in the centre of the channel had a velocity* $\mathbf{v_{FD}} = [\mathbf{1}, \mathbf{0}, \mathbf{0}]$*. The edges of the channel were fixed,* $\mathbf{v} = 0$*, and* $\mathbf{v_z} = 0$ *on the top and bottom boundaries. The analytic solution was* $p = 0$ *and* $\mathbf{v_{x,y}} = 0$ *everywhere and* $\mathbf{v_z} = 1$ *at the FD boundary, decaying linearly to* 0 *on the edges.*

3.1.1.1 Pressure Gradient in a Blocked Channel

The problem of a pressure gradient in a blocked channel was developed to test the capability of FD boundaries at capturing a discontinuity in pressure within the fluid domain. Of specific interest, was the relative capacity of discontinuous and continuous pressure interpolations in capturing this discontinuity and the impact the choice of pressure basis had on the velocity solution. The results, for the different mesh refinements, were

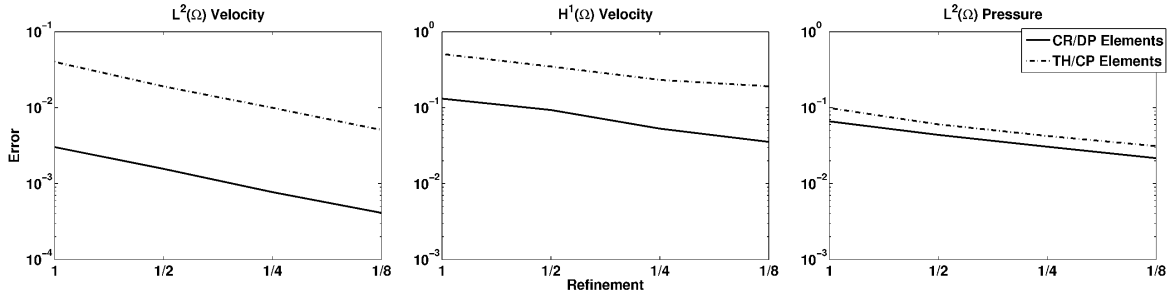

FIGURE 3.2. *Convergence of the pressure gradient in a blocked channel problem. Meshes, of various refinements (x axis) were constructed using either CR/DP or TH/CP elements. The y axis shows either the L^2 norms of the velocity and pressure error, or the H^1 semi–norm of the velocity error. Average slope of the L^2 velocity norm:* 0.96 *for CR/DP elements,* 0.99 *for TH/DP elements; H^1 velocity norm:* 0.63 *for CR/DP elements,* 0.47 *for TH/DP elements; and L^2 pressure norm:* 0.54 *for CR/DP elements,* 0.56 *for TH/DP elements. A rate of* 1 *is equivalent to $\mathcal{O}(h)$ convergence.*

Convergence of $\mathrm{L}^2(\Omega_f)_{\mathbf{v}}$

Element \ h	1	1/2	1/4	1/8
CR/DP	3.02×10^{-3}	1.67×10^{-3}	8.09×10^{-4}	4.11×10^{-4}
TH/CP	3.99×10^{-2}	1.90×10^{-2}	9.94×10^{-3}	5.08×10^{-3}

Convergence of $\mathrm{H}^1(\Omega_f)_{\mathbf{v}}$

Element \ h	1	1/2	1/4	1/8
CR/DP	1.31×10^{-1}	9.32×10^{-2}	5.30×10^{-2}	3.54×10^{-2}
TH/CP	5.09×10^{-1}	3.48×10^{-1}	2.32×10^{-1}	1.91×10^{-1}

TABLE 1

The L^2 semi-norms and H^1 norms of the velocity error in the non–transient pressure gradient in a blocked channel problem. Columns indicate the norm values on various grid refinements.

compared with the analytic solution projected onto the 2D mid–plane of the box. Problem convergence is shown in figure 3.2 and table 1. Error, particularly with respect to the $L^2(\Omega)_{\mathbf{v}}$ norm, was approximately one order of magnitude lower in the CR/DP meshes than in the TH/CP ones. The CR/DP meshes also had lower pressure error, although the difference was less significant, largely due to high pressures localised to elements intersecting the FD, see figure 3.4. Convergence rates for the two element types were comparable.

Visualising the solutions highlights the significance of the element type on numerical accuracy. Figure 3.3 shows the $\mathbf{x}$ and $\mathbf{y}$ components of the velocity solutions for the $h/2$ and $h/8$ mesh refinements. Continuous flow through the channel – *i.e.* across the FD – occurs in all simulations. Flow was substantially higher for the TH/CP meshes, to the extent that even the most refined TH/CP result had greater flow than that observed in least refined CR/DP mesh. Additionally, velocity error in the $\mathbf{y}$ direction was both higher in the TH/CP meshes and not as localised to the FD as it was in the CR/DP case.

Examining the pressure solution, figure 3.4, the reason for the significantly higher velocity error in the TH/CP meshes is evident. While pressure error was not substantially higher in the TH/CP problems, the error was

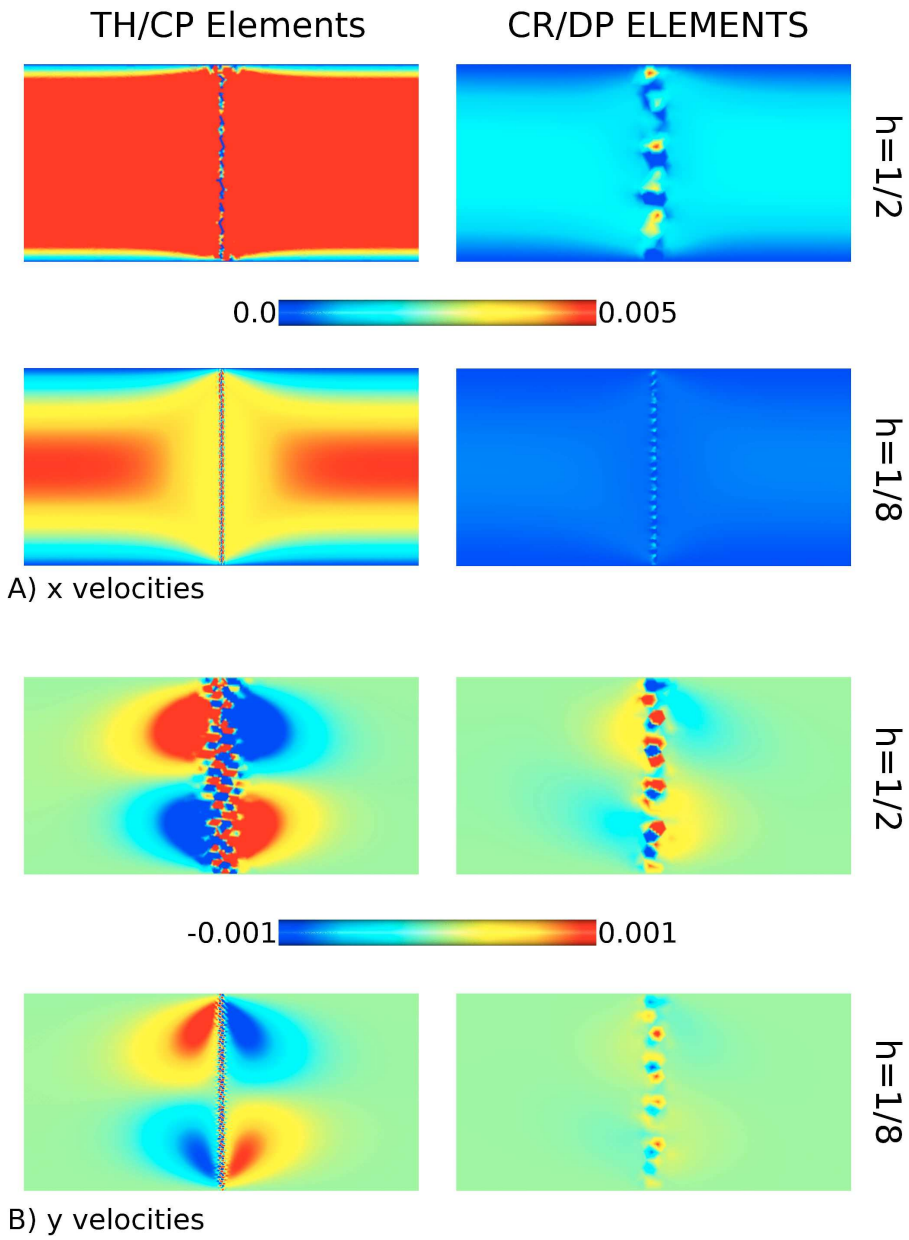

FIGURE 3.3. *Fluid velocities from the simulation results of the pressure gradient in a blocked channel problem. A) velocities in the* **x** *direction. B) velocities in the* **y** *direction. Results are shown for the* $h/2$ *and* $h/8$ *meshes, TH/CP results are on the left, CR/DP on the right.*

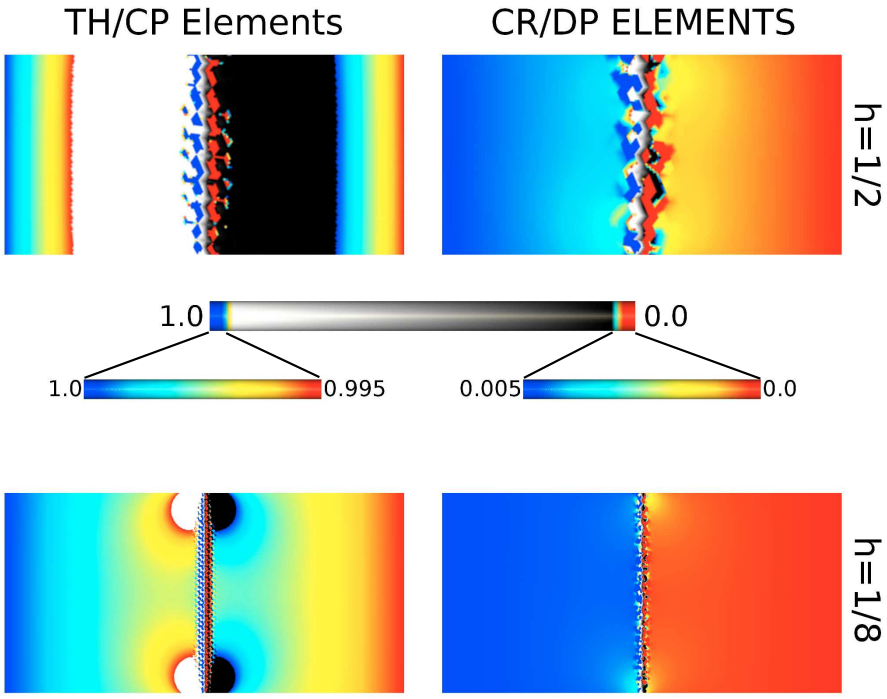

FIGURE 3.4. *Pressure results from the simulations of the pressure gradient in a blocked channel problem. Results are shown for the $h/2$ and $h/8$ TH/CP (left) and CR/DP (right) meshes. Three pressure scales are used, white to black for intermediate pressures; blue to red (left) for pressures close to 1, relevant to the left sides of each plot; and blue to red (right) for pressures close to 0, relevant to the right sides of each plot.*

spread out away from the FD boundary, rather than localised to it as it was in the CR/DP case. This error spread was due to the continuous pressure field. Discontinuous pressures limit the ability of the pressure gradient across the FD from spreading to other elements, thereby reducing flow over the FD boundary.

This problem demonstrates the impact of the choice of fluid element type in simulating FD problems where there is a pressure discontinuity in the fluid solution. Discontinuous pressures significantly increase the accuracy of both the pressure and velocity solutions for such problem types.

3.1.1.2 Sliding Boundary

The sliding boundary problem was designed to test whether the greater accuracy of CR/DP elements, observed in the previous section, occurs when no pressure gradient is present in the fluid. The results, for the same mesh refinements as the pressure gradient in a blocked channel problem, were compared with the analytic solution, again projected onto the 2D mid–plane of the box. Problem convergence is shown in figure 3.5 and table 2. Error and convergence rates were roughly comparable for the velocity L^2 norm, as well as the H^1 semi–norm. The L^2 Pressure norm and convergence properties were slightly worse using CR/DP elements, however this can be attributed to local error in the vicinity of the FD due to the choice of a discontinuous basis. It is apparent from these convergence results, that the choice of continuous or discontinuous pressure basis functions does not significantly influence the simulation accuracy for this problem.

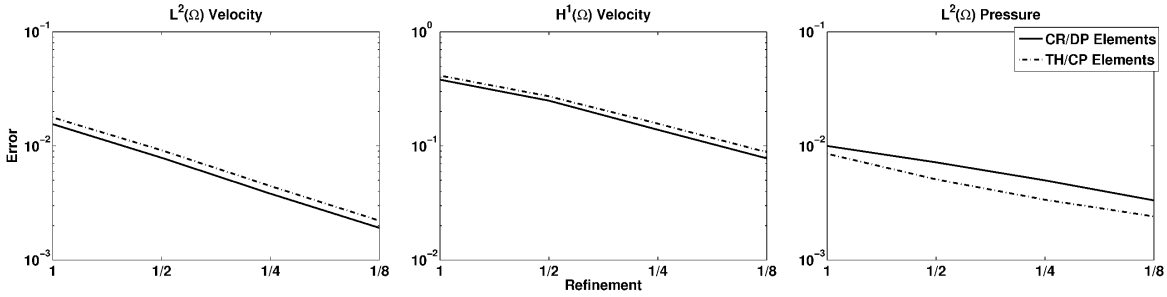

FIGURE 3.5. *Convergence of the sliding boundary problem. Meshes, of various refinements (x axis) were constructed using either CR/DP or TH/CP elements. The y axis shows either the L^2 norms of the velocity and pressure error, or the H^1 semi–norm of the velocity error. Convergence rates, equivalent to the mean slope, were L^2 velocity norm:* 1.01 *for CR/DP elements,* 1.00 *for TH/DP elements; H^1 velocity semi–norm:* 0.76 *for CR/DP elements,* 0.74 *for TH/DP elements; and L^2 pressure norm:* 0.53 *for CR/DP elements,* 0.61 *for TH/DP elements. A rate of* 1 *is equivalent to $\mathcal{O}(h)$ convergence.*

Convergence of $\mathrm{L}^2(\Omega_f)_{(\mathbf{v}-\mathbf{v}_{ref})}$

Element \ h	1	1/2	1/4	1/8
CR/DP	1.55×10^{-2}	7.87×10^{-3}	3.81×10^{-3}	1.91×10^{-3}
TH/CP	1.78×10^{-2}	9.17×10^{-3}	4.45×10^{-3}	2.21×10^{-3}

Convergence of $\mathrm{H}^1(\Omega_f)_{(\mathbf{v}-\mathbf{v}_{ref})}$

Element \ h	1	1/2	1/4	1/8
CR/DP	3.81×10^{-1}	2.49×10^{-1}	1.39×10^{-1}	7.79×10^{-2}
TH/CP	4.13×10^{-1}	2.72×10^{-1}	1.57×10^{-1}	8.81×10^{-2}

TABLE 2

The L^2 semi-norms and H^1 norms of the velocity error in the non–transient sliding boundary problem. Columns indicate the norm values on various grid refinements.

Visualising the error provides a comparison of the spatial distribution of error in the results. Figure 3.6 shows the velocity and figure 3.7 the pressure error for the two basis types. From these figures, it is apparent that the regional error spread is also comparable between CR/DP and TH/CP elements in this problem. In both cases, error is largely confined to the $\mathbf{v_x}$ velocity components and localised on the FD boundary – particularly with respect to pressure.

This test problem indicates that in problems where there is no pressure gradient across the FD, the choice of either continuous or discontinuous pressures is not significant with respect to solution accuracy. For problems where there is not a significant gradient across the FD, TH/CP elements might be more appropriate as they require fewer degrees of freedom for a given mesh refinement than their equivalent CR/DP counterparts. The results of these two analytic problems highlight the importance of the choice in element type and the problems in which both might be appropriate.

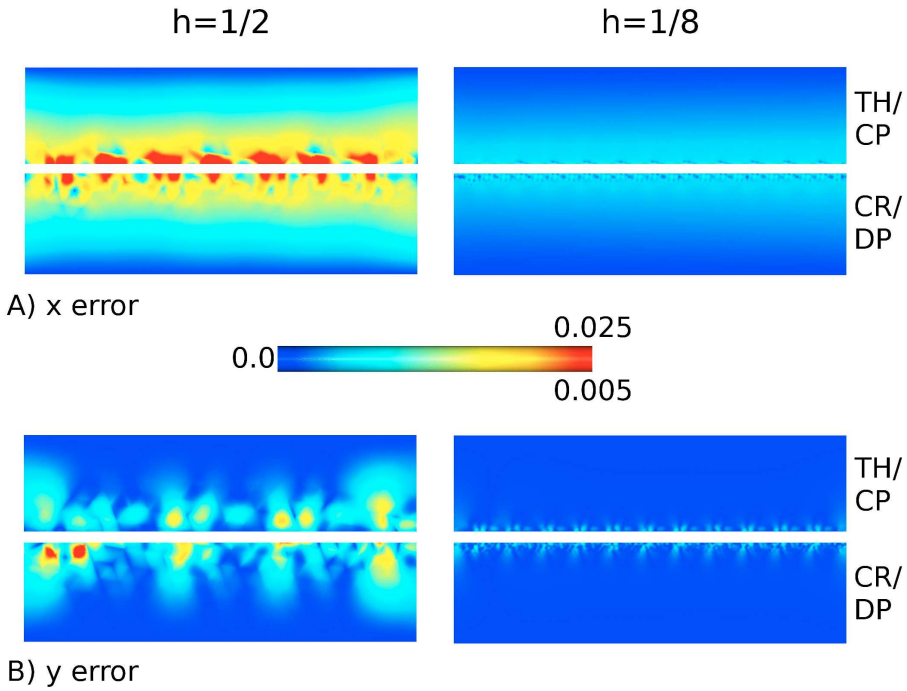

FIGURE 3.6. *Velocity error for the sliding boundary problem. A) magnitude of the* $\mathbf{x}$ *component* ($|\mathbf{v}_\mathbf{x}|$) *of velocity error, B) the magnitude of the* $\mathbf{y}$ *component. The results for the* $h/2$ *and* $h/8$ *mesh refinements are shown on the left and right respectively. Since the error is largely symmetric, only one half for each element type is shown and the results directly compared.*

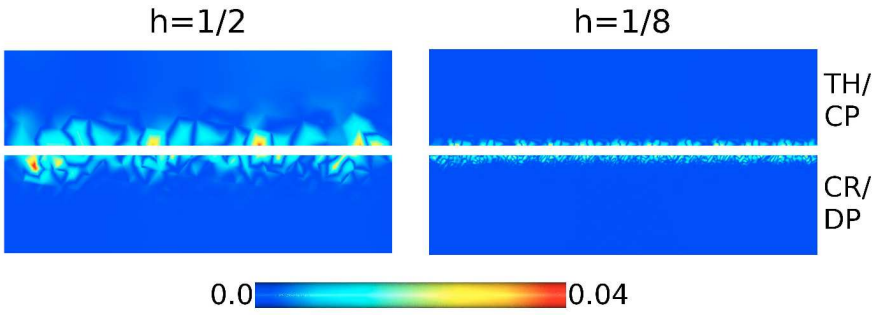

FIGURE 3.7. *Pressure error* ($|p|$) *for the sliding boundary problem. The results for the* $h/2$ *and* $h/8$ *mesh refinements are shown. As the error is largely symmetric only one half for each element type is shown.*

3.1.1.3 FICTITIOUS DOMAIN ALIGNMENT

The meshes for the results presented in sections 3.1.1.1 and 3.1.1.2 were constructed so that the FD mesh did not align with the fluid element faces. To test the impact of FD alignment on the numerical solutions to the analytic problems, additional fluid meshes, each with $CL = 0.08$ – *i.e.* the same as the least refined mesh from the convergence study – were constructed so that the FD boundary was exactly aligned with the surfaces of the fluid elements. The problems were then re–run using these meshes.

For the pressure gradient in a blocked channel problem, the TH/CP mesh performed comparably to the least

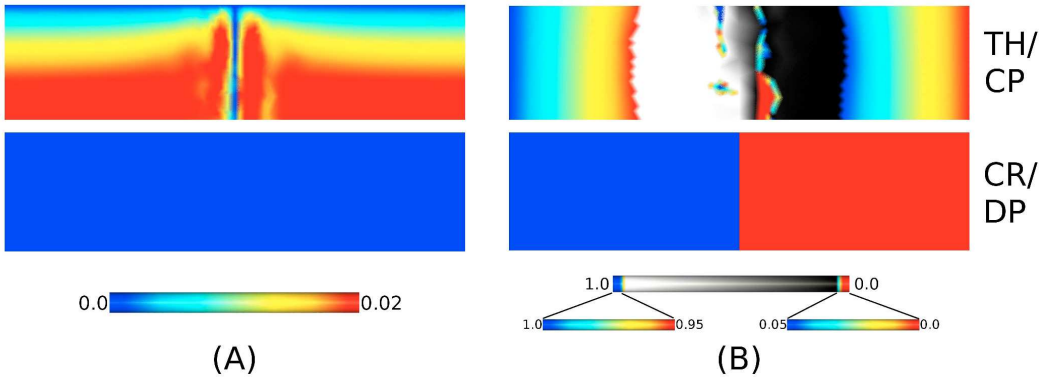

FIGURE 3.8. *Error for the pressure gradient in a blocked channel problem. A) velocity magnitude error* ($|\mathbf{v}|$)*, B) pressure error.*

refined of the meshes used in the convergence study. The CR/DP mesh, in contrast, produced the analytical solution within the tolerance of the numerical scheme. Visualisation of this result is shown in figure 3.8. For the sliding boundary problem, error in both the CR/DP and TH/CP cases, was approximately $\approx 10^{-15}$, *i.e.* within the machine precision.

These simulations highlight the conclusions drawn from the convergence results of the analytic problems – for problems where a pressure gradient is present across the FD, discontinuous pressures are better, otherwise the choice of element type makes no significant difference to the solution. While having the FD align with the fluid element faces improves simulation accuracy, within an ALE scheme the need to maintain this alignment presents significant challenges. In particular, in cases where there is significant mesh or FD movement, the fluid mesh will either get distorted, or, if the FD/fluid element alignments are recalculated, mesh velocities could be large, which in turn will result in additional error. Furthermore, if the FD approaches the fluid boundary, elements could get highly distorted in order to maintain alignment.

3.1.2 Convergence of Fictitious Domain and Dirichlet Boundaries

The analytic problems showed the capability of the FD method to approximate boundaries within the fluid domain. However, it is also important to understand how the use of FD affects the fluid solution compared with other boundary definitions, such as Dirichlet. This section introduces the problem of channel flow around an immersed cylinder[34, 45] to compare FD and Dirichlet boundaries at both low and high Reynold's numbers, $\mathcal{R}$, for CR/DP and TH/CP elements. The problem geometry and boundary conditions are given in figure 3.9. The cylinder was applied as either a FD or using Dirichlet boundary conditions. In the FD case, both TH/CP and CR/DP elements were considered.

Solving this problem under steady state (non–transient Navier–Stokes formulation) conditions results in the formation of two symmetric vortices stemming off the downstream surface of the cylinder. The size of these vortices is governed by the Reynold's number, with characteristic length and velocity values taken as the inlet

flow velocity and diameter of the cylinder, respectively. Considering the transient form of the Navier–Stokes equations, the steady state solution (for Reynold's numbers of 49 – 260) has been shown to be unstable[133], eventually leading to the breakdown in the steady flow pattern. Under these conditions, the transient solution produces a periodic steady state whereby vortices are periodically shed from the cylinder.

This section firstly (3.1.2.1) presents a convergence study of the steady state problem to determine the comparative accuracy of the FD scheme compared with the application of an equivalent Dirichlet boundary. Secondly, the solution to the transient, periodic problem is analysed in section 3.1.2.2, comparing the capability of TH/CP and CR/DP element types at capturing vortex shedding from the cylinder.

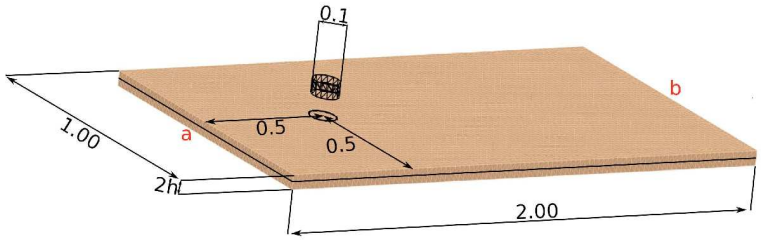

FIGURE 3.9. ***Flow past a circular cylinder.*** *The problem of flow past a circular cylinder was defined such that:* $\Gamma_f^D = [1, 0, 0]$ *on the leading edge (a) and sides of the box,* $\Gamma_f^N = 0$ *was prescribed on the trailing edge (b), while symmetry boundary conditions, i.e. zero flow in the direction normal to the plane, were prescribed on the top and bottom faces of the box. The cylinder, diameter 0.1, was prescribed as either* $\Gamma_f^D = 0$*, where it was approximated by a multifaceted boundary, or as a FD where* $\mathbf{v}_{Fd} = 0$*.*

3.1.2.1 Steady State Channel Flow around an Immersed Cylinder

To test the effect of FD prescribed boundaries on the numerical performance of the global scheme, the steady state problem of flow past a circular cylinder was considered. This problem was used to undertake a convergence study to determine the comparative accuracy and convergence rates between Navier–Stokes simulations with either FD or non–FD prescribed boundaries at different mesh refinements and Reynold's numbers. Four different mesh refinements were used for the study with CLs of h, $h/2$, $h/4$, $h/8$, where $h = 0.08$. At each mesh refinement, non–transient Navier–Stokes simulations were run at $\mathcal{R} = 0.1$ and 50 for both the FD (CR/DP and TH/CP elements) and Dirichlet prescribed cylinder cases. The results were compared with the results of the same simulations performed on a reference mesh, with $CL = h/16$, where the cylinder was prescribed as a Dirichlet (TH/CP) condition. Fluid meshes were TET$(1, 2, 1)$ for the Dirichlet and TH/CP FD cases and TET$(1, 2cr, 1dc)$ for the CR/DP FD case. FD meshes were TRI$(1, 0)$. Problem degrees of freedom ranged from $\approx 2 \times 10^4$ for $CL = h$ to $\approx 1 \times 10^6$ for $CL = h/8$ in the TH/CP; and $\approx 6 \times 10^4$ for $CL = h$ and $\approx 3 \times 10^6$ for $CL = h/8$ in the CR/DP meshes. The reference mesh had $\approx 3 \times 10^6$ degrees of freedom.

The velocity and pressure errors, projected onto the reference solution, are visualised in figures 3.10 and 3.11. In all cases, the error from the Dirichlet applied cylinder simulations was noticeably lower than either FD

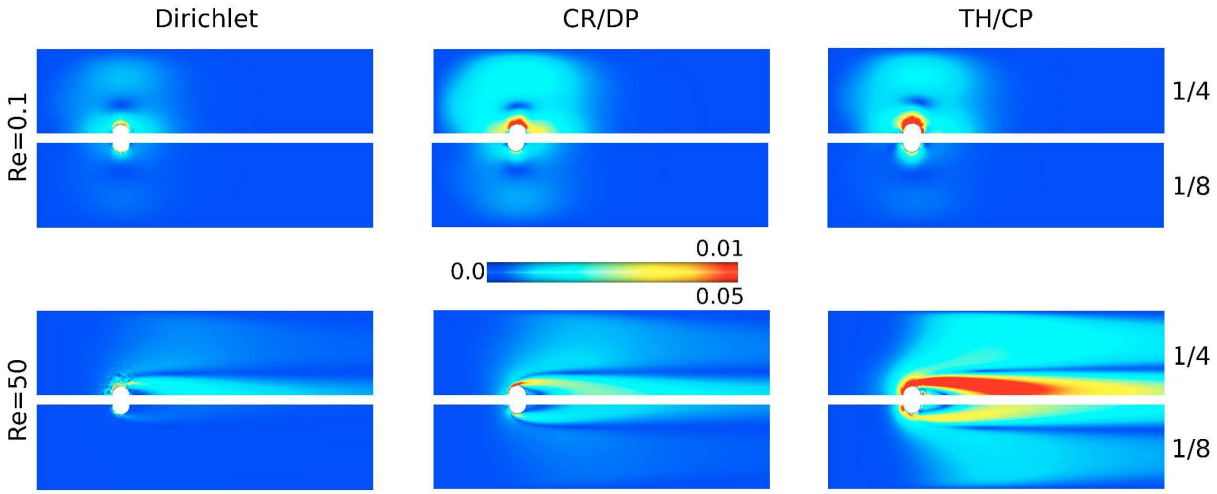

FIGURE 3.10. *The velocity error, $|\mathbf{v} - \mathbf{v}_{ref}|$, from the channel flow around an immersed cylinder problem. The error is projected onto the reference mesh for both the $\mathcal{R} = 0.1$, top row, and $\mathcal{R} = 50$, bottom row, problems. The top half on both the top and bottom rows shows the error from the $h/4$ results and the bottom half shows the $h/8$ results. The left hand figures show the error from when the cannula was prescribed as a Dirichlet boundary, the centre and right figures show the error from the FD cylinder results using CR/DP and TH/CP elements respectively.*

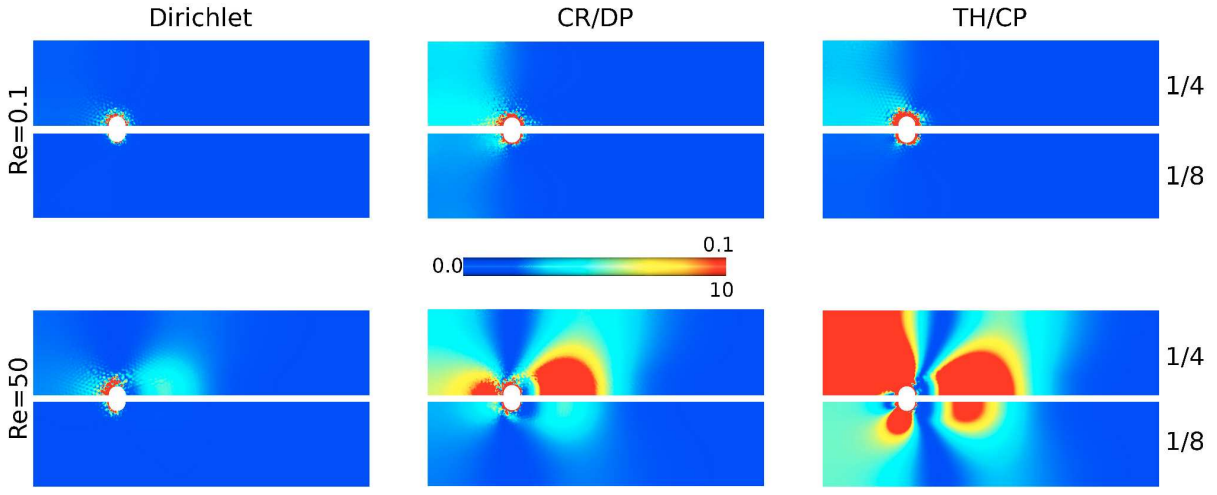

FIGURE 3.11. *The pressure error, $|p|$, from the channel flow around an immersed cylinder problem. The error is projected onto the reference mesh for both the $\mathcal{R} = 0.1$, top row, and $\mathcal{R} = 50$, bottom row, problems. The top half on both the top and bottom rows shows the error from the $h/4$ results and the bottom half shows the $h/8$ results. The left hand figures show the error from when the cannula was prescribed as a Dirichlet boundary, the centre and right figures show the error from the FD cylinder results using CR/DP and TH/CP elements respectively.*

case. For the low Reynold's number results, error was roughly comparable between the CR/DP and TH/CP problems. However, error was substantially higher in the TH/CP case when $\mathcal{R} = 50$. The convergence results, figure 3.12 and tables 3, 4 and 5, confirm this observation with both error and rate of convergence broadly comparable between the TH/CP and CR/DP FD cases when $\mathcal{R} = 0.1$. Both FD problems converged slower than the equivalent Dirichlet problem. In the high Reynold's number case, FD using discontinuous pressures performed significantly better than the TH/CP case (although both are worse than the Dirichlet results).

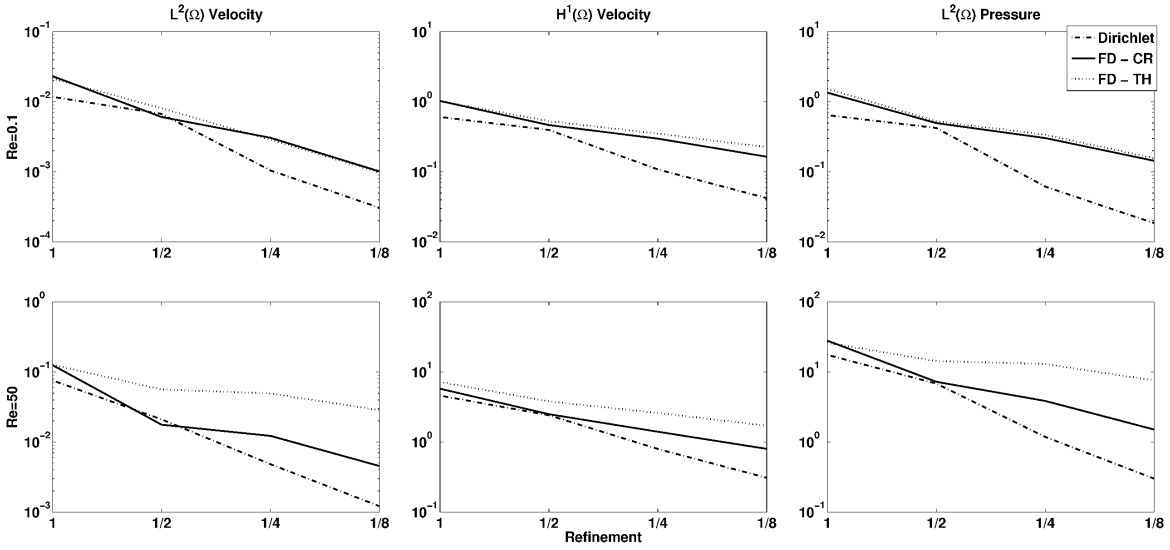

FIGURE 3.12. *Convergence of non–transient Navier–Stokes simulations of flow past a circular cylinder. The cylinder was prescribed as either a FD or as a Dirichlet boundary condition (non–FD). For the FD problems, both CR/DP (FD-CR) and TH/CP (FD-TH) meshes were considered. Results for* $\mathcal{R} = 0.1$*, top row, and* 50*, bottom row, are shown. The x axis gives the mesh refinement with respect to h, while the y axis shows either the* L^2 *norms of the velocity and pressure error, or the* H^1 *semi–norm of the velocity error.*

	$\mathcal{R} = 0.1$			$\mathcal{R} = 50$		
	Dirichlet	CR/DP	TH/CP	Dirichlet	CR/DP	TH/CP
$L^2(\Omega)_{(\mathbf{v}-\mathbf{v}_{ref})}$	1.75	1.51	1.48	1.99	1.59	0.72
$H^1(\Omega)_{(\mathbf{v}-\mathbf{v}_{ref})}$	1.28	0.88	0.73	1.30	0.95	0.69
$L^2(\Omega)_{(p-p_{ref})}$	1.71	1.08	1.10	1.96	1.41	0.60

TABLE 3

L^2 velocity and pressure, and H^1 velocity convergence rates for non–transient Navier Stokes simulations of flow past a circular cylinder. Rates are equivalent to the mean slopes in figure 3.12. A rate of 1 *is equivalent to* $\mathcal{O}(h)$ *and* 2 *is equivalent to* $\mathcal{O}(h^2)$ *convergence.*

It was noted that in general, the error of a non–FD case, with a given CL of h/n, was determined to be roughly comparable to the CR/DP FD case with $CL = h/2n$, particularly at higher mesh refinements. This observation is useful when considering local mesh refinement around a FD.

A final demonstration of the relative performance of FD compared with Dirichlet boundaries in the non–transient flow past a circular cylinder problem is provided in figure 3.13, which shows the simulation results

Convergence of $\mathrm{L}^2(\Omega_f)_{(\mathbf{v}-\mathbf{v}_{ref})}$ for $\mathcal{R} = 0.1$

Element \ h	1	1/2	1/4	1/8
Dirichlet	1.17×10^{-2}	6.72×10^{-3}	1.05×10^{-3}	3.06×10^{-4}
CR/DP	2.32×10^{-2}	6.06×10^{-3}	3.06×10^{-3}	1.01×10^{-3}
TH/CP	2.15×10^{-2}	8.08×10^{-3}	2.88×10^{-3}	9.82×10^{-4}

Convergence of $\mathrm{H}^1(\Omega_f)_{(\mathbf{v}-\mathbf{v}_{ref})}$ for $\mathcal{R} = 0.1$

Element \ h	1	1/2	1/4	1/8
Dirichlet	6.09×10^{-1}	3.97×10^{-1}	1.08×10^{-1}	4.21×10^{-2}
CR/DP	1.03×10^{0}	4.66×10^{-1}	2.98×10^{-1}	1.64×10^{-1}
TH/CP	1.02×10^{0}	5.30×10^{-1}	3.51×10^{-1}	2.25×10^{-1}

TABLE 4

The L^2 semi-norms and H^1 norms of the velocity error with $\mathcal{R} = 0.1$ in the flow past a circular cylinder problem. Columns indicate the norm values on various grid refinements.

Convergence of $\mathrm{L}^2(\Omega_f)_{(\mathbf{v}-\mathbf{v}_{ref})}$ for $\mathcal{R} = 50$

Element \ h	1	1/2	1/4	1/8
Dirichlet	7.57×10^{-2}	2.10×10^{-2}	4.82×10^{-3}	1.21×10^{-3}
CR/DP	1.25×10^{-1}	1.77×10^{-2}	1.22×10^{-2}	4.53×10^{-3}
TH/CP	1.27×10^{-1}	5.62×10^{-2}	4.94×10^{-2}	2.84×10^{-2}

Convergence of $\mathrm{H}^1(\Omega_f)_{(\mathbf{v}-\mathbf{v}_{ref})}$ for $\mathcal{R} = 50$

Element \ h	1	1/2	1/4	1/8
Dirichlet	4.59×10^{0}	2.41×10^{0}	7.94×10^{-1}	3.08×10^{-1}
CR/DP	5.77×10^{0}	2.49×10^{0}	1.40×10^{0}	7.98×10^{-1}
TH/CP	7.19×10^{0}	3.80×10^{0}	2.60×10^{0}	1.71×10^{0}

TABLE 5

The L^2 semi-norms and H^1 norms of the velocity error with $\mathcal{R} = 50$ in the flow past a circular cylinder problem. Columns indicate the norm values on various grid refinements.

for the $h/8$ Dirichlet and CR/DP FD meshes. All the visible flow features and pressure gradients present in the non–FD case are captured using FD.

3.1.2.2 Transient Flow at High Reynold's Numbers

To test the relative performance of FD compared with Dirichlet boundaries at higher Reynold's numbers, the transient problem needs to be considered. Choosing a Reynold's number of 200, the problem was run, using either FD (CR/DP or TH/DP elements) or Dirichlet boundaries to describe the cylinder, until the periodic steady state had been reached. To reduce computational expense, locally refined meshes were constructed

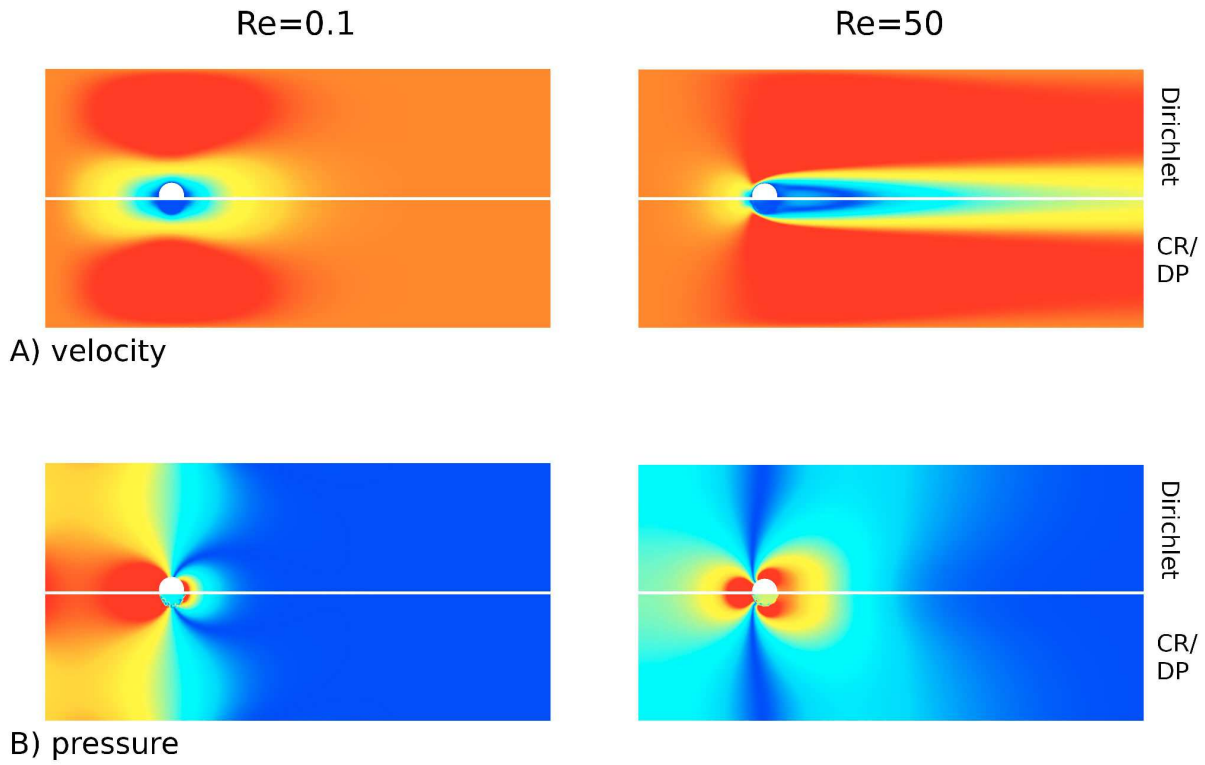

FIGURE 3.13. *Simulation results, at both* $\mathcal{R} = 0.1$ *and* 50*, for the* $h/8$ *Dirichlet applied cylinder and the CR/DP FD cylinder cases. As the results are symmetric only half is shown and the results are directly compared. A) the velocity magnitude,* $|\mathbf{v}|$*, and B) the pressure. The scale, blue to red, ranges between* 0 *and* 1.1 *for the velocity results, between* 0 *and* 15 *for the* $\mathcal{R} = 0.1$ *pressures and between* 0 *and* 150 *for the* $\mathcal{R} = 50$ *pressures.*

where the region around the cylinder had a $CL = h/8$ decaying to $h/4$ for the remainder of the mesh. Problem degrees of freedom were $\approx 2.1 \times 10^5$, 1.1×10^6 and 3.2×10^5 in the Dirichlet, FD CR/DP and FD TH/CP cases respectively. The simulations were performed with a time step of $0.01s$. A visualisation of the results is shown in figure 3.14.

During the periodic steady state solution, vortices are shed off the cylinder and migrate downstream. As each vortex is shed, another develops near the downstream wall of the cylinder. The remaining vortex, being larger and more dominant, grows and eventually detaches from the cylinder, leaving a newly developed vortex in its place. In the numerical simulations, the period of this behaviour was $\approx 0.54s$ in the Dirichlet and CR/DP cases. This corresponded well with the observations of Nordberg[133] who experimentally measured a period of $0.55s$. The TH/CP results diverged slightly more from the experimental results with a period of $\approx 0.57s$.

Of more significance than the oscillatory period was the nature of vortex shedding in the various cases. In the Dirichlet and CR/DP results, vortices formed close to the cylinder and shed in a comparable manner. This can be seen in the similarity of the results in figure 3.14. However, in the TH/CP case, vortex formation and shedding was further downstream from the cylinder. As a result, the tail downstream from the cylinder was elongated and the results did not correlate well with the Dirichlet solution.

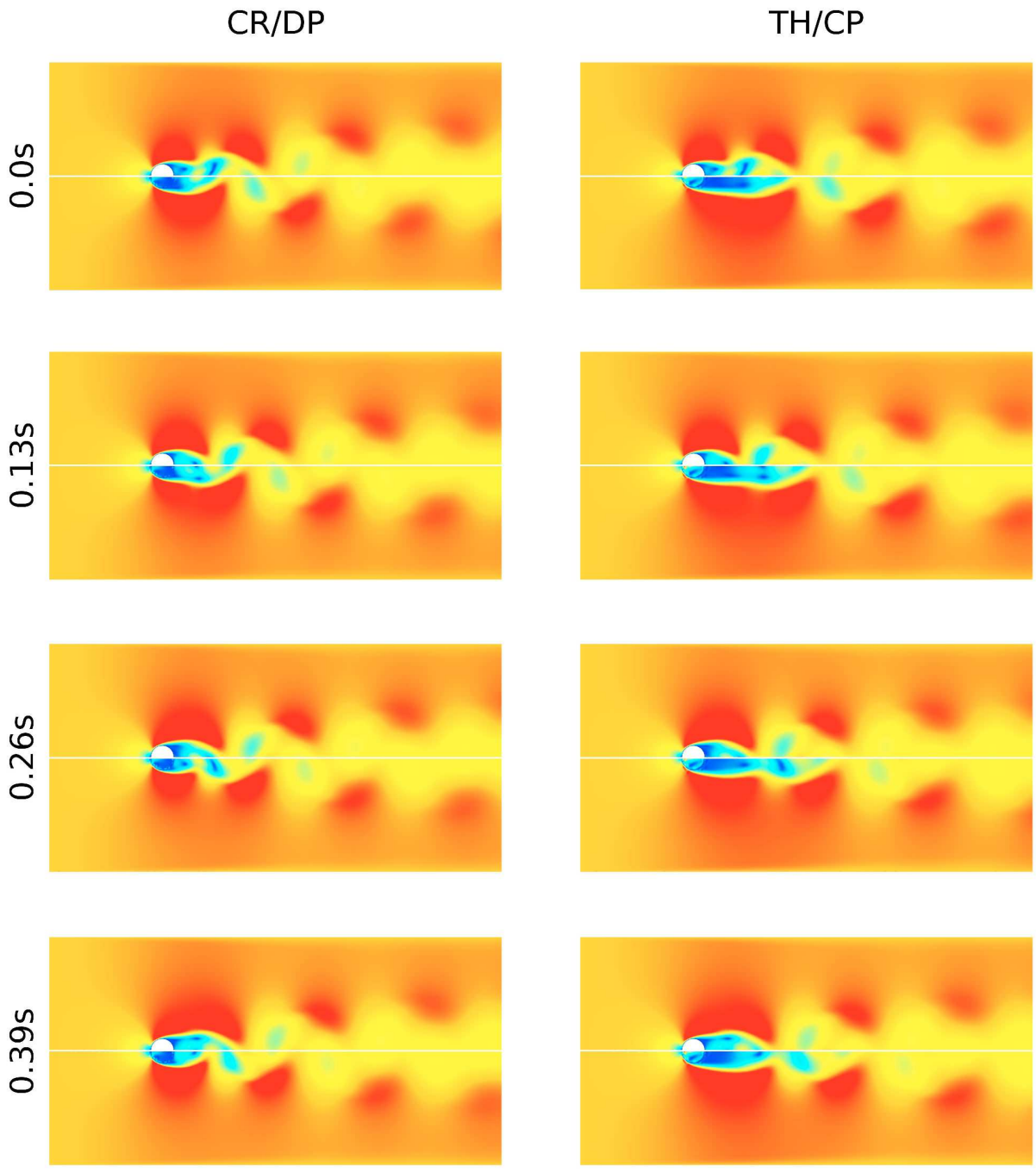

FIGURE 3.14. *Vortex shedding from the circular cylinder at* $\mathcal{R} = 200$. *Colour shows velocity magnitude,* 0 *to* $1.2ms^{-1}$, *blue to red, through one vortex shedding cycle. The top half of each sub–figure is the Dirichlet solution, the bottom half either the CR/DP results (left) or the TH/CP results (right). The period of the observed vortex shedding was* $0.54s$ *in the Dirichlet and CR/DP results and* $0.57s$ *in the TH/CP results.*

These results further demonstrate that at higher Reynold's numbers using continuous pressures with FD significantly reduces solution accuracy. In comparison, CR/DP elements performed well, capturing all major flow features observed in the Dirichlet solution.

3.1.3 Convergence of Fictitious Domain within the Fluid–Solid Coupling Scheme

The results presented in sections 3.1.1 and 3.1.2 provide an indication of the capability of FD to resolve boundaries, as well as the relative performance of FD compared with Dirichlet prescribed boundary conditions. However, none of the problems presented involved the full global system – *i.e.* fluid–solid coupling with FD. Additionally, the test problems presented so far have been thin 3D slices, therefore an understanding of the 3D system performance is also required. This section presents a convergence study of the full system (section 3.1.3.1) and a demonstration problem to highlight the fidelity of the method in 3D (section 3.1.3.2).

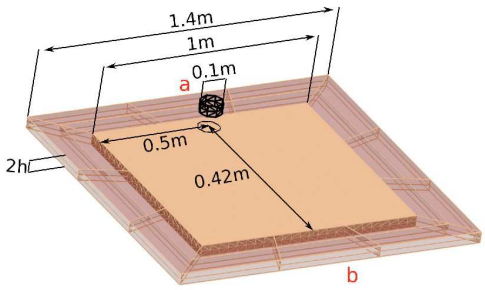

Figure 3.15. ***Fluid immersed cylinder encased in a hyperelastic box.*** *The problem of a fluid immersed cylinder encased in a hyperelastic box was defined such that: Ω_f, brown, was encased by Ω_s, transparent, with the coupling interface defined as $\Gamma_c = \Gamma_s \cap \Gamma_f$. The cylinder, diameter $0.1m$, was prescribed as a FD. The boundary conditions applied were, $\Gamma_s^D = 0$ on the bottom edge (b), symmetry boundary conditions on the top and bottom faces of the box and $\Gamma_s^N = 0$ on all other solid boundaries. The FD was moved in the direction of the top edge (a) as defined in section 3.1.3.1. Here h refers to the CL of the fluid meshes.*

3.1.3.1 Fluid Immersed Cylinder Encased in a Hyper–Elastic Box

To test the convergence of the fluid–solid coupled system with an immersed FD, the simulation of a fluid immersed cylinder encased in a hyperelastic box was developed. This problem, constructed to test the full range of possible interactions, including contact and release, was used for a convergence study. The capacity to simulate such interactions is critical to capturing the full range of cardiac motion under LVAD support, therefore it was important to understand how the numerical scheme behaves in such circumstances. The problem geometry and boundary conditions are given in figure 3.15. The cylinder, prescribed as a FD, was displaced, in the direction of the top edge of the box, with respect to figure 3.16, with a sinusoidal velocity profile for $\mathbf{v}_{Fd}$ consisting of an initial velocity of 0, a period of $0.4s$ and a magnitude of $1ms^{-1}$. This gave maximum and minimum velocities of 1 and $-1ms^{-1}$ respectively. Fluid viscosity and density were $1cP$ and

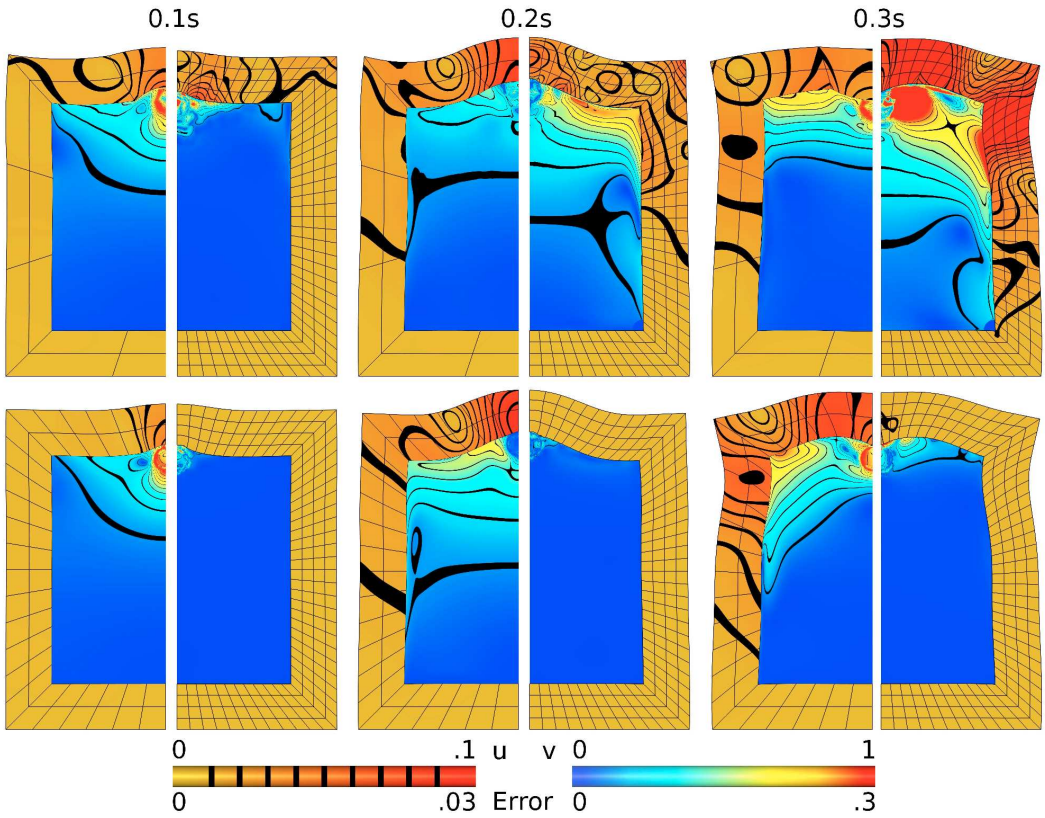

FIGURE 3.16. *The simulation velocity results and error for the problem of a fluid immersed cylinder encased in a hyperelastic box after 0.1s, 0.2s and 0.3s. The top row gives the results for the least refined, $CL = h$, simulation, while the bottom row shows the most refined, $CL = h/4$ and time step size of $\mathcal{O}(h^3)$, results. The problem solution is symmetric, therefore the results have been separated into halves, whereby the left half shows magnitudes of fluid velocity and solid displacement while the right half gives the error, $|\mathbf{v} - \mathbf{v}_{ref}|$, interpolated onto the reference mesh at that time instance. Note that there are different scales for velocity/displacement ($\mathbf{u}/\mathbf{v}$) and error magnitudes.*

$1Kg \cdot m^{-3}$ respectively, while the solid was described using the neo–Hookean material law, where $\mu = 5$.

The problem was run for 0.3s for a variety of different mesh refinements, with CLs of h, $h/2$ and $h/4$, and time step refinements, $\mathcal{O}(h)$, $\mathcal{O}(h^2)$ and $\mathcal{O}(h^3)$, where the time step for $CL = h$ was 0.02s. The results were compared with a reference solution which was calculated using a highly refined mesh with $CL = h/8$ and time step refinement of $\mathcal{O}(h^2)$. For the fluid problem $h = 0.04m$, while for the solid problem $h = 0.33m$ in the circumferential direction around the box. The fluid meshes were TET$(1, 2, 1)$[1] while the solid meshes were HEX$(2, 2, 1)$. The FD meshes, TRI$(1, 0)$, were refined such that their CL was equivalent to the relevant fluid mesh. Problem degrees of freedom ranged from $\approx 2 \times 10^3$ solid and $\approx 3.5 \times 10^4$ fluid for $CL = h$ to $\approx 8 \times 10^3$ solid and $\approx 6 \times 10^5$ fluid for $CL = h/4$. Due to its size and making use of the problems symmetry, the reference solution was solved on a half mesh and consisted of $\approx 1.3 \times 10^4$ solid and $\approx 1 \times 10^6$ fluid degrees of freedom.

[1]Note TET(1,2,1) elements were chosen for this problem for both computational reasons – DOF number for CR/DP meshes increases at a higher rate with refinement than for TH/CP meshes – and in order to maintain consistency between the interpolation orders of the fluid and solid problems – so that the rate of increase in DOFs was comparable between Λ_s^h and Λ_f^h with refinement.

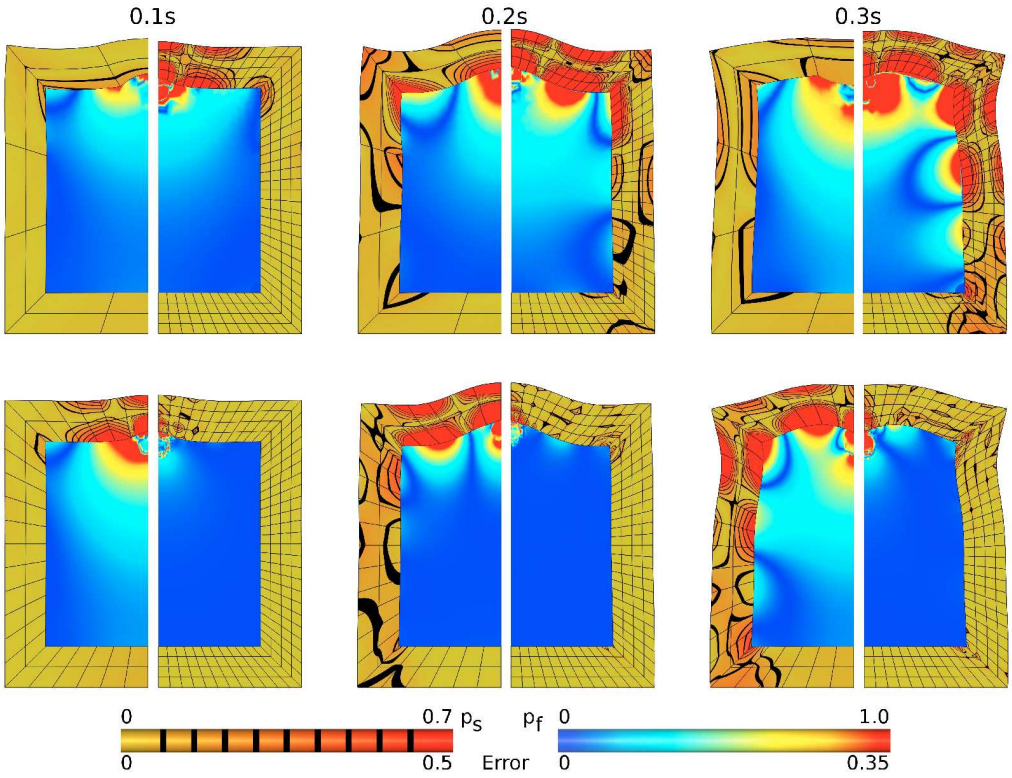

FIGURE 3.17. *The simulation pressure results and error for the problem of a fluid immersed cylinder encased in a hyperelastic box after 0.1s, 0.2s and 0.3s. The top row gives the results for the least refined, $CL = h$, simulation, while the bottom row shows the most refined, $CL = h/4$ and time step size of $\mathcal{O}(h^3)$, results. The problem solution is symmetric, therefore the results have been separated into halves, whereby the left half shows magnitudes of fluid velocity and solid displacement while the right half gives the error, $|p - p_{ref}|$, interpolated onto the reference mesh at that time instance.*

The simulation results, error and convergence are presented in figures 3.16, 3.17 and 3.18, and tables 6 and 7.

Fluid Convergence				Solid Convergence			
Norm \ $\triangle t$	$\mathcal{O}(h)$	$\mathcal{O}(h^2)$	$\mathcal{O}(h^3)$	Norm \ $\triangle t$	$\mathcal{O}(h)$	$\mathcal{O}(h^2)$	$\mathcal{O}(h^3)$
$\mathrm{L}^2(\mathcal{I}, \mathrm{L}^2(\Omega_f)_{(\mathbf{v}-\mathbf{v}_{ref})})$	1.30	2.01	2.03	$\mathrm{L}^2(\mathcal{I}, \mathrm{L}^2(\Omega_s)_{(\mathbf{u}-\mathbf{u}_{ref})})$	1.27	2.18	2.39
$\mathrm{L}^2(\mathcal{I}, \mathrm{H}^1(\Omega_f)_{(\mathbf{v}-\mathbf{v}_{ref})})$	1.12	1.44	1.46	$\mathrm{L}^2(\mathcal{I}, \mathrm{H}^1(\Omega_s)_{(\mathbf{u}-\mathbf{u}_{ref})})$	1.21	2.09	2.20
$\mathrm{L}^2(\mathcal{I}, \mathrm{L}^2(\Omega_f)_{(p-p_{ref})})$	0.91	1.23	1.24	$\mathrm{L}^2(\mathcal{I}, \mathrm{L}^2(\Omega_s)_{(p-p_{ref})})$	1.23	1.41	1.43

TABLE 6

Convergence rates of the velocity/displacement L^2–norm and H^1–semi-norm, as well as the pressure L^2–norm in the fluid immersed cylinder encased in a hyperelastic box problem over the time interval $\mathcal{I} \in [0, 0.3]$. Rates were calculated as the mean slopes of figure 3.18. A convergence rate of 1 is equivalent to $\mathcal{O}(h)$, while 2 is equivalent to $\mathcal{O}(h^2)$.

Both the fluid and solid problem components show good spatial and temporal convergence with mesh and time step refinement. As visualised in figures 3.16 and 3.17, both velocity and pressure error were noticeably reduced with refinement. As expected, the lower mesh refinements did not capture the same complexity in solution behaviour. Considering the results from section 3.1.2, improved convergence would be expected for CR/DP elements, however, the high degree of both temporal and spatial refinement required for the reference solution

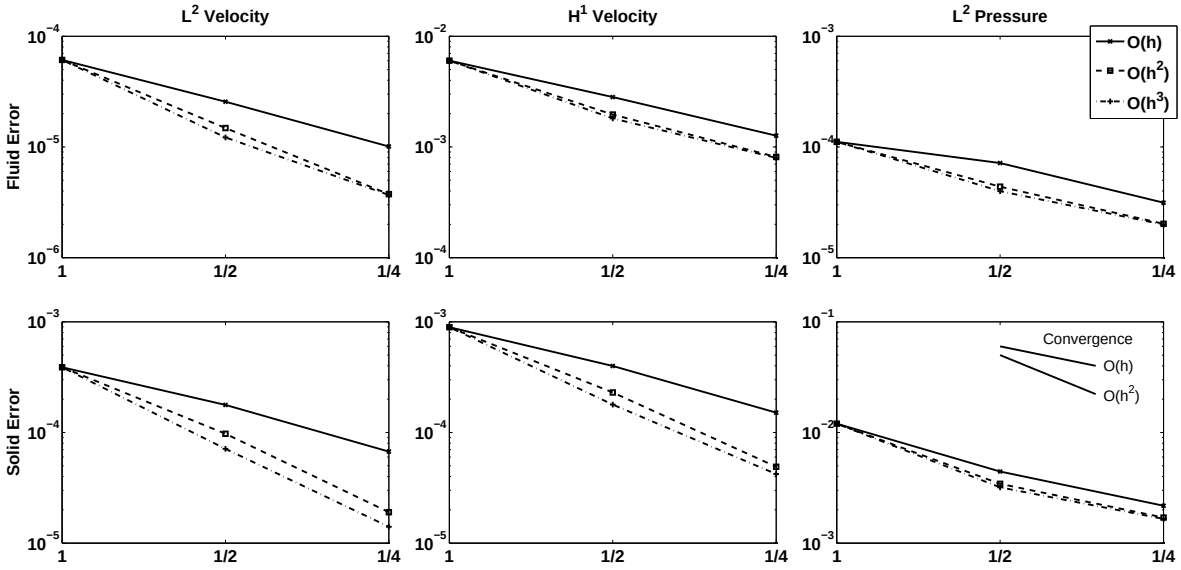

FIGURE 3.18. *Convergence of the problem of a fluid immersed cylinder encased in an elastic box. Fluid error is displayed on the top row while the solid error is on the bottom. $L^2(\mathcal{I}, L^2(\Omega_i))$ norms of the velocity/displacement and pressure error were calculated along with the $L^2(\mathcal{I}, H^1(\Omega_i))$ semi–norm of the velocity/displacement error, $\mathcal{I} \in [0, 0.3]$ is the time interval. The three lines show the convergence of the problem with time step refinement of $\mathcal{O}(h)$, $\mathcal{O}(h^2)$ and $\mathcal{O}(h^3)$. Refinement as a multiple of h is given on the x axis. Convergence, shown on the figure bottom right, gives the slopes for $\mathcal{O}(h)$ and $\mathcal{O}(h^2)$ convergence.*

Convergence of $\max\left(\mathrm{L}^2(\mathcal{I}, \mathrm{L}^2(\Omega_f)_{(\mathbf{v}-\mathbf{v}_{ref})}), \mathrm{L}^2(\mathcal{I}, \mathrm{L}^2(\Omega_s)_{(\mathbf{u}-\mathbf{u}_{ref})})\right)$

$\triangle t \setminus h$	1	1/2	1/4
$\mathcal{O}(h)$	3.89×10^{-4}	1.77×10^{-4}	6.72×10^{-4}
$\mathcal{O}(h^2)$	3.89×10^{-4}	9.74×10^{-5}	1.90×10^{-5}
$\mathcal{O}(h^3)$	3.89×10^{-4}	7.11×10^{-5}	1.40×10^{-5}

Convergence of $\max\left(\mathrm{L}^2(\mathcal{I}, \mathrm{H}^1(\Omega_f)_{(\mathbf{v}-\mathbf{v}_{ref})}), \mathrm{L}^2(\mathcal{I}, \mathrm{H}^1(\Omega_s)_{(\mathbf{u}-\mathbf{u}_{ref})})\right)$

$\triangle t \setminus h$	1	1/2	1/4
$\mathcal{O}(h)$	6.02×10^{-3}	2.82×10^{-3}	1.27×10^{-3}
$\mathcal{O}(h^2)$	6.02×10^{-3}	1.96×10^{-3}	8.12×10^{-4}
$\mathcal{O}(h^3)$	6.02×10^{-3}	1.81×10^{-3}	7.96×10^{-4}

TABLE 7

Maximum L^2–norm and H^1–semi-norm in the fluid and solid domains in the fluid immersed cylinder problem over the time interval $\mathcal{I} \in [0, 0.3]$. Columns indicate the norm values on various grid refinements, while rows scale temporally as powers of h.

makes this impractical with current computational resources. What these results do is provide confidence that the numerical scheme developed is convergent and therefore simulation error is limited by mesh size as theory would predict[52].

3.1.3.2 Fluid Immersed Sphere Encased in a Hyper–Elastic Box

The problem outlined above can be extended to a sphere immersed in a fluid cube. This increases the computational requirements of the problem, making it impractical to use it for convergence analysis. However, it provides a demonstration of the capability of the model to simulate the complex 3–dimensional interactions of immersed bodies with both the surrounding fluid and elastic bodies. The simulation is outlined in figure 3.19 which visualises the results at critical points that highlight the models ability to simulate both contact and release.

3.2 Lumped Parameter Boundary Problems

As outlined in section 2.5.5, two different fixed point schemes were developed to couple lumped parameter models to the 3D finite element problems used in this thesis. This section presents numerical results relating to the implementation of these schemes. Two test problems were created to test each of the two methods. The first, a cube test problem (section 3.2.1), was developed to verify the implementation of the volume constraint solid Lagrange multiplier method. The second, a bent pipe flow problem (section 3.2.2), was created to demonstrate the issues relating to direct Neumann/lumped parameter coupling and show how prescribing the velocity profile as a boundary condition resolves some of the associated issues. The problem descriptions are given in figure 3.20.

3.2.1 Verification of the Solid Cavity Volume Constraint Lagrange Multiplier

The volume constraint Lagrange multiplier problem was simulated on a cube consisting of 48 HEX(3,3,2) elements and $\approx 5.5 \times 10^3$ degrees of freedom. It was run for 20 time steps of $0.01s$. The solution was verified by comparing the results with a cube inflated using the Lagrange multiplier solution for $\lambda_{0D} \in \Omega_s$ as a normal stress applied to the interior cavity wall. The volume change, pressure/λ_{0D} solution and error are given in figure 3.22. The results show that the Lagrange multiplier constraint calculates the volume change and the solution for λ_{0D} is equivalent to the normal stress on the interior cavity wall.

3.2.2 0D–3D Coupling for Flow through a Bent Pipe

The flow through a bent pipe problem was developed to test the 0D/3D prescribed profile boundary condition and demonstrate the issues with coupling 0D lumped parameter models to 3D fluid problems directly as a Neumann stress on the boundary. The problem was run for 3 cases, firstly, where both Γ_A and Γ_B were coupled to the 0D model directly as Neumann stresses; secondly, where the the 0D model was coupled as a prescribed profile on Γ_A and as a Neumann stress on Γ_B; and thirdly, where the prescribed profile condition was applied to both Γ_A and Γ_B. To test the stability of the coupling schemes, meshes of 3 different refinements,

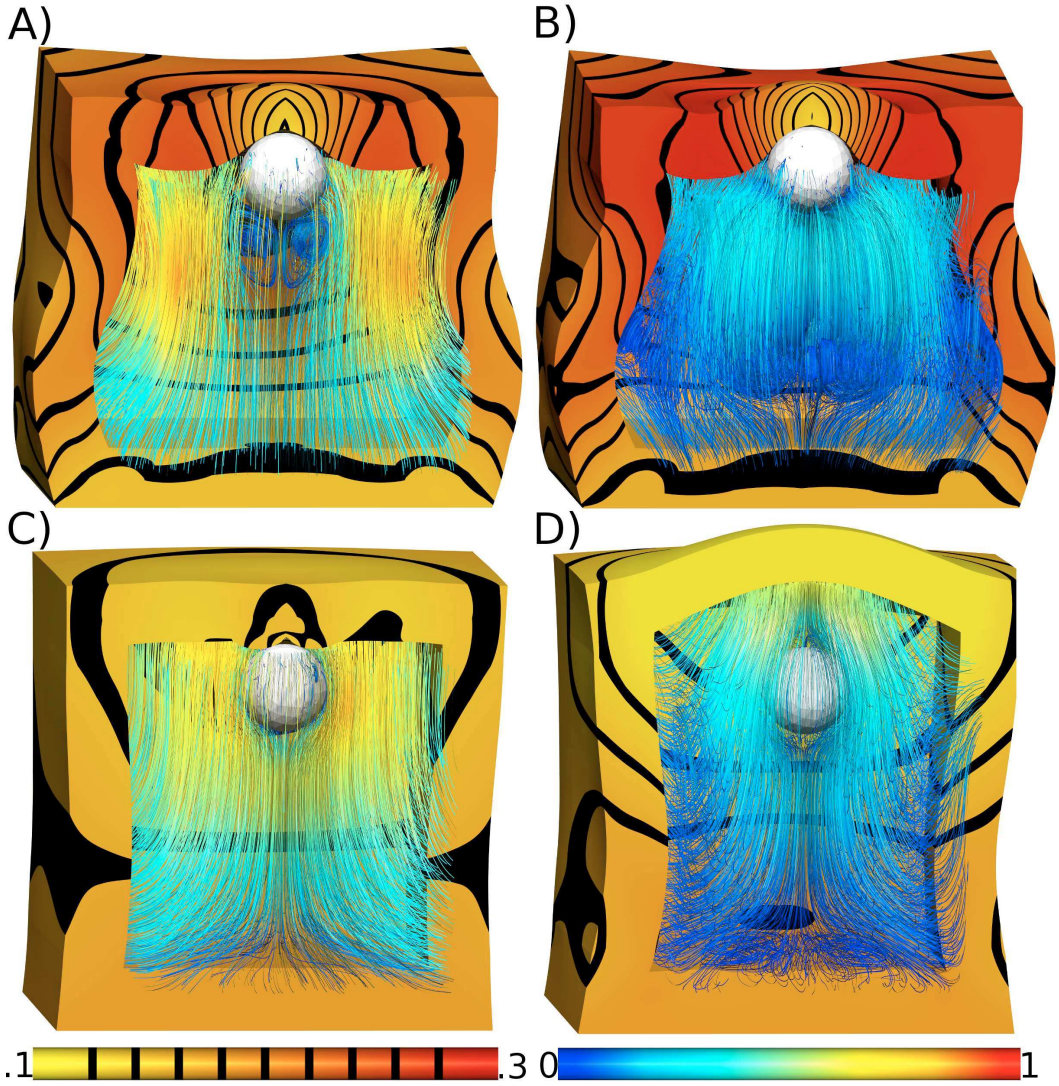

FIGURE 3.19. *Contact and release of a sphere immersed in fluid with a surrounding hyperelastic box. A),* $0.33s$*, shows the box coming into contact with the sphere, B),* $0.5s$*, the point of maximum contact, C),* $0.74s$*, the point of release of the box from the sphere and D),* $1.2s$*, rebound of the box from the sphere. The colour bars show solid displacement (left) and fluid velocity (right) magnitudes. The sphere, diameter* $0.25m$ *with* 360 *constant FD elements, was immersed in a* $1m \times 1m \times 1m$ *fluid box made from* $\approx 5 \times 10^4$ *TET*$(1, 2, 1)$ *elements. The fluid was in turn encased by an elastic, neo–Hookean (*$\mu = 10$*), solid, thickness* $0.2m$ *made from* 432 *HEX*$(3, 2, 1)$ *elements. Initial fluid and solid velocity was* $-1ms^{-1}$ *in the* z *direction with a Reynold's number of* 25*. The bottom face of the solid was rapidly decelerated. The problem was solved for* $2.5s$ *over* 250 *time steps. The fluid and solid problems consisted of* $\approx 2.2 \times 10^5$ *and* 1.4×10^4 *degrees of freedom respectively.*

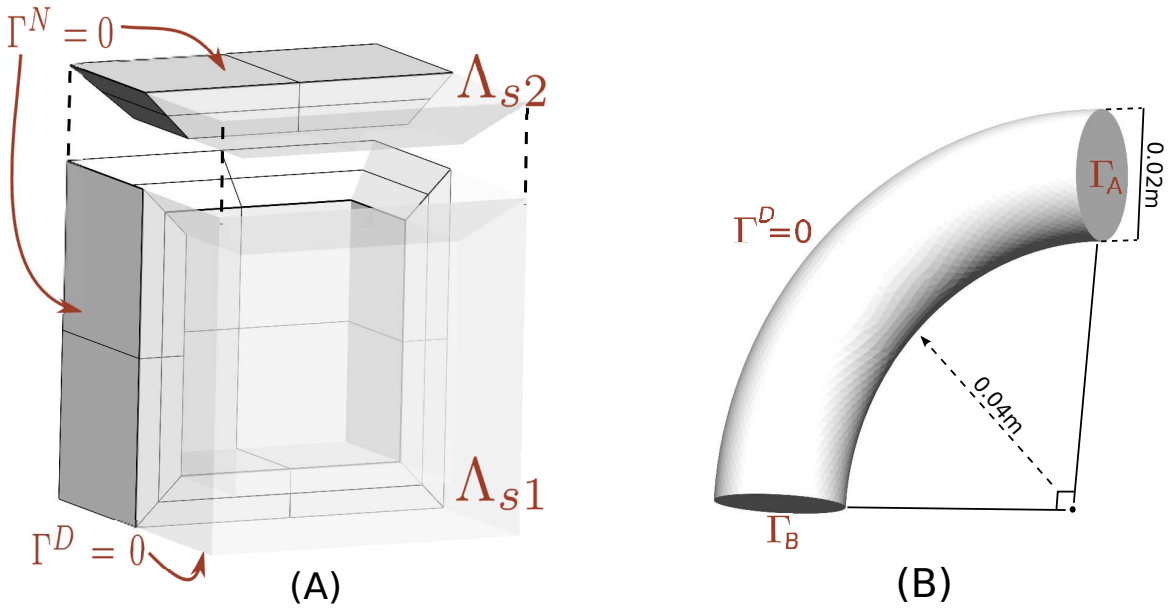

FIGURE 3.20. *Problems developed to test the implementation of the 0D/3D coupling schemes outlined in this thesis. Left, the volume constraint solid Lagrange multiplier problem, right, the bent pipe flow problem.*

A) ***Volume constraint solid Lagrange multiplier problem.*** *The problem consisted of a* $1 \times 1 \times 1$ *cavity encased in a hyperelastic solid,* 0.2 *thick. The exterior bottom face,with respect to the figure, was fixed and all other external faces left free,* $\Gamma^N = 0$*. The solid was broken into two domains,* Λ_{s1} *and* Λ_{s2}*, coupled together (to test the method for multi–solid domain problems), each with the same solid viscosity,* $\mu = 10$*. The volume change Lagrange multiplier was applied to the internal cavity wall and was coupled as the LV in the Windkessel lumped parameter model used for the cardiac problems, see chapter 5. The volume change is presented in figure 3.22. The problem was verified by applying the solution for* λ_{0D} *as a normal pressure to the internal cavity and comparing the resulting solid solutions.*

B) ***Bent pipe flow problem.*** *The problem consisted of a circular pipe, radius* $0.02m$*, bent through a* 90° *arc of radius* $0.04m$*. The no slip,* $\Gamma^D = 0$*, condition was applied to the exterior wall of the pipe, while the 0D/3D coupling methods, either prescribed profile (*Γ^P*) or Neumann (*Γ^N*)) were applied to either end of the pipe,* Γ_A *and* Γ_B*. Inward flow on* Γ_B *was taken to be positive. The pipe was coupled as the Aorta, with the Aortic valve fixed open, to the Windkessel lumped parameter model used for the cardiac problems.*

$CL = h, h/2, h/4$ ($h = 0.04$), were constructed. Element types were TET(1,2,1) and problem degrees of freedom ranged from 1.5×10^4 to 3.5×10^5. The problem cases were run on each mesh at 4 different time step refinements, $\delta t = 0.01, 0.005, 0.0025, 0.00125$ seconds. For the cases where at least one of the boundaries were coupled as prescribed profiles, the cavity pressure, inputted into the lumped parameter model, is calculated as an average of the integrated cavity pressure, equation 2.95.

For the first and second problem cases, the problem was unstable and failed regardless of mesh or time step refinement. Times to failure for the all Neumann stress and Neumann/profile cases are given in tables 8 and 9 respectively. The velocity magnitudes on Γ_A at selected time points, as well as the point of failure, for the least and most refined meshes, $\delta t = 0.00125s$, are shown in figure 3.23. Unusual behaviour with respect to mesh refinement was observed, as time to failure decreased in the $h/2$ cases and subsequently increased in the $h/4$

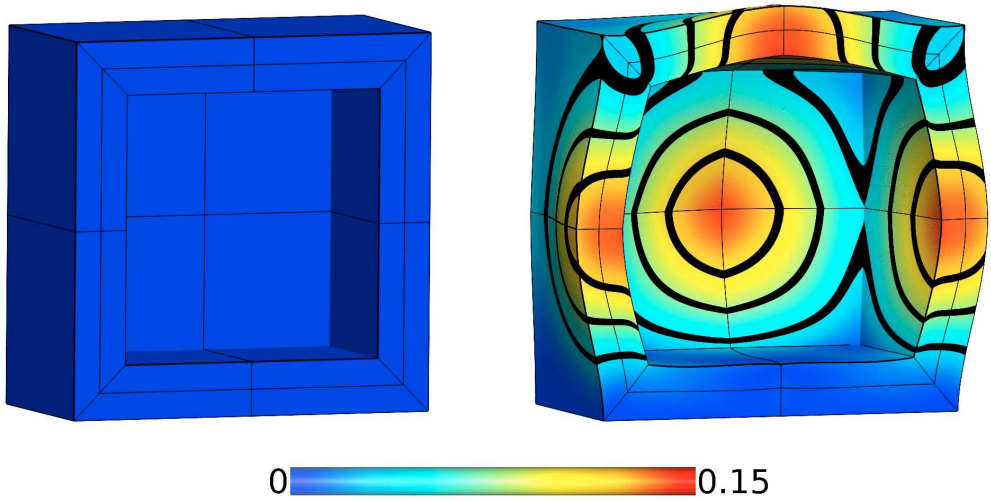

FIGURE 3.21. *Initial state, left, and solution after 20 time steps to the volume constraint Lagrange multiplier problem. Volume change of the cavity was* $0.1m^3$.

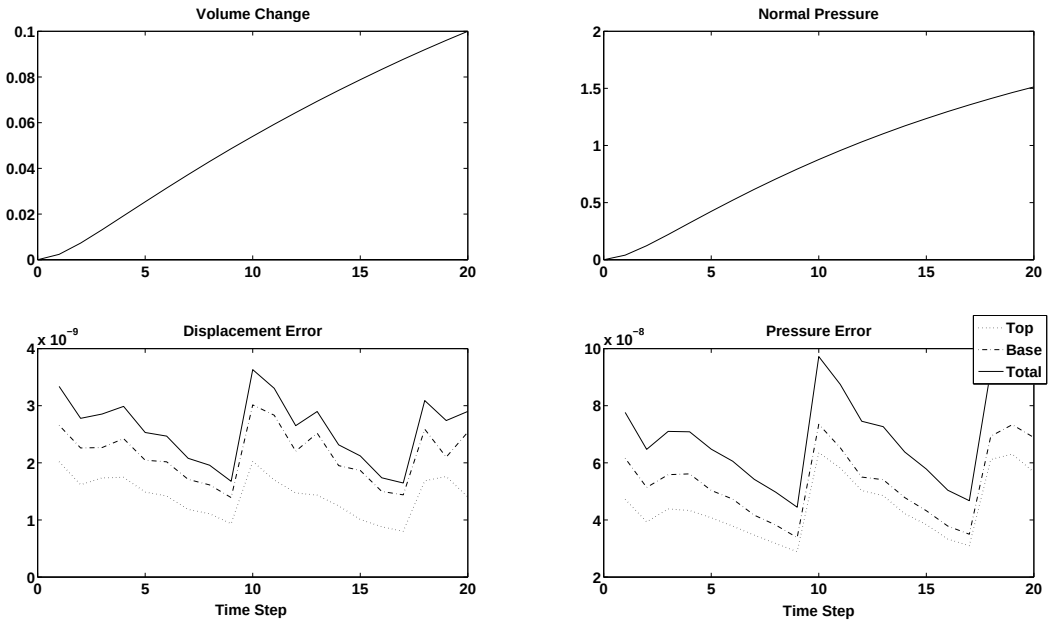

FIGURE 3.22. *Results and error for the volume change Lagrange multiplier problem. Top left and right, the volume change and associated normal pressure (*i.e. *solution for* λ_{0D}*). Bottom left and right, the* $|l_2|$*-norm of the displacement and pressure error compared with the equivalent problem inflated using the solution for* λ_{0D} *as a normal pressure on the interior cavity wall.*

cases. A potential reason for this is that higher velocity gradients can be approximated in more refined meshes. Therefore, the initial decrease in time to failure can be accounted for as velocity gradients increase with mesh refinement. In the $h/4$ cases, the increase in time to failure might be due to improved approximation of these high gradients.

	$\delta t = 0.01s$	$\delta t = 0.005s$	$\delta t = 0.0025s$	$\delta t = 0.00125s$
h	0.04	0.055	0.0675	0.06875
h/2	0.02	0.03	0.0375	0.0425
h/4	0.04	0.055	0.0475	0.05125

TABLE 8

Time to failure in seconds for the bent pipe flow problem with Neumann pressure 0D/3D coupling on both Γ_A and Γ_B. Results are shown for the various mesh (h) and time step (δt) refinements used.

	$\delta t = 0.01s$	$\delta t = 0.005s$	$\delta t = 0.0025s$	$\delta t = 0.00125s$
h	0.05	0.07	0.0825	0.08375
h/2	0.03	0.04	0.0475	0.0475
h/4	0.05	0.07	0.065	0.06875

TABLE 9

Time to failure in seconds for the bent pipe flow problem with Neumann pressure 0D/3D coupling on Γ_A and prescribed profile 0D/3D coupling on Γ_B. Results are shown for the various mesh (h) and time step (δt) refinements used.

In the final case, where the lumped parameter model was coupled as a prescribed profile on both boundaries, none of the problems failed. For this reason, the different mesh and time step refinements were used to test the stability of the Windkessel model when coupled to the fluid problem. Since the problem effectively has a Dirichlet condition applied to all boundaries, the pressure field was not unique. Therefore, one of the pressure degrees of freedom half way down the tube was fixed based on an average of the Windkessel model pressures at either end of the Aorta – *i.e.* the LV and arterial pressures, see chapter 5. The results from the prescribed profile pipe flow simulations are given in figure 3.24.

The bent pipe flow simulations highlight the issues with coupling 0D lumped parameter models to 3D fluid problems. Mesh and time step refinement may have reduced the magnitude of the error when directly coupling the 0D model as a Neumann stress boundary condition, however, it did not improve the stability of the system. The prescribed profile condition, in contrast, is stable, however, it requires *a priori* knowledge of the flow profile on the boundary – which is not always available. In spite of this, it is clearly a more appropriate method for 0D/3D coupling as firstly, a solution is possible, and secondly, the impact of inaccuracies in the flow profile on the solution should decrease with distance from the 0D/3D boundary. Additionally, the prescribed profile results show that the lumped parameter model is stable when coupled to the various refinements of the fluid problem.

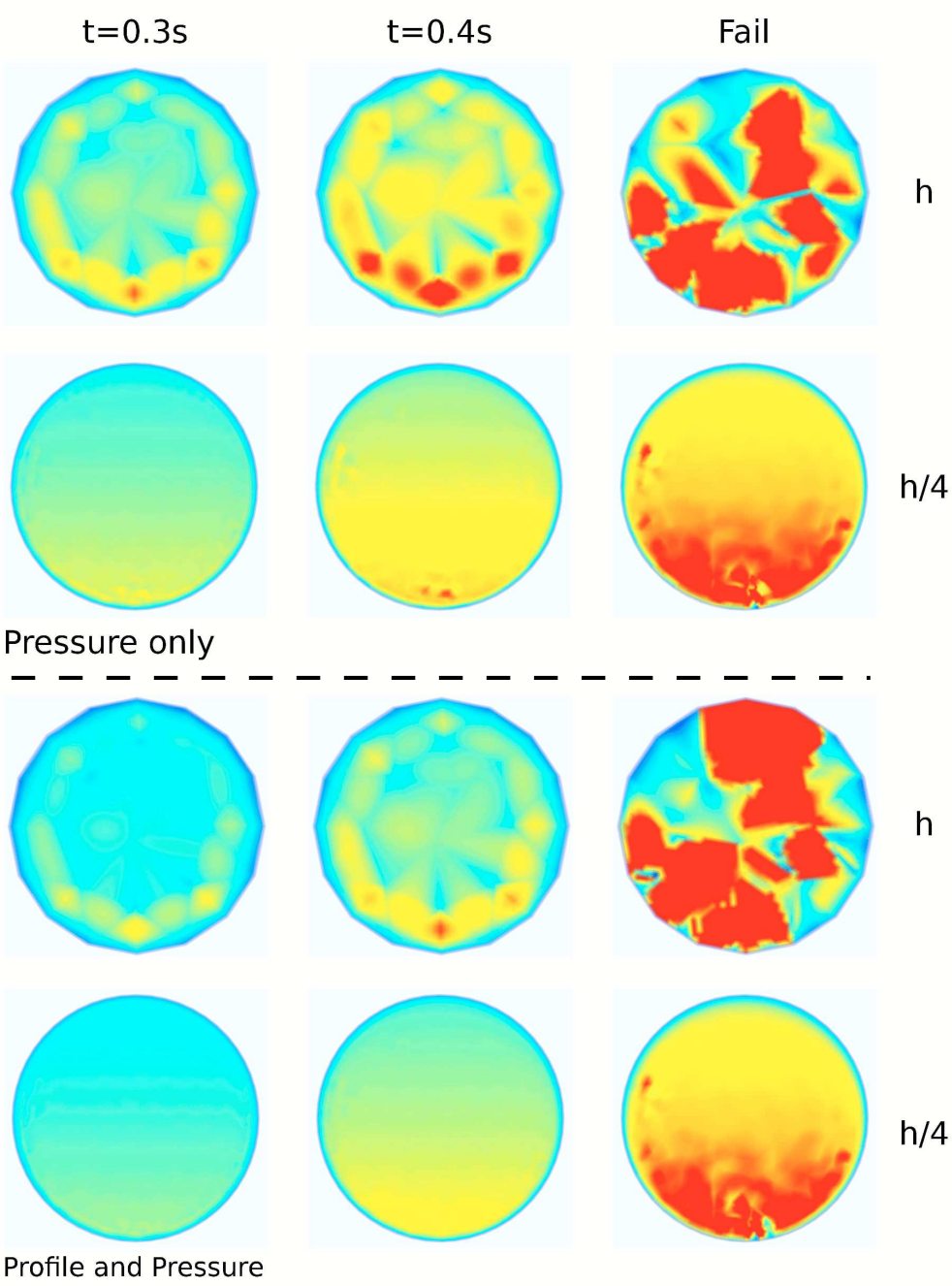

FIGURE 3.23. *Velocity magnitudes (0 to $0.2ms^{-1}$, blue to red) on Γ_A for $t = 0.3s$, $t = 0.4s$ and the point of failure for least and most refined meshes of the flow through a bent pipe problem. The top two rows show the results from when the lumped parameter model was coupled as a Neumann stress on both Γ_A and Γ_B. The bottom two rows show the results from when the lumped parameter model was coupled as a prescribed profile on Γ_B and as a Neumann stress on Γ_A.*

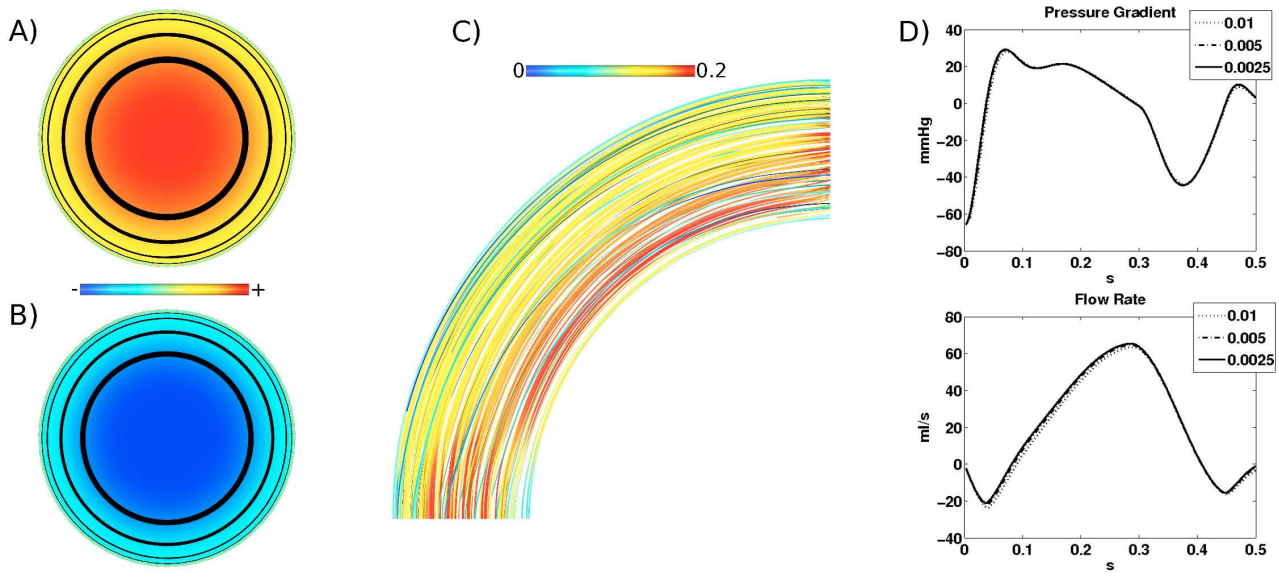

FIGURE 3.24. *The solution to the flow through a bent pipe when the lumped parameter model is coupled as a prescribed profile on both Γ_A and Γ_B. A) and B), the prescribed Poiseuille profile for inward and outward flow on Γ_A and Γ_B. C) streamlines showing flow through the pipe at $t = 0.25s$, colour shows velocity magnitude – note the higher velocity on the interior curve of the pipe. D) the pressure gradient across the pipe and the prescribed flow rate.*

3.3 Fluid Element Types for Coupling with High Tension Solids

The numerical scheme outlined in chapter 2 was developed to facilitate the coupling of non–conforming fluid and solid meshes. Considering two meshes, $\mathcal{T}_h(\Lambda_f)$ and $\mathcal{T}_h(\Lambda_s)$, coupled together using this method, the scheme enables different polynomial orders to be used to define elements within either mesh. As a result, for both numerical and convenience reasons, problems are often constructed where both elements and interpolation functions do not conform on Γ_c. In such circumstances, as long as the Lagrange multiplier space adheres to the requirements outlined in Nordsletten *et al.*[136] (*i.e.* the Lagrange multiplier space is nested in the most refined solution space of either coupled mesh), principle sources of error on Γ_c arise due to two reasons. Firstly, different interpolation spaces may provide different representations of the same field, for example a quadratic function cannot exactly describe a cubic field. This introduces error in the velocity constraint on the interface, as it may not be possible for fluid and solid velocities to exactly match. However, as shown in Nordsletten[134] and Nordsletten *et al.*[136] this effect is minor for adequately refined problems[2]. The second source of error stems from the projection of the tractions, equated on the coupling domain Ξ, onto Γ_f^C and Γ_s^C. If different spatial interpolations are used to approximate Λ_f and Λ_s, the surface normal directions will not precisely align across the interface. As a result, while the tractions will be equated on Ξ, their projections will result in forces being applied to the fluid and solid domains at subtly different angles, causing error.

[2]If the interpolation order is the same in both coupled domains, velocities will match across the interface to within problem tolerance[134].

The purpose of this section is to investigate the impact of various spatial interpolation functions on the error caused by this misalignment of tractions on the interface. As the error will increase with greater interface tractions, a problem – the contracting isovolumetric cylinder problem, section 3.3.1 – was developed featuring active tension in the solid to ensure high tractions across Γ_c. To investigate problem behaviour for different choices of spatial basis two numerical studies were performed to investigate problem convergence (section 3.3.2), as well as transient problem error (section 3.3.3). Finally, as the contractile phases in the cardiac cycle are characterised by high solid tensions – which result in high interface tractions – an example of this error in an LV problem is presented in section 3.3.4.

3.3.1 Contracting Isovolumetric Cylinder

The contracting cylinder problem was developed to investigate the effect of high interface tractions on problem behaviour. The problem description and boundary conditions are defined in figure 3.25. To enforce contractile behaviour on the solid, a simple transient tension profile was developed where tension, T, in the fibre direction was,

$$\begin{aligned} T &= T_{max}\,\beta\,tanh^2\left(\tfrac{t}{t_r}\right), \\ \beta &= tanh(a(\lambda - b)),\ \ \lambda = \sqrt{2\mathbf{E}_{F,\mathbf{ff}} + 1}\,, \end{aligned} \tag{3.1}$$

where T_{max} is the maximum tension, t_r is a constant defining the temporal rate of increase in T, and a and b are constants that define a length dependence function β introduced for problem stability. In order to define β, a measure of strain in the fibre direction, λ, was defined from the Green strain tensor rotated into the fibre direction, $\mathbf{E}_{F,\mathbf{ff}}$ (see section 4.2). The contraction parameters were chosen so that stability issues would arise in linear tetrahedral fluid meshes once solid tension had plateaued, parameter values are given in table 10.

T_{max}	t_r	a	b
45	0.1	10	0.7

Table 10

Active solid tension parameters for the contracting cylinder problem.

To test the impact of different element types on problem behaviour, different fluid meshes were constructed using linear and curvilinear descriptions of the spatial geometry. In the curvilinear cases the spatial interpolation space was chosen to be the same order as velocity solution space. *i.e.* for a given element type,

$$\text{ELEM}(i,\, j,\, k),$$

$i = j$ in the curvilinear and $i = 1$ in linear cases. For this section curvilinear and linear problems refer to the spatial interpolation of the fluid mesh. All solid meshes were constructed using curvilinear hexahedral elements, type HEX(3, 3, 2), while the fibres were defined using a cubic interpolation scheme.

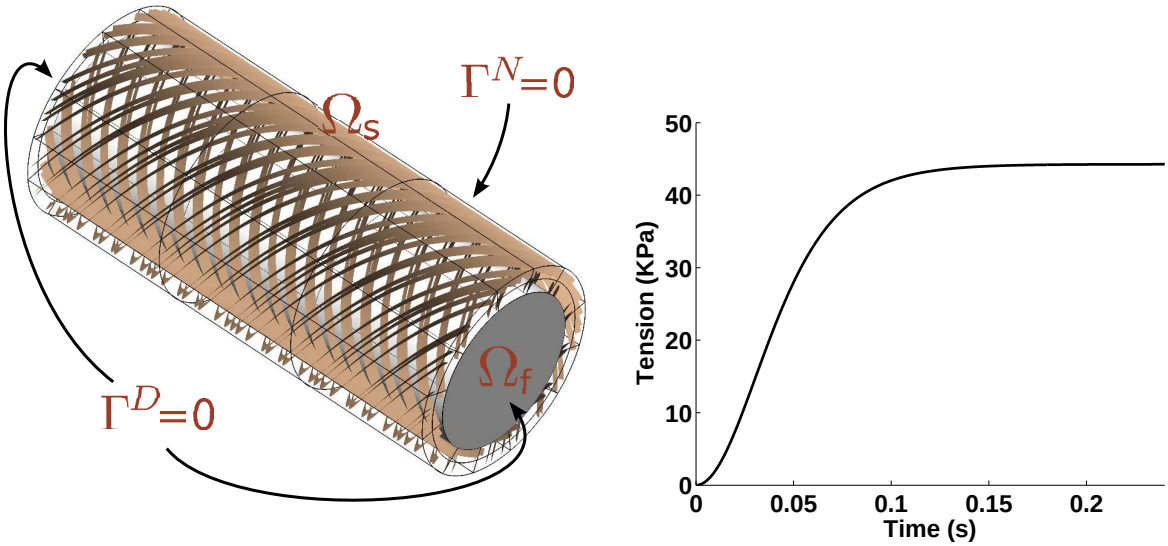

FIGURE 3.25. ***Contracting Isovolumetric Cylinder Problem.*** *The problem consisted of a fluid cylinder, radius* $0.01m$*, length* $0.06m$*, encased by a fibrous solid, thickness* $0.0033m$*, with fibres* $\pm 60^\circ$ *relative to the interior/exterior solid walls respectively. Solid and fluid displacements/velocities were fixed to zero at both ends of the cylinder, while the exterior solid wall was left free,* $\mathbf{v}(\cdot, 0)$ *and* $\mathbf{u}(\cdot, 0)$ *were zero. Simulation duration was* $0.24s$*. Fluid viscosity and density, chosen to be roughly comparable to blood values, were,* $\mu = 5cP$ *and* $\rho = 1000kg \cdot m^{-3}$*, while the solid was described using a transversely isotropic form of the Costa constitutive law, see section 4.2, with parameters* $b = [25, 4, 4, 10, 10, 4]$ *and* $C = 250Pa$*. Contraction, in the fibre direction, was defined according to equations 3.1, with the resulting tension shown right. As the contractile forces in the problem are symmetric, analytic velocity and displacement solutions are zero, while fluid and solid pressures are dependent on the contraction model and solid constitutive law.*

3.3.2 PROBLEM CONVERGENCE

A convergence study was performed to determine expected problem behaviour with mesh and time step refinement. Meshes at three refinement levels – $CL = h$, $h/2$ and $h/4$, where $h = 0.004m$ (fluid) and $h = 0.01m$ (solid) were generated. Element types were chosen so that the fluid and solid meshes were non–conforming with respect to both mesh structure and interpolation order. For this study, fluid meshes were constructed using quadratic linear (TET(1, 2, 1)) and curvilinear (TET(2, 2, 1)), while solid meshes were constructed from cubic hexahedral (HEX(3, 3, 2)) elements. Due to minimal through wall variation in the solid solution, transmural refinement was not performed and all solid meshes were two elements thick. Problem degrees of freedom for the fluid ranged from $\approx 1.7 \times 10^4$ to 4.2×10^5, and for the solid from $\approx 8.3 \times 10^3$ to 1.3×10^5.

Due to the high tensions generated in the solid, time step size was required to be small to ensure convergence of the Newton scheme. As a result, it was not feasible to run a convergence study for the full $0.24s$ simulation duration[3], therefore analysis could only be made of the lower tension temporal regions of the problem. The

[3]For the least refined problem to run for the full $0.24s$ duration time step was required to be $\approx 0.0002s$. In this case the most refined problem would have required approximately $20,000$ time steps.

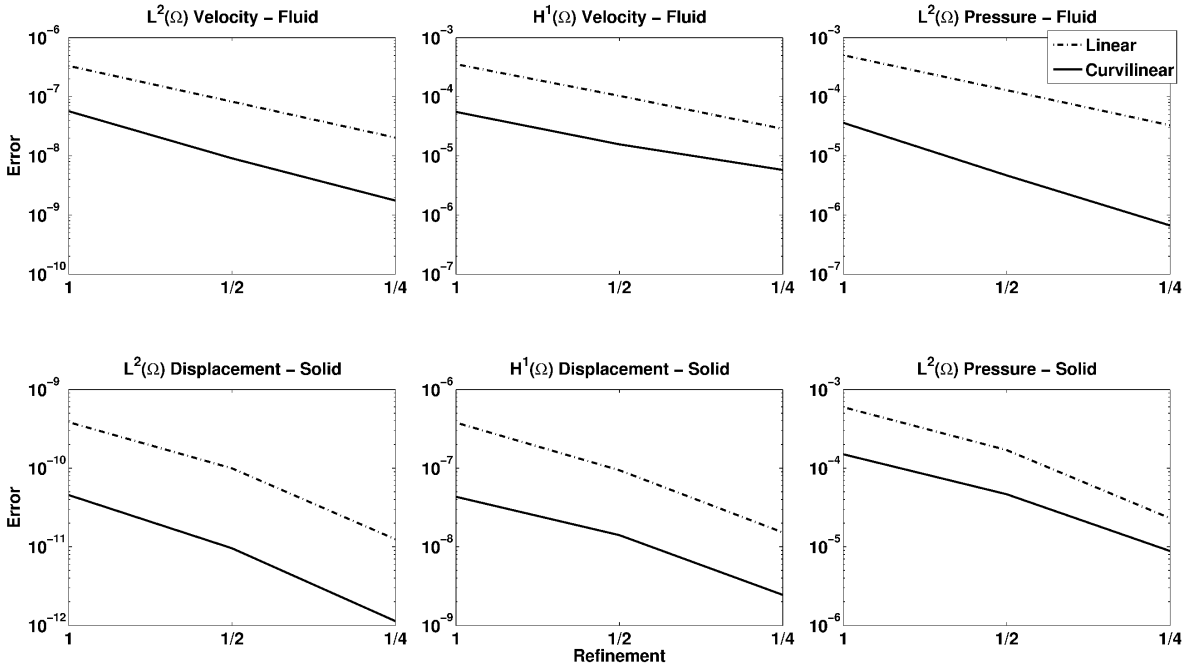

FIGURE 3.26. *Convergence results from the contracting cylinder problem. Fluid error is displayed on the top row, while solid error is on the bottom. Shown are the $L^2(\mathcal{I}, L^2(\Omega_i))$ norms of the velocity/displacement and pressure error, along with the $L^2(\mathcal{I}, H^1(\Omega_i))$ semi–norm of the velocity/displacement error, where $\mathcal{I} \in [0,\, 0.025s]$ is the time interval, $i = [f,\, s]$. Convergence rates, equivalent to the figure slopes, are provided in table 11*

Fluid Convergence			Solid Convergence		
Norm \ $\triangle t$	Linear	Curvilinear	Norm \ $\triangle t$	Linear	Curvilinear
$\mathrm{L}^2(\mathcal{I}, \mathrm{L}^2(\Omega_f)_{\mathbf{v}})$	2.02	2.51	$\mathrm{L}^2(\mathcal{I}, \mathrm{L}^2(\Omega_s)_{\mathbf{u}})$	2.47	2.66
$\mathrm{L}^2(\mathcal{I}, \mathrm{H}^1(\Omega_f)_{\mathbf{v}})$	1.82	1.68	$\mathrm{L}^2(\mathcal{I}, \mathrm{H}^1(\Omega_s)_{\mathbf{u}})$	2.32	2.08
$\mathrm{L}^2(\mathcal{I}, \mathrm{L}^2(\Omega_f)_{(p-p_{ref})})$	1.97	2.88	$\mathrm{L}^2(\mathcal{I}, \mathrm{L}^2(\Omega_s)_{(p-p_{ref})})$	2.35	2.04

TABLE 11

Convergence rates of the velocity/displacement L^2–norm and H^1–semi-norm, as well as the pressure L^2–norm in the contracting isovolumetric cylinder problem over the time interval $\mathcal{I} \in [0, 0.025]$. Rates were calculated as the mean slopes in figure 3.26. A convergence rate of 1 is equivalent to $\mathcal{O}(h)$, 2 is equivalent to $\mathcal{O}(h^2)$ and 3 is equivalent to $\mathcal{O}(h^3)$.

problem was run for $0.025s$ with a time step, for $CL = h$, of $0.0005s$. Time step refinement was $\mathcal{O}(h^2)$.

In this problem, the true velocity/displacement solutions are zero. Fluid and solid pressures, in contrast, depend on the solid contraction and constitutive parameters. To obtain a reference pressure solution, a solid only problem was run on an $h/8$ solid mesh, using the Lagrange multiplier volume constraint (see section 2.5.5.2) to impose isovolumetric conditions on the cylinder cavity. The Lagrange multiplier solution, λ_{0D}, provided the reference for the fluid pressure results. As a cylinder cannot be exactly described using cubic elements, some error was introduced into the problem as simulated solid displacements, in the solid case, were not exactly zero. This error reduces with solid refinement and was equivalent in both the linear and curvilinear cases.

Convergence of $\max\left(\mathrm{L}^2(\mathcal{I},\mathrm{L}^2(\Omega_f)_{\mathbf{v}})\,,\,\mathrm{L}^2(\mathcal{I},\mathrm{L}^2(\Omega_s)_{\mathbf{u}})\right)$

Elements \ h	1	1/2	1/4
Linear	3.33×10^{-7}	8.28×10^{-8}	2.03×10^{-8}
Curvilinear	5.70×10^{-8}	9.07×10^{-9}	1.76×10^{-9}

Convergence of $\max\left(\mathrm{L}^2(\mathcal{I},\mathrm{H}^1(\Omega_f)_{\mathbf{v}})\,,\,\mathrm{L}^2(\mathcal{I},\mathrm{H}^1(\Omega_s)_{\mathbf{u}})\right)$

Elements \ h	1	1/2	1/4
Linear	3.55×10^{-4}	1.04×10^{-4}	2.86×10^{-5}
Curvilinear	5.54×10^{-5}	1.57×10^{-5}	5.79×10^{-6}

TABLE 12

Maximum L^2–norm and H^1–semi-norm in the fluid and solid domains in the contracting isovolumetric cylinder problem over the time interval $\mathcal{I}\in[0,0.025]$. Columns indicate the norm values on various grid refinements.

Convergence rates and error are shown in figure 3.26 and tables 11 and 12, while a visualisation of the interface velocity/displacement error in the h and $h/2$ results at $t=0.025s$ is presented in figure 3.27. Observed error was consistently lower in the curvilinear results compared with the linear cases. With respect to convergence, L^2 fluid velocity and solid displacement convergence rates were higher in the curvilinear results than in the linear case, however, higher H^1 rates were observed. This can be explained by the dominance of the solid in this problem. The reduction in interface error stabilises the solid, reducing 'warping' (see figure 3.30), thereby substantially reducing gradient errors in the system. This also helps explain the higher rate of solid pressure convergence observed in the linear case. Note that the observed convergence rates were relatively high (*i.e.* greater then $\mathcal{O}(h^2)$ in most cases) as error reduction occured due to a combination of refinement and geometric convergence. These results indicate that the minimum degree of refinement for stable solid behaviour under high tensions is greater when using linear spatial fluid elements. Examining the spatial variation of error, in the linear case, velocity error appeared relatively evenly spread across the interface. However, in the curvilinear case, this error appeared localised to either end of the cylinder with refinement, possibly due to the effects of the Dirichlet boundary on the solid.

3.3.3 Transient Error

The convergence results from the previous section show the relative error caused by the choice of spatial interpolation for the fluid mesh in the fluid–solid coupled problem. However, it is important to understand how this error behaves through time in high interface traction problems. The simulation was run for $0.24s$ using the $CL=h$ fluid meshes from the convergence study with both linear and curvilinear quadratic and Crouzeix–Raviart tetrahedral element types. Additionally, two further cases were analysed, the linear quadratic $h/2$ mesh from the convergence study and a curvilinear cubic hexahedral mesh of refinement $h/3$ with respect to the solid mesh. All fluid meshes were coupled to the $CL=h$ solid mesh from the convergence study. Fluid degrees of freedom were $\approx 6.2\times10^4$ for the Crouzeix–Raviart and $\approx 5.0\times10^4$ for the cubic hexahedral cases. Due to the high rate of tension change, in order to resolve the contracting problem through the full simulation duration ($0.24s$) a time step of $0.0002s$ was used. To account for error caused by the solid cubic

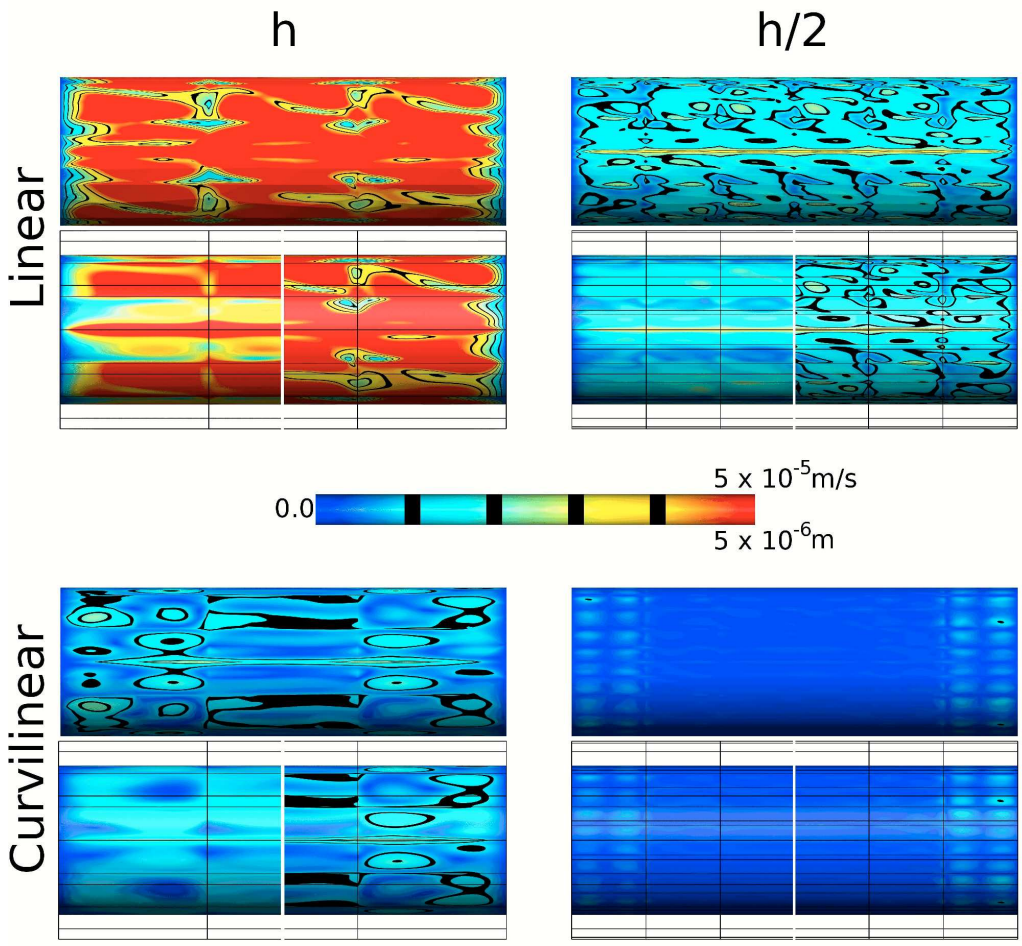

FIGURE 3.27. *Fluid and solid velocity magnitude error, $|\mathbf{v}|$, as well as solid displacement magnitude error, $|\mathbf{u}|$, at $t = 0.025s$ on the fluid/solid interface in the convergence study of the contracting cylinder problem. The h and $h/2$ results are visualised. In each case – linear and curvilinear spatial tetrahedral elements – the top row shows fluid and the bottom row solid error. The solid error is divided in halves, left, displacement error, right, velocity error. The scale, blue to red, gives the respective errors in m/s (velocity) and m (displacement).*

mesh approximation of the cylindrical geometry, and to provide a reference solution for the pressure results, the solution was compared with an equivalent solid only simulation performed using the $CL = h$ solid mesh.

Solution error for the quadratic tetrahedral element types is shown in figure 3.28, while the error for the other tested element types is shown in figure 3.29. In the problems analysed, instabilities were observed in the linear cases of the quadratic and Crouzeix–Raviart problems. As solid tension began to plateau, these solutions began to oscillate, with increasing fluid error and rapidly varying solid error. The period of these oscillations was $\approx 0.001s$. Refinement of the linear quadratic case prevented these oscillations from occurring, however, error was still greater than in the less refined curvilinear case in both the fluid and solid problems. For the other element types, curvilinear Crouzeix–Raviart tetrahedrals performed slightly better – as expected due to their higher order spatial approximation – than the curvilinear quadratic case. This performance difference was most

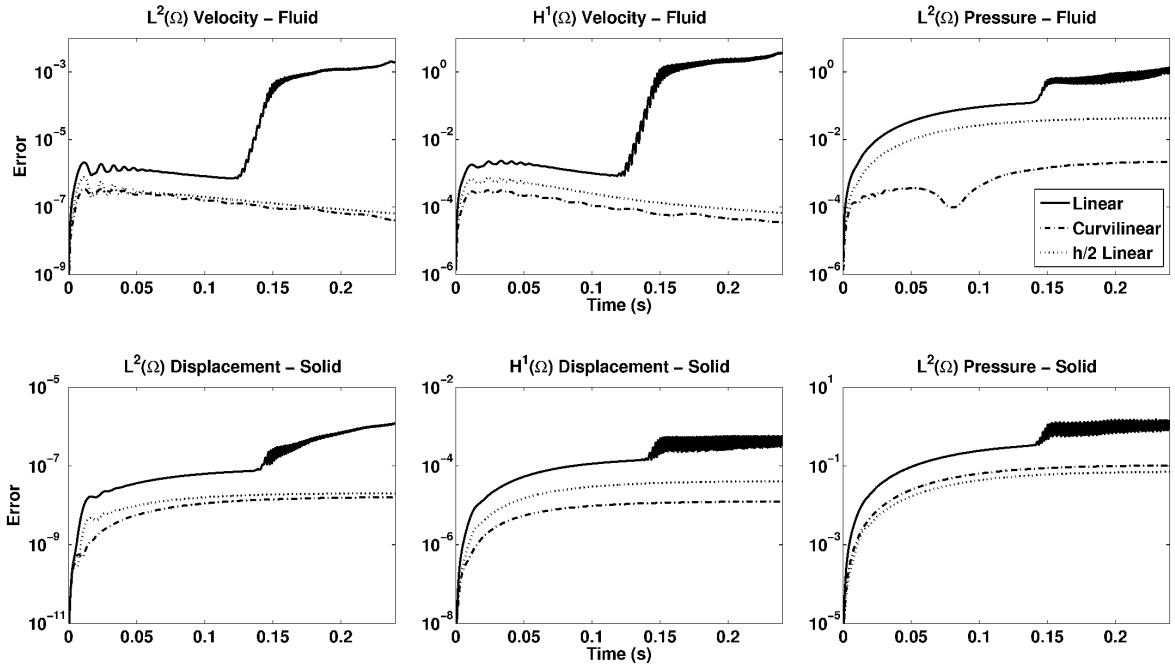

FIGURE 3.28. *Transient error in the contracting cylinder problem. The $L^2(\Omega_i)$ norms of the velocity/displacement and pressure error, along with the $H^1(\Omega_i)$ semi–norm of the velocity displacement error, is shown for the fluid (top row) and solid (bottom row) results. $i = [f, s]$. Displayed is the error from the linear, curvilinear and $h/2$ linear quadratic fluid tetrahedral problems,* i.e. *element types $TET(k, 2, 1)$, where $k = [1, 2]$.*

notable in the solid problem. Solution oscillation was observed in the linear Crouzeix–Raviart case, however, unlike with linear quadratics, the oscillations caused the simulation to fail. As expected, curvilinear cubic hexahedrals performed significantly better than all other element types as, in this case, the approximation of the interface in both the fluid and solid domains was exact.

In all the results in which oscillatory behaviour was not observed, solid error plateaued along with solid tension. Fluid velocity/displacement error, in contrast, reached an early peak before dissipating as viscous loss (this rate is low due to low fluid viscosity). This early peak was probably due to initial solid displacement caused by inaccuracies in the approximation of the cylindrical geometry. This is evidenced by the similar errors in the cubic hexahedral case and the curvilinear tetrahedral solutions prior to the early peak. Following the peak, ringing was observed in the cubic hexahedral case as error oscillated between the fluid and solid domains. This effect was masked in the other cases as additional error was introduced to the system due to inaccuracies in the interface approximation.

Considering the spatial distribution of the error, a visualisation of the interface velocity/displacement error from the quadratic tetrahedral cases is shown in figure 3.30. Accumulation of error was observed in the solid (visible as increased solid displacement error) in both the linear and curvilinear cases. This accumulation plateaued in the curvilinear case, visible between $0.1s$ and $0.15s$, however, in the linear case the onset of oscillatory behaviour is visible as interface distortion at $0.15s$.

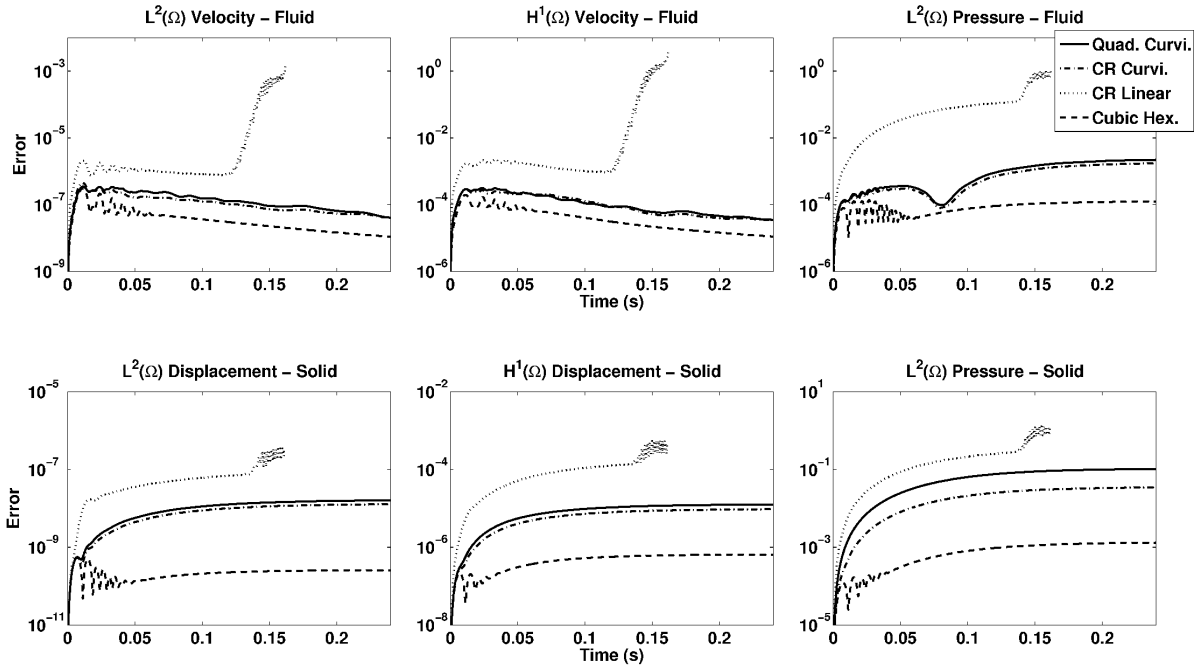

FIGURE 3.29. *Transient error in the contracting cylinder problem. The $L^2(\Omega_i)$ norms of the velocity/displacement and pressure error, along with the $H^1(\Omega_i)$ semi–norm of the velocity displacement error, is shown for the fluid (top row) and solid (bottom row) results. $i = [f, s]$. Displayed is the error from the linear and curvilinear Crouzeix–Raviart (CR) element types ($TET(k, 2cr, 1dc)$, $k = [1, 2cr]$) and curvilinear cubic hexahedral (Cubic Hex.) element type ($HEX(3, 3, 2)$). The curvilinear quadratic fluid element results (Quad. Curvi.) are shown as a reference with respect to figure 3.28. Note that the linear Crouzeix–Raviart simulation failed shortly after the solution began to oscillate.*

3.3.4 Error in an LVAD Supported LV Problem

The contracting cylinder results highlight the importance of the choice of spatial interpolation in problems with high interface tractions. At low tractions, error caused by differences in the interpolation of the coupled interface, does not significantly affect the simulation results. However, this error can accumulate causing either simulation failure or oscillations in both the fluid and solid solutions on the interface. To demonstrate this effect in a physical problem, a comparison between linear and curvilinear element types in an LVAD supported LV during isovolumetric contraction (IVC) is shown in figure 3.31. Simulation parameters are described in chapter 5. Comparing solid and fluid velocities on the interface, the solution at low tensions, early in IVC, was comparable and fairly smooth. As tension increases, error and element distortion, was observed at the interface in the linear tetrahedral case. This caused both increased error and simulation failure in this case.

3.4 Newton–Raphson/Line–Search Modifications

The Newton–Raphson/line search modifications were implemented to improve the numerical performance of the system. This section presents an analysis of the impact these modifications had on time step duration and the

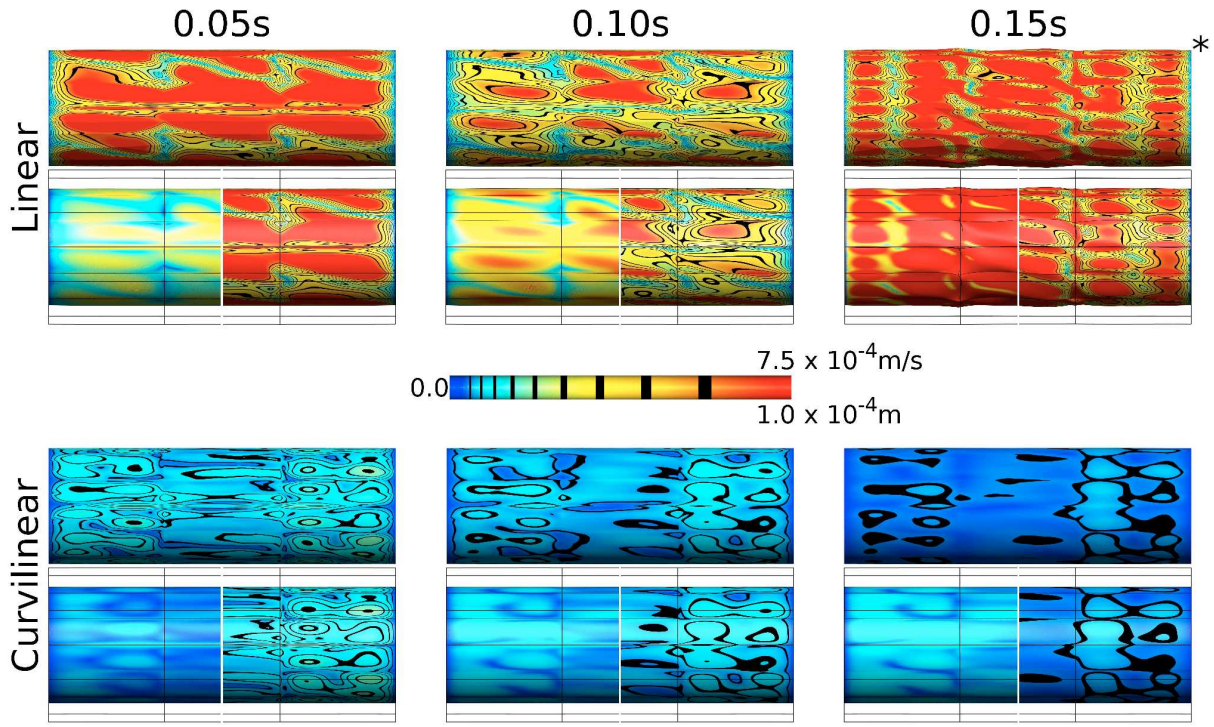

FIGURE 3.30. *Fluid and solid velocity magnitude* $|\mathbf{v}|$ *error, as well as solid displacement magnitude* $|\mathbf{u}|$ *error, at* $t = 0.05$, 0.10 *and* $0.15s$ *on the fluid/solid interface in the contracting cylinder problem. Results are visualised for the quadratic linear and curvilinear problems,* i.e. *element types* $TET(k, 2, 1)$*, where* $k = [1, 2]$*. In each case – linear and curvilinear spatial tetrahedral elements – the top row shows fluid and the bottom row solid error. The solid error is divided in halves, left, displacement error, right, velocity error. The scale, blue to red, gives the respective errors in* m/s *(velocity) and* m *(displacement). The asterisk on the* $0.15s$ *linear figure indicates that for this figure the velocity scale is different, here* 0 *to* $0.5m/s$*, blue to red.*

number of Newton iterations/sub–iterations required for convergence[4]. Four problems were analysed, the fluid immersed cylinder encased in a hyper–elastic box problem (section 3.1.3.1); the contracting cylinder problem (linear and curvilinear quadratic cases, section 3.3); an isovolumetric coupled cube problem (section 3.4.1); as well as the full cardiac cycle problem from chapter 5. The problems were selected to study different aspects of the coupled system performance – isovolumetric with low mesh velocity (contracting cylinder), isovolumetric with high mesh velocity (coupled cube problem) and FD immersed in a coupled fluid (fluid immersed cylinder and the cardiac cycle problem).

3.4.1 Isovolumetric Cube Problem

The isovolumetric cube problem was developed, and parameters chosen, so that it would exhibit high mesh velocities under isovolumetric conditions – *i.e.* similar to LV problems during IVC and IVR. Such problems

[4]Note that the results give the number of Newton iterations + the number of sub-iterations. The mean number of sub-iterations per time step is equivalent to the mean Newton iterations less the mean number of Jacobian matrix inverses.

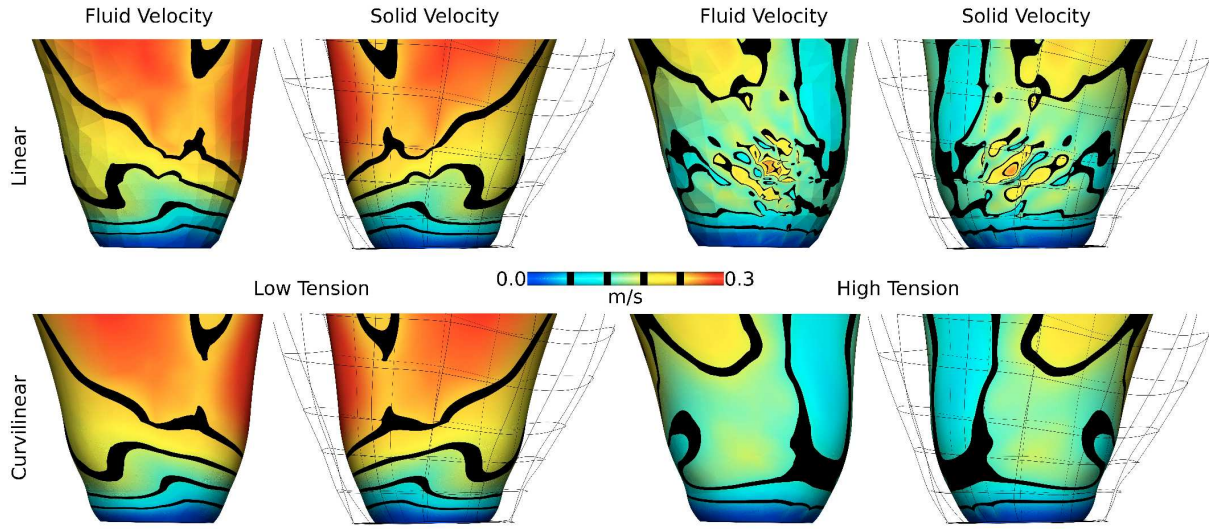

FIGURE 3.31. *A comparison of the relative performance of linear and curvilinear spatial tetrahedrons (TET(i, 2cr, 1dc), $i = [1, 2cr]$) during isovolumetric contraction (IVC) in the LVAD supported LV problem. With the exception of the choice in spatial interpolation, simulation meshes and degrees of freedom were the same. Fluid and solid interface velocities are shown at the apical region of the LV for low tension (early IVC) and high tension (late IVC) moments during contraction. Note that distortions in the solid due to error in the linear spatial tetrahedron case caused the simulation to fail in late IVC.*

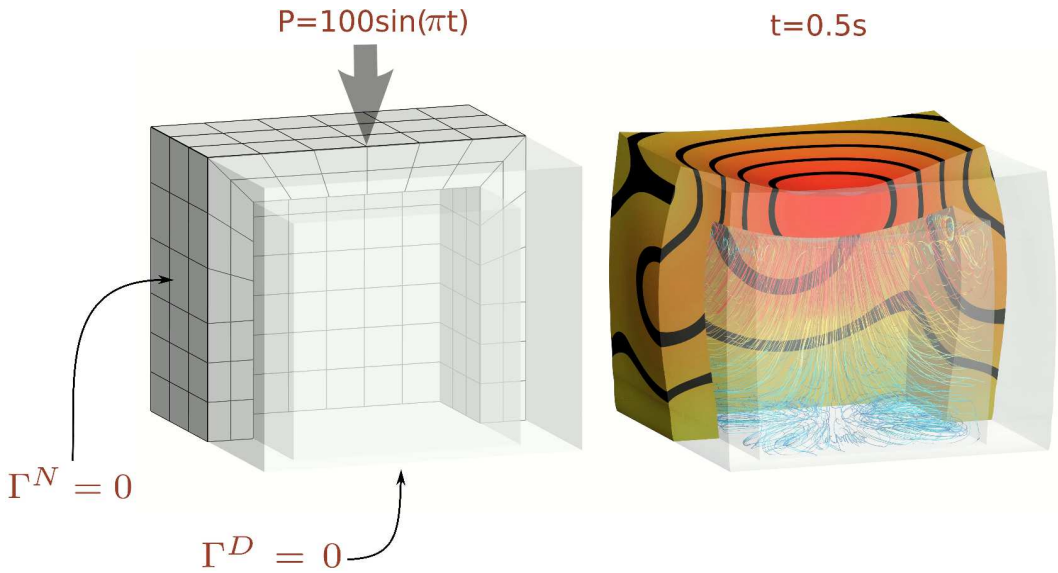

FIGURE 3.32. *A visualisation of the problem setup for the isovolumetric cube problem.*

Left, problem setup. *A fluid cube, $1m \times 1m \times 1m$, was encased on 5 sides by an elastic solid, thickness $0.1m$. The bases of the fluid cube and solid wall were fixed. A sinusoidal pressure was applied to the top face of the solid, all other solid faces were left free. For the simulation, fluid viscosity was $0.008cP$, with a density of $1.0kg \cdot m^{-3}$. Solid neo–Hookean shear modulus was either $290Pa$ or $350Pa$.*

Right, a visualisation of the solution at t=0.5s. *The colours represent velocity/displacement magnitudes of the fluid/solid respectively – fluid, blue to red, ranges from 0.0 to $0.25ms^{-1}$; solid, yellow to red, ranges from 0.0 to $0.2m$.*

are often numerically challenging to solve, therefore an understanding of numerical performance under these conditions is important. The problem description is given in figure 3.32. The fluid mesh consisted of $\approx 4.8 \times 10^4$ TET(2,2,1) elements, while the solid mesh had 360 HEX(3,3,2) elements. Total system degrees of freedom were $\approx 3.2 \times 10^5$. The simulation was run for 100 time steps of $0.01s$.

Two problem cases were run, with solid shear modulii of $290Pa$ and $350Pa$ for the first and second cases respectively. Parameters were chosen to demonstrate the performance of the Newton–Raphson/line search modifications under different conditions – both numerically challenging ($\mu = 290Pa$) and relatively simple ($\mu = 350Pa$).

3.4.2 Relative Performance of the Implemented Numerical Methods

The simulations were performed four times, testing the impact of different solution methods. The four cases were: 1) No matrix reuse – where the Jacobian matrix inverse was solved at each Newton iteration; 2) No line search – where no form of line search was used and the full Newton step was taken each time; 3) No line search mod – the line search algorithm was used with $\zeta = 1$ (see section 2.5.3.1); 4) All – all methods implemented were incorporated to provide a baseline for comparison. In each case, with exception of the method excluded, all other implemented numerical methods were used. For example, in the no matrix reuse case, both the line search and the line search modification (where ζ equals the sub–iteration convergence criteria) were used. Tables 13 to 16 provide a comparative analysis of the effect of the implemented methods on system performance. All problems except the fluid immersed cylinder, which was solved on one 2.4GHz processor with 4Gb memory, were solved on one 8 processor node of the OERC[212] cluster SAL.

	Mean Newton Iterations	Mean Matrix Inverses	Mean Time Step Duration
No Matrix Reuse	7.3	7.3	$204s$
No Line search	8.7	1.1	$46s$
No Line search Mod	8.7	1.1	$46s$
All	8.8	1.1	$47s$

Table 13

Comparison of the mean Newton iterations, Jacobian matrix inverses and time step duration for the least refined fluid immersed cylinder encased in a hyperelastic box problem (in this case fluid elements were TET(2,2,1)).

In most cases reusing the Jacobian inverse was most significant in terms of reducing time step duration. Of note was that even in the fluid immersed cylinder encased in a hyperelastic box problem, where the matrix structure changes each time step due to FD motion, reusing the Jacobian inverse substantially reduced solution time. With respect to the line search modification, performance was not significantly improved, compared with the no line search case, when the convergence parameter $\zeta = 1$ was chosen. Incorporating the modification, *i.e.* making ζ equivalent to the the sub–iteration convergence criteria, improved convergence behaviour in certain cases, however in others the impact was minor. In one case (the fluid immersed cylinder encased in a hyperelastic box problem), the impact was negative, as entering line search did not reduce the number of matrix

$\mu = 290Pa$

	Mean Newton Iterations	Mean Matrix Inverses	Mean Time Step Duration
No Matrix Reuse	7.88	7.88	$2760s$
No Line search	16.65	3.05	$1364s$
No Line search Mod	16.65	3.05	$1364s$
All	15.24	0.14	$381s$

$\mu = 350Pa$

	Mean Newton Iterations	Mean Matrix Inverses	Mean Time Step Duration
No Matrix Reuse	4.39	4.39	$1482s$
No Line search	11.75	0.059	$268s$
No Line search Mod	11.75	0.059	$268s$
All	11.75	0.059	$268s$

TABLE 14

Comparison of the mean Newton iterations, Jacobian matrix inverses and time step duration for the isovolumetric cube problem, solid shear modulii cases $\mu = 290Pa$ (top row) and $\mu = 350Pa$ (bottom row).

Linear Case

	Mean Newton Iterations	Mean Matrix Inverses	Mean Time Step Duration
No Matrix Reuse	5.84	5.84	$112s$
No Line search		failed after 608 time steps	
No Line search Mod	11.22	0.48	$30.8s$
All	12.83	0.36	$29.3s$

Curvilinear Case

	Mean Newton Iterations	Mean Matrix Inverses	Mean Time Step Duration
No Matrix Reuse	1.60	1.60	$44.85s$
No Line search	8.26	0.013	17.2
No Line search Mod	8.26	0.013	17.2
All	8.26	0.013	17.2

TABLE 15

Comparison of the mean Newton iterations, Jacobian matrix inverses and time step duration for the linear and curvilinear quadratic cases of contracting cylinder problem (section 3.3.3).

inversions performed. Additionally, greater work was required to compute the additional residual evaluations. In the cases where the modification was effective, substantially fewer matrix inversions were required and solve time was reduced.

Regarding the isovolumetric cube problem, smaller improvement than expected in solve time was observed in the no line search and no line search mod cases when the solid shear modulus equaled $290Pa$. This was due to the solution 'bouncing' either side of the converged solution, consistently reducing $|\mathscr{R}(\mathbf{X}^m)|_{l_2}$, however, only by a small percentage at each iteration. Effectively, this meant line search was never used and convergence stalled

	Mean Newton Iterations	Mean Matrix Inverses	Mean Time Step Duration
No Matrix Reuse	4.98	4.98	$2388s$
No Line search	10.29	0.59	$482.8s$
No Line search Mod	10.13	0.40	$390.0s$
All	9.84	0.086	$248.8s$

TABLE 16

Comparison of the mean Newton iterations, Jacobian matrix inverses and time step duration for the full cycle LVAD supported LV problem (chapter 5). Note that for the problem where the Jacobian inverse was computed at each Newton iteration, it was impractical to simulate the full cardiac cycle, therefore 100 time steps were solved in each cardiac phase (see the following section) and the weighted average, based on phase duration, was calculated. Additionally, due to slow convergence during the systolic phase, a similar weighted average was used for the no line search and no line search mod cases during systole.

(up to 30 matrix inversions were required during some time steps). The line search modification prevented this from occuring, resulting in significantly fewer matrix inversions being required and substantially reducing solution time. In the $\mu = 350Pa$ case solid displacements and fluid velocities were lower and, as a result, convergence behaviour was more straight forward.

In the curvilinear case of the contracting cylinder problem, no improvement was observed as a result of the line search modifications. Due to the minimal solid displacement and fluid velocity in this problem, few matrix inversions were required. Therefore line search was not needed to improve convergence rates. Regarding the linear case, the line search modification significantly reduced the number of matrix inversions required for solution. The minimal impact that this made on solution time was due to the relative efficiency in inverting small problem matrices (in larger problems this has more of an impact).

In most cases incorporating all the implemented numerical methods resulted in the lowest average Jacobian matrix inverses solved per time step, as well as the lowest mean time step duration. In general, the line search modifications had less impact on problems which exhibited slower and/or lower magnitude changes. Where the impact was negative, the effect was minor in comparison with overall solve time. These results show that the Newton–Raphson/line search modifications significantly improved the solve time for coupled fluid–solid finite element problems. Additionally, they demonstrate that when required the line search modifications prevent problem convergence from stalling. Given the size of the large problems solved in this thesis, for example the full cardiac cycle simulations consisted of 2880 time steps per cycle, these improvements had a large impact on overall computation time.

3.4.3 LV Full Cycle

The cardiac cycle has four distinct phases, isovolumetric contraction, systole, isovolumetric relaxation and diastole. System behaviour in each phase is significantly different, ranging from, isovolumetric phases with rapidly changing solid stress and fluid pressure, through to diastole and systole, when large volumes of fluid enter/leave the LV cavity. Tables 17 to 20 show the impact of the implemented numerical methods on the system performance in each phase.

	Mean Newton Iterations	Mean Matrix Inverses	Mean Time Step Duration
No Matrix Reuse	5.98	5.98	2870s
No Line search	10.28	0.135	254.7s
No Line search Mod	10.28	0.135	254.7s
All	10.59	0.11	249.2s

TABLE 17

Comparison of the mean Newton iterations, matrix inverses and time step duration for the isovolumetric contraction phase of the LVAD supported LV problem. Note that since the LVAD was incorporated in the model, this section was not strictly isovolumetric.

	Mean Newton Iterations	Mean Matrix Inverses	Mean Time Step Duration
No Matrix Reuse	4.88	4.88	2340s
No Line search	13.22	2.44	1357s
No Line search Mod	12.55	1.53	912.3s
All	10.45	0.073	242.2s

TABLE 18

Comparison of the mean Newton iterations, matrix inverses and time step duration for the systole phase of the LVAD supported LV problem.

	Mean Newton Iterations	Mean Matrix Inverses	Mean Time Step Duration
No Matrix Reuse	5.01	5.01	2398s
No Line search	10.72	0.086	276.1s
No Line search Mod	10.74	0.085	275.8s
All	10.84	0.080	273.7s

TABLE 19

Comparison of the mean Newton iterations, matrix inverses and time step duration for the isovolumetric relaxation phase of the LVAD supported LV problem. Note that since the LVAD was incorporated in the model, this section was not strictly isovolumetric.

	Mean Newton Iterations	Mean Matrix Inverses	Mean Time Step Duration
No Matrix Reuse	3.95	3.95	1895s
No Line search	6.31	0.088	206.4s
No Line search Mod	6.31	0.088	206.4s
All	6.40	0.086	207.8s

TABLE 20

Comparison of the mean Newton iterations, matrix inverses and time step duration for the diastole phase of the LVAD supported LV problem.

As before, reusing the Jacobian matrix inverse dramatically improved solution time. This is unsurprising given the high computational cost of matrix inversion. Of note was the poor performance of the no line search and no line search mod cases during systole. This was due to the convergence behaviour during this phase, where, as in the isovolumetric cube problem, the solution would 'bounce' either side of the converged solution.

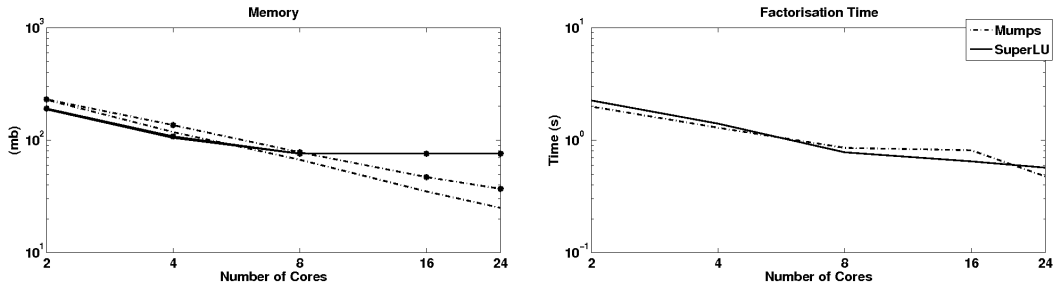

(a)

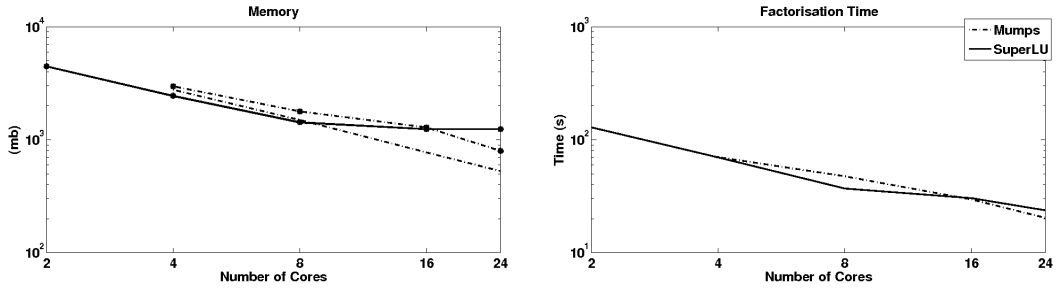

(b)

FIGURE 3.33. *Memory use and factorisation time for fluid only problem matrices solved using Mumps and SuperLU. In the memory plots, lines with asterisks denote the maximum memory used by a processor, lines without asterisks give the average memory used by all processors. Where no marker is shown, the matrix solve failed.*

a) ***Small fluid matrix.*** *The fluid only problem matrix from the unrefined mesh in the channel flow around an immersed cylinder problem (section 3.1.2.1). The matrix was an* $57,175 \times 57,175$ *sparse matrix with* $\approx 4 \times 10^6$ *non–zero entries.*
b) ***Large fluid matrix.*** *The fluid only problem matrix from the refined mesh in the channel flow around an immersed cylinder problem. The matrix was an* $858,402 \times 858,402$ *sparse matrix with* $\approx 8 \times 10^7$ *non–zero entries. The Mumps matrix solver failed when using* 2 *cores.*

Overall, the Newton–Raphson/line search modifications made a significant difference to solution time in the LVAD supported LV problem.

3.5 Direct Matrix Solvers

Two direct matrix solvers were used in cHeart, SuperLU and Mumps. This section compares their relative performance, with respect to memory use, solution time and scalability, on a variety of matrix sizes and types. The matrix types compared were: fluid only, fluid–solid coupled and fluid–solid coupled with FD. In the first two cases a small and large problem matrix were tested, while for the fluid–solid coupled with FD case, one small problem matrix was compared along with the matrices from two LVAD supported LV problems (small and large – problems 4.5.2) and 4.5.1. Each matrix was solved on 2, 4, 8, 16 and 24 processors on the OERC[212] cluster SAL – machine specifications 2.53GHz Quad core processors, 8 cores per node, 3GB memory per core.

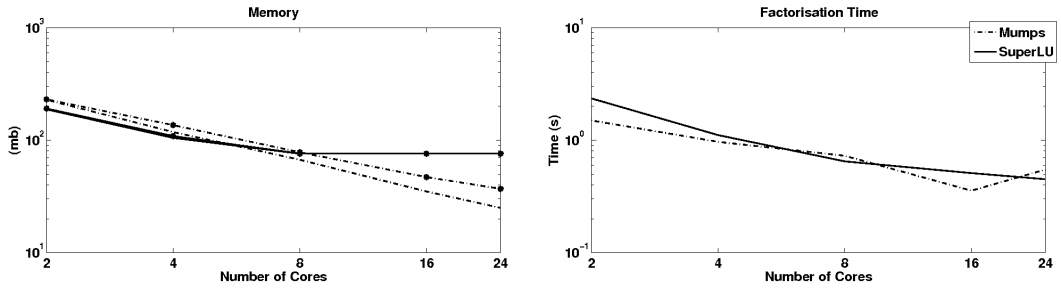

(a)

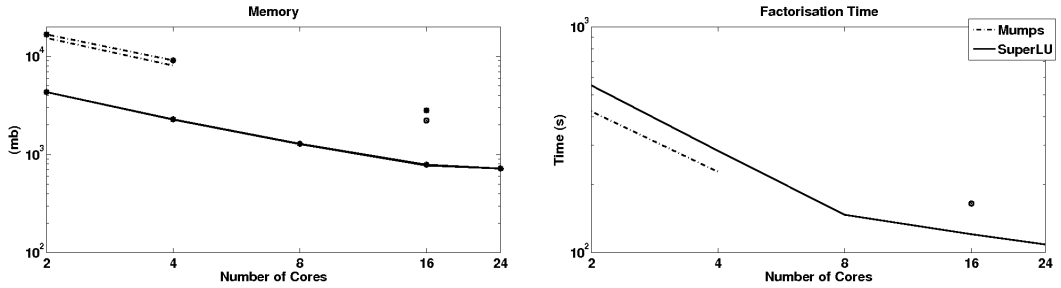

(b)

FIGURE 3.34. *Memory use and factorisation time for coupled fluid–solid problem matrices solved using Mumps and SuperLU. In the memory plots, lines with asterisks denote the maximum memory used by a processor, lines without asterisks give the average memory used by all processors. Where no marker is shown, the matrix solve failed.*

a) ***Small fluid–solid coupled matrix.*** *Test problem not featured in this thesis. The matrix was an* $33,804 \times 33,804$ *sparse matrix with* $\approx 3.5 \times 10^6$ *non–zero entries.*
b) ***Large fluid–solid coupled matrix.*** *Isovolumetric cube problem matrix from section section 3.4.1. The matrix was an* $273,348 \times 273,348$ *sparse matrix with* $\approx 4.7 \times 10^7$ *non–zero entries. The Mumps matrix solver failed when using* 8 *and* 24 *cores.*

The results are compared in plots 3.33 to 3.35.

The results comparing the two direct matrix solvers implemented in cHeart show no major difference in solution time. The average memory use, in contrast, was significantly lower with the SuperLU solver for all problem types except fluid only. Additionally, the distribution of memory, *i.e.* the range between average and maximum memory use, across the cores was more even for the SuperLU solver. This is significant in larger problems, as a greater distribution increases the likelihood that one of the cores will not have sufficient memory to solve the matrix. This was the primary reason that the Mumps matrix solver failed on the larger matrices tested. Specifically, while mumps attempts to estimate the memory required prior to the solve, the failure is because the estimation method used is less accurate with higher processor numbers[56]. This makes the solver unstable for large problems, as even if it solves at one Newton iteration, it may not be able to calculate a solution at the next.

A final feature of the memory distribution plots was that memory use for the SuperLU solver plateaus at higher core numbers. This was because the row permutation algorithm (in SuperLU this is a large diagonal

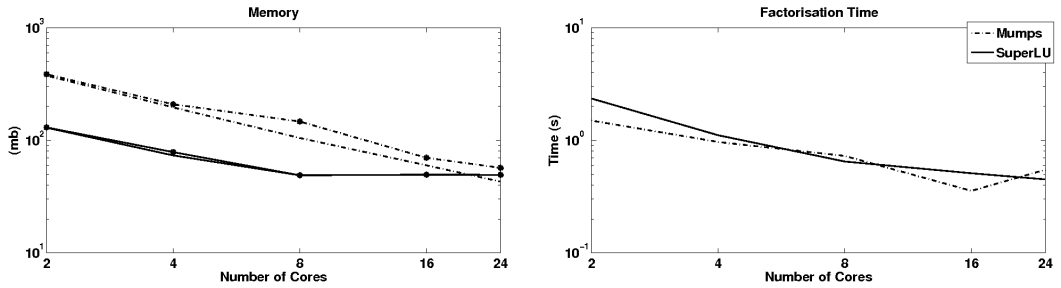

(a)

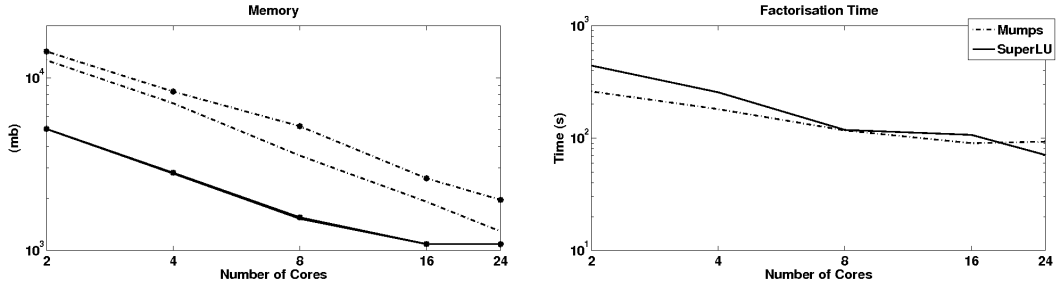

(b)

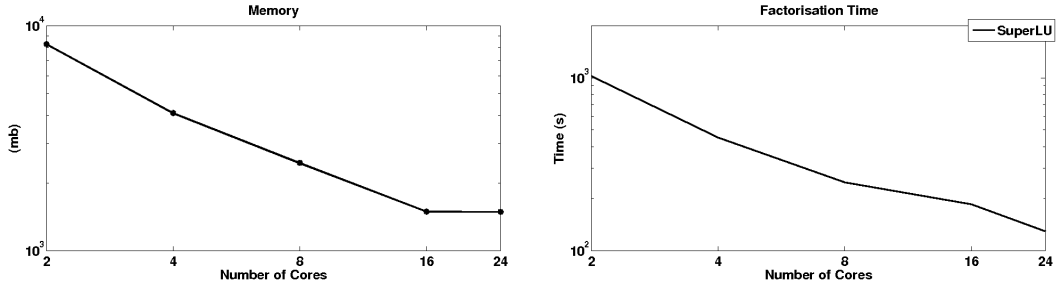

(c)

FIGURE 3.35. *Memory use and factorisation time for fluid–solid coupled with FD problem matrices solved using Mumps and SuperLU. In the memory plots, lines with asterisks denote the maximum memory used by a processor, lines without asterisks give the average memory used by all processors. Where no marker is shown, the matrix solve failed.*

a) ***Small fluid–solid coupled FD matrix.*** *The unrefined problem matrix from the fluid immersed cylinder encased in a hyper–elastic box test problem (section 3.1.3.1). The matrix was an* $35,895 \times 35,895$ *sparse matrix with* $\approx 2.8 \times 10^6$ *non–zero entries.*

b) ***Small LVAD supported LV matrix.*** *The LVAD supported LV problem matrix from section 4.5.2. The matrix was an* $564,219 \times 564,219$ *sparse matrix with* $\approx 6.9 \times 10^7$ *non–zero entries.*

c) ***Large LVAD supported LV matrix.*** *The LVAD supported LV problem matrix from the CR/DP problem in section 4.5.1. The matrix was an* $778,333 \times 778,333$ *sparse matrix with* $\approx 1 \times 10^8$ *non–zero entries. The Mumps matrix solver failed when using less than* 40 *cores. For* 40 *cores, the Mumps solver took* 122*s and used an average of* 1163*mb per core, with a maximum of* 1719*mb.*

method[29]) is not parallelised, therefore once the memory required for factorisation reduces below that needed for the row permutation, further memory reduction will not occur. Note that if the matrix structure does not change, the row permutation can be reused. However, for FD problems where the FD and/or fluid mesh are moving, the matrix structure will change and the row permutation will not be able to be reused.

Based on these results, SuperLU was used as the solver for most of the large simulations presented in this thesis – in particular the LV problems.

3.6 Discussion of Numerical Methods and Convergence

In this chapter, the behaviour, accuracy and convergence properties of the numerical methods and schemes implemented as part of this thesis were tested. The results can be broadly separated into two categories, those related to improving solution time, and those linked to reducing problem error.

With respect to solution time, the results in section 3.4 demonstrated that the Newton Raphson/line search modifications significantly improved numerical performance. They also show that without correct selection of the criteria for entering the line search algorithm, reusing the Jacobian inverse might not improve solve time. Given the size of large fluid–solid coupled finite element schemes (upwards of 5×10^5 degrees of freedom and 1×10^3 time steps), without these improvements to the numerical scheme, solving a fluid–solid coupled LV problem through the full cardiac cycle would not be feasible. Additionally, the robustness of the matrix inversion process is important to provide confidence that a well posed problem will solve. To this end, the comparison between direct matrix solvers in section 3.5 demonstrated the stability of SuperLU (*c.f.* Mumps), which was the primary reason for its use in the larger simulations performed in this thesis.

This chapter highlighted the importance of element types in the numerical accuracy of the finite element scheme. The fictitious domain convergence results (section 3.1) showed the importance of using discontinuous pressures to capture pressure gradients across FD boundaries within the fluid domain. While the contracting isovolumetric cylinder problem (section 3.3) demonstrated the impact of curvilinear, compared with linear, spatial interpolation schemes in reducing error in problems with high tractions across the fluid–solid interface. For numerical simplicity, the FD method was implemented specifically for fluid meshes constructed from linear tetrahedrons. To facilitate the integration of these results (along with reducing computation cost), the mesh update algorithm (section 2.5.4) was adapted so that internal tetrahedrons were updated linearly, while curvilinear spatial information was maintained only on the fluid boundary. As such, error, caused by the use of curvilinear fluid elements in conjunction with the FD scheme, was limited to instances where the FD comes into contact with the fluid boundary.

Finally, the results in this chapter (combined with previous numerical validation and verification in Nordsletten[134, 136]) provide confidence that the numerical scheme is convergent and, with respect to the lumped parameter coupling, stable. As such it provides a base from which the more complicated LV simulations can be developed.

Part II

The Ventricular Model

4 Diastole in Normal and Supported Left Ventricles

The results and methods presented in the previous chapters describe the models developed to simulate fluid–solid interactions in an LVAD supported heart. To extend these models to study LV function, the cardiac geometry and constitutive behaviour need to be defined. To this end, the ventricular model is introduced in sections 4.1 and 4.2. Using this model, simulations were performed (section 4.4) to compare diastolic behaviour in a normal and an LVAD supported LV in order to provide an understanding of how LVAD support impacts passive LV function.

The FD method was developed to facilitate the simulation of the full range of cardiac motion in an LVAD supported LV. To provide confidence that this method is capable of resolving LV flow features and material deformations under physiological conditions, a comparison was performed between LVs with Dirichlet and FD prescribed cannula geometries (section 4.5). Additionally, to demonstrate that the use of the the FD method to prescribe the LVAD cannula enables contact between the endocardial wall and the LVAD cannula to be captured, a simulation of contact is presented in section 4.5.2.

Finally, analysis of large 3D fluid–solid coupled simulations often requires the use of specific tools to facilitate interpretation of the results. Of specific interest with respect to LVAD support is the residence time of blood within the LV. Therefore, to provide an estimate of the extent to which blood pools within the cavity, a particle tracking algorithm was developed (section 4.3) and was used to investigate the impact of cannula length on the residence time of blood in the ventricular chamber (section 4.6).

4.1 An Anatomical Left Ventricular Model

Image data taken from a normal subject was used to construct myocardial mesh geometries for both a normal and LVAD implanted LV. This section details the fitting and mesh generation procedures for both the normal and LVAD LV geometries.

4.1.1 Geometric Fitting

A model left ventricle was constructed based on 36 cine MRI sequences (collected at the Royal Brompton Hospital) taken from a 70Kg, healthy, male subject, apex to base. Image spatial resolution was $1.7mm \times 1.7mm$ in the MRI image plane with a through plane resolution of $3.4mm$[112]. A sampling of the endocardial and

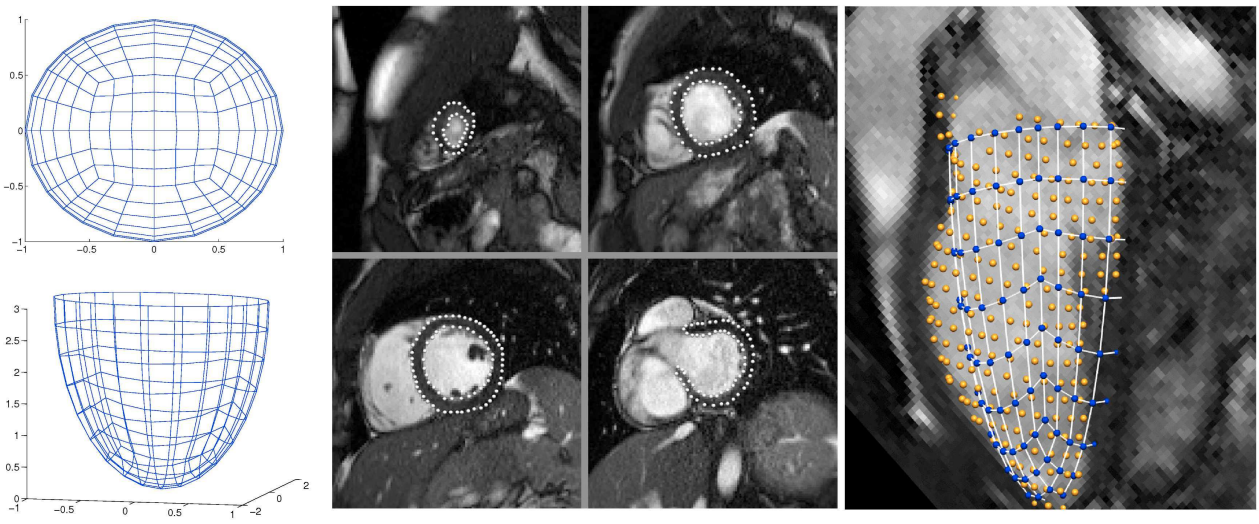

FIGURE 4.1. *Left, the reference ellipse for the normal LV mesh, centre digitised MRI images and right the reference ellipse rotated to align with the digitised data cloud. Note the structure of the reference ellipse mesh, which consists of an internal square of elements and outer rings of elements that are formed radially out from the inner square. The 2D computational domain, $\Lambda_\chi(\vartheta)$, for the finite difference smoothing problem is shown top left.*

epicardial surfaces of the LV was extracted as a series of data points at end–diastole. The volume meshes were constructed by fitting surface meshes to the digitised samplings and linearly interpolating between them.

The surface meshes were constructed from ellipsoidal topologies which were fitted to the data points using `CMISS`[210]. A common issue with hexahedral LV meshes is the existance of 'collapsed' elements (*i.e.* where one element face effectively has zero area) at the LV apex[123, 182, 160]. Therefore, to ensure all surface (and the resulting volume) elements were rectangular (hexahedral), a novel ellipsoidal geometry was constructed to build the normal LV mesh. Figure 4.1 shows this ellipsoidal morphology in both its reference configuration and after rotating to align with the digitised data cloud. Due to the presence of the LVAD cannula, the LVAD LV ellipsoidal geometry was simpler, consisting of elements constructed radially out from a central point in the apical region.

The `CMISS` fitting procedure, outlined in Fernandez *et al.*[41], uses a least–squares minimisation technique to fit C1 continuous Hermite surface elements[123] to the digitised data cloud. Mesh smoothness was ensured by weighting derivative terms to penalise arc curvature on the fitted surface. Volume models were constructed from the fitted surface models by linear interpolation between the corresponding nodes on the endo/epicardial surfaces. Refinement was performed transmurally providing greater through wall mesh resolution. The resulting myocardial geometry was defined using cubic curvilinear elements.

The fitted myocardial geometries form a cavity within which the fluid mesh can be constructed. Using a surface tessellation algorithm outlined in Nordsletten *et al.*[139] triangulated surface meshes were constructed from which, using the software package `CUBIT`[65], linear tetrahedral meshes were constructed to epresent the fluid domain. Higher order curvilinear approximations of the fluid domain were constructed by projecting nodes from the fluid interface onto the corresponding solid boundary.

4.1.1.1 Normal LV Mesh

Construction of the normal LV mesh was complicated by the requirement for local element coordinate continuity between adjacent elements. This requirement is due to the mapping of derivative information between elements in the fitting procedure. Due to the nature of the ellipse topology, reference element coordinate ($\boldsymbol{\phi}$) directions within the finite element mesh could not be made consistent. This resulted in problems with the fit at the intersection between the inner square of elements and the outer elements, see figure 4.2. To correct for these problems, the fitted mesh was smoothed by solving the Laplacian problem over elements either side of the inner square and outer elements in the 2D reference ellipse domain, $\Lambda_\chi(\vartheta)$ (see figure 4.1),

$$\nabla^2_\vartheta \mathbf{x} = 0, \text{ in } \Lambda_\chi, \tag{4.1}$$

where ϑ are the coordinates of Λ_χ. The system was solved using a five point finite difference scheme with boundary conditions equal to the nodal values either side of the smoothed domain. Derivative information was preserved by extending the finite difference scheme to 9 points at boundary nodes. The node coordinates, $\mathbf{x}^h$, projected onto $\Lambda_\chi(\vartheta)$, $\vartheta = \mathcal{P}^{\Lambda_\chi}_\Omega(\mathbf{x})$, formed the computational grid for the finite difference scheme. The final fitted end diastolic and end systolic meshes are shown in figure 4.2.

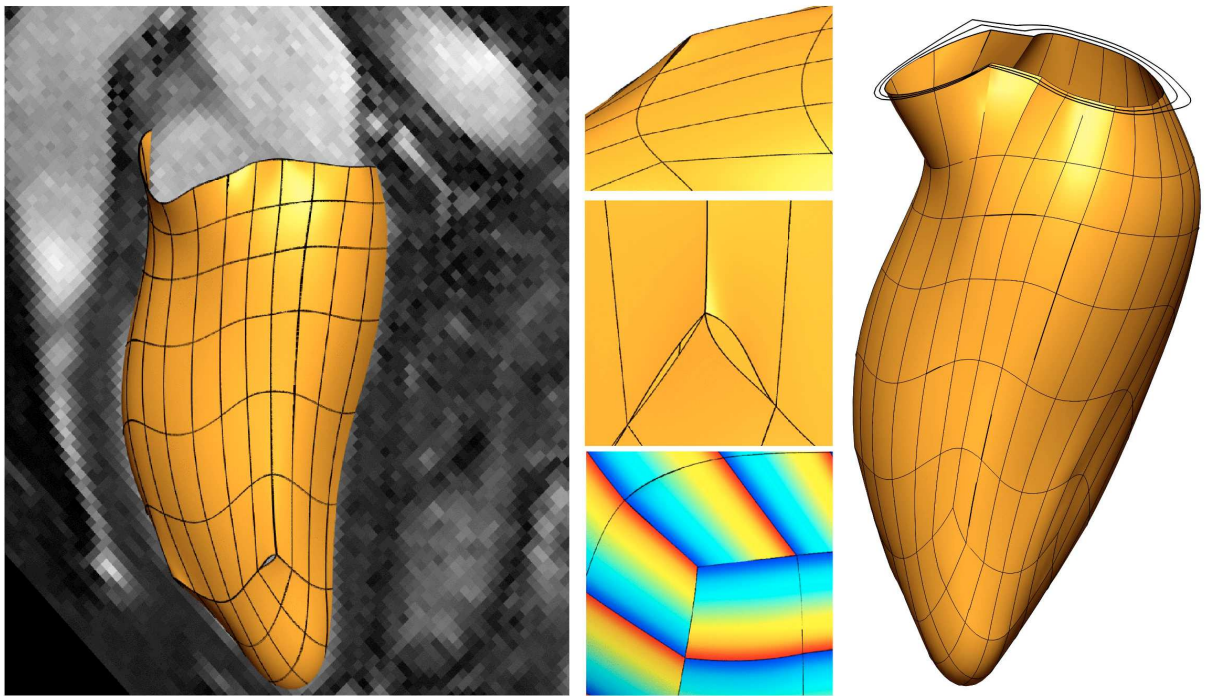

Figure 4.2. *Left, the endocardial fitted surface mesh for the normal LV geometry. Centre, top and middle, close up of the fitting errors caused by the local coordinate discontinuity between elements either side of the inner element square. Centre, bottom, local coordinate directions, blue to red, in this region. Right, the final fitted endocardial mesh, after smoothing.*

Due to thinning of the myocardium at the apex, the final fitted normal LV mesh was broken into two regions. A mid–wall region consisting of 432 cubic hexahedral elements with a through wall thickness of 3 elements and an apical region of 36 cubic hexahedral elements where through wall thickness was 1 element. The two regions were coupled together using the methods outlined in chapter 2.

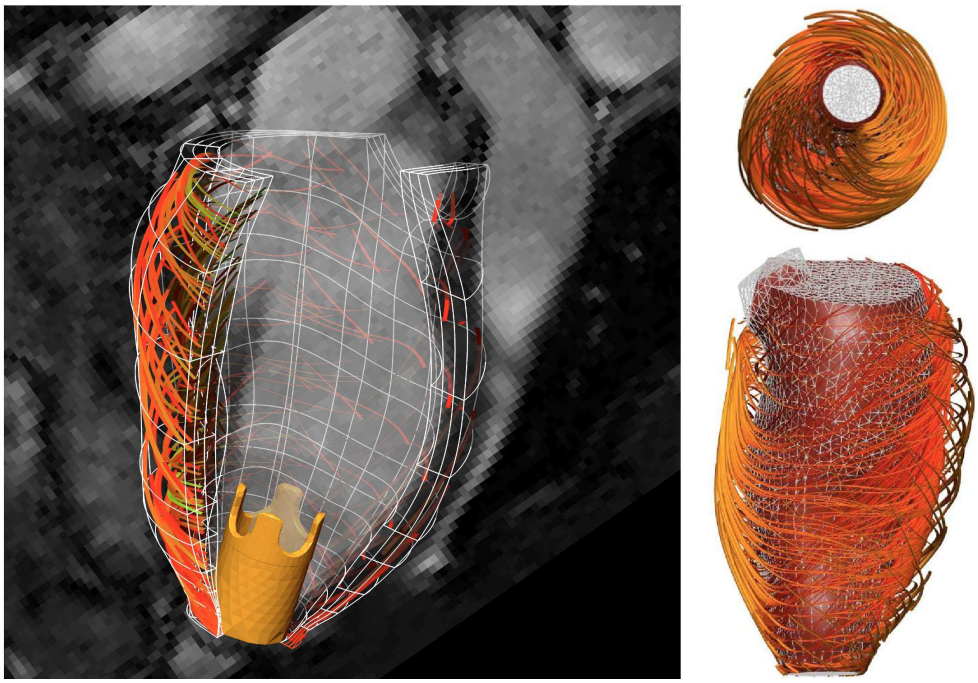

FIGURE 4.3. *Left, the fitted LVAD LV mesh with the LVAD cannula attached at the apex. The streamlines show the fibre orientation through the myocardial wall. Right, the fluid mesh constructed from the endocardial surface, surrounded by myocardial fibres. Note the fluid mesh at the apex, top right, does not, in this case, include the FD cannula.*

4.1.1.2 LVAD LV MESH

The LVAD LV mesh was constructed from 324 cubic hexahedral elements with a through wall thickness of 3 elements. Depending on whether the LVAD cannula was prescribed as a Dirichlet boundary or as a FD, different fluid mesh boundary tessellations were constructed – either incorporating the cannula or leaving the apical boundary flat, see figure 4.3. Cannula geometry was provided by Berlin Heart[209].

4.1.2 MODEL LAMINAR STRUCTURE

Based on the results of LeGrice *et al.*[96, 94], an idealised fibre geometry, $\pm 60^o$ on the endo/epicardial surfaces, was defined within the myocardial geometry. The sheet direction, $\mathbf{s}$, is defined on the endo/epicardial surfaces as the surface normal, $\mathbf{n}_s$, in the direction of the interior LV cavity. With respect to an LV orientation, $\mathbf{d}_{lv}$, the circumferential direction, $\mathbf{d}_{cir} = \mathbf{n}_s \times \mathbf{d}_{lv}$ is defined. The fibre direction is calculated by rotating $\mathbf{d}_{cir}$ by $\pm 60^o$ about $\mathbf{s}$, depending on the surface. Finally, the normal direction on the surfaces is $\mathbf{n} = \mathbf{f} \times \mathbf{s}$, *i.e.* orthogonal to the fibre and sheet directions. Linearly interpolating through the wall enables the fns coordinate frame to be defined at all node points (and therefore continuously) throughout the mesh. The interpolation order of fibre field can be independent of the spatial and variable interpolation orders, therefore the element type ELEM is redefined for Costa law solids as,

$$\text{ELEM}(i,\ j,\ k,\ l),$$

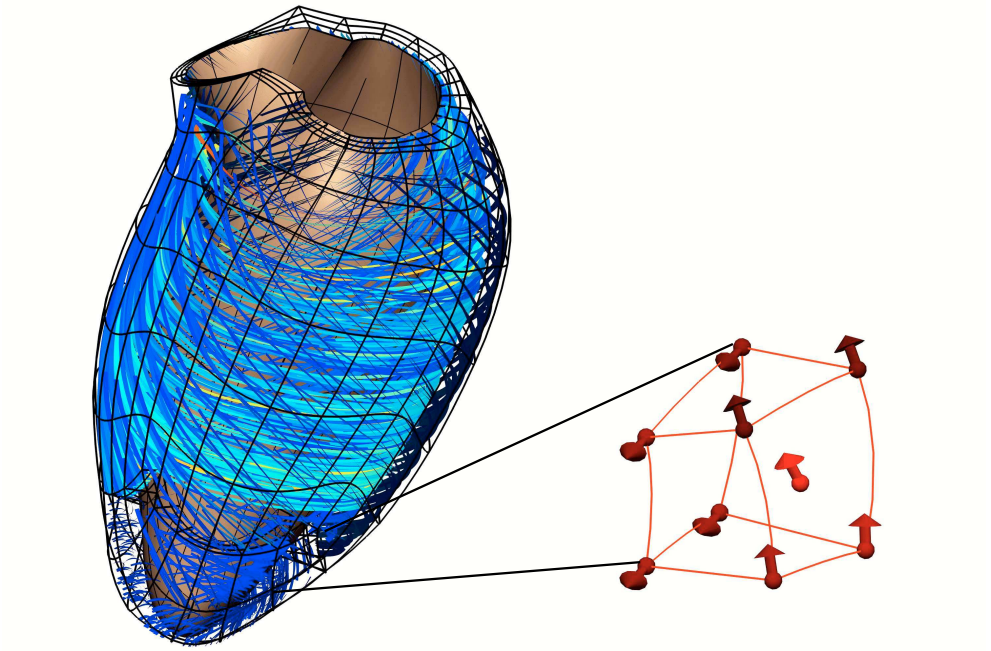

FIGURE 4.4. *Left, streamlines showing the fibre orientation through the myocardial wall in the normal LV mesh. Right, an element from the apical mesh with fibre orientations defined at the element corner nodes. the mid–wall point (red) has its orientation defined by linearly interpolating the surface values through the wall.*

where the fibre field is defined using l^{th} order interpolation functions. Figure 4.3 shows the fibres within the LVAD LV mesh, while figure 4.4 shows the fibre orientations both in the normal LV mesh and in an element contained within the mesh. Note that at the apex, $\mathbf{n}_s = \mathbf{d}_{lv}$, therefore, $\mathbf{d}_{cir}$ is undefined, creating a singularity, a solution to this issue is presented in the following section.

4.2 Costa Constitutive Law

To describe the behaviour of myocardial tissue, a modified form of the Costa constitutive law[137] was implemented for the LV models presented in this thesis. In this law, the strain energy relationship, W, is defined as an exponential function of strains in the fibre, sheet and normal (fsn) directions,

$$W(\mathbf{E}_F) = \frac{C}{2}\left(e^{Q(\mathbf{E}_F)} - 1\right), \; Q(\mathbf{E}_F) = \sum_{i,j\in[1,3]} \alpha_{ij}(\mathbf{E}_F)_{ij}(\mathbf{E}_F)_{ji}. \tag{4.2}$$

Here, $\mathbf{E}_F$ is the green strain tensor, $\mathbf{E}$ (defined in the Cartesian coordinate frame), rotated into the fsn coordinate frame, such that,

$$\mathbf{E}_F = \mathbf{Q}\mathbf{E}\mathbf{Q}^T, \quad \mathbf{E} = \frac{1}{2}(\mathbf{F}^T\mathbf{F} - \mathbf{I}), \tag{4.3}$$

$\mathbf{F}$ is the deformation gradient tensor defined in equation 2.5 and $\mathbf{Q}$ is a rotation tensor defined as,

$$\mathbf{Q} = [\mathbf{f}, \mathbf{s}, \mathbf{n}], \tag{4.4}$$

where $\mathbf{f}$, $\mathbf{s}$, $\mathbf{n}$, are the vectors defining the fsn directions. Considering the stress contribution from $W(\mathbf{E}_F)$, the Cauchy stress tensor, $\hat{\boldsymbol{\sigma}}_F$, in the fsn coordinate frame, is,

$$\hat{\boldsymbol{\sigma}}_F(\mathbf{E}_F) = \frac{1}{2}\mathbf{F}_F\left(\frac{\partial W}{\partial \mathbf{E}_F} + \frac{\partial W}{\partial \mathbf{E}_F^T}\right)\mathbf{F}_F^T, \tag{4.5}$$

where $\mathbf{F}_F$ is the deformation gradient tensor rotated into the fsn coordinate frame. Rotating back into Cartesian coordinates, the Cauchy stress, $\hat{\boldsymbol{\sigma}}$, is,

$$\hat{\boldsymbol{\sigma}}(\mathbf{E}) = \mathbf{Q}^T\hat{\boldsymbol{\sigma}}_F\mathbf{Q}. \tag{4.6}$$

In the literature[27], two forms of the constants α_{ij} are defined, corresponding to orthotropic and transversely isotropic materials. Due to the different material behaviour in each of the three principle directions, only the orthotropic form is considered here. The constants α are therefore defined as,

$$\alpha = \begin{pmatrix} b_1 & b_4 & b_5 \\ b_4 & b_2 & b_6 \\ b_5 & b_6 & b_3 \end{pmatrix}. \tag{4.7}$$

The values of b determine the degree of fibre anisotropy as well as the strength of the non–linear material response. Note that the values are problem specific and, for this chapter, are defined in tables 1 and 2. From this definition, the second Piola–Kirchoff stress tensor[1] in the fibre frame, $\mathbf{S}_F$, is given by,

$$\begin{aligned}
\mathbf{S}_F &= \frac{1}{2}\left(\frac{\partial W}{\partial \mathbf{E}_F} + \frac{\partial W}{\partial \mathbf{E}_F^T}\right) \\
&= \frac{C}{4}e^{Q(\mathbf{E}_F)}\left(\frac{\partial Q}{\partial \mathbf{E}_F} + \frac{\partial Q}{\partial \mathbf{E}_F^T}\right) \\
&= Ce^{Q(\mathbf{E}_F)}\begin{pmatrix} b_1(\mathbf{E}_F)_{11} & b_4(\mathbf{E}_F)_{12} & b_5(\mathbf{E}_F)_{13} \\ b_4(\mathbf{E}_F)_{21} & b_2(\mathbf{E}_F)_{22} & b_6(\mathbf{E}_F)_{23} \\ b_5(\mathbf{E}_F)_{31} & b_6(\mathbf{E}_F)_{32} & b_3(\mathbf{E}_F)_{33} \end{pmatrix} \\
&= Ce^{Q(\mathbf{E}_F)}\mathbf{G}(\mathbf{E}_F).
\end{aligned} \tag{4.8}$$

Therefore the Cauchy stress from equation 4.6 is defined with respect to its coefficients as,

$$\hat{\boldsymbol{\sigma}}(\mathbf{E}) = Ce^{Q(\mathbf{E}_F)}\mathbf{F}\mathbf{Q}^T(\mathbf{G}(\mathbf{E}_F))\mathbf{Q}\mathbf{F}^T. \tag{4.9}$$

The fibre map, as outlined in section 4.1.2, introduces a singularity near the apex due to the radial fibre definition in the model. Additionally, the myocardial microstructure near the apex has been observed to be less structured than other parts of the wall and has a higher density of connective proteins such as collagen.

[1]The second Piola–Kirchoff stress tensor is defined with respect to the reference configuration and maps forces in the reference configuration to areas in the reference configuration, $\mathbf{S} = \jmath\mathbf{F}^{-1}\hat{\boldsymbol{\sigma}}\mathbf{F}^{-T}$

Therefore, the material model near the apex would be expected to be more isotropic with parameters somewhere between those of the sheet normal and fibre directions. To reflect this, the constitutive law was modified to transform the orthotropic law to one which is more isotropic in the apical regions. The isotropic strain energy function at the apex is defined as,

$$W_{iso} = \frac{C_2}{2}(e^{K^2\mathbf{E}:\mathbf{E}}), \tag{4.10}$$

C_2 and K are constants controlling the isotropic stiffness and non–linear stress–strain relationship respectively. With respect to the second Piola–Kirchoff stress tensor $\mathbf{S}_{iso}$,

$$\hat{\boldsymbol{\sigma}}_{iso} = \mathbf{F}\mathbf{S}_{iso}\mathbf{F}^T, \quad \mathbf{S}_{iso} = C_2K^2e^{K^2\mathbf{E}:\mathbf{E}}\mathbf{E}. \tag{4.11}$$

To control the decay of $\boldsymbol{\sigma}_{iso}$ at distances away from the apex, a density function Ψ is defined. In the normal LV mesh the apex is defined as a point, $\boldsymbol{\eta}_A$. However, in the LVAD mesh the apex is considered to be a plane due to the manor of attachment of the LVAD cannula to the ventricular myocardium. The plane is defined using the point $\boldsymbol{\eta}_A$ and the normal $\mathbf{n}_A$. Ψ is defined differently for each case, where,

$$\Psi(\boldsymbol{\eta}) = e^{-C_\Psi|\boldsymbol{\eta}-\boldsymbol{\eta}_A|^2}, \qquad \text{Normal LV Mesh} \tag{4.12a}$$

$$\Psi(\boldsymbol{\eta}) = e^{-C_\Psi|(\boldsymbol{\eta}-\boldsymbol{\eta}_A)\cdot\mathbf{n}_A|}, \qquad \text{LVAD Mesh} \tag{4.12b}$$

C_Ψ is a positive constant that controls the decay of Ψ. Combining equations 4.11 and 4.9 the Cauchy stress tensor, $\hat{\boldsymbol{\sigma}}$, for the modified Costa law is defined,

$$\hat{\boldsymbol{\sigma}} = (1-\Psi)\hat{\boldsymbol{\sigma}}_{Costa} + \Psi\hat{\boldsymbol{\sigma}}_{iso} - p\mathbf{I}. \tag{4.13}$$

4.2.1 Verification of Implementation

The modified Costa constitutive law was implemented in cHeart. Verification of implementation was achieved by considering the case of simple shear[2] of a cube. Consider a cube, dimension $1 \times 1 \times 1$ (see figure 4.5), by fixing the face $z = 0$, shear in the x direction on the face $z = 1$, can be defined from the deformation gradient tensor, $\mathbf{F}$,

$$\mathbf{F} = \begin{bmatrix} 1 & 0 & k \\ 0 & 1 & 0 \\ 0 & 0 & 1 \end{bmatrix},$$

where k is the deformation in the x direction on the top face. The Green strain tensor is therefore defined as,

$$\mathbf{E} = \begin{bmatrix} 0 & 0 & \frac{k}{2} \\ 0 & 0 & 0 \\ \frac{k}{2} & 0 & \frac{k^2}{2} \end{bmatrix}.$$

[2]Note that for the verification problem the isotropic stiffness component was ignored.

Defining the fibre orientation as $\mathbf{f} = [0,\ 0,\ 1]$, $\mathbf{s} = [1,\ 0,\ 0]$, $\mathbf{n} = [0,\ 1,\ 0]$,

$$\mathbf{Q} = \begin{bmatrix} 0 & 1 & 0 \\ 0 & 0 & 1 \\ 1 & 0 & 0 \end{bmatrix},$$

and $\mathbf{E}_F$ is,

$$\mathbf{E}_F = \begin{bmatrix} 0 & 0 & 0 \\ 0 & \frac{k^2}{2} & \frac{k}{2} \\ 0 & \frac{k}{2} & 0 \end{bmatrix}.$$

Substituting $\mathbf{E}_F$ into equation 4.9, the Cauchy stress is defined as,

$$\hat{\boldsymbol{\sigma}} = Ce^{b_2\frac{k^4}{4}+b_6\frac{k^2}{2}}\mathbf{F}\mathbf{Q}^T \begin{bmatrix} 0 & 0 & 0 \\ 0 & b_2\frac{k^2}{2} & b_6\frac{k}{2} \\ 0 & b_6\frac{k}{2} & 0 \end{bmatrix} \mathbf{Q}\mathbf{F}^T,$$

which expands to,

$$\hat{\boldsymbol{\sigma}} = Ce^{b_2\frac{k^4}{4}+b_6\frac{k^2}{2}} \begin{bmatrix} 2b_6\frac{k^2}{2} + b_2\frac{k^4}{2} & 0 & b_6\frac{k}{2} + b_2\frac{k^3}{2} \\ 0 & 0 & 0 \\ b_6\frac{k}{2} + b_2\frac{k^3}{2} & 0 & b_2\frac{k^2}{2} \end{bmatrix}.$$

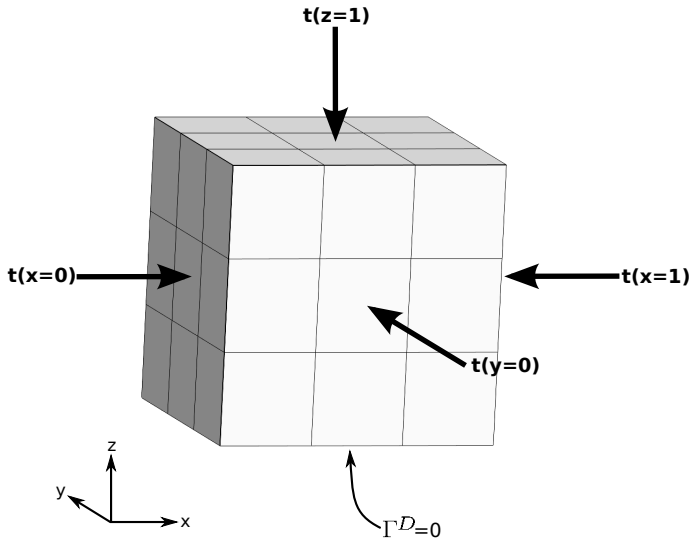

FIGURE 4.5. *Problem setup for simple shear of a cube. A* $1m \times 1m \times 1m$ *cube was sheared in the x direction by applying the tractions calculated in section 4.2.1.1 to the* 5 *free faces, holding the* 6^{th} *face,* $z = 0$ *fixed.*

$C(KPa)$	$b1$	$b2$	$b3$	$b4$	$b5$	$b6$
1.25	18.5	3.67	2.00	8.13	6.06	2.66

TABLE 1

Orthotropic Costa law parameters determined experimentally for a canine heart[27].

4.2.1.1 APPLIED TRACTIONS

Traction, on the boundary, is defined as $\mathbf{t} = \boldsymbol{\sigma} \cdot \mathbf{n}$, where $\mathbf{n}$ is the outward normal on the boundary surface. Noting that the outward normal is with respect to the physical domain (*i.e.* the deformed state), the outward normals on the 5 unfixed surfaces of the cube ($x = 0$, $x = 1$, $y = 0$, $y = 1$, $z = 1$) in the case of simple shear are,

$$\begin{aligned}
&\mathbf{n}(x = 0), \quad [-\tfrac{1}{a},\ 0,\ \tfrac{k}{a}]^T,\\
&\mathbf{n}(x = 1), \quad [\tfrac{1}{a},\ 0,\ -\tfrac{k}{a}]^T,\\
&\mathbf{n}(y = 0), \quad [0,\ -1,\ 0]^T,\\
&\mathbf{n}(y = 1), \quad [0,\ 1,\ 0]^T,\\
&\mathbf{n}(z = 1), \quad [0,\ 0,\ 1]^T,
\end{aligned}$$

where $a = \sqrt{1 + k^2}$. Therefore, calculating $\boldsymbol{\sigma} \cdot \mathbf{n}$ [3], the applied tractions that give the deformation described by $\mathbf{F}$ are,

$$\begin{aligned}
&x = 0, \quad [-db_6\tfrac{k^2}{2},\ 0,\ -db_6\tfrac{k}{2}]^T,\\
&x = 1, \quad [db_6\tfrac{k^2}{2},\ 0,\ db_6\tfrac{k}{2}]^T,\\
&y = 0, \quad [0,\ 0,\ 0]^T,\\
&y = 1, \quad [0,\ 0,\ 0]^T,\\
&z = 1, \quad [d(b_6\tfrac{k}{2} + b_2\tfrac{k^3}{2}),\ 0,\ db_2\tfrac{k^2}{2}]^T,
\end{aligned}$$

where $d = Ce^{b_2\frac{k^4}{4} + b_6\frac{k^2}{2}}$.

4.2.1.2 VERIFICATION OF SIMPLE SHEAR WITH THE COSTA CONSTITUTIVE LAW

The tractions calculated above were applied as surface tractions on a cube to verify the implementation of the Costa constitutive law. The cube consisted of 27 HEX$(3, 3, 1)$ elements and the deformation, k was set at $0.1m$. The Costa law parameters were taken from Costa *et al.*[27] for a canine LV and are given in table 1. The L_2 norm of the displacement error, compared with an analytic evaluation of the cube under simple shear, was 2.63×10^{-14}, *i.e.* within the tolerance parameters for the problem. Figure 4.6 shows the deformed 27 element cube.

[3] Note here $p = 0$, therefore in this case $\boldsymbol{\sigma} \cdot \mathbf{n} = \hat{\boldsymbol{\sigma}} \cdot \mathbf{n}$.

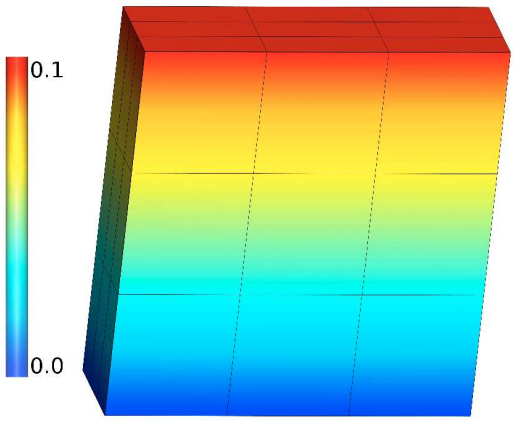

FIGURE 4.6. *Deformed 27 element cube after surface tractions, calculated to produce simple shear, were applied to the 5 free faces. x direction is to the right, z is vertical and y is into the image. Scale is in metres.*

4.2.2 Fitting Costa Constitutive Parameters – Zero Stress Estimation

Cardiac models built from in–vivo images are typically fitted to known points in the cardiac cycle – for example, the geometry presented in section 4.1 was fitted to the end–diastolic configuration. Therefore, at the point of fit there is residual strain within the myocardium which needs to be accounted for by providing an estimate of the zero–stress, or reference state of the myocardium. As the Costa equations become increasingly non–linear with increasing strain, inaccurate estimation of the reference configuration may lead to an inaccurate estimation of the stress/strain material response.

To address this problem, a fitting procedure was developed to scale the Costa parameters to match an empirical pressure–volume relation derived from excised human heart data. From these measurements, Klotz *et al.*[83] determined a simple exponential relationship for estimating the non–linear LV pressure–volume curve. For a given cavity volume, V, LV pressure, P, is given as,

$$P = \alpha V^{\beta}, \tag{4.14}$$

where α and β are determined based on a single measurement of in–vivo LV pressure and volume, P_m and V_m, as well as estimates of the volume at $30mmHg$, V_{30}, and the zero stress volume, V_0. α and β are defined as,

$$\alpha = \frac{30}{V_{30}^{log(P_m/20)/log(V_m/V_{30})}}, \tag{4.15a}$$

$$\beta = \frac{log(P_m/30)}{log(V_m/V_{30})} \tag{4.15b}$$

and V_{30} and V_0 as,

$$V_{30} = V_0 + \frac{\left(\frac{V_m - V_0}{V_{30} - V_0} - V_0\right)}{\left(\frac{P_m}{A_n}\right)^{(1/B_n)}}, \tag{4.16a}$$

$$V_0 = V_m(0.6 - 0.006P_m), \tag{4.16b}$$

where A_n and B_n are constants equal to 27.8 and 2.76 respectively.

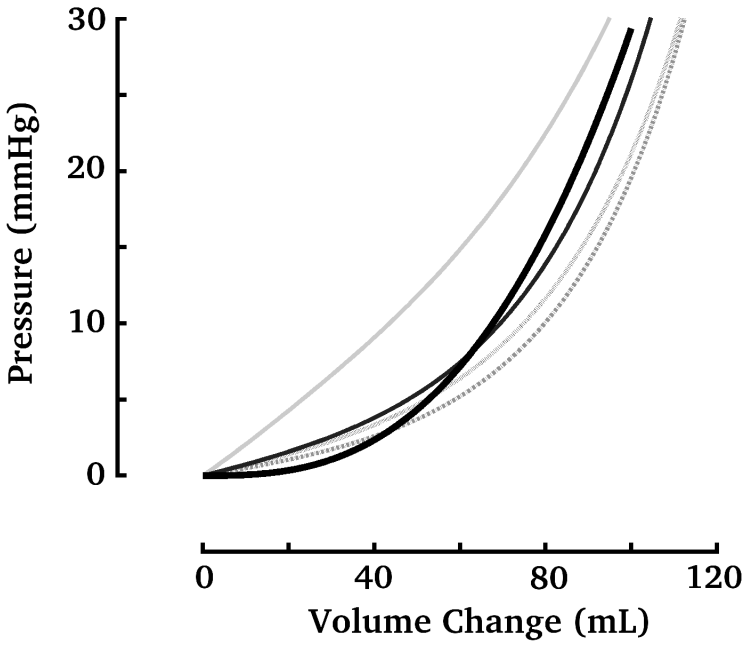

FIGURE 4.7. *Tuning of the passive Costa constitutive parameters. The experimentally derived passive pressure–volume relationship is shown as the thick black line. Convergence of the simulated relationship is shown as iterations, light to dark, where updates of the scalar β are chosen to minimise the cost function $\bar{\Upsilon}$. The constant C was scaled to give the desired end diastolic pressure.*

This relationship was used to fit the pressure–volume response of the geometric model. By adjusting the Costa parameter C to ensure the desired end–diastolic pressure, the parameters b_i and K were scaled by the scalar κ to produce more linear or non–linear responses, as shown in figure 4.7. The initial parameters were selected based on the observed anisotropy in canine and porcine hearts[175].

For a given set of Costa parameters, $(C, \kappa b_i, \kappa K)$, the undeformed reference state of the heart model can be determined using the techniques outlined in Rajagopal *et al.*[162] [4]. The undeformed state was reached when the total LV cavity volume equaled V_0. Scaling C by the ratio P_m/P_c, where P_c was the end–diastolic pressure for the Costa parameter set $(C, \kappa b_i, \kappa K)$, an inflation simulation was conducted, from the predicted undeformed state, giving a passive pressure–volume relationship for $(C, \kappa b_i, \kappa K)$. This relationship was then compared with the estimated relationship from the Klotz model.

[4]In this method the zero stress state is determined by using the update vector from equation 2.61 to update the reference state, $\mathcal{T}_h(\Lambda_s)$, while the deformed state, $\mathcal{T}_h(\Omega_s)$, is kept constant.

$C(Pa)$	$C_2(Pa)$	$b1$	$b2$	$b3$	$b4$	$b5$	$b6$	K	C_Ψ
296.57	296.57	38.99	7.55	4.21	17.15	12.82	5.64	38.99	4000

TABLE 2

Costa law parameters for the normal LV myocardial mesh, fitted from the zero–stress estimation problem. These parameters are used for both the normal and LVAD supported simulations presented in this chapter.

Perturbing the scalar κ, the process was iteratively repeated to minimise a cost function $\bar{\Upsilon}$, where,

$$\bar{\Upsilon}(C, \kappa b_i, \kappa K) = \int_0^{Vm} (P_{sim} - P_{est})^2 dV \tag{4.17}$$

and P_{sim} is the simulated model pressure, and P_{est} the estimated pressure from the Klotz model, at a volume V. As the equation 4.17 is non–linear, an iterative approach was used to minimise the constraint using a non–linear least–squares approach. Figure 4.7 shows the passive pressure inflation of the LV model compared with the estimated Klotz relationship. The final, tuned, Costa parameters are given in table 2. These parameters were used for the LV simulations presented in this chapter. While tuned for the normal LV mesh, the same parameters were used for the LVAD supported mesh, where the zero–stress configuration was solved assuming the same end–diastolic pressure. Visualisation of the zero stress normal LV and LVAD supported LV meshes is shown in figure 4.8.

4.3 Particle Tracking

In order to analyse flow behaviour and estimate residence times of fluid within the ventricular chamber, a particle tracking algorithm was implemented. This section details the algorithm, while the results of a cannula length study, where the algorithm was used to determine the residence times of blood within the LV chamber, are given in section 4.6.

A point $p \in \Omega_f$ has, at time t, an associated velocity, $\mathbf{v}(\mathbf{x}_p, t)$, where $\mathbf{x}_p$ are the Eulerian coordinates and $\boldsymbol{\eta}_p$ the Lagrangian coordinates of p. The position of $p(t)$ can be defined using the Lagrangian mapping,

$$\mathbf{x}_p(t) = \mathcal{P}^{\Omega_f}_{\Lambda_p}(\boldsymbol{\eta}_p, t),$$

Λ_p is the Lagrangian fluid reference domain (in contrast to the ALE reference domain Λ_f). Considering a discrete system at time t^m, the discrete mapping is defined as,

$$\mathcal{P}^{\Omega_f}_{\Lambda_p}(\boldsymbol{\eta}_p, t^m) = \triangle^m_t \mathbf{v}(\boldsymbol{\eta}_p, t^m) + \mathcal{P}^{\Omega_f}_{\Lambda_p}(\boldsymbol{\eta}_p, t^{m-1}), \tag{4.18}$$

where $\mathbf{v}(\boldsymbol{\eta}, t^m)$ is the material velocity of p and $\mathcal{P}^{\Omega_f}_{\Lambda_p}(\boldsymbol{\eta}_p, 0) = \boldsymbol{\eta}_p$.

p is seeded in an element e_i, located in the mesh $\mathcal{T}_h(\Lambda_f)$. With respect to the reference element, $\hat{e}$, p has local coordinates $\phi(t)$. Interpolating the velocity field at $t = t^0$, where t^0 is the time p is seeded in the domain, enables, using equation 4.18, the position of p to be updated using a piecewise constant approximation of $\mathbf{v}(\boldsymbol{\eta}, t^m)$.

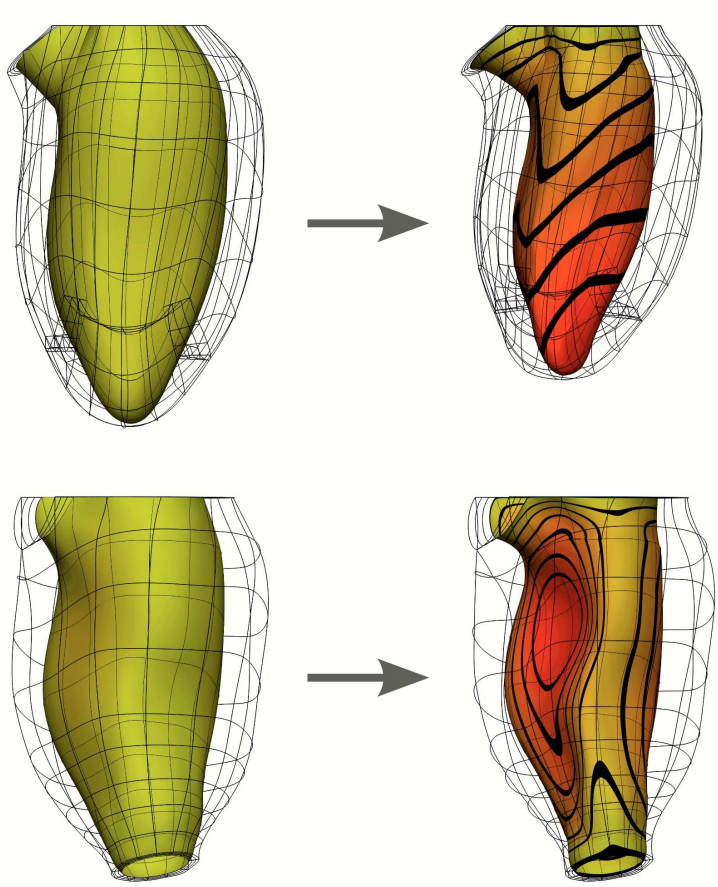

FIGURE 4.8. *The zero–stress reference states of the normal LV, top row, and LVAD supported LV, bottom row, meshes. Deformation, yellow to red, ranges from* 0 *to* $0.018m$. *End diastolic LV volume was* $165ml$ *and the normal LV model was tuned to an end–diastolic pressure of* $9.75mmHg$ *giving a zero stress volume,* $V_0 = 89.3ml$. *The normal Costa parameters were also used for the LVAD mesh and the zero–stress state was determined using the same end–diastolic pressure.*

As p moves, there is no guarantee in subsequent time steps that p will be located within e_i. As a result, a search algorithm was developed to minimise the cost of finding $p \in \mathcal{T}_h(\Lambda_f)$. At time step t^m, the algorithm performs the following steps,

1. Check whether $p \in e_i$, if yes exit.
2. Check whether $p \in e_{N(1)}, \cdots, e_{N_i(n)}$, where $e_{N_i(:)}$ is a precomputed list of all elements that share a node with e_i. If $p \in e_{N(j)}$ exit.
3. If p has not been found in either steps 1 or 2, the time interval, $\triangle_t^m$, is reduced and the steps are repeated. This process is repeated until the node is either found, or if $\triangle_t^m < tol$ in which case p is either assumed to have left the mesh (if $e_i \in \Gamma$), or a global search is performed. tol is a user defined minimum time step size.

Once p has been found $\mathbf{v}(\boldsymbol{\eta}, t^m)$ can be interpolated based on the velocity solution at t^m. Given that there is no guarantee of congruence between the time step size for the fluid solution and that of the particle tracking algorithm, the fluid solution is interpolated using a piecewise linear approximation in time.

Analysing flow fields and evaluating residence times requires multiple particles to be seeded. The algorithm was developed to enable seeding on boundaries, with specified elements or in user defined regions.

4.4 Diastole in Normal and LVAD Supported Left Ventricles

The normal and LVAD LV models introduced in sections 4.1 and 4.2 were used to perform simulations of diastole in normal and LVAD supported LVs. With the exception of the LVAD cannula, the same boundary conditions were applied in both cases. The results of the simulations were used to compare the hemodynamic and myocardial behaviour of the LV during diastole both with and without LVAD support.

For this study, the reference myocardial meshes from section 4.2.2 were used. The element types for the solid and fluid meshes were HEX(3,3,2,3) and TET(1,2,1), respectively. For the supported LV mesh, the LVAD was prescribed as a Dirichlet boundary. The fluid meshes were constructed so that their characteristic length was the same, $2.6mm$ in each case. The fluid meshes consisted of $\approx 4.3 \times 10^4$ tetrahedral elements and $\approx 2 \times 10^5$ degrees of freedom for the LVAD fluid mesh and $\approx 3.8 \times 10^4$ tetrahedral elements and $\approx 1.7 \times 10^5$ degrees of freedom for the normal fluid mesh. For the solid problems, degrees of freedom were $\approx 3.3 \times 10^4$ for the LVAD myocardial mesh and $\approx 5.2 \times 10^4$ for the normal mesh.

Simulation meshes and boundary condition definitions are provided in figure 4.9. Simulations were initiated from the estimated zero stress configuration with an initial cavity pressure of $0Pa$. Mitral valve inflow was prescribed as an ellipse with a time varying minor radius on the mitral boundary, Γ_M, the velocity profile and valve radii are given in figure 4.10, while the rates of flow and volume change are shown in figure 4.11. LVAD cannula outflow was prescribed as a circle of radius $7.5mm$ on the outflow boundary, Γ_O. The flow profiles on both Γ_M and Γ_O was defined as Poiseuille. Simulations were run for a total of 400 time steps of $0.0012s$ to give a diastolic period of $0.5s$. The results of the simulations are presented in figures 4.12 to 4.15.

4.4.1 Comparison of Results

A comparison of the flow features and myocardial displacements is presented, at various time points, in figure 4.12. Fluid cavity pressures are compared in figures 4.13 and 4.14 and finally the energy transfers in the two problems are compared in figure 4.15.

4.4.1.1 Flow and Displacement Features in Diastole

In the normal LV, the predominant observed flow feature was the formation of a large ring vortex during early diastole. This vortex partially dissipated during diastasis, before enlarging to fill most of the LV cavity in late diastole. Additionally, a small vortex formed at the apex during late diastole. The presence of the LVAD substantially altered these features. In the LVAD case, the vortex still formed, however its enlargement and

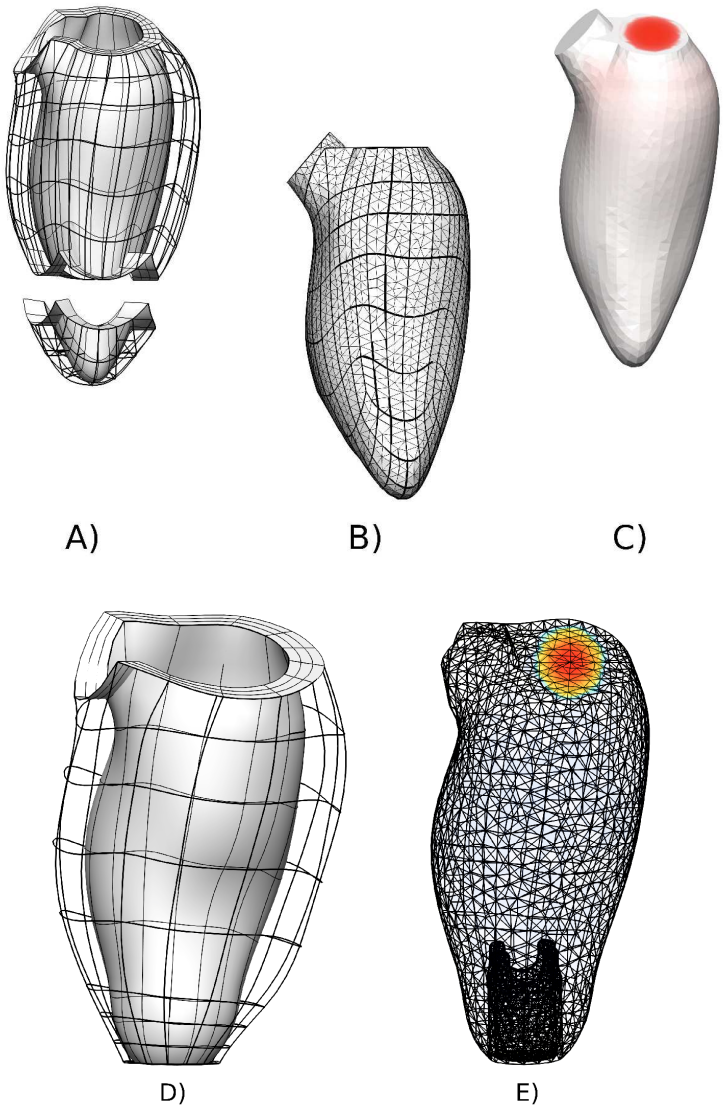

FIGURE 4.9. *Computational meshes for the normal and supported LV problems. (A) shows the normal LV myocardial mesh, consisting of an apical region, 1 element thick, coupled into a the mid–wall region, 3 elements thick. The epicardial boundary is free,* $\Gamma_s^N = 0$*, while the basal boundary (top boundary in (A)) is fixed. The endocardial boundary is the interface,* Γ_s^C*, which is visible as the solid black lines in (B). Also visible in (B) are the fine black lines which represent* Γ_f^C*. The fluid mesh for the normal LV problem is shown in (C), where the mitral inflow region is coloured red. All other boundaries, including the Aorta, have a no slip boundary condition applied. The same conditions from (A) apply to the LVAD myocardial mesh (D), however, in addition the apical boundary (bottom boundary in (D)) is fixed. The fluid mesh (E) has the same boundary conditions as (C) on the basal and interface boundaries. The LVAD cannula is attached as the apex, either as an FD or Dirichlet boundary and the cannula outflow is prescribed on the boundary at the base of the cannula.*

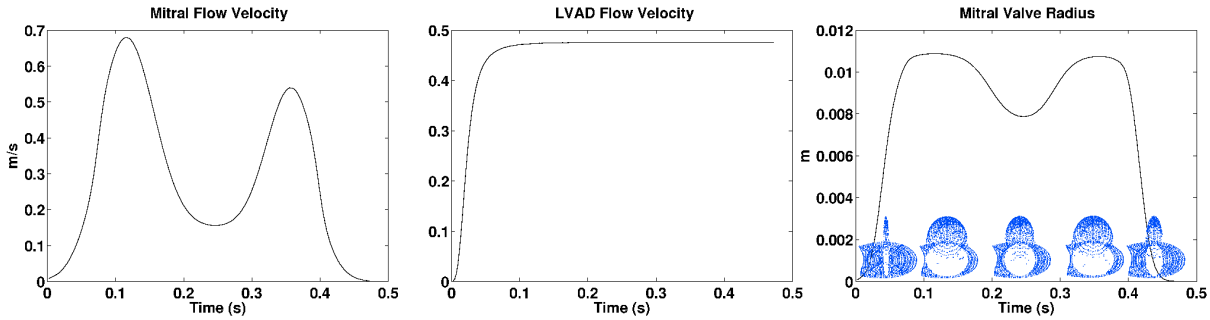

FIGURE 4.10. *Left and centre, peak flow velocity on the mitral inflow and cannula outflow boundaries respectively. Inflow velocities were taken from measurements in Kilner* et al.[76] *for the heart at rest, while cannula outflow velocity was chosen to give a stroke volume of* $75mL \cdot s^{-1}$. *Right, the variation in mitral valve radius through the simulation. The blue sub–figures show the radius changing on the valve plane and the flow profile.*

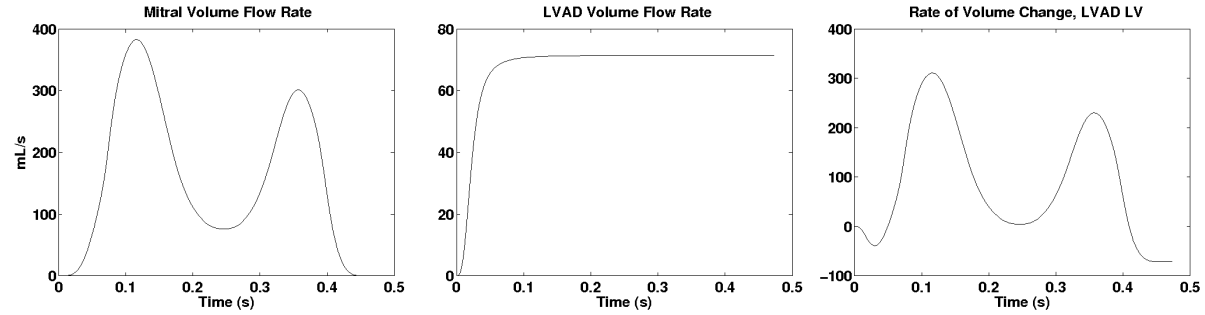

FIGURE 4.11. *Left and centre, flow rates across the mitral inflow and cannula outflow boundaries respectively. Right, the rate of volume change for the supported LV problem. Note that the rate of volume change for the normal LV problem is the same as the mitral inflow.*

symmetry was continually broken down due to disturbance from the cannula flow. During periods of peak flow, see $0.13s$ and $0.38s$ in figure 4.12, suction from the cannula led to a uniaxial flow feature to form through the cavity. This flow feature broke down rapidly when inflow velocity declined. Another important feature observed in the supported LV diastolic simulation was the formation of helical flow features at the apex around the cannula base. These can be clearly seen at $0.25s$, $0.31s$ and $0.38s$ in figure 4.12.

Due to the reduced volume change, myocardial displacement was substantially less in the LVAD LV problem than in the normal case. Despite this difference, the behaviour of fluid ventricular pressure was relatively similar between the two problems. Accompanying each inflow peak were pressure waves (see figures 4.13 and 4.14) which caused local displacements to increase. At $0.13s$, peak displacement was observed at the basal region in the two problems. As inflow declined, peak displacement shifted to the apical region, see $0.19s$. During diastasis, the energy that accompanied the peak velocity in early diastole dissipated, which was reflected in a more even distribution of solid displacement, see $0.25s$. This process repeated itself as inflow peaked again during late diastole. This energy transfer is discussed further in section 4.4.1.2 and can be seen in the oscillations in potential energy observed in figure 4.15.

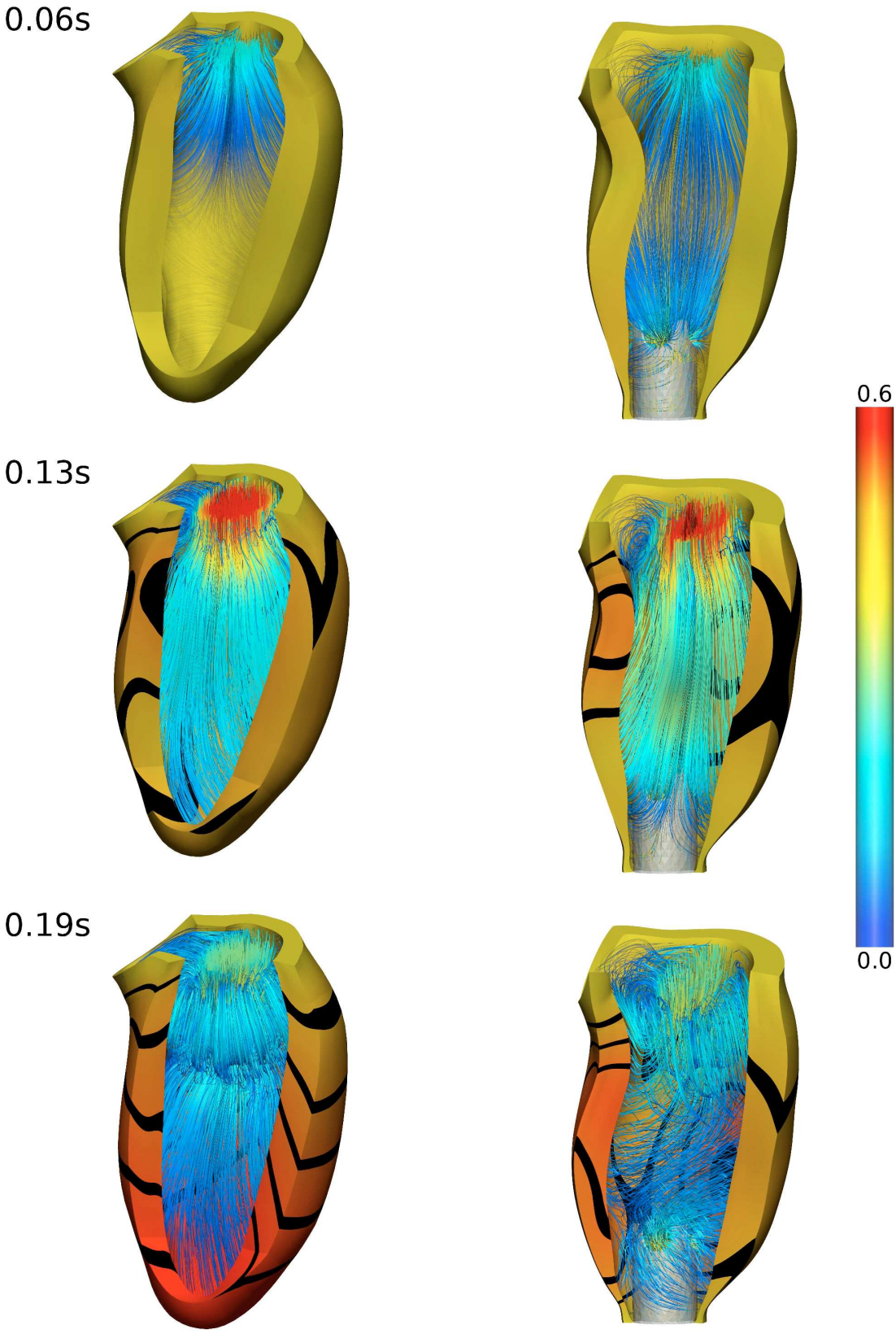
0.06s
0.13s
0.19s
0.6
0.0

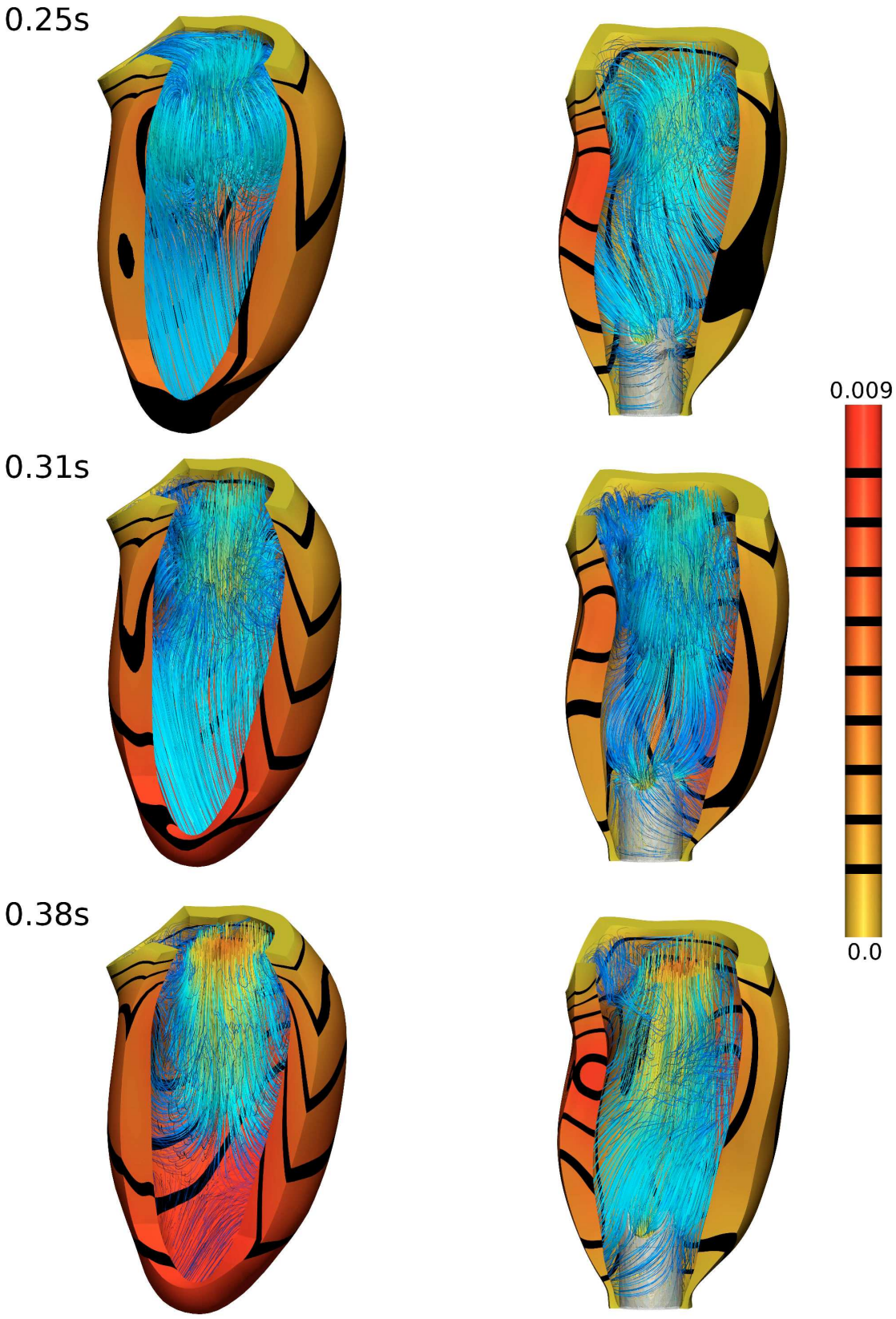
0.25s
0.31s
0.38s
0.009
0.0

FIGURE 4.12. *Comparison of simulated normal and supported LV flow features and myocardial displacements during diastole. Results are compared at various time points selected to represent early diastole – 0.06s, 0.13s and 0.19s – diastasis – 0.25s – and late diastole – 0.31s, 0.38s and 0.44s. Fluid velocities vary between* 0 *and* $0.6ms^{-1}$*, while solid displacements range from* 0 *to* $0.009m$*.*

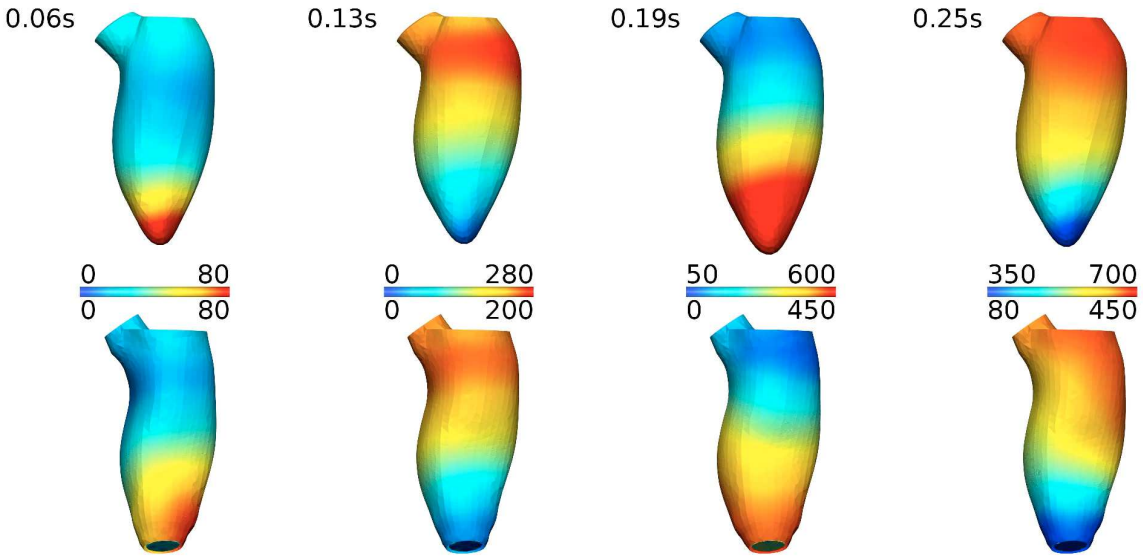

FIGURE 4.13. *Fluid pressure (Pascals) during early diastole (*0.06*s to* 0.19*s) and diastasis (*0.25*s). Normal LV results are shown on the top row, LVAD results on the bottom. Note the pressure wave that forms at peak inflow during early diastole at* 0.13*s and the significantly lower fluid pressures in the LVAD problem.*

4.4.1.2 Pressure and Energy Transfer during Diastole

The predominant fluid pressure feature observed during the simulations of diastole, in both the supported and normal LV cases, was the formation pressure waves accompanying peaks in inflow velocity. Figures 4.13 and 4.14 show these waves forming and traveling through the ventricular cavity. While peak pressures are significantly lower in the supported case, since mitral inflow is the same in each problem and the geometries are roughly comparable, the behaviour of the pressure waves is the same as in the normal LV case. Due to the rigid boundary conditions applied to the basal and cannula boundaries, reflection of these waves may be amplified, however, the presence of pressure waves is consistent with *in vivo* observations[28]. Additionally, it is interesting to note how the range in ventricular pressure peaks when the wave reaches the apex. This peak leads to bulging at the apex, seen at $0.44s$ in figure 4.14.

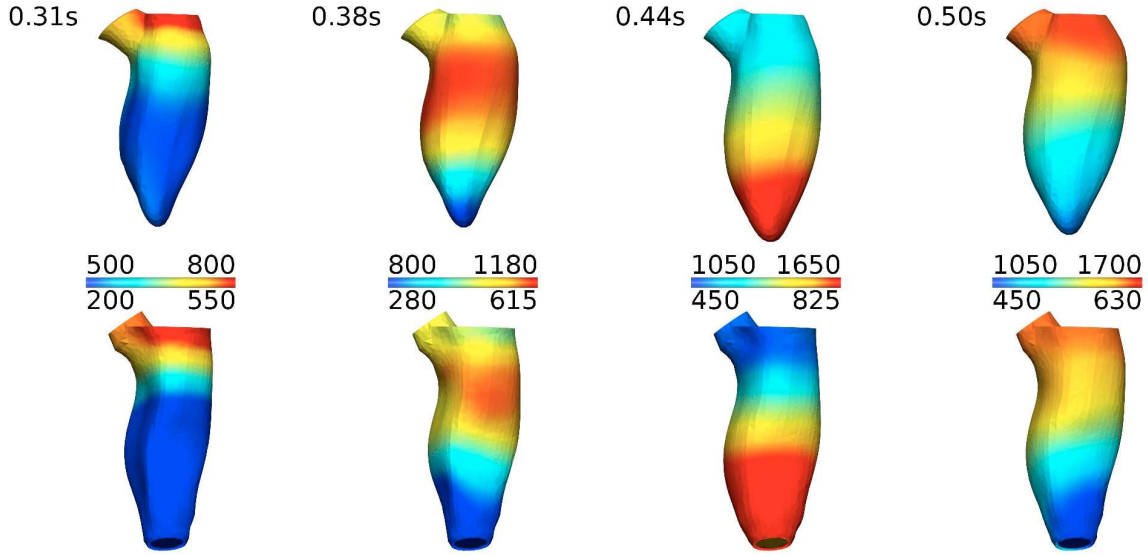

Figure 4.14. *Fluid pressure (Pascals) during late diastole. Normal LV results are shown on the top row, LVAD results on the bottom. Note the formation of a new pressure wave at* $0.31s$ *accompanying the increase in mitral inflow with late diastole.*

Figure 4.15 shows the rates of change in myocardial potential energy and fluid kinetic energy and viscous loss (equations for these metrics are provided in appendix B). For both problems, the rate of viscous energy dissipation is substantially lower than the rates of change in kinetic and potential energy due to the relatively low viscosity of blood. The higher velocities induced by the cannula flow in the LVAD simulation leads to greater peaks in kinetic energy and consistently higher rates of viscous energy dissipation. However, the lower volume change during diastole results in lower potential energy storage by the myocardium. Overall, the volume unloading sees a substantial reduction in the total energy added to the system, $0.015J$ compared with $0.037J$ in the normal LV case. The reason for this discrepancy was the continuous output of energy via the LVAD cannula in the LVAD case.

The pressure waves during diastole lead to energy transfer between the fluid and solid. In the normal LV case, the rate of total energy change is relatively smooth, peaking in early and late diastole. In contrast, both kinetic and potential energy oscillate relatively rapidly and counter–cyclically. These oscillations reflect transfer of

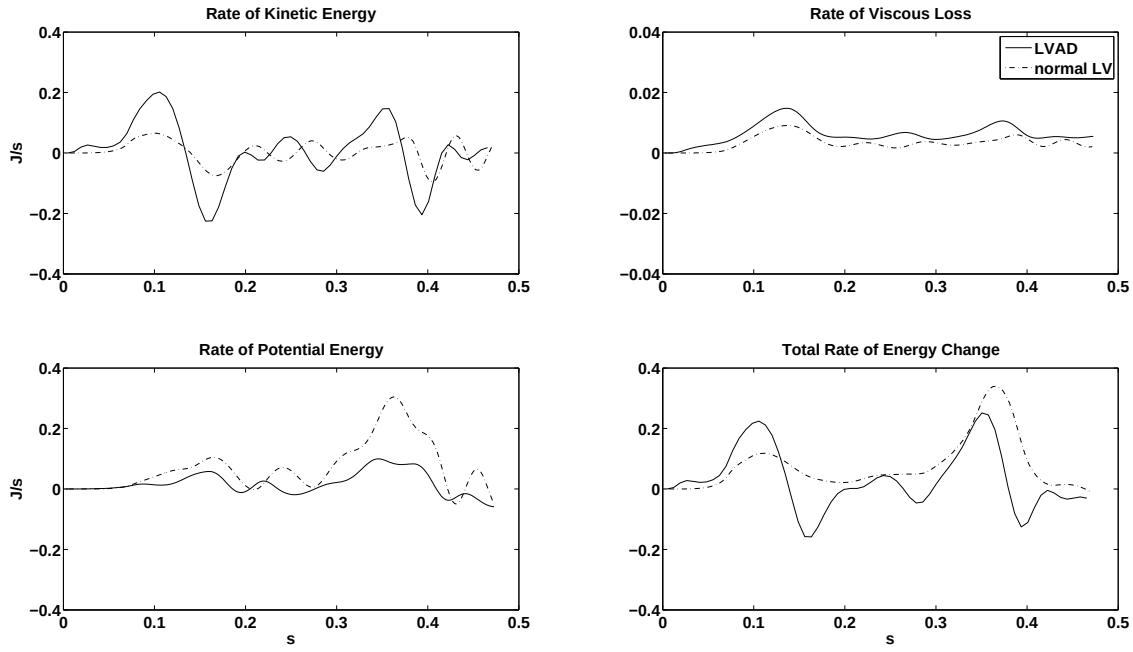

FIGURE 4.15. *Rates of energy change calculated from the simulations of normal and LVAD supported LVs in diastole. All units are in J/s. Total energy change, equivalent to the energy added to the system, is the summation of myocardial potential energy and fluid kinetic energy and viscous loss. Note the greater magnitudes in kinetic energy and viscous loss in the LVAD case, while conversely potentially energy is substantially lower. Overall energy change is lower in the LVAD supported case.*

energy between fluid momentum and solid stress. The presence of the LVAD disrupts this transfer and the resulting total energy change is not as smooth. This difference is due to the cannula outflow reducing solid displacement, and as a result reducing potential energy, thus inhibiting the smooth transfer of energy between the fluid and solid domains.

4.5 Fictitious Domain prescribed LVAD Cannulas

The simulations presented in the previous section provide an interesting insight into the differences in diastolic ventricular behaviour in normal and LVAD supported hearts. However, by applying the LVAD cannula as a Dirichlet boundary, the LVAD model is unable to capture the full range of cardiac motion and is therefore unable to simulate a full cardiac cycle. This is due to the potential collapse of the computational mesh as the LVAD cannula comes into close proximity with the myocardial wall. A FD method was implemented to deal with the interaction between the cannula and the myocardial wall. The convergence results presented in chapter 3 provide confidence in the numerical scheme implemented. However, they do not demonstrate how capable a FD is at resolving the flow features and material deformations observed in an LVAD supported LV at physiological Reynold's numbers. Additionally, to be applicable for investigations into the effect of LVAD implantation on cardiac function, it needs to be shown that the FD method implemented can replicate suction. To test these questions, two simulations were performed. The first (section 4.5.1) comparing LV simulation

results from simulations where the cannula was prescribed as either a FD or a Dirichlet boundary; and the second (section 4.5.2) testing the ability of the FD scheme to capture contact between the myocardium and the cannula.

4.5.1 Comparison of LV Simulations using Fictitious Domain and Dirichlet Prescribed LVAD Cannulas

To study the effect of prescribing the LVAD cannula as a FD rather than a Dirichlet boundary, a simulation of passive LV behaviour was developed. The problem was defined such that the LVAD cannula did not come into close contact with the myocardium, removing the possibility of numerical issues in the Dirichlet problem. The simulation inflow and outflow profiles are provided in figure 4.16, while the boundary conditions are the same as those used for the LVAD supported diastolic simulations in the previous section (figure 4.9). Three simulations were performed, one where the cannula was prescribed as a Dirichlet boundary on the fluid mesh and two where the cannula was prescribed as a FD within the fluid. The two FD simulations compared the effect of different element types – Crouzeix–Raviart with discontinuous pressure and Taylor–Hood with continuous pressure.

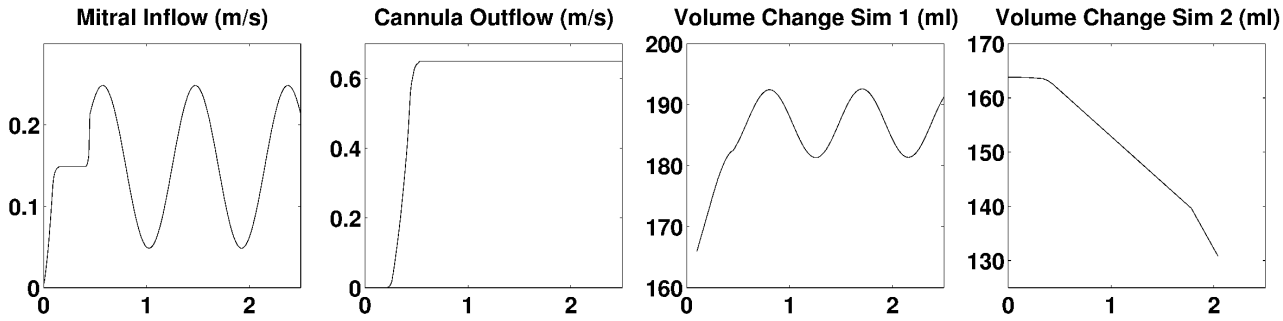

Figure 4.16. *In the simulation to compare the FD and Dirichlet prescribed cannula models, the mitral valve inflow velocity was gradually increased to a mean value of* $0.15ms^{-1}$*. It was then held constant while the cannula outflow velocity was increased. To simulate repeated diastolic inflow pulses, the inflow velocity was then oscillated in a sinusoidal pattern with a period of* $1s$ *and a magnitude of* $0.2ms^{-1}$*. The resulting volume change of the ventricular cavity is shown (Sim 1). To simulate suction, the mitral valve was considered to be closed and only the cannula outflow was prescribed. The resulting volume change is shown (Sim 2). Time is displayed on the x axis.*

The same myocardial mesh was used in all problems, consisting of 324 HEX(3,3,1,1) elements and $\approx 3.1 \times 10^4$ degrees of freedom. Different fluid meshes were constructed for each case. The mesh for the Dirichlet prescribed cannula simulation consisted of $\approx 5.7 \times 10^4$ linear tetrahedrals and 2.6×10^5 degrees of freedom. For the meshes constructed to incorporate the FD cannula, the results comparing the accuracy of FD and Dirichlet techniques (section 3.1) were used to select the appropriate fluid mesh size for comparison with the Dirichlet results. The resulting fluid meshes consisted of $\approx 1.1 \times 10^5$ TET(1,2,1) elements and $\approx 5.0 \times 10^5$ degrees of freedom, for the continuous pressure FD problem; and $\approx 4.1 \times 10^4$ TET(1,2CR,1DC) elements with $\approx 7.2 \times 10^5$ degrees of freedom for the discontinuous pressure case. The FD mesh was constructed so that it had a comparable CL to the continuous pressure fluid mesh. For this problem it consisted of 1848 TRI(1,0) elements. The simulations were run for $2.5s$ with time steps of $0.1s$. To ensure that the endocardial wall did not come into close proximity

with the cannula, the reference myocardial mesh was taken as the fitted end diastolic mesh. Additionally, inflow via the mitral valve was increased prior to the commencement of outflow from the LVAD cannula.

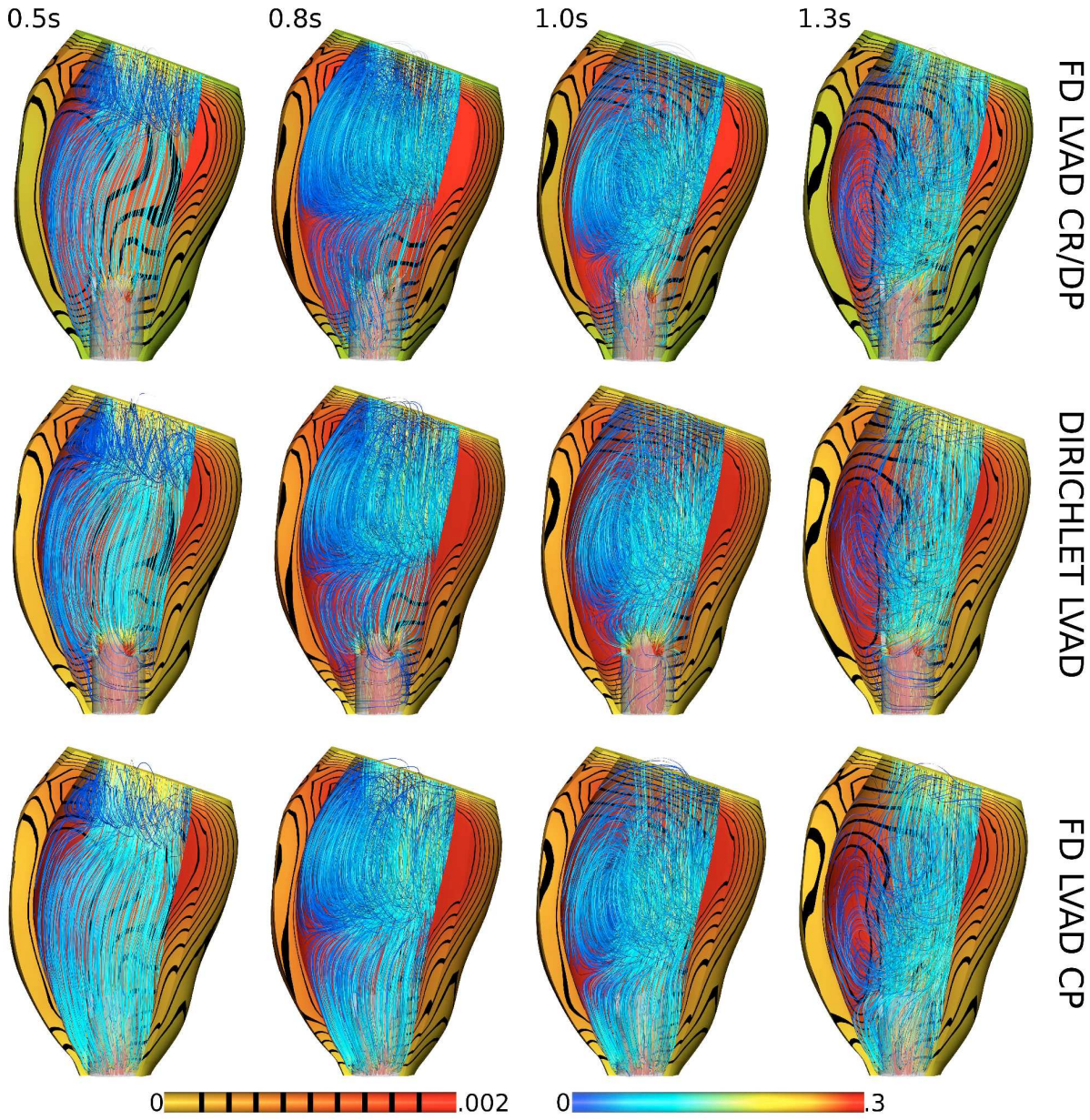

FIGURE 4.17. *Streamlines and myocardial displacements for the three simulations. Top row, the LVAD prescribed as a FD with discontinuous fluid pressures. Middle row, the LVAD prescribed as a Dirichlet boundary. Bottom row, the LVAD prescribed as a FD with continuous fluid pressures. Fluid velocities are in* ms^{-1} *and solid displacements are in* m*. The selected time points compared are* $0.5s$*, once the cannula velocity has ramped up and mitral inflow is close to peak;* $0.8s$*, where mitral inflow is declining;* $1.0s$*, minimum mitral inflow; and* $1.3s$*, where mitral inflow is increasing.*

The flow streamlines and myocardial displacements, at selected time points, from the three simulations are presented in figure 4.17. A comparison of pressures at the same time points is given in figure 4.18, while the the rates of energy change are provided in figure 4.19.

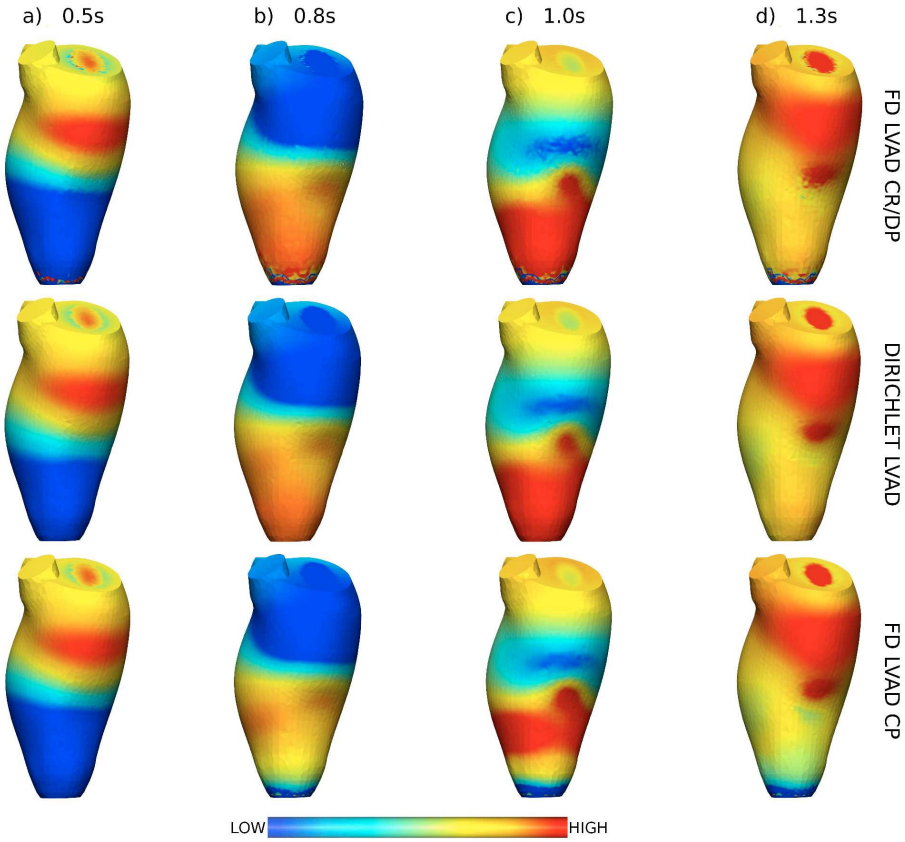

FIGURE 4.18. *Fluid pressures for the three simulations. Top row, the LVAD prescribed as a FD with discontinuous fluid pressures. Middle row, the LVAD prescribed as a Dirichlet boundary. Bottom row, the LVAD prescribed as a FD with continuous fluid pressures. Visibly lower apical fluid pressures are observed in the continuous pressure case, while pressure discontinuities lead to the spurious pressures observed in the discontinuous pressure case. Due to volume change, the pressure range varies between each time point, however, within each time point the pressure scale is the same for the three simulations. Pressure waves are observed moving through the ventricular cavity in conjunction with peaks in mitral inflow velocity.*

In all three simulations the main vortex formation is observed. Additionally, the discontinuous pressure FD case captures the helical flows around the cannula base observed in the Dirichlet cannula results. However, when continuous pressures are used in conjunction with the FD cannula, substantial leakage through the cannula wall is observed, as the pressure field is unable to capture the pressure discontinuity between the interior and exterior of the cannula. As a result, in this case the flow features observed at the cannula base in the other two problems are not observed. This issue with the pressure discontinuity is apparent in figure 4.18, where apical pressures in the continuous pressure FD case are substantially lower. This leakage also manifests itself in the rate of viscous energy dissipation, figure 4.19, which is substantially higher in the continuous pressure case. Spurious pressures are observed at the apex in the discontinuous pressure case, however, this is localised to elements intersecting the FD.

Overall, these results show that simulations using a FD cannula and discontinuous pressures are capable of replicating the flow features, pressures and energies observed when the cannula is prescribed as a Dirichlet boundary. With the exception of viscous loss, all three simulations have similar myocardial displacements and rates of energy transfer. The results provide confidence in the capability of the FD method to simulate LV

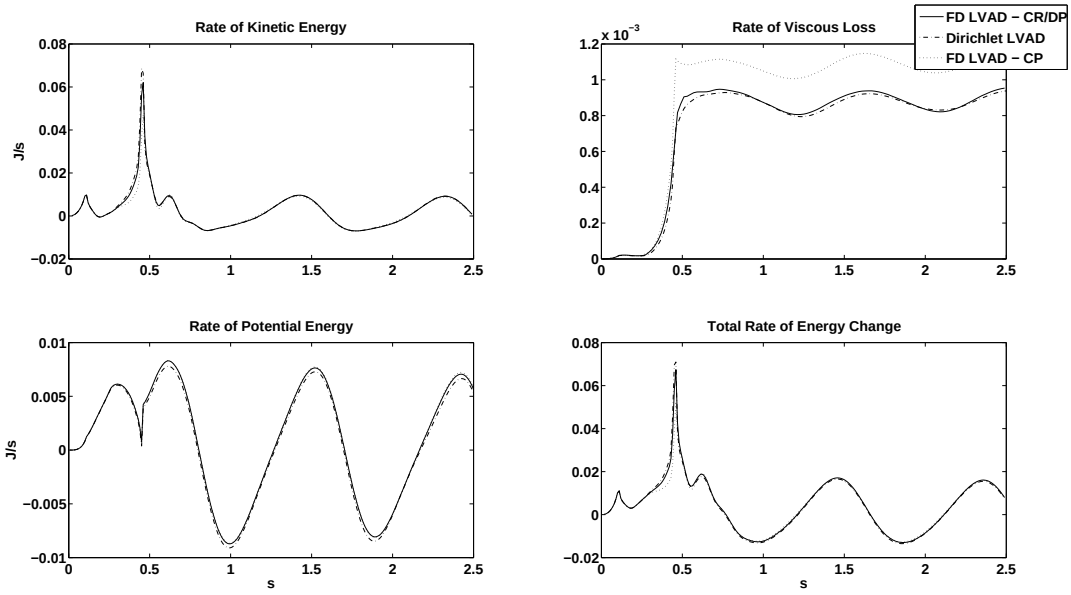

FIGURE 4.19. *Rates of energy change for the three simulations. All units are in J/s. The spikes in the rates of kinetic, potential and total energy around $0.5s$ occur in response to the ramp up in LVAD cannula outflow between $0.25s$ and $0.5s$. Note the substantial discrepancy in viscous energy dissipation in the continuous pressure/FD cannula case.*

function under LVAD support.

4.5.2 Simulation of Contact between the Myocardium and the LVAD Cannula

A simulation bringing an LVAD supported ventricle into contact was performed to demonstrate the effectiveness of using a FD cannula for replicating contact scenarios inside the ventricular chamber. The same myocardial mesh, as used to compare of FD and Dirichlet prescribed cannulas, was applied, however, for computational efficiency, a less refined fluid mesh was constructed, consisting of $\approx 2.9 \times 10^4$ TET(1,2CR,1DC) elements and 5.2×10^5 degrees of freedom. The FD cannula mesh was created such that it had a comparable CL to the fluid mesh and consisted of 640 TRI(1,0) elements. For this simulation, the mitral valve was considered to be closed (*i.e.* zero velocity on Γ_M) and the cannula outflow and simulation volume change are given in figure 4.16. The simulation was run for 200 time steps of $0.04s$. A smaller time step than used in the previous LVAD simulations was chosen to ensure contact between the endocardium and the cannula occurred gradually.

Figure 4.20 shows the fluid flow profile and material deformation as the ventricle is brought into contact. The streamlines show unidirectional flow towards the LVAD cannula. Suction occurred most strongly on the section of the endocardium that was initially closest to the cannula mouth. In the absence of contraction, the myocardial response was passive which, due to the non–linear nature of the constitutive law, resulted in an exponential growth in strain energy during the simulation. This, combined with large element distortion

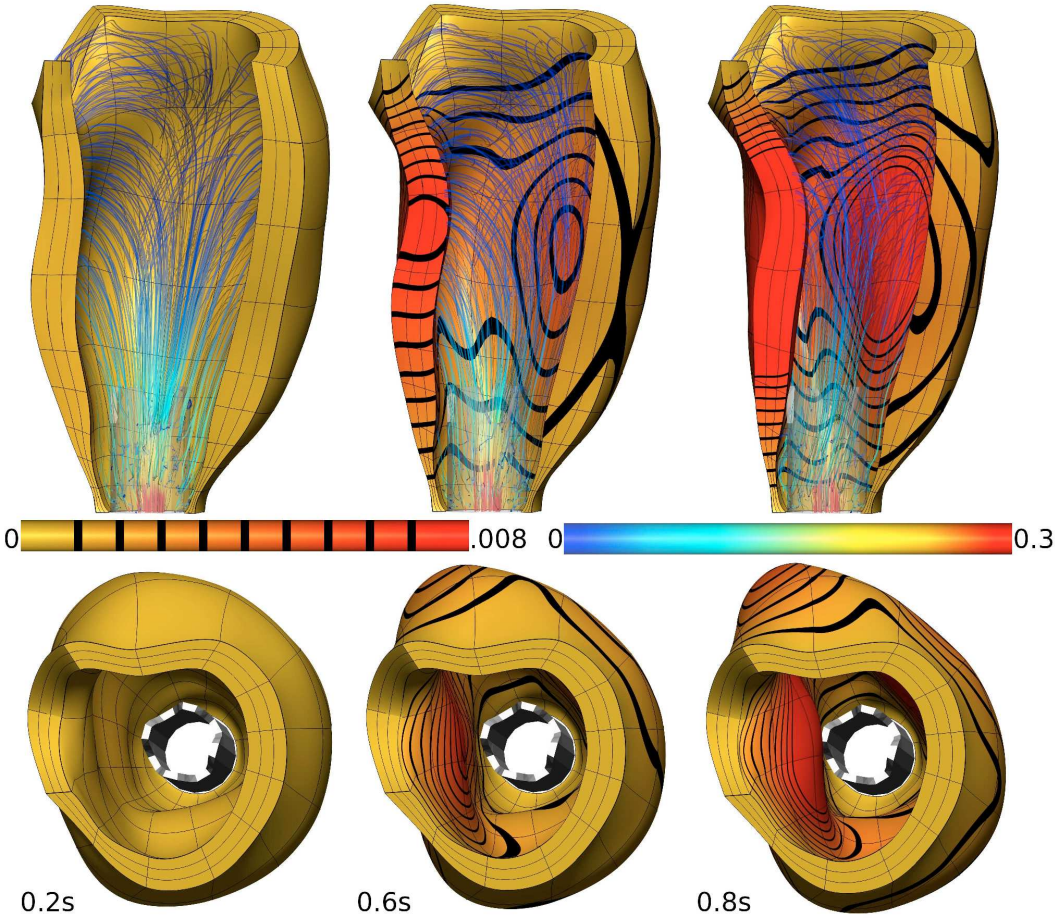

FIGURE 4.20. *Material displacement and fluid streamlines as the ventricle is brought into suction under LVAD support. Results show the establishment of cannula outflow, 0.2s, the drawing in of the myocardial wall, 0.6s, and the establishment of contact, 0.8s. Note that the section of the myocardium in close proximity to the cannula is brought into suction first.*

as material deformation increased, prevented greater reduction in ventricular volume. The results show that using the FD method to apply the cannula boundary enables simulation of the complex contact situations that occur in LVAD supported ventricles.

4.6 Cannula Length Study

A study was undertaken to examine the effect of LVAD cannula length on residence times in a passively filled LV. Residence times were determined using the particle tracking algorithm outlined in the section 4.3. Of interest was the effect of cannula length on the pooling of blood at the LV apex.

The simulation protocol was the same as that outlined in figure 4.9. In this study, the reference myocardial mesh was taken as the fitted end diastolic mesh to prevent interactions between the cannula and the myocardium. Different fluid meshes were constructed depending on cannula length – prescribed as a Dirichlet boundary for this problem. The element types used were HEX(3,3,1,1) for the solid and TET(1,2,1) for the fluid. Problem

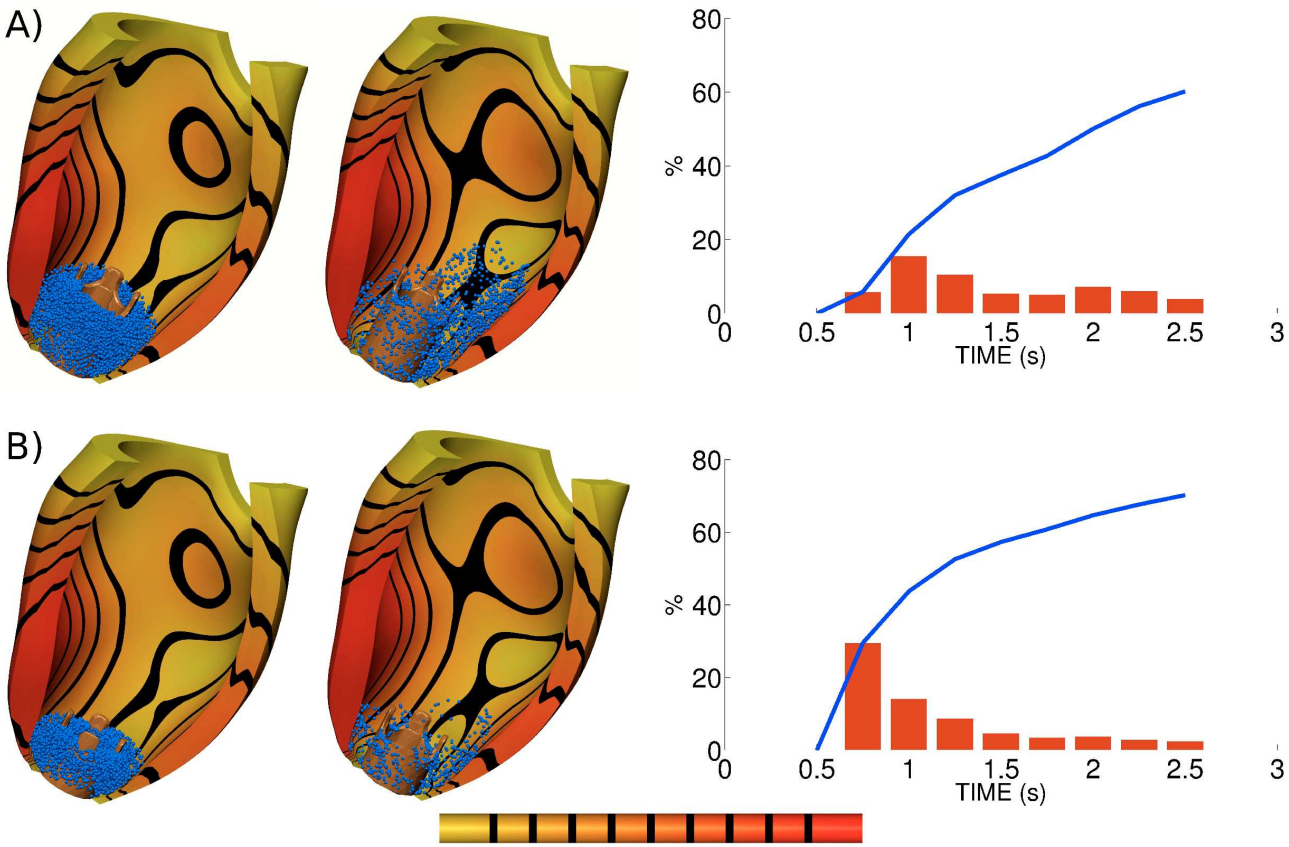

FIGURE 4.21. *Simulation results for the cannula length study, A) the full length cannula, B) the half length cannula. Left, in both A) and B), are the seeded particles at* $t = 0.5s$*, while the central figures show the distribution of particles after* $2.5s$*. The plots show the cumulative percentage of particles that have exited the LV via the cannula (blue line) and the percentage of particles leaving the LV over time intervals of* $0.25s$ *(red bars). The scale, giving the magnitude of myocardial deformation, is* 0.0 *to* $0.0038mm$*, yellow to red.*

degrees of freedom were $\approx 2.7 \times 10^4$ for the solid meshes and $\approx 2.2 \times 10^5$ for the fluid. Note that the fluid meshes were constructed to have roughly the same number of degrees of freedom for each cannula length. Two cannula lengths were tested, a 'full' length cannula, $29.4mm$, and a 'half' length cannula, $15.2mm$.

Due to the passive myocardial response, a sinusoidal Mitral valve flow profile was prescribed, shown in figure 4.16, sim 1. Cannula outflow, also shown in figure 4.16, was ramped up to $0.65ms^{-1}$ between $t = 0.2s$ and $t = 0.5s$ and the simulation was run for 250 time steps of 0.1s. Poiseuille flow profiles were proscribed for each flow.

To analyse the recirculation of blood at the LV apex under LVAD support, particles were seeded at the apex beneath the cannula mouth. Particles were seeded at $0.5s$, *i.e.* after the cannula outflow velocity had reached maximum. Roughly 6000 particles were seeded in the half cannula problem, while approximately 11000 were seeded in the full cannula case. This discrepancy was due to the greater volume available for seeding in the full cannula geometry.

The particle seeding, distribution after $2.5s$ and the rate of efflux of particles from the LV are shown in figure

4.21. Of note is the greater rate of particle efflux in the half cannula geometry. This indicates that the shorter cannula is better able to draw blood away from the apex, preventing pooling. Interestingly, the vortical formations around the cannula base, seen in figures 4.12 and 4.17, play a significant role in preventing pooling of blood in the full cannula case. This is evidenced by the equivalence in the percentage of particles removed from the LV after $2.5s$. However, this effect is demonstrably slower as can be seen from the slope of the cumulative efflux curves in the two problems.

4.7 Summary – Passive Coupled LV models

The methods and results presented in this chapter form the foundation of the LV simulations presented in the remainder of this thesis. The results comparing LV function in problems where the cannula is prescribed as either a Dirichlet boundary or a FD, provide confidence in capability of the numerical scheme, introduced in previous chapters, to simulate LV function. Additionally, the simulation drawing the myocardium into contact with the cannula shows that the scheme is capable of capturing the full range of cardiac motion.

Due to the large number of degrees of freedom and complex mesh structure, LV simulations are computationally complex to perform, therefore convergence studies on the LV model are impractical with current computational capabilities. However, considering the results from chapter 3, the good agreement between the FD and Dirichlet cannula problems indicate that the models are capturing the major flow features. Additionally, the less refined fluid mesh used in section 4.5.1 solved significantly faster ($\approx 3\times$) than the discontinuous pressure/FD cannula mesh used in section 4.5.2, while still resolving the high Reynold's number flow (≈ 1000) through the LVAD cannula.

The remainder of this thesis focuses on extending the LVAD supported LV model developed in this chapter to the full cardiac cycle (chapter 5) before using the fitting and parameter tuning methods to extend the model to a patient geometry (chapter 6).

5 Simulating the Cardiac Cycle under LVAD Support

The LV model introduced in the previous chapter provides a passive representation of cardiac behaviour. To facilitate simulations of the full cardiac cycle the model must incorporate myocardial contraction, as well as a representation of the systemic circulatory systems to provide boundary conditions that feedback to model behaviour. This chapter extends the LVAD supported LV model to incorporate the full cardiac cycle, introducing a myocardial contraction model (section 5.1) and lumped parameter Windkessel model (section 5.2), which are coupled to the LV model. A Simulation of supported LV behaviour, through multiple cardiac beats, is then presented in section 5.3.

5.1 Myocardial Contraction Model

Many different contraction models exist in the literature, ranging from complex, biophysically based models[160, 126, 176, 202], through to simpler models designed to capture basic gross metrics such as length dependency and rate of tension development[128, 74]. For the simulations presented in this chapter, the contraction model applied by Nordsletten *et al.*[137] was used. This model is a biophysically based model, derived from human myocyte experimental data. Model parameters are given in table 1.

Contraction of the heart wall is stimulated by an electrochemical wave, which propagates through the myocardium. Due to a lack of comprehensive electrical activation data for human hearts, in particular with respect to LVAD patients, a spatially homogeneous activation pattern was used to induce cardiac contraction. Activation, at time $t = 0$, stimulates a parameterisation of the intracellular calcium transient,

$$Ca_i^{2+}(t) = Ca_d + \delta Ca(\frac{t}{T})^p e^{(p(1-\frac{t}{T}))}, \tag{5.1}$$

where T is the period of the cardiac cycle, $[Ca_d]$ is the baseline cytosolic calcium concentration, while δCa and p are concentration and exponential constants fitted to the data. The increase in $[Ca_i^{2+}]$ at $t = 0$ facilitates myocyte contraction via the cross bridge cycle, where the strength of activation was considered to be proportional to the number of strongly bound myosin/actin contractile units.

Assuming periodic steady–state conditions in myocyte behaviour, an ODE model, given by equation 5.2, is introduced which focuses on the length dependent variability in active tension (see appendix C for derivation). Here, $\lambda = \sqrt{2\mathbf{E}_{F,\mathbf{ff}} + 1}$ denotes the strain in the fibre direction and z the concentration ratio of strongly bound myosin with respect to total myosin.

$$\frac{d^2z}{dt^2} + a_1(\lambda, [Ca_i^{2+}])\frac{dz}{dt} + a_2(\lambda, [Ca_i^{2+}])z = g(\lambda, [Ca_i^{2+}]), \tag{5.2}$$

Model parameter	Active tension model parameter values	Parameter units
Ca_d	200	nM
δCa	1080	nM
T	60	$m \cdot s$
p	0.4	–
k_2	8.57×10^{-3}	$m \cdot s^-1$
k_3	2.00×10^{-2}	$m \cdot s^-1$
n_{ref}	5.21	–
β_n	-1.48×10^{-1}	–
Ca_{50}	5.60×10^{-1}	μM
β_{Ca}	-8.55×10^{-1}	μM
T_{ref}	180	kPa
C_T	37	–
l	1.12	–
l_{max}	1.12	–

TABLE 1

Parameter values used for the Calcium transient and active tension models given in equations 5.1 and 5.2.

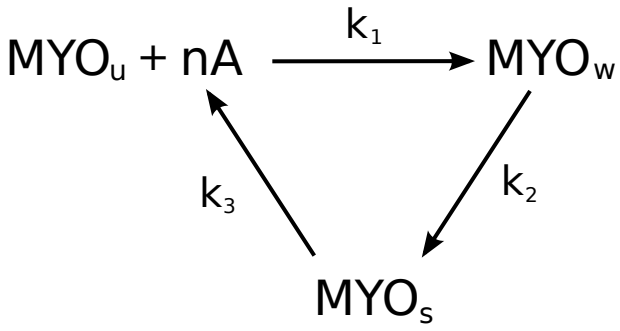

FIGURE 5.1. *Reaction schematic for myofilament kinetics, assuming myocytes in the cell are at periodic steady state with heavily buffered concentrations of [ADP], [ATP] and [Pi]. MYO_u is unbound myocin, A is exposed actin, MYO_w represents the weakly bound myocin–actin complex and the parameter $n(\lambda)$ denotes the average number of exposed actin subunits required for unsterically hindered myosin binding. MYO_s is the strongly bound myosin–actin complex that results in force generation. $k_{1:3}$ are the rate constants.*

The scalar coefficients a_1, a_2 and the right hand side term, g, given by equations 5.3, are functions of the reaction constants, $k_1(\lambda)$, k_2, k_3 and $n = n(\lambda)$, describing the rate at which myocin and actin bind to form the strongly bound actin/myocin complex, see figure 5.1.

$$a_1(\lambda, [Ca_i^{2+}]) := k_2 + k_3 + k_1[Ca_i^{2+}]^n, \tag{5.3a}$$

$$a_2(\lambda, [Ca_i^{2+}]) := k_2k_3 + k_1(k_2 + k_3)[Ca_i^{2+}]^n, \tag{5.3b}$$

$$a_1(\lambda, [Ca_i^{2+}]) := k_1k_2[Ca_i^{2+}]^n. \tag{5.3c}$$

Using the steady state of equation 5.2,

$$z = \frac{[Ca_i^{s+}]^n}{\frac{k_3}{k_1} + \left(1 + \frac{k_3}{k_2}\right)[Ca_i^{2+}]^n}, \tag{5.4}$$

the model parameters were fitted to human experimental data. Assuming k_1 and n are length dependent,

$$n = n_{ref}\left(1 + \beta_n(\lambda - l_{max})\right), \tag{5.5a}$$

$$\frac{1}{k_1} = \frac{k_2 + k_3}{k_3 k_2}\left(Ca_{50}(1 + \beta_{Ca}(\lambda - l_{max}))\right)^n, \tag{5.5b}$$

where, β_n and β_{Ca} define the length dependence relationship with respect to the strain at which peak tension is generated, l_{max}. The model was fitted to observed length dependent steady state behaviour – *i.e.* linear variation in the half–activation of z and linear variation in the hill parameter, n – with the length dependence of k_1 fitted to results from Gwathmey and Hajjar[59], while the length dependence of n was calculated to fit the results of van der Velden *et al.*[196], see figure 5.2. In addition to the steady state fitted parameters, dynamic traces of the tension transient[195] were used to select the remaining parameters, see figure 5.3.

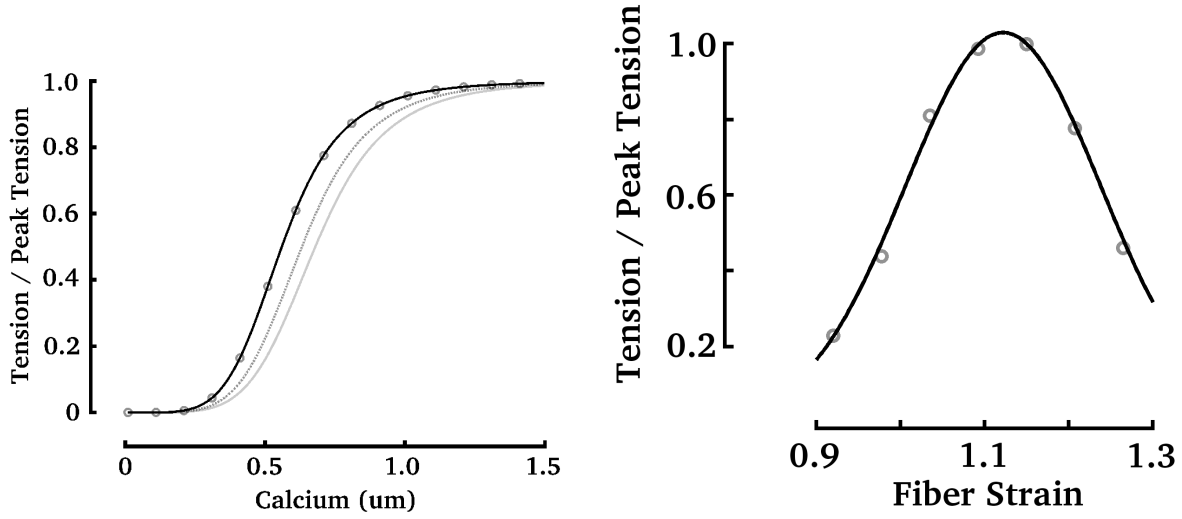

FIGURE 5.2. *Steady state behaviour of the active contraction model compared with human myocyte data. Left, the steady–state relationship between calcium concentration and developed tension normalised by the tension at calcium saturation. The circles represent the data from the experimental fit in Gwathmey[59]. Three model curves are also plotted varying in colour from black to light gray, corresponding to sarcomere lengths of 2.3, 2.0 and 1.8, respectively. Right, Normalised peak tension as a function of fibre strain, λ. Circles represent the measurements from van der Velden[196]. Note $\lambda = 1$ was considered equivalent to a sarcomere length of 2.0.*

The generation of active tension was incorporated into the model by modifying equation 4.13 (see section 4.2), by adding an active stress tensor, $\hat{\boldsymbol{\sigma}}_a$. Active tension is given as a scaling of the fraction, z, orientated in the fibre direction. As with the passive material behaviour, the generation of active tension approaches isotropy near the apex,

$$\hat{\boldsymbol{\sigma}}_a = A_o z(1 - \Psi)\mathbf{F}(\mathbf{f} \otimes \mathbf{f})\mathbf{F}^T + A_o z \Psi \mathbf{F}\mathbf{F}^T, \tag{5.6}$$

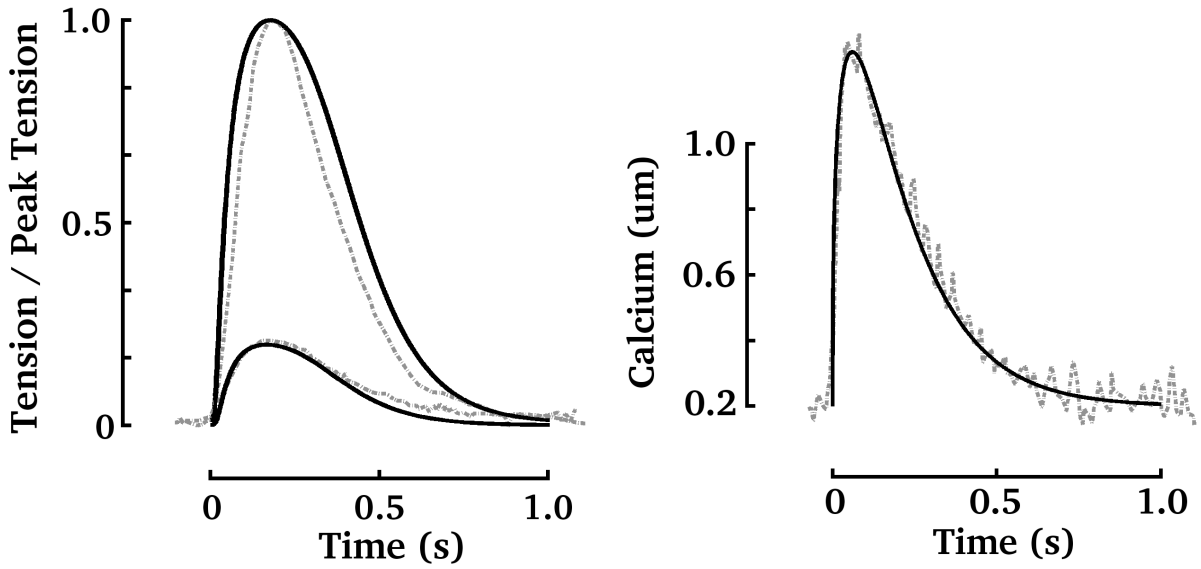

FIGURE 5.3. *Transient behaviour of the active contraction model compared with human myocyte data. Left, transient active tension traces compared to experimental measurements in Vahl[195] at sarcomere lengths of 2.3 (larger curves) and 1.8 (smaller curves). Right, the fitted calcium transient superimposed over the experimental measurements from Vahl. In both figures the dashed lines denote experimental data and the solid lines refer to model data. Note* $\lambda = 1$ *was considered equivalent to a sarcomere length of 2.0.*

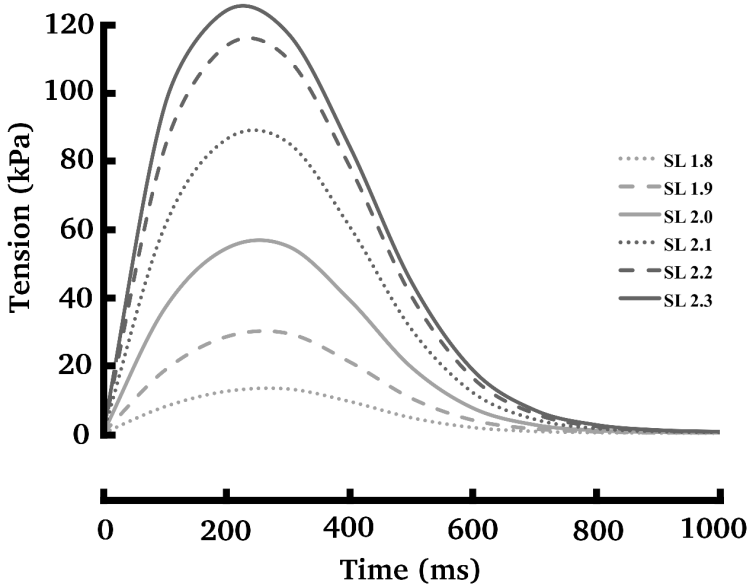

FIGURE 5.4. *Model tension development over time for different sarcomere lengths. Note* $\lambda = 1$ *was considered equivalent to a sarcomere length of 2.0.*

where $A_o = K_o exp(-C_T(\lambda - l)^2)$ and $K_o = T_{ref}(1 + \frac{k_3}{k_2})$. Here T_{ref} defines peak myocardial tension and C_T is an additional length dependence constant fitted to give the desired transient length/tension relationship, see figure 5.4. The final Cauchy stress tensor, incorporating hydrostatic, passive and active characteristics of tissue behaviour is,

$$\boldsymbol{\sigma} = -p\mathbf{I} + (1 - \Psi)\hat{\boldsymbol{\sigma}}_{Costa} + \Psi\hat{\boldsymbol{\sigma}}_{iso} + \hat{\boldsymbol{\sigma}}_a. \tag{5.7}$$

5.2 Cardiac Windkessel Models

To simulate multiple beats of the cardiac cycle the boundary conditions on the model need to react in response to cardiac output and ventricular pressures. Windkessel models provide a lumped parameter representation of the circulatory networks, which can be coupled to the 3D finite element model using the techniques outlined in section 2.5.5. These models exist with varying complexities, ranging from three or four element models, useful for providing resistance to ventricular ejection[74, 128], through to models that provide representations of the pulmonary and systemic circulatory networks, as well as the cardiac chambers[148, 199, 143]. For this thesis, the Shi–Korakianitis Windkessel model[86, 85] was selected to couple to the LV finite element model.

The Shi–Korakianitis model has the advantage of providing representations of atrial function, as well as the aortic sinus – *i.e.* representations of both the inflow and outflow boundary conditions on the ventricle. Additionally, the model has been used for lumped parameter investigations into LVAD function[178], therefore its behaviour in the presence of an LVAD is known. Due to the 0D/3D coupling methods used, a modified form of the Shi–Korakianitis model was developed and is outlined in section 5.2.1. A simple valve model was also developed and is presented in section 5.2.2.

5.2.1 Modified Shi–Korakianitis Windkessel Model

The model consists of modular ODE representations of the pulmonary and systemic circulatory networks, the four heart chambers, as well as the four ventricular valves, see figure 5.5. The model equations and parameter values are provided in appendix D. The modular nature of the model facilitated the substitution of Windkessel components, for example the ventricular chambers, for their 3D finite element representations, with the flow rates, $\mathbf{Q}$, and pressures, P, acting as boundary conditions.

To enable coupling of the model to the valve boundaries on the ventricular cavities, the published valve models were modified. Due to the mass term in the governing equations, fluid flow exhibits inertia to changes in velocity. Therefore, for the model to be coupled to fluid boundaries using the prescribed profile method, see section 2.5.5, the equations describing valve flow must incorporate resistance to both the flow rate and acceleration. This was accomplished by including an inductance term, L, in the valve equations. Additionally, since the valve model implemented to describe the mitral and aortic valves, see section 5.2.2, differs from that in the original Shi–Korakianitis model[1] the valve flow resistance was modified. Considering flow through an

[1] Valve opening in Korakianitis and Shi[86] was described as a function of the angular position of the valve leaflets. Since the valves

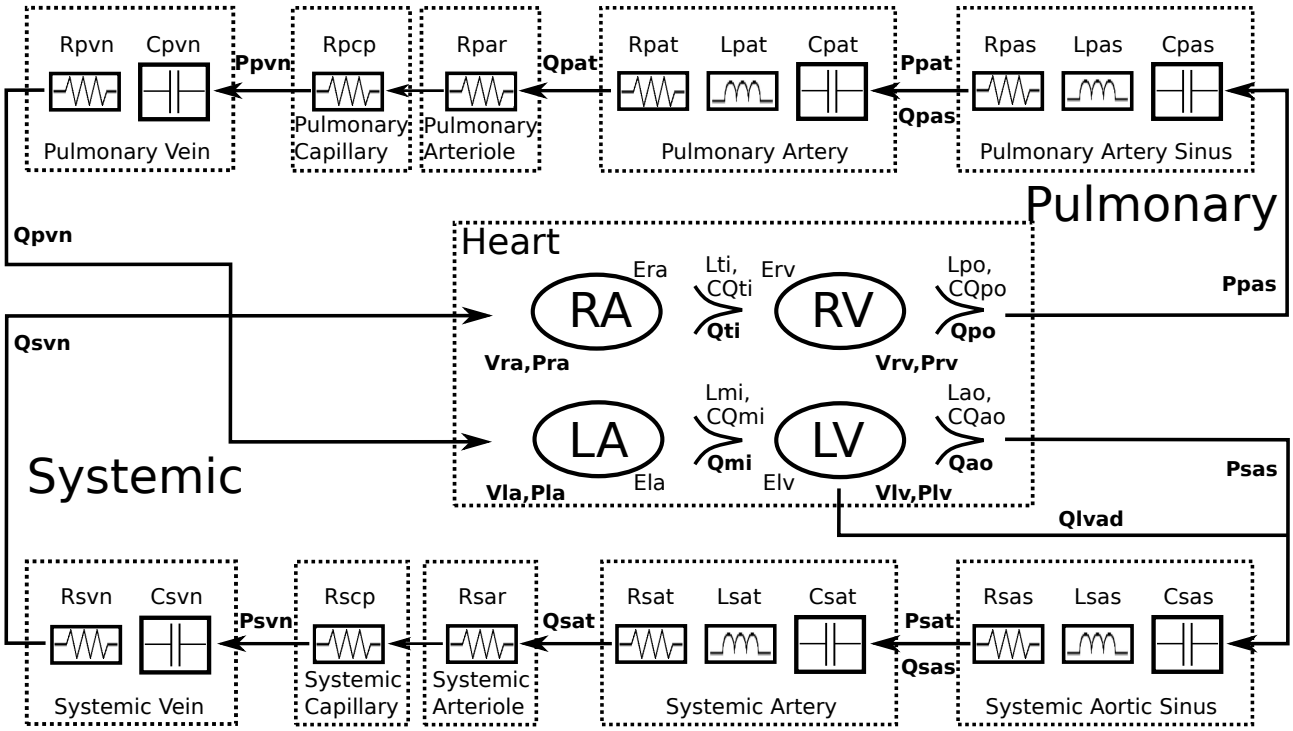

FIGURE 5.5. *Schematic representation of the Shi–Korakianitis Windkessel model. Top half represents the pulmonary, bottom half the systemic, circulatory networks. The heart chambers and valves are shown in the centre. The circulatory networks are described as a series of capacitors, resistors and inductors, while the heart chambers are modelled as elastic shells. Model variables are in bold, parameters are shown associated with their respective model components. Parameter values and model equations are given in appendix D. The figure is based on a diagram in Korakianitis and Shi*[86].

orifice, resistance to flow at steady state can be derived from Bernoulli's equation (see appendix D), as,

$$CQ_{valve} = A(t)\left(\frac{2}{\rho\left(1-\left(\frac{A(t)}{A_{max}}\right)^2\right)}\right)^{0.5}, \tag{5.8}$$

where ρ is fluid density, $A(t)$ is the area of the open valve at time t, and A_{max} is the area of the cavity cross–section on the down stream side of the annulus.

Incorporating these additions, the modified one way valve equation between two chambers, 1 and 2, is,

$$\mathbf{Q}_{valve} = \begin{cases} CQ_{valve}(P_1-P_2)^{0.5} - L_{valve}\frac{d\mathbf{Q}_{valve}}{dt}, & \text{if } P_1 > P_2 \\ -L_{valve}\frac{d\mathbf{Q}_{valve}}{dt}, & \text{else} \end{cases}, \tag{5.9}$$

for flow in the direction from chamber 1 to chamber 2. L_{valve} was scaled by $(P_1/P_2)^2$ when $P_2 > P_1$ to ensure

in the model developed in this thesis were described on a planar surface, valve opening was defined using functions on the valve boundary.

flow deceleration was dependent on the pressure gradient. Note that for coupling to solid only models, CQ_{valve} was considered to be constant. The other Windkessel equations were implemented as published.

5.2.1.1 Windkessel Results

To demonstrate the behaviour of the modified Shi–Korakianitis Windkessel model, it was run in isolation in two cases, the first with the LVAD off and the second with $Q_{LVAD} = 60ml \cdot s^{-1}$, until a steady state was reached. The Windkessel model was tuned (see appendix D.2) so that in the LVAD off case, end–diastolic pressure was $\approx 9.75mmHg$ and the stroke volume was $\approx 70ml$. The same parameters were used for the LVAD on case. Pressure volume loops and Wigger diagrams showing the model behaviour are given in figures 5.6 and 5.7.

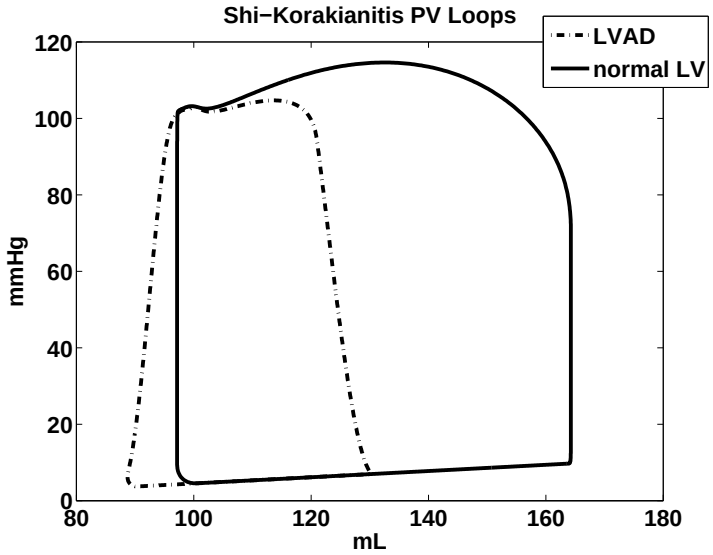

Figure 5.6. *Pressure–volume loops for the Windkessel model with the LVAD off and with an LVAD flow rate of* $60ml \cdot s^{-1}$. *The model was tuned so that end–diastolic pressure was* $\approx 9.75mmHg$ *with a stroke volume of* $70ml$ *in the LVAD off case.*

Turning the LVAD on caused substantial volume unloading in the model. Additionally, pressure unloading was observed with peak pressure during systole and diastole declining. From the Wigger's diagrams, notable features include the decreased range in aortic pressure, caused by continual flow from the LVAD preventing pressure decreasing once systole had finished. A decrease in left atrial pressure was observed, caused by the increased flow from the LA to the LV, due to LV volume unloading, decreasing LA volume. Finally, right atrial pressure increased due to the greater flow through the systemic network when the LVAD was on.

5.2.2 Aortic and Mitral Valve Functions

To facilitate coupling of the LV model to the Windkessel lumped parameter model, simple functions were developed to define the opening of the mitral and aortic valves. The valves were defined on the boundaries of the fluid mesh as the functions, $Mi(R_{mi})$ and $Ao(R_{ao})$ for the mitral and aortic valves respectively, where

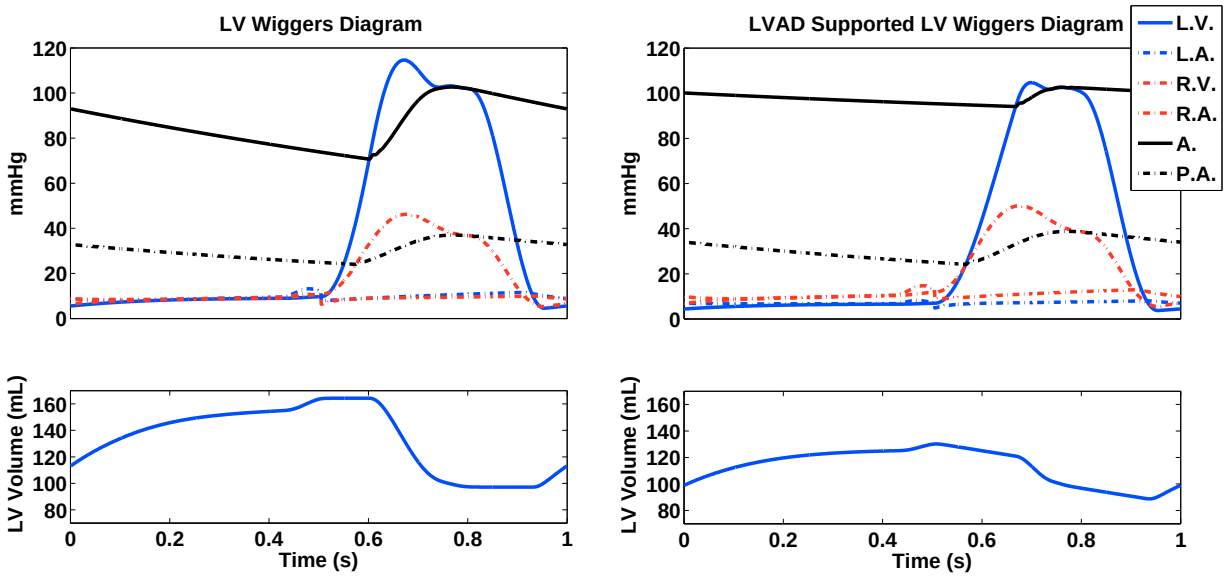

FIGURE 5.7. *Wigger's diagrams for the LVAD off, left, and* $Q_{LVAD} = 60ml \cdot s^{-1}$*, right, cases.*

$R_{mi}(\mathbf{Q}_{mi})$ and $R_{ao}(\mathbf{Q}_{ao})$ are the radii of opening of the mitral and aortic valves at the flow rates $\mathbf{Q}_{mi}$ and $\mathbf{Q}_{ao}$. $R_{mi}(\mathbf{Q}_{mi})$ and $R_{ao}(\mathbf{Q}_{ao})$ were defined using the same function,

$$R_{valve} = R_{max}\tan^{-1}(c\mathbf{Q}_{valve})(2/\pi), \tag{5.10}$$

where R_{max} is the radius of the fully open valve, $valve = mi/ao$, and c is a constant that defines the extent of valve opening for a given flow rate. c was chosen so that the time duration for valve opening matched observed human data, $\approx 24ms$ for the aortic valve[147] and $\approx 46ms$ for the mitral valve[215]. The valves were considered fully open when $R_{valve} > 0.9R_{max}$, see figure 5.8. For stability R_{valve} was updated using $\mathbf{Q}_{valve}$ from the previous time step.

The mitral valve was defined as an ellipse with a fixed major axis, R_{maj}. The magnitude of the minor axis was was equal to R_{mi}. The function $Mi(R_{mi})$ was therefore defined, for any angle Θ with respect to the ellipsoid major axis, as,

$$Mi(Rmi, \Theta) = \frac{R_{maj} \times R_{mi}}{\sqrt{R_{maj}cos^2(\Theta) + R_{mi}sin^2(\Theta)}}. \tag{5.11}$$

A quadratic flow profile was defined over the open valve.

To approximate the tricuspid aortic valve, $Ao(R_{ao})$ was defined, using measurements from Zoghbi *et al.*[219], based on the maximum radius of opening, R_{max}, and the minimum angle, Θ, between points on the valve surface and the tricuspid axes, see figure 5.8. For any angle Θ and radius R_{ao}, $Ao(R_{ao})$ was defined as,

$$Ao(R_{ao}, \Theta) = \left(\left(\frac{\pi}{3} - \Theta\right)\frac{3}{\pi}\right)^2 (R_{max} - R_{ao})\left(\frac{(R_{ao}/R_{max})^2}{(R_{ao}/R_{max})^2 + 0.001}\right) + R_{ao}. \tag{5.12}$$

As with the mitral valve, a quadratic flow profile was defined over the open valve.

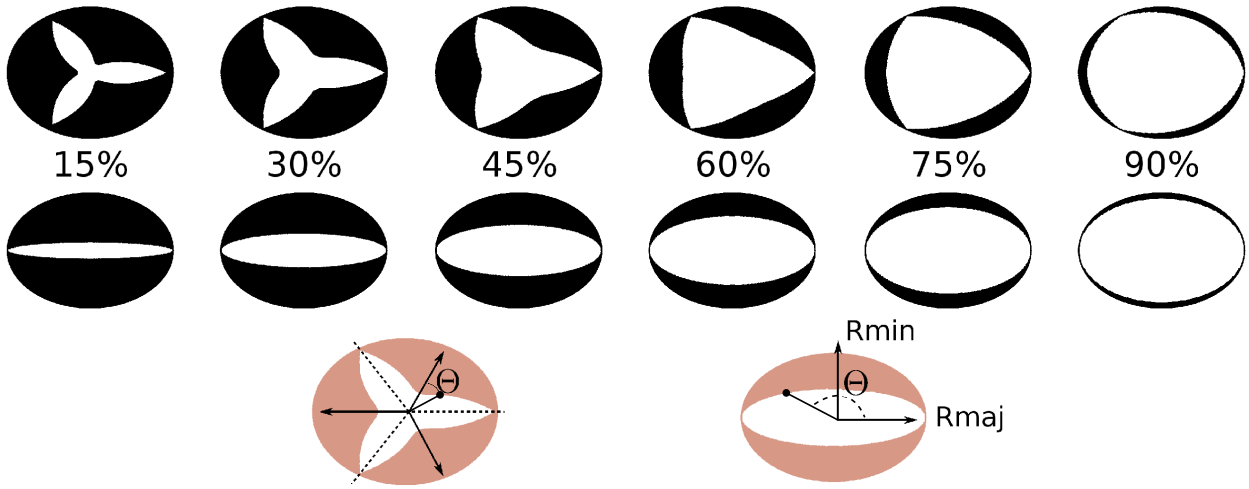

FIGURE 5.8. *The aortic tricuspid (top) and mitral bicuspid (middle) valve models from 15% to 90% open. Flow profile was prescribed as a quadratic function over the open region. The bottom row defines the axes for the valve models. For the aortic valve, Θ was defined as the minimum angle between the tricuspid axes (arrows) and any point on the valve boundary, while while for the mitral valve, Θ was the angle between the major axis of the ellipsoid, R_{maj}, and any point on the valve boundary.*

5.3 Fluid-Solid Coupled Simulation of an LVAD Supported LV Through the Full Cardiac Cycle

Incorporating the Windkessel and contraction models into the LV geometry presented in chapter 4, a simulation of the full cardiac cycle under LVAD support was developed. This section presents the results from this simulation. A visualisation of model results is given in section 5.3.1, pressure volume relationships in section 5.3.2 and the variance in myocardial work, as well as fluid and solid energies in section 5.3.3. A particle tracking study investigating the residence times of particles seeded at different points during diastole is outlined in section 5.3.4, while a comparison of the simulations results with a solid only full cardiac cycle simulation is given in section 5.3.5

The simulation was run for three heart beats, with a period of $1s$, to enable convergence on a repeating pressure volume loop, and was commenced at end–diastole, since at this point there is no residual active tension in the myocardium. The contraction model parameters and LVAD flow rate (chosen to be $60ml \cdot s^{-1}$) were tuned to ensure aortic outflow at each cardiac beat. The Windkessel model was also tuned, assuming that the ventricle was already unloaded when the simulation was initiated, so that the simulation would start from a point close to the converged pressure–volume loop.

The same myocardial mesh from the LVAD diastole simulations was used, however, considering the results from section 3.3, a TET(2cr,2cr,1dc) fluid mesh was constructed consisting of $\approx 2.4 \times 10^4$ elements and $\approx 4.3 \times 10^5$ degrees of freedom. A TRI(1,0) FD mesh was used to describe the LVAD cannula. Time step size was chosen based on the rate of change of the system at given points in the cardiac cycle and ranged from $0.0001s$ during isovolumetric contraction to $0.001s$ during diastole. In total, each cardiac beat consisted of 2880 time steps. Other model conditions were defined as per the previous fluid–solid coupled LV simulations outlined in this

thesis.

5.3.1 LV Hemodynamics under LVAD Support

Model behaviour varied significantly both between and within each cardiac phase. This section presents a visualisation of the model results from diastole in the second simulated heart beat, broken up into each cardiac phase. Here $t = 0$ corresponds to the start of diastole.

5.3.1.1 Diastole

A visualisation of model behaviour during diastole is provided, at selected time points, in figures 5.9 (fluid streamlines and myocardial displacements) and 5.10 (pressure). Unlike the simulations presented in chapter 4, there is residual stress in the myocardium (both active and passive) at the commencement of diastole. The reduction in active tension that characterises isovolumetric relaxation continues into early diastole. As a result, LV pressure declines during this period ($0.02s$ and $0.07s$ in figure 5.10) sucking blood into the LV. Due to the presence of the LVAD, flow is largely uniaxial, base to apex, at the commencement of diastole. The rapid increase in flow across the mitral valve sees vortices form during peak mitral inflow. These enlarge during diastasis to engulf the whole LV by late diastasis ($0.32s$ and $0.40s$ in figure 5.9). Diastasis also sees the beginning of helical flow around the cannula base, which continues through to end diastole.

As with the passive diastole simulations in the previous chapter, LV pressure is characterised by formation of pressure waves, corresponding to periods of peak inflow, that travel down the ventricle. Due to the large variation in diastolic inflow, as well as the low cavity pressures, variance in LV pressure is high during this phase. The final cessation of diastole occurs when myocardial contraction begins to increase LV pressure. The pressure increase can be seen with the break down of this wave between $0.46s$ and $0.5s$ in figure 5.10.

Myocardial behaviour during this period was largely passive – except for during early diastole – and as a result displacement was predominantly outward from the central ventricular axis. Untwisting of the the myocardium, due to the reduction in active tension, was largely completed during isovolumetric relaxation, see section 5.3.1.4, and was therefore not significant in model behaviour during this phase.

5.3.1.2 Isovolumetric Contraction

Simulated isovolumetric contraction lasted for $0.07s$, during which cavity pressure rose from $\approx 9mmHg$ to $\approx 90mmHg$. This section presents a visualisation of model results during this period, with myocardial displacement and streamlines of fluid flow given in figure 5.12 and fluid pressure in figure 5.11.

Ventricular flow during this phase was characterised by the break down of the diastolic flow structures as the myocardium begins to contract. The remnants of late diastolic inflow can be seen at $0.515s$ in figure 5.12, however by $0.53s$ this has largely disappeared to be replaced by a new vortex formation, driven by LVAD cannula outflow, seen at $0.545s$ and $0.56s$. Due to the presence of the LVAD cannula, this period was not

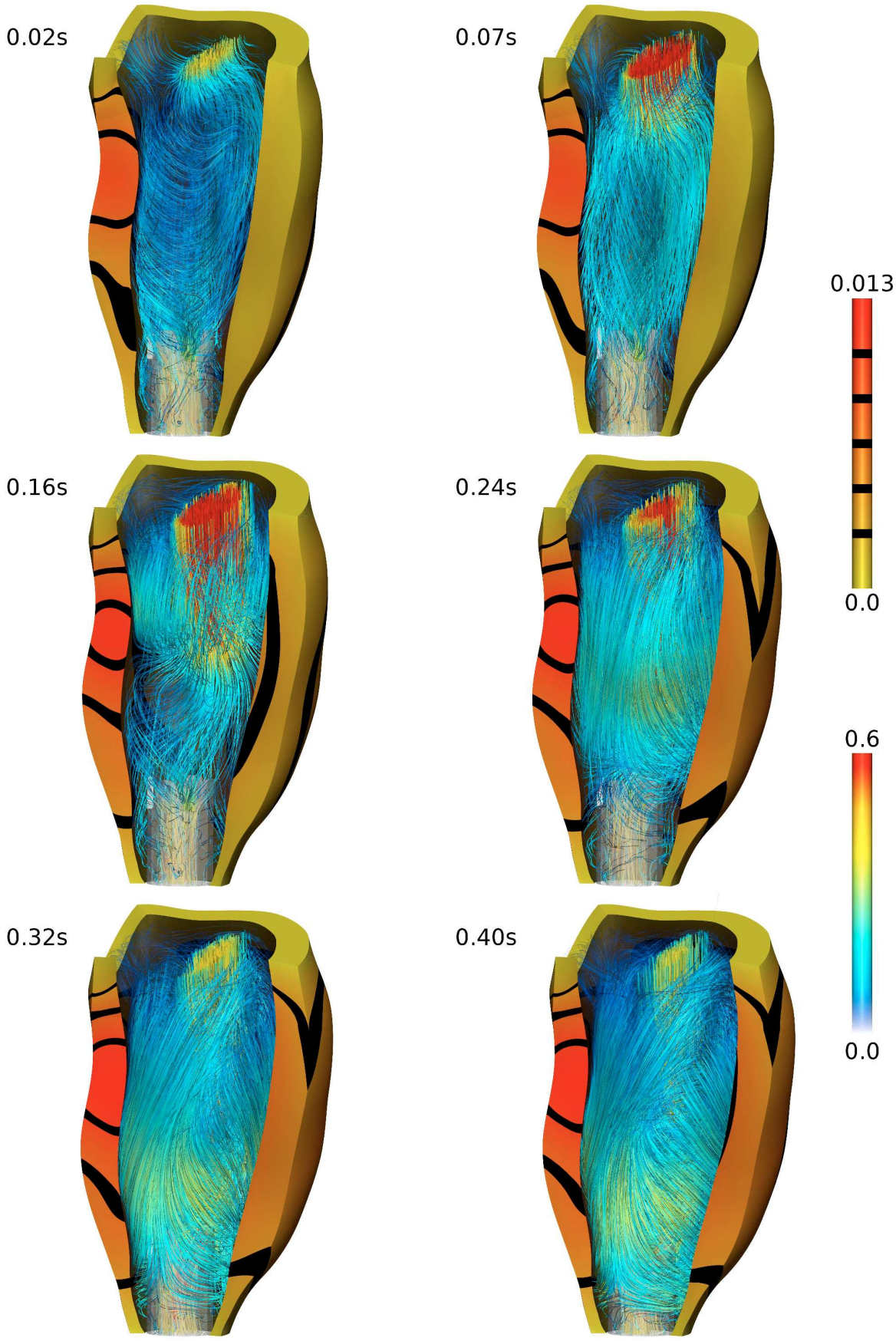
0.02s
0.07s
0.16s
0.24s
0.32s
0.40s
0.013
0.0
0.6
0.0

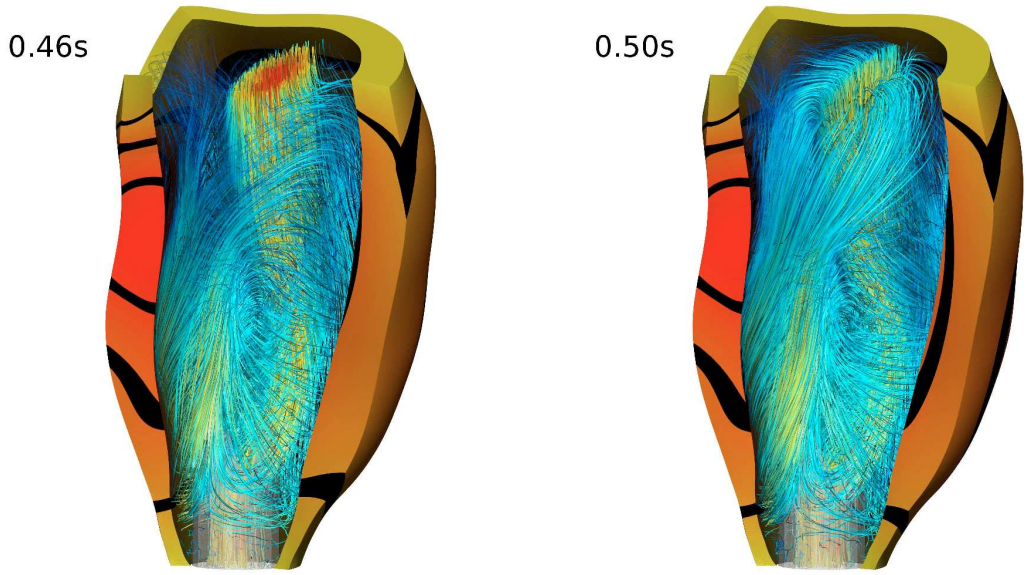

FIGURE 5.9. *Myocardial displacement and streamlines of blood flow during diastole in an LVAD supported LV. The diastolic period was* 0.5s*, the results visualised show early diastole (*0.02s, 0.07s, 0.16s*), diastasis (*0.24s, 0.32s, 0.4s*) and end diastole (*0.46s *and* 0.5s*). Blood velocity is in* ms^{-1} *and myocardial displacement is in metres.*

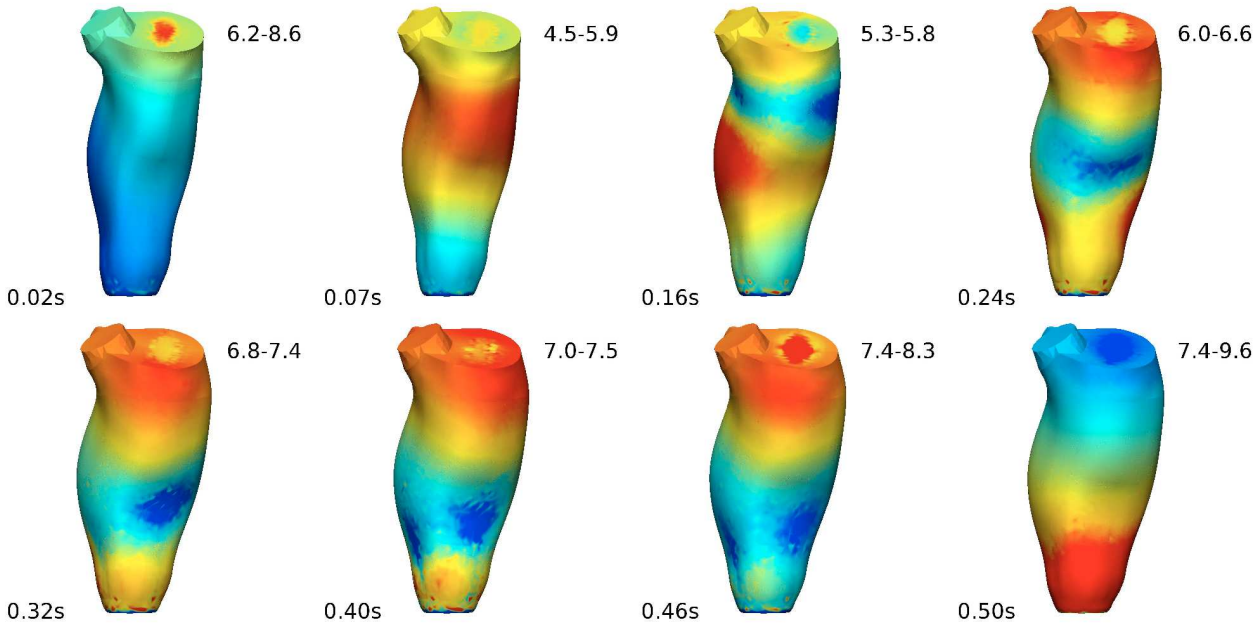

FIGURE 5.10. *Fluid pressure during early diastole (*0.02s, 0.07s, 0.16s*), diastasis (*0.24s, 0.32s, 0.4s*) and end diastole (*0.46s *and* 0.5s*). Pressure is in* $mmHg$*, scale, blue–red, is shown at the top right of each figure.*

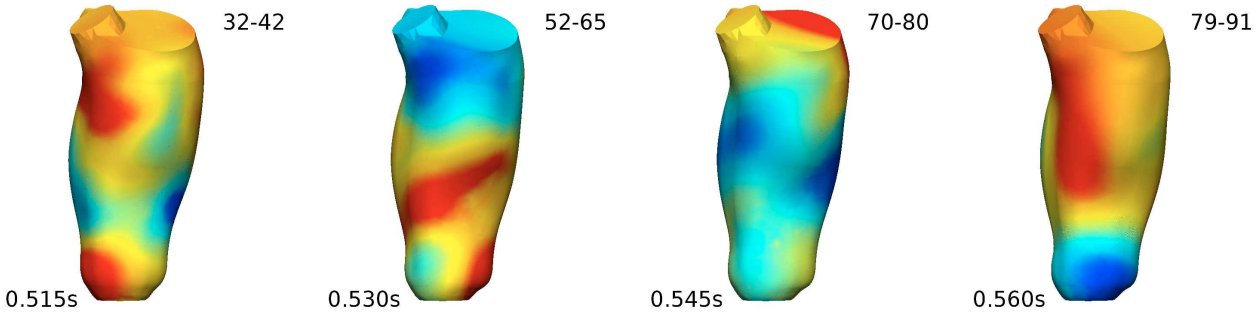

FIGURE 5.11. *Fluid pressure during isovolumetric contraction visualised at selected time points,* $0.515s$*,* $0.530s$*,* $0.545s$ *and* $0.56s$*. Pressure is in* $mmHg$*, scale, blue–red, is shown at the top right of each figure.*

strictly isovolumetric, as LV volume continued to decrease, slowing the rate of pressure generation. Myocardial behaviour during this period was characterised by twisting, see figure 5.25, and, partly due to the homogeneous initiation of contraction, myocardial wall movement in an apical direction (see bottom right corner of the sub–figures in 5.12).

Pressure during IVC was less structured, compared with fluid pressure during diastole and systole, and tended to reflect movement of fluid within the cavity. Due to the absence of fluid outflow across the aortic valve during this phase, flow was relatively unstructured, however outflow continued via the LVAD cannula. The unstructured behaviour can be explained by the force/length relationship of the myocardium in response to interaction with the fluid in the LV cavity. Flow moving to one region of the cavity caused extra stain in the myocardium in that area. This increased the local force of contraction increasing local pressure and causing flow to start moving away from the region.

5.3.1.3 SYSTOLE

Systole, during the LV simulation, lasted for $\approx 0.08s$. Due to LVAD outflow, this period was relatively short as the the LVAD both reduced peak LV pressure and increased systemic pressure. This section presents a visualisation of model results during this period, with fluid pressure given in figure 5.13 and myocardial displacement and streamlines of fluid flow given in figure 5.14.

Early systole ($0.573s$ and $0.587s$ figure 5.14) saw the establishment of uniaxial flow from the LV cavity into the aorta. The flow features observed during IVC break up during the first part of this phase. By mid–diastole ($0.60s$ and $0.613s$) outflow via the aortic valve was fairly consistent, however, due to continual outflow via the LVAD cannula, apical flow was less homogeneous, with some flow in this region diverted towards the cannula mouth. Late systole saw the gradual reduction in aortic outflow and the cessation of uniaxial flow towards the aortic valve, as the majority of outflow is now occurring via the LVAD cannula. Myocardial motion was predominantly inwards, towards the central axis of the ventricular chamber. Since peak tension occurs during this phase, the myocardium remained twisted.

During early systole, high pressure was located at the apex ($0.573s$ in figure 5.14), causing flow acceleration towards the opening aortic valve. This initiates a pressure wave that traveled up the ventricle ($0.587s$), however,

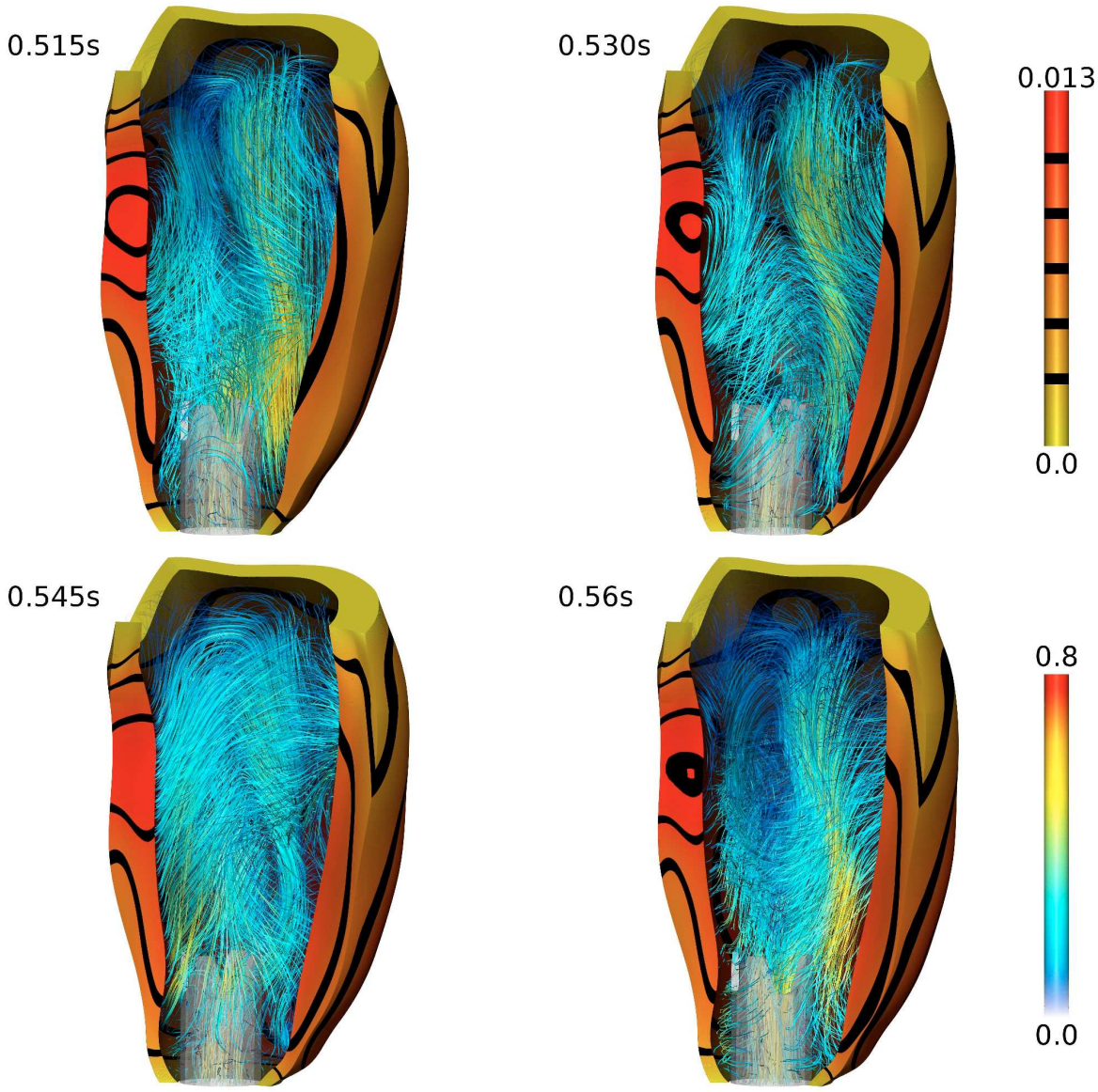

FIGURE 5.12. *Myocardial displacement and streamlines of blood flow during isovolumetric contraction in an LVAD supported LV. Simulated IVC lasted for* $0.07s$ *and results are visualised at four time instances,* $0.515s$*,* $0.530s$*,* $0.545s$ *and* $0.56s$*. Blood velocity is in* ms^{-1} *and myocardial displacement is in metres.*

pressure in the aortic region remained lower around the aortic valve at this point, continuing the acceleration of aortic flow. During mid–systole the range in pressure through the LV cavity reduces ($0.613s$) as outflow acceleration has finished and uniaxial outflow is established. Finally, at end–systole, a high pressure region forms at the aortic mouth causing rapid flow deceleration ($0.627s$). This causes a pressure wave that spreads down the ventricle ($0.64s$).

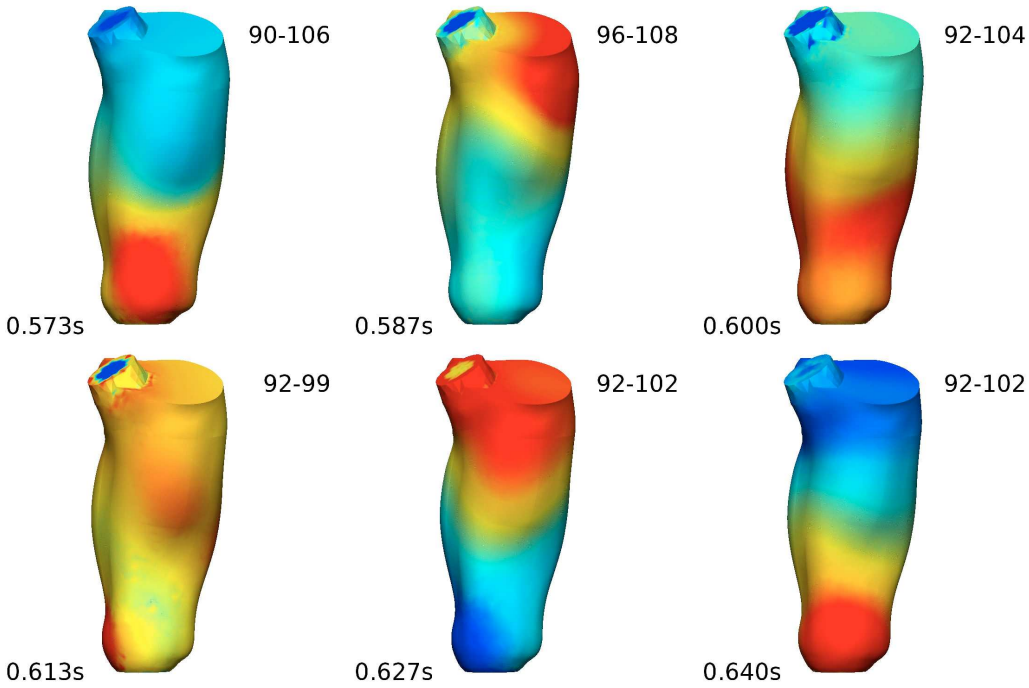

FIGURE 5.13. *Fluid pressure at selected time points during systole. Early systole (*0.573*s and* 0.587*s), mid diastole (*0.60*s and* 0.613*s) and late diastole* 0.627*s and* 0.64*s. Pressure is in mmHg, scale, blue–red, is shown at the top right of each figure.*

5.3.1.4 Isovolumetric Relaxation

Isovolumetric relaxation, during the LV simulation, lasted for $\approx 0.35s$. Continual outflow from the LVAD cannula meant that LV volume gradually decreased during this period. This section presents a visualisation of model results during IVR with myocardial displacement and streamlines of fluid flow given in figure 5.15 and fluid pressure in figure 5.16.

The predominant flow feature observed during this period was a vortical feature driven by the LVAD cannula outflow. This feature was sustained throughout IVR. During IVR, active myocardial tension from the contraction model gradually reduced and the myocardium untwisted (see figure 5.25). Due to the slow rate of myocardial relaxation in this simulation, and subsequent untwisting of the myocardium, active solid behaviour did not substantially alter the flow features observed during this phase.

During IVR, the range in ventricular cavity pressures was relatively low, however, pressure was consistently higher at the apex. This was caused by the LVAD outflow, which caused fluid to be drawn to the apex. Fluid that did not exit via the cannula, pooled in the apical region, increasing pressure in this region.

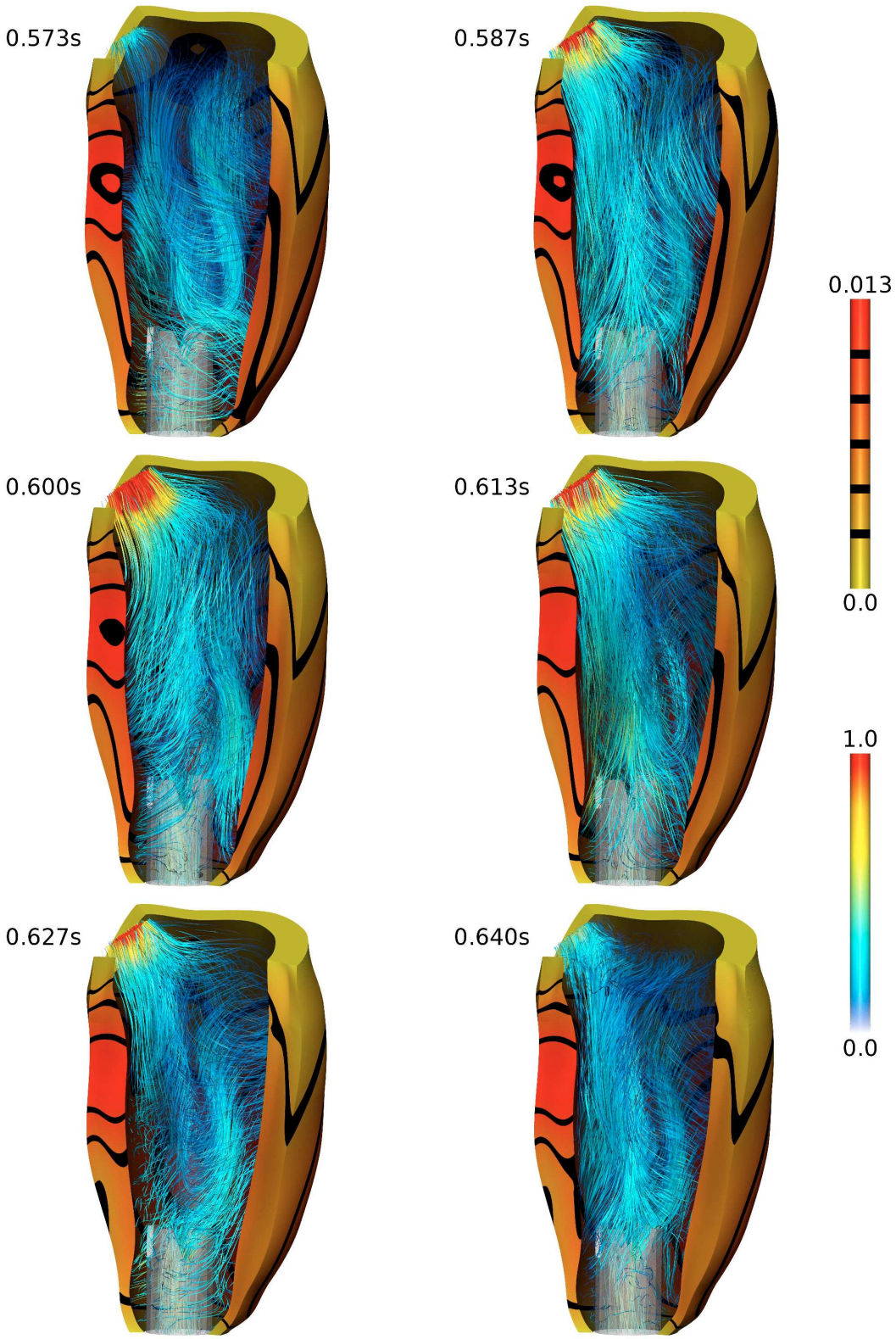

FIGURE 5.14. *Myocardial displacement and streamlines of blood flow during systole in an LVAD supported LV. Systolic period was* 0.08*s. Results are visualised at early systole (*0.573*s and* 0.587*s), mid systole (*0.60*s and* 0.613*s) and late systole* 0.627*s and* 0.64*s. Blood velocity is in* ms^{-1} *and myocardial displacement is in metres.*

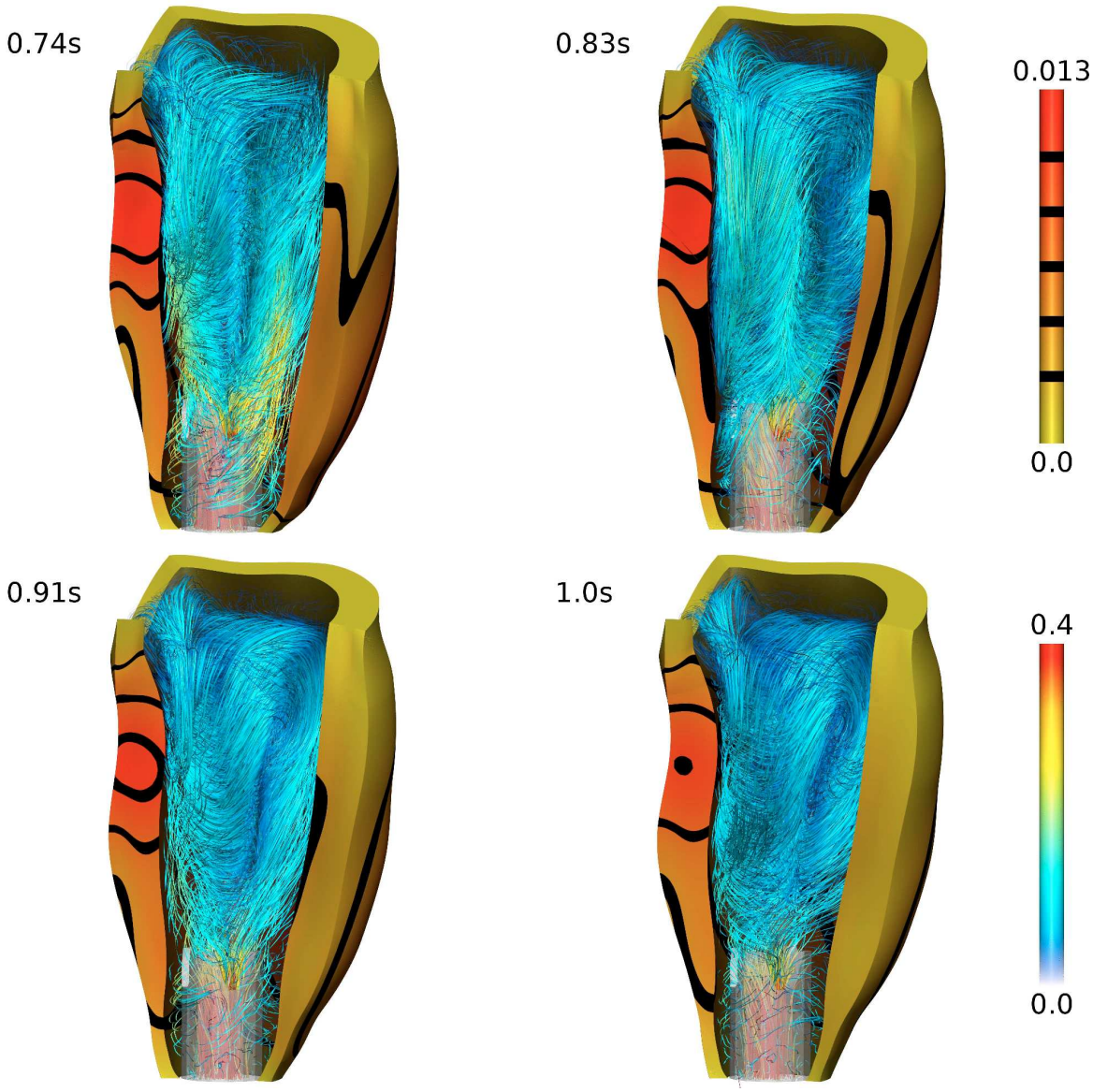

FIGURE 5.15. *Myocardial displacement and streamlines of blood flow during isovolumetric relaxation in an LVAD supported LV. IVR period was* 0.35*s. Results are visualised at* 0.74*s,* 0.83*s,* 0.91*s and* 1.0*s. Blood velocity is in* ms^{-1} *and myocardial displacement is in metres.*

5.3.2 Pressure Volume Relationships in the LVAD Supported LV

LV performance can be characterised by gross metrics, such as the pressure volume relationship and the Wigger's diagram. To demonstrate model behaviour both through the cardiac cycle and over multiple beats, this section presents the simulated LV pressure volume relationship, figure 5.17, Wigger's diagram, figure 5.18, and valve flow across the aortic and mitral valves, figure 5.19. LV pressure in these figures was the mean value integrated over the LV cavity.

The rapid rise in pressure during isovolumetric contraction can be seen in the slope of the PV loop in figure 5.17

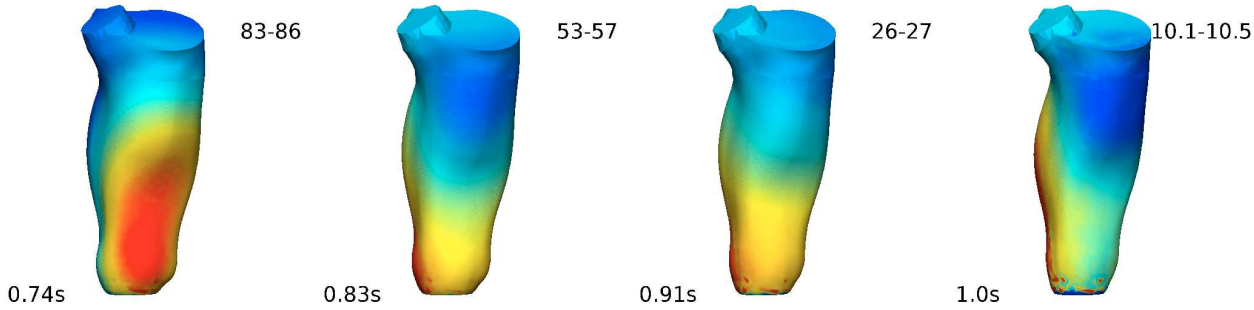

FIGURE 5.16. *Fluid pressure at selected time points during isovolumetric relaxation. Results are visualised at selected time points, 0.74s, 0.83s, 0.91s and 1.0s. Pressure is in mmHg, scale, blue–red, is shown at the top right of each figure.*

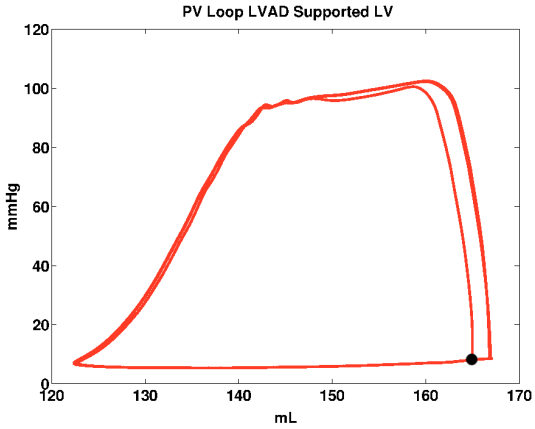

FIGURE 5.17. *Pressure volume loop from the three cardiac cycles of the LVAD supported LV simulation. The black dot indicates the initiation point of the simulation.*

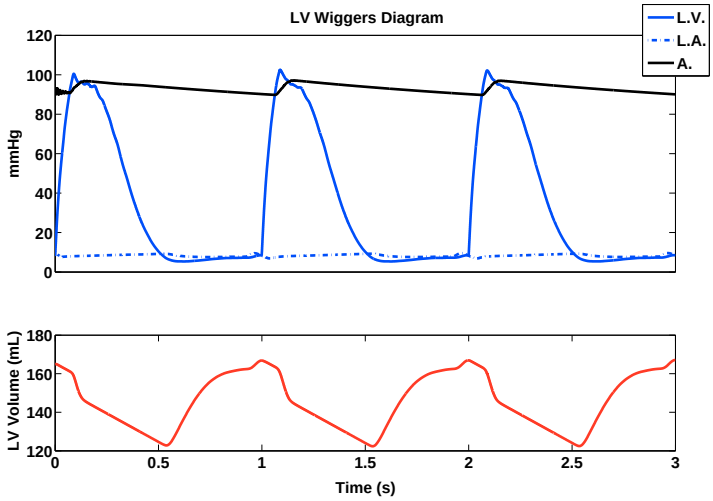

FIGURE 5.18. *Wigger's plot of LV dynamics over three simulated heart beats. Top, LV, LA and Aortic (A.) pressures, bottom LV volume.*

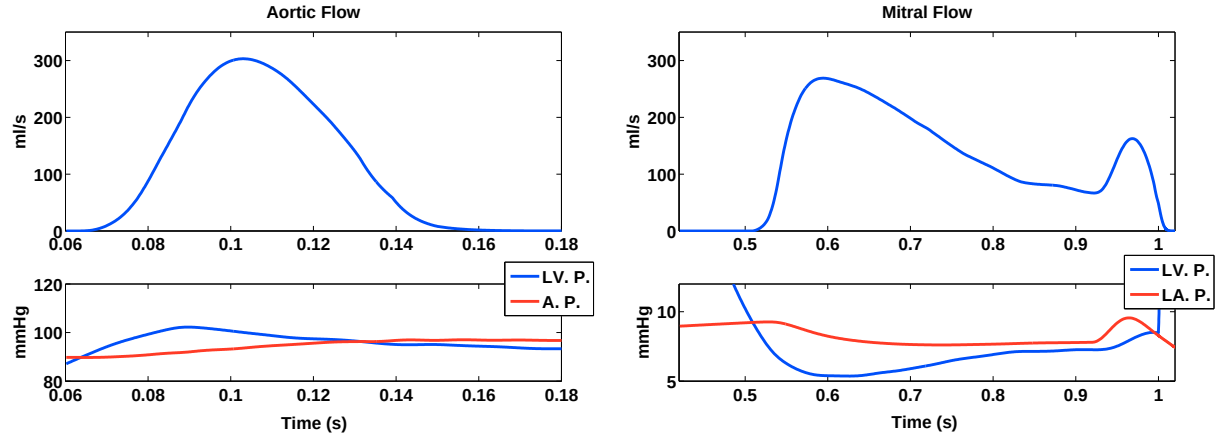

FIGURE 5.19. *Top rows, simulated flow profiles from the aortic and mitral valves. Bottom left, LV (LV. P.) and aortic (A. P.) pressures, bottom right, LV and LA pressures.*

during this phase . Pressure continued to increase after the opening of the aortic valve and peak LV pressure was reached during systole, at $\approx 103mmHg$. Pressure remained relatively stable throughout systole and early isovolumetric relaxation, before declining to $\approx 9.5mmHg$, where the mitral valve opened. Through diastole, LV pressure initially declined rapidly, causing acceleration of mitral inflow (see figure 5.19). Around $0.6s$ LV pressure stabilised, causing cessation of mitral inflow acceleration, before gradually increasing as mitral inflow began to decline. Due to LVAD outflow keeping LV pressure low, mitral inflow remained relatively high during diastasis. Through this period, LV inflow was only slightly higher than cannula outflow, resulting in a plateau in LV pressure. Atrial contraction saw late peaks in both LV pressure and mitral inflow. Finally, the initiation of contraction caused the process to repeat.

After one simulated heart beat, the model converged on a repeating LV pressure volume loop – seen by the overlap of the PV loops from the second and third heart beats in figure 5.17. This highlights the stability of both the 3D finite element model, as well as its coupling to the Windkessel model.

5.3.3 Myocardial Work and LV Energy During the Cardiac Cycle

An understanding of the energetics of the heart is crucial to quantifying the impact of LVAD implantation on LV function. This section presents an analysis of the energy transfers between the various model components during a cardiac cycle of the simulated LVAD supported LV.

In the LV model, energy can be stored as either fluid kinetic energy (which can be dissipated as viscous loss), or as elastic potential energy within the myocardium (which cannot be dissipated due to the hyperelastic material law). Energy can be freely transfered between these two forms. Energy sources to the model come from myocardial contraction, which performs work, driving the build up of cavity pressure and the expulsion of blood from the chamber during systole; and the Windkessel model, which drives flow across the mitral

boundary during diastole. Energy sinks occur at the aortic and LVAD boundaries, where fluid is removed from the system. Additionally, on all boundaries where flow either enters or leaves the system, energy can be advected by the fluid. Appendix B provides a description of the energetics equations used in the LV analysis.

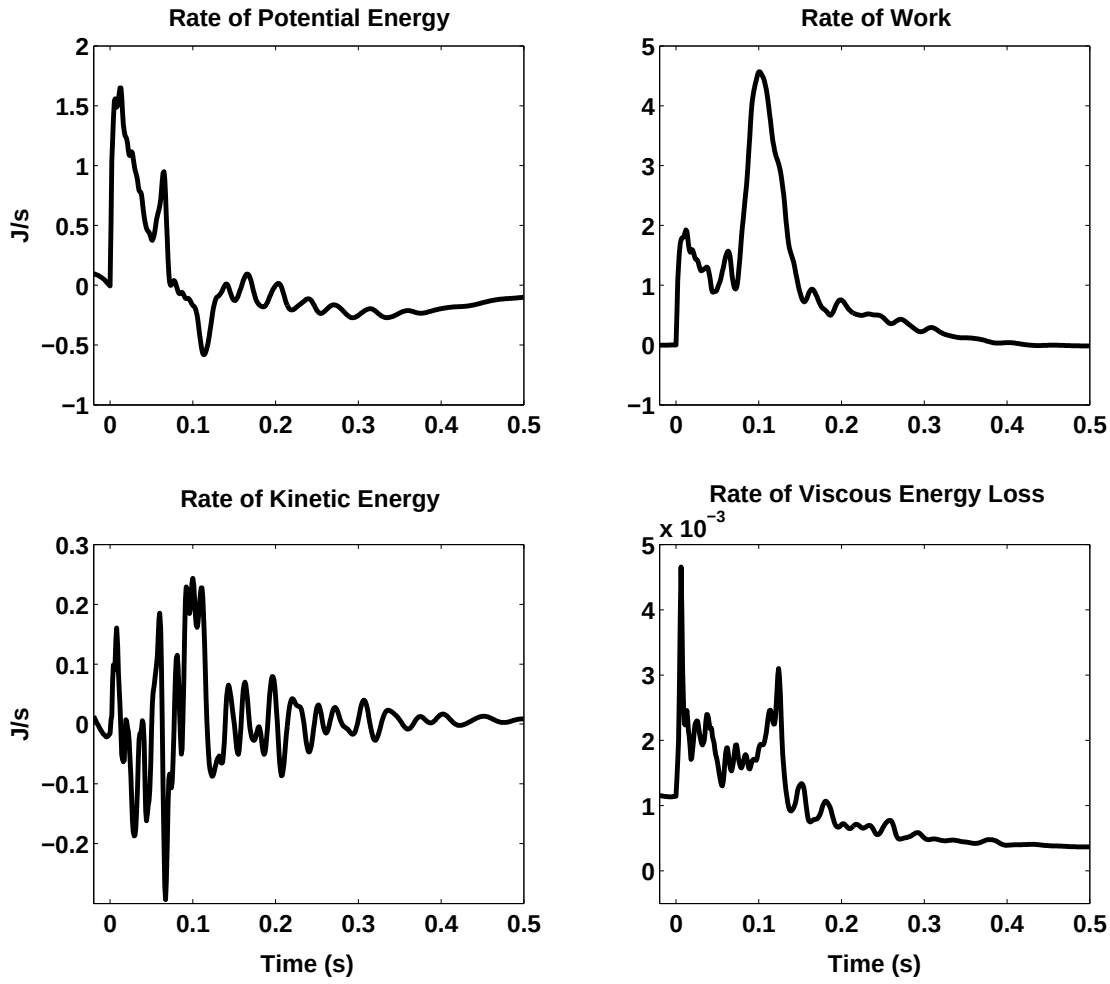

FIGURE 5.20. *Rates of energy and myocardial work during the contractile phases (IVC, systole and IVR) in the LVAD supported LV fullcycle simulation. These results were taken from the third simulated heart beat,* 0.0*s was the beginning of IVC.*

Figures 5.20 and 5.21 show the rates of change of kinetic energy, potential energy, myocardial work, as well as viscous energy dissipation, during systole and diastole respectively. Figure 5.22 shows the energy output, both power and advective gains/losses, from the system across the valve/LVAD cannula boundaries. The results are presented for the third simulated heart beat. During this beat, total myocardial work performed was $0.39J$, with an increase in potential energy (due to minor variations in the start and end point of the cardiac cycle) of $0.0064J$. The change in kinetic energy over the same period was $-7.4 \times 10^{-5}J$.

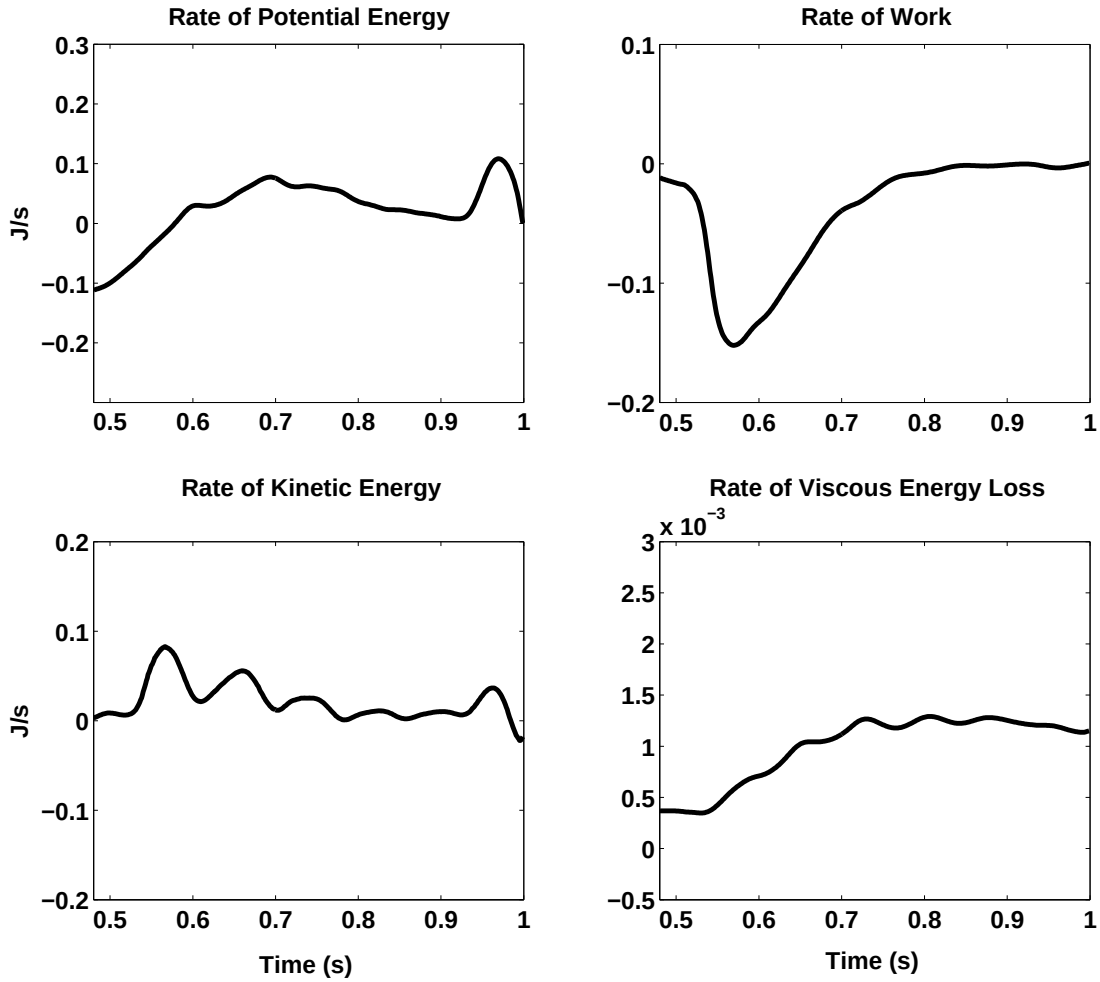

FIGURE 5.21. *Rates of energy and myocardial work during diastole in the LVAD supported LV fullcycle simulation. These results were taken from the third simulated heart beat,* 0.0*s was the beginning of IVC.*

5.3.3.1 Energy Transfer During the Contractile Phases

During the contractile phases (IVC, systole and IVR) of the cardiac cycle the predominant driving energy for LV behaviour was the work performed by the myocardium. Due to the homogeneous activation of contraction, the rate of work rapidly increased at the beginning of IVC. This induced a nearly equivalent increase in myocardial potential energy, as the myocardium twisted and began to build up LV cavity pressure. The ventricular wall motion led to an increase in kinetic energy and a corresponding peak in fluid viscous energy loss. For the remainder of IVC, the rate of work plateaued as the non–linear myocardial material response resisted further deformation. This corresponded to a decrease in the rate of potential energy build up. Throughout this phase the rate of kinetic energy oscillated as momentum shifts led to energy being transfered between the fluid and solid domains.

The opening of the aortic valve during systole resulted in a rapid increase in the rate of myocardial work. In

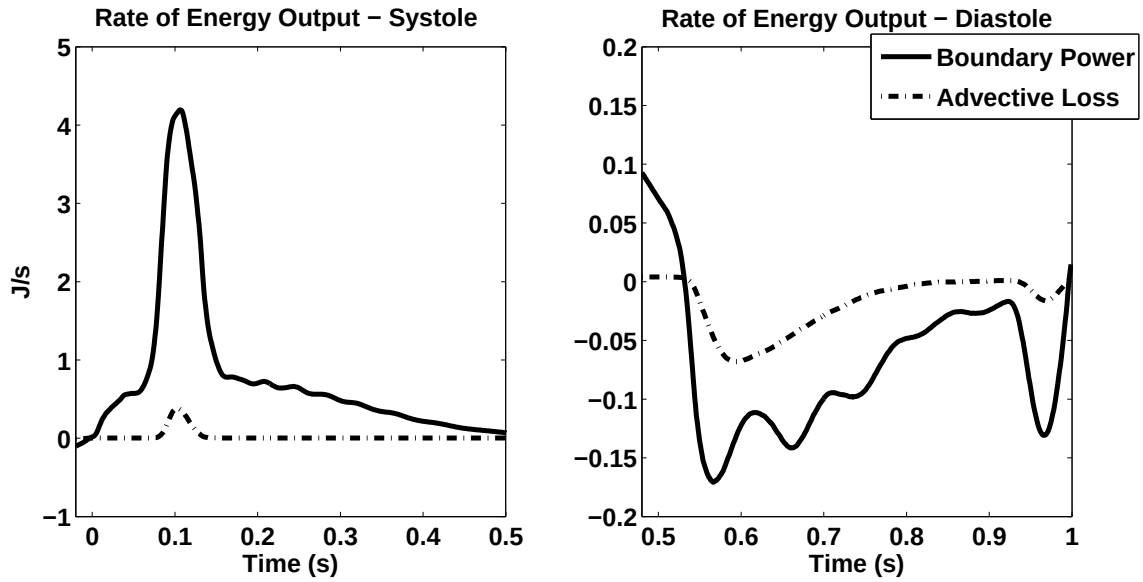

FIGURE 5.22. *Rate of model energy output during systole, left, and diastole, right. The rate of energy output was defined as the total power outputted from the LV model over the valve and LVAD cannula boundaries, as well as any advective gains/losses. Boundary power was equivalent to* $\int_{\Gamma_f} \mathbf{t}(t) \cdot \mathbf{v}(t)\, d\mathbf{x}$ *on the valve/LVAD boundaries, while advective energy loss was* $\frac{\rho}{2} \int_{\Gamma_f} |\mathbf{v}(t)|^2 \mathbf{v}(t) \cdot \mathbf{n}\, d\mathbf{x}$ *on the same boundaries, see appendix B. Note negative energy implies energy added to the system.*

contrast, due to the reducing cavity volume, solid potential energy declined during this period. The outflow from the ventricle increased fluid velocities within the cavity, leading to a peak in kinetic energy, along with viscous dissipation. The bulk of the work performed by the myocardium in systole was transported across the aortic valve, into the Windkessel model (see figure 5.22). Due to the high outflow velocity, there was a peak in boundary advective loss during this period.

The closure of the aortic valve at the start of IVR led to rapid reductions in the rate of myocardial work, kinetic energy increase and fluid viscous dissipation. Once the valve was closed, IVR was characterised by energy oscillations between the myocardium and the fluid. These oscillations were driven by momentum and pressure shifts within the fluid cavity. Throughout IVR, both myocardial work and potential energy gradually declined as the myocardium relaxed. Viscous energy loss through this period was low, stabilising on a baseline rate due to the presence of the LVAD.

Continuous output from the LVAD occurred throughout the cardiac cycle. As pressure increased/decreased throughout the contractile phases the power output over the cannula boundary increased/decreased correspondingly. Since LVAD outflow was constant, advective loss was also constant ($\approx 0.004J \cdot s^{-1}$).

This section discussed the gross energy metrics during the contractile phases in the simulated supported LV. Of additional interest is the spatial distribution of work within the myocardium during these phases. This is presented in figure 5.28, and is discussed in section 5.3.5.

5.3.3.2 Energy Transfer During Diastole

Diastolic filling of the myocardium was driven by the pressure gradient between the LA and the LV. During early diastole, this pressure gradient increased as the myocardium relaxed, evidenced by the negative rate of change in myocardial potential energy. Additionally, due to the inflation of the cavity, negative work was performed, resulting from the residual tension in the contraction model. As mitral inflow increased during this phase, kinetic energy in the fluid increased and there was a corresponding increase in the rate of viscous loss.

The latter part of early diastole, as well as diastasis, was characterised by oscillations in the rate of kinetic energy change as momentum shifts caused energy to be transfered between the fluid and solid domains. Additionally, the pressure waves observed during this phase, see section 5.3.1.1, resulted in oscillations in the rate of energy input across the mitral valve (see figure 5.22). The rate of increase in potential energy declined slowly throughout diastasis, stabilising close to zero towards the end of this phase as mitral inflow approached LVAD outflow. Myocardial work in diastasis also tended towards zero as the remaining active tension was negligible.

Late diastole saw final peaks in the rates of potential and kinetic energies. Due to the non–linear response of the myocardium, the peak in potential energy was substantially greater than that during early diastole. This was matched by a peak in the rate of energy input across the mitral valve.

During diastole, the ratio of advective energy gains/losses to boundary power over the valve/LVAD boundaries was greater due to the lower cavity pressures reducing boundary tractions. As a result, advective energy transfer across the boundaries was more significant during this phase.

5.3.4 Residence Times in the Supported LV

To analyse residence times of fluid within supported LV simulation, the particle tracking algorithm outlined in section 4.3 was used. Of interest were the comparative residence times of particles seeded at different points within the diastolic period. Particles were seeded on the mitral inflow plane at intervals of $0.046s$, with an initial seed time of $0.02s$ and final seed time of $0.048s$ from the commencement of the first diastolic period (*i.e.* $0.5s$ into the LV simulation). 1200 particles were seeded at each interval. The particles were tracked for the remaining $2.5s$ of simulation time. A visualisation of particle movement during the simulation is shown in figure 5.23 and an analysis of the results is provided in figure 5.24.

The most notable feature of this analysis, seen in figure 5.24, was the significantly slower rate of particle expulsion amongst particles seeded during early diastole, compared with those seeded during diastasis and late diastole. Examining the particle movement in figure 5.23, the reasons for this discrepancy are apparent. Particles seeded early tend to spread out through the ventricle as vortices develop. This results in only a small percentage being drawn into the cannula mouth and the remainder being caught in the vortices and pushed out towards the basal region of the LV. Particles seeded later benefit from the pre–established vortical flow features and are drawn directly towards the cannula mouth (see $0.5s$ in figure 5.23). Therefore the particles seeded early tend to be either expelled from the ventricle, via the cannula, or spread out around the cannula

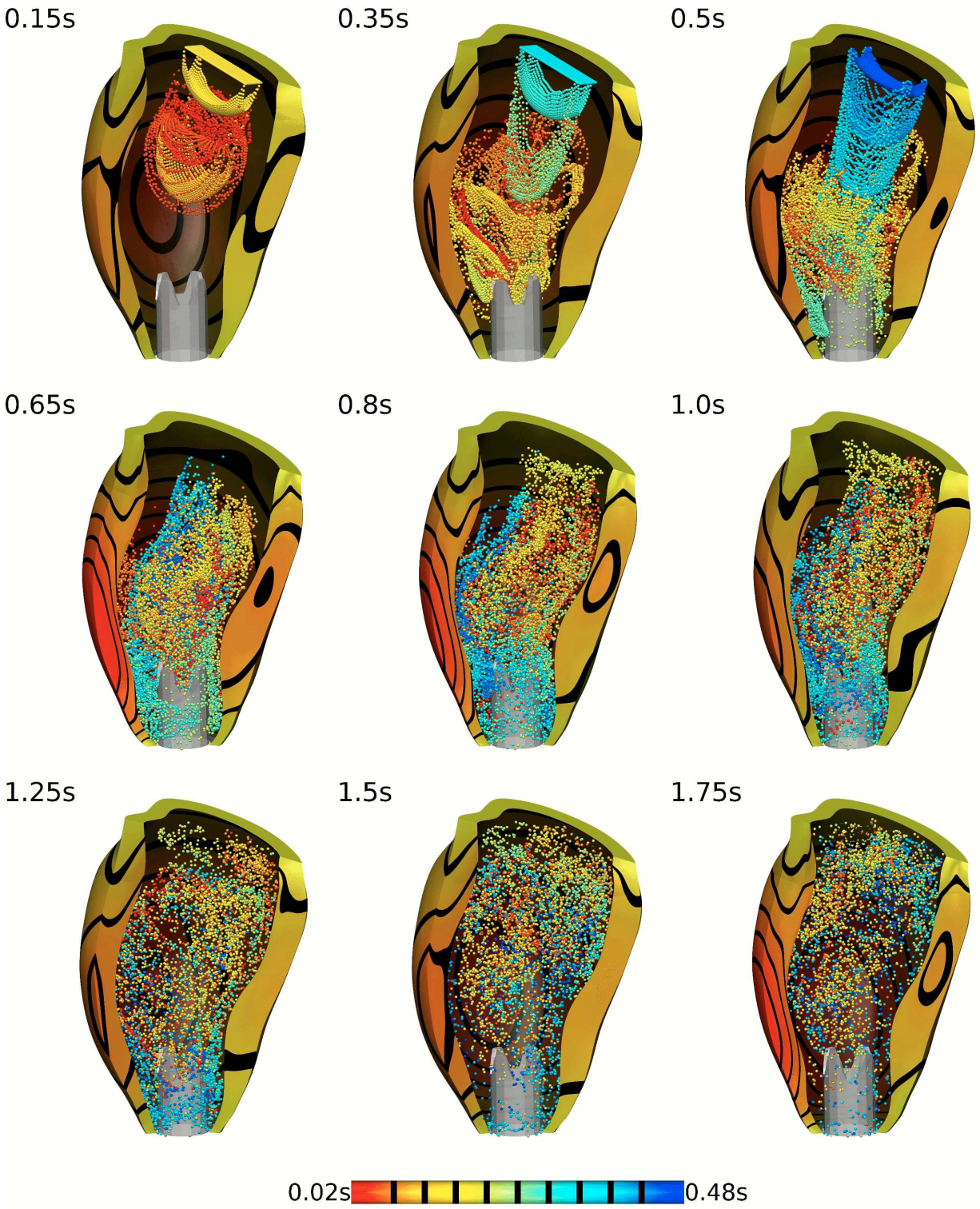

FIGURE 5.23. *Seeded particles coloured by their seed time with respect to the first set of seeded points. Particles were seeded at intervals of* 0.046*s with an initial seed time of* 0.02*s and final seed time of* 0.48*s into diastole. Particle locations are shown at selected time points, during diastole (*0.15*s,* 0.35*s and* 0.5*s), systole, (*0.65*s), isovolumetric relaxation (*0.8*s and* 1.0*s), as well as second instances of diastole (*1.25*s and* 1.5*s) and isovolumetric relaxation* 1.75*s. Note* $t = 0$ *is equivalent to the commencement of diastole.*

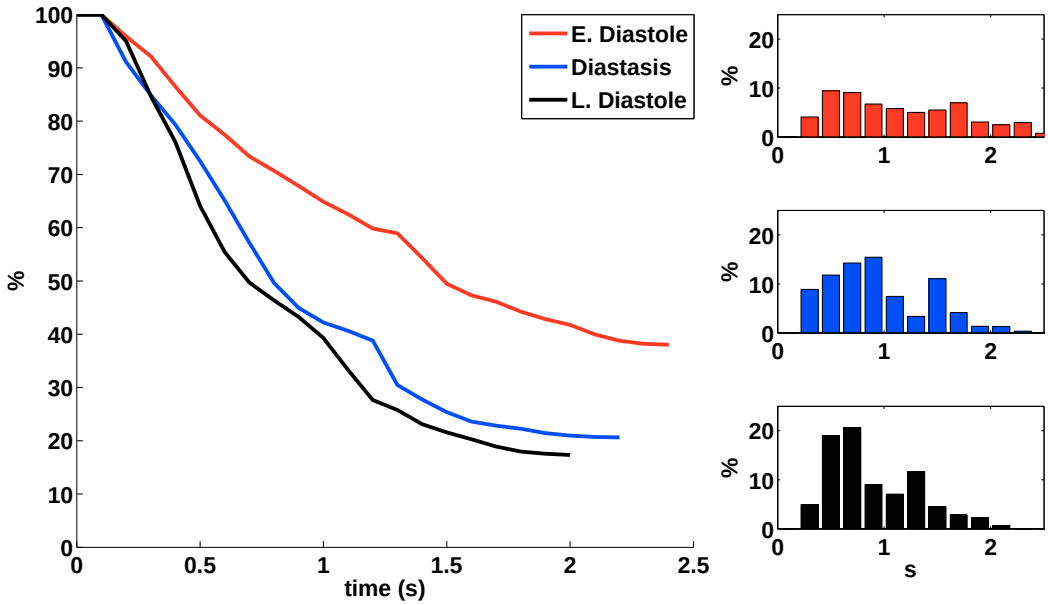

FIGURE 5.24. *Results from the particle seeding analysis of the LVAD supported LV simulation. Results are summarised by the period of diastole within which they were seeded* – i.e. *early diastole (seed times from* $0.02s$ *to* $0.18s$*), diastasis (seed times from* $0.23s$ *to* $0.36s$*) and late diastole (seed time from* $0.36s$ *to* $0.48s$*). Left, the percentage of points remaining in the LV over time from seeding. Right, the percentage of points exiting the LV over discrete time intervals after seeding. Time is given as the time from the mean point of each seeding interval.*

base. Due to the relatively low quantity of blood expelled via the aortic valve during systole, particles located in the basal region of the heart are unlikely to exit the ventricle during this period. Additionally, migration towards the basal region is slow. Since the particles in this region are predominantly those seeded during early diastole (see $0.65s$, $0.8s$ and $1.0s$), residence times for these particles are longer.

An additional feature observed in the particle tracking results, was the mixing of particle groups through time. The results at $0.15s$ and $0.35s$ show clear sheets of particles spreading out through the LV cavity. By $0.5s$ the particles seeded early have begun to mix. Examining the results between $0.65s$ and $1.0s$, two discernible groups of results are apparent – those seeded early and located at the basal region, and those seeded late and predominantly located in the apical region. Finally, the results between $1.25s$ and $1.75s$ show the breakdown of these groups, with particles spread relatively evenly through the LV. This is highlighted by the relatively comparable rates of particle expulsion between the groups observed after $\approx 1.25s$.

Unfortunately, due to slow leakage across the FD cannula, determination of residence times of blood located around the cannula base is not feasible. However, observed velocities in this region were low, indicating that the pooling of blood at the cannula base was an issue.

5.3.5 Comparison with a Solid Only Cardiac Model

Many ventricular models in the literature[123, 182, 126, 130] involve simulations of myocardial behaviour where the fluid within the LV cavity is represented as a uniform pressure on the endocardial wall. However, to our knowledge, there has yet to be a study of the impact a physical representation of the fluid has on these simulations. This section presents the results of a solid only LVAD supported LV simulation and compares these results with the coupled fluid–solid simulation presented above. The gross pressure volume metrics are discussed in section 5.3.5.1, a comparison of work and energy between the two models is provided in section 5.3.5.2, and the spatial distribution of work is examined in section 5.3.5.3.

A solid only simulation, over the full cardiac cycle, was performed on an LVAD supported LV. The same myocardial mesh was used as in the coupled fluid–solid LV model and the simulation was coupled to the Windkessel model using the Lagrange multiplier volume constraint introduced in section 2.5.5.2. The simulation was initiated at the same point as the coupled simulation, using the same Windkessel and contraction parameters and initial conditions. With the exception of the endocardial wall (where the volume constraint condition was applied), boundary conditions on the myocardium were also the same. As above, the simulation was run for three cardiac beats, however, in this case each beat consisted of 200 time steps of $0.005s$.

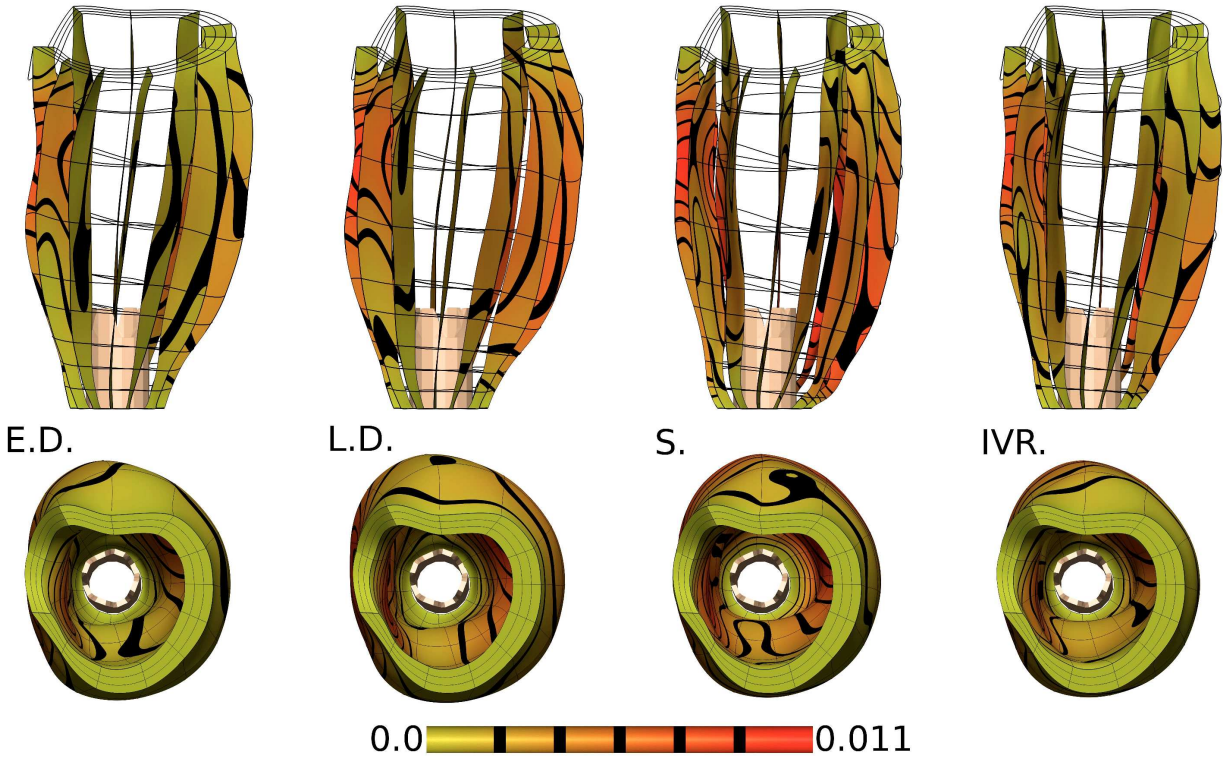

Figure 5.25. *A visualisation of the solid only simulation results at early (0.15s) and late diastole (0.45s), systole (0.6s) and IVR (0.8s), where 0.0s is defined as the beginning of diastole. The colour scheme represents myocardial displacement, scale in m. Note the LVAD is shown to provide a reference and was not part of the simulation.*

Snapshots of the results in each cardiac phase are shown in figure 5.25. In this figure the slight twisting and apical movement of the myocardium during contraction is visible, however, as above twisting was limited by

the fixed apex due to the presence of the LVAD cannula.

5.3.5.1 Comparison of Gross LV Metrics

Using the Lagrange multiplier (representing LV cavity pressure) and Windkessel model results, the gross LV metrics for the solid only model could be compared with those from the fluid–solid coupled LV simulation. Figure 5.26 shows a comparison of the the pressure volume relationships between the two models. The solid model converged on a similar pressure volume loop to the coupled model. Minor discrepancies included a slightly lower peak LV pressure and stroke volume. Additionally, the oscillations in ventricular pressure, observed in the coupled model due to pressure waves and momentum shifts within the fluid, are not present as cavity pressure was homogeneous and solid momentum was not included in the model.

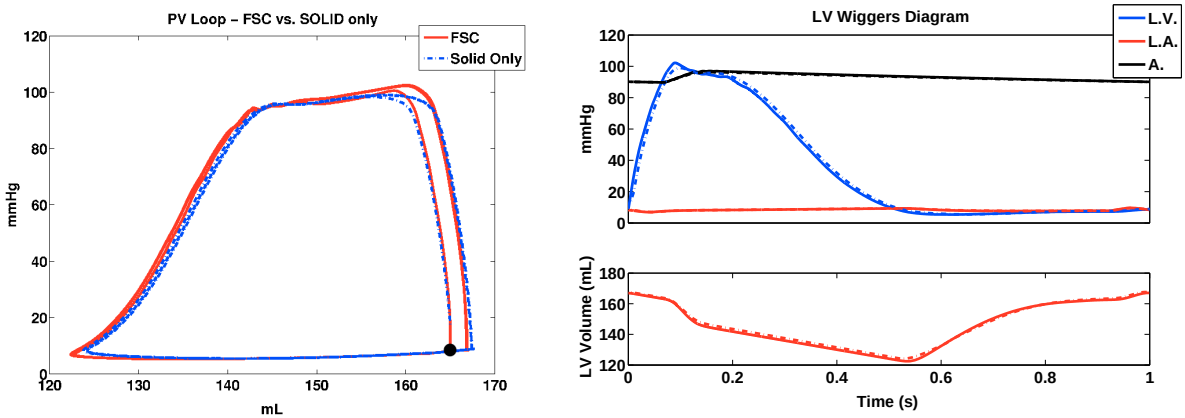

Figure 5.26. *Comparison of the pressure volume loops and Wigger's diagrams from the solid only and solid–fluid coupled supported LV simulations. Solid only results are the dashed lines. The pressure volume loop show the results from all three simulated beats, the black dot shows the initial starting point. The Wigger's diagram shows LV pressure and volume, along with LA and Aortic (A.) pressures, from the third simulated heart beats.*

The boundary conditions on the LV model were possibly responsible for the closeness in the pressure volume relationships observed in the two simulations. By fixing both the apex and the base, myocardial movement was restricted. This led to potentially lower endocardial fluid velocities than would have been present if more myocardial motion was possible. As a result, the impact of the fluid on the overall pressure volume relationship was reduced.

5.3.5.2 Comparison of Cardiac Energy and Work

A comparison of myocardial work, rates of potential energy and energy output from the third cardiac beat of each model is presented in figure 5.27. For the solid only simulation, energy output was equivalent to the work performed by the endocardium against the cavity pressure as there were no kinetic forms of energy within the model, or loses via either viscous or advective processes. Over the third cardiac beat, the total work performed by the myocardium in the solid only model was $0.36J$ (compared with $0.39J$ in the coupled model) and the change in potential energy, due to minor variations in the start and end points of the cardiac cycle, was $0.012J$

(compared with $0.0064J$ in the coupled model). Since no energy sinks were present in the solid only model, energy output was $0.35J$ over the third cardiac beat. In the coupled model, power output to the Windkessel model over the valve/LVAD boundaries was $0.36J$, roughly comparable to the solid only model.

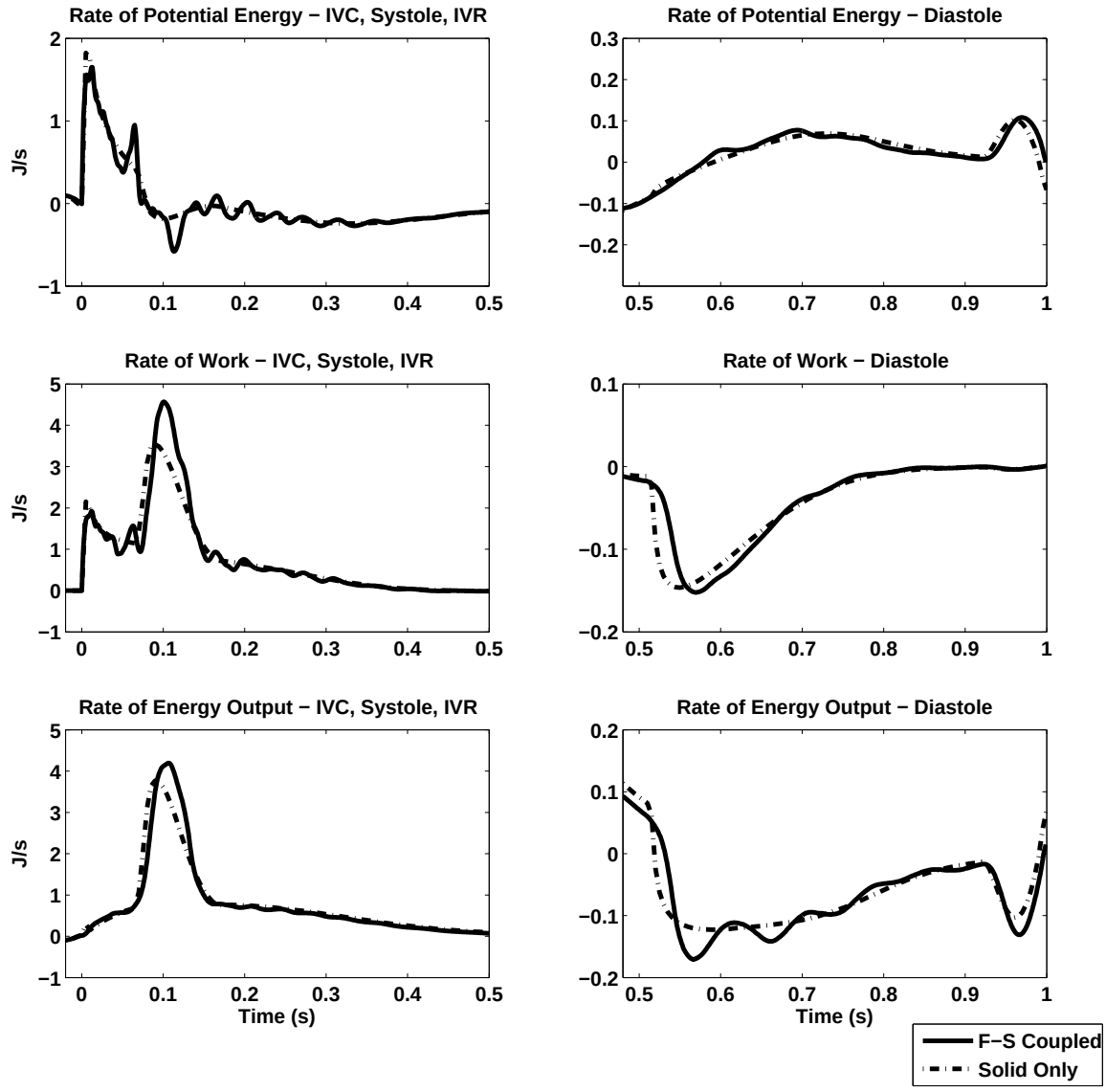

FIGURE 5.27. *A comparison of the rates of potential energy and work during the contractile phases (IVC, Systole and IVR), left, and diastole, right, between the solid only and coupled fluid–solid LVAD supported LV simulations. Additionally, the cardiac energy output, defined as the power output across the valve and LVAD boundaries, is displayed. Note that for the solid only simulations this is equivalent to the work performed by the myocardium on the entire LV cavity. However, for the fluid–solid coupled simulations, energy can be stored as kinetic energy in the fluid, or lost through viscous dissipation and boundary advection. Therefore, it is equivalent to the tractions acting on the valve/LVAD boundaries, see figure 5.22.*

With the exception of energy oscillations due to the transfer of energy between the fluid and solid domains, the same general trends were observed as discussed in section 5.3.3. Of note was the significantly greater rate

of myocardial work during systole. Due to advective losses on the aortic boundary, when transfered to energy output across the aortic boundary, this discrepancy was reduced.

5.3.5.3 Spatial Variation of Work

In the solid only model the ventricular cavity is represented as a homogeneous pressure on the endocardial surface. As a result, there is roughly equivalent resistance to endocardial work throughout the cavity, *i.e.* traction on the endocardial surface is,

$$\mathbf{t}_{endo} = -p\mathbf{I} \cdot \mathbf{n}, \tag{5.13}$$

where p is a constant. In contrast, in the coupled LV model traction is,

$$\mathbf{t}_{endo} = (\mu \mathcal{D}_{\mathbf{x}}\mathbf{v} - p\mathbf{I}) \cdot \mathbf{n}, \tag{5.14}$$

where, as shown in section 5.3.1, both pressure and velocity vary significantly throughout the fluid volume. The impact of this variation on the energetics of the myocardium can be highlighted by examining the spatial variation of work in the LV. Figure 5.28 compares the spatial variation of work and work intensity during the contractile phases of the cardiac cycle in the third heart beats of the solid only and coupled LVAD supported LV simulations.

In the solid only model the spatial variation of work intensity was fairly uniform. As a result, the largest contribution to myocardial work came from the mid–wall sections of the thicker myocardial regions. In contrast, in the fluid–solid coupled results, large variations, both positive and negative, in regional work intensity were observed. While the total magnitude of work performed by the myocardium at each point was roughly comparable, due to the heterogeneity in observed work intensity, the magnitude of work in local regions was substantially greater.

The primary reasons for the large variation in work and work intensity in the coupled LVAD supported LV results were the large momentum and pressure shifts observed in the fluid. A stronger local contractile force results in an increase in local pressure. This forces fluid away from this local region to another part of the LV cavity. The outflow from this region will reduce local strain, causing positive work. In contrast, in the regions in which flow is incoming, strain will be increased, causing negative work. Due to the force length response, these changes in strain reverse the discrepancy in local force generation, resulting in the oscillations in work and work intensity observed. In the solid only case, stronger local contractile force impacts overall cavity pressure only. As a result, its impact on LV pressure is spread over the entire endocardium. This results in the much more homogeneous work and work intensities observed in the solid only case.

5.4 Discussion of LVAD Supported LV Simulations

This chapter presented the first, to our knowledge, biophysically based coupled fluid–solid model of an LVAD supported LV. The model, coupled to a Windkessel model of the systemic circulatory system, converged on a stable pressure volume loop over 3 cardiac beats. Additionally, an analysis of residence times within the model was outlined. Finally, the simulation results were compared with equivalent results from a solid only model.

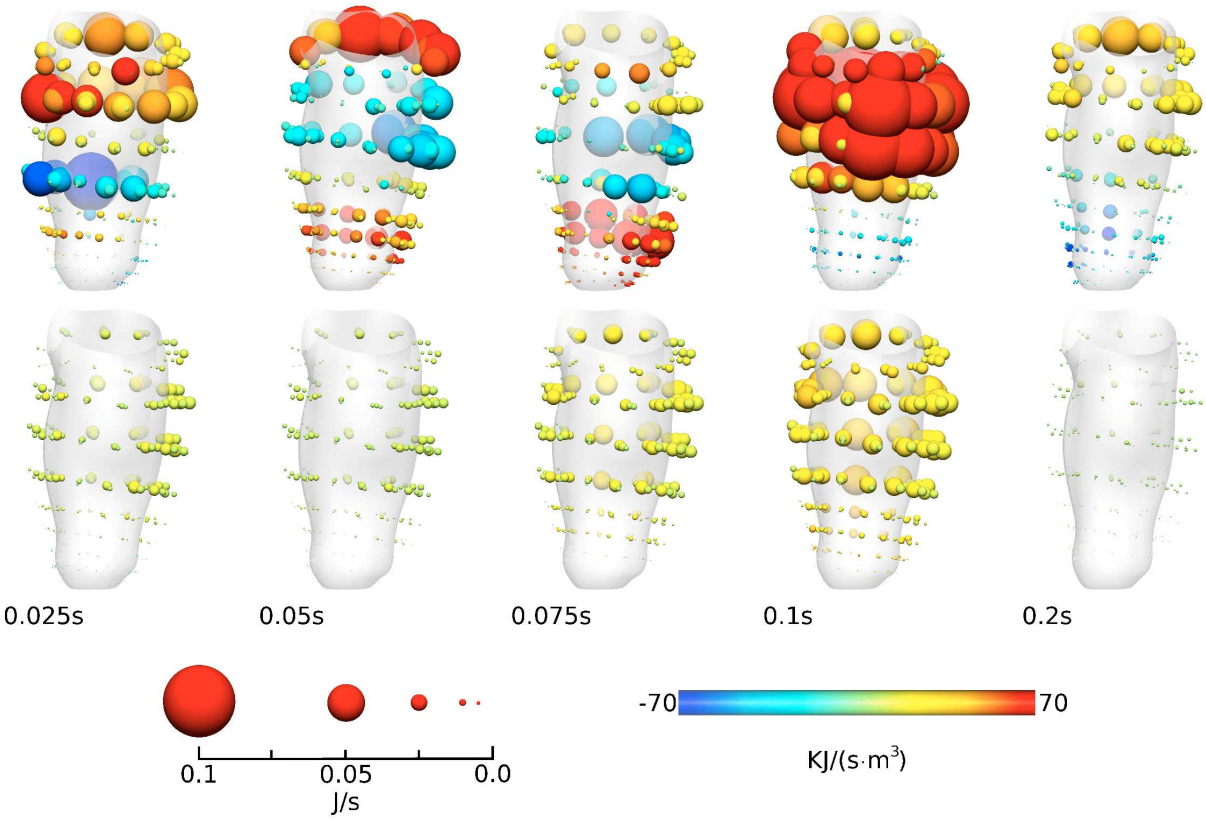

FIGURE 5.28. *Spatial distribution of work during IVC (*0.025*s and* 0.05*s), systole (*0.075*s and* 0.1*s) and IVR (*0.2*s) in the fluid–solid coupled (top row) and solid only (bottom row) supported LV simulations. For reference,* 0.0*s was the beginning of IVC. The visualised results are from the third simulated heart beat in each simulation. Spheres are located at myocardial element centrepoints and are scaled by the magnitude of elemental rate of work ($J \cdot s^{-1}$). Sphere colour, blue to red, is the mean intensity of work ($J \cdot s^{-1} \cdot m^{-3}$) within the element. Total rate of work in the LV at each visualised time point was:* 0.025*s –* $1.46J \cdot s^{-1}$ *(solid only),* $1.42J \cdot s^{-1}$ *(coupled);* 0.05*s –* $1.21J \cdot s^{-1}$ *(solid only),* $0.98J \cdot s^{-1}$ *(coupled);* 0.075*s –* $2.21J \cdot s^{-1}$ *(solid only),* $1.12J \cdot s^{-1}$ *(coupled);* 0.1*s –* $3.34J \cdot s^{-1}$ *(solid only),* $4.56J \cdot s^{-1}$ *(coupled); and* 0.2*s –* $0.64J \cdot s^{-1}$ *(solid only),* $0.75J \cdot s^{-1}$ *(coupled).*

This represented the first, again to our knowledge, comparison between coupled fluid–solid and solid only LV simulations present in the literature.

From the model, two primary results were observed that warrant further investigation. The first, related to the the relatively low recirculation rates observed in particles entering the LV chamber during early diastole. This was primarily due to the low aortic outflow during systole. The result indicates the importance of aortic opening on blood recirculation in an LVAD supported LV. The second key result was the extent of heterogeneity observed in myocardial work. Further investigation is required to determine the extent of this variance with other geometries and boundary conditions. Additionally, of interest is its impact on myocardial energetics and energy consumption.

With respect to the modelling of cardiac mechanics, the comparison between the solid only and fluid–solid coupled LV simulations highlights the relevance of each modelling type to different physiological problems. The gross pressure, volume and energy metrics from the solid only results were roughly comparable to those

observed in the full fluid–solid coupled simulation. This indicates that for physiological problems where only gross metrics are of interest, a solid only LV model provides a good approximation of the results from a fully coupled model. However, the heterogeneity in the spatial distribution of work and work intensity, limits the capacity of solid only models to address problems relating to local myocardial behaviour.

As with any computational biological model, various limitations restrict the capacity of the model to replicate true physiological behaviour. For the coupled fluid–solid LV model presented in this chapter, the primary limitations revolve around the boundary conditions applied to the model. Restricting apical and basal movement limits the capacity of the endocardium to move freely. While the presence of the LVAD cannula naturally restricts apical movement, a representation of physiological basal movement would require either a mathematical description of its behaviour, or a model of the LA to be coupled to the LV model. Additionally, since the model considers the LV in isolation, the impact of external forces, specifically on the inflow and outflow boundaries, can only be approximated. Improvements to the prescribed profile 0D/3D coupling method could be obtained through an a priori knowledge of mitral and aortic flow profiles. However, ultimately, separation of the 0D/3D interface from the LV, via either cannula or models of the LA and the aorta, is desirable. Finally, the impact of the smoothness of the endocardial surface, along with the absence of papillary muscles and valves, on fluid mechanics in the LV is unknown.

Part III

Patient Customisation

6 A Patient Model of an LVAD Supported LV

The previous chapter presented a model of left ventricular function under LVAD support in a normal LV. However, during heart failure, the size, geometry and behaviour of the LV are profoundly altered, typically resulting in ventricular dilation coupled with reduced contractile strength. To understand how these changes impact the hemodynamics of the LV, along with myocardial function, the model must be customised to patient geometries and constitutive properties. Customising the model in this way enables an experimental platform to be built, on which the impact of variations in the LVAD treatment protocol can be tested.

This chapter presents a patient model, developed from data provided by Berlin Heart[209] and Philips Research[213], that was used to investigate the impact of LVAD support on the failing heart. The model construction and parameter tuning is outlined in section 6.1, while the results from simulations performed on the model are presented in section 6.2.

6.1 Patient Model

The patient model was developed from a CT scan of a 53 year old, male, LVAD implant recipient. The resulting image sequence, taken at end diastole, was used to construct a geometric model of the LV (section 6.1.1). Due to a paucity of pressure data taken at the time of imaging, the passive (section 6.1.2) and active (section 6.1.3) material parameters were fitted to comparable LVAD patient data found in the literature. The resulting fitted model was then used to investigate the impact of a variety of LVAD flow regimes on ventricular function. The experimental protocol for this investigation is provided in section 6.1.4.

6.1.1 Patient Customised Myocardial Geometry

A patient customised LV geometry was constructed based on 422 CT image slices taken from a 53 year old dilated cardiomyopic heart failure patient with an implanted LVAD. The spatial resolution of the image stack was $0.4mm \times 0.4mm$, in the CT image plane, and $0.6mm$ in the through plane direction. Digitisation of the image data was performed by Philips Research and the resulting binary segmentation was used to construct the geometric myocardial mesh. Figure 6.1 details the mesh generation procedure.

The myocardial mesh was created using the procedure outlined in Lamata *et al.*[91]. This method involves the construction of a cubic Hermite template mesh which is warped, using a variational technique, to match the

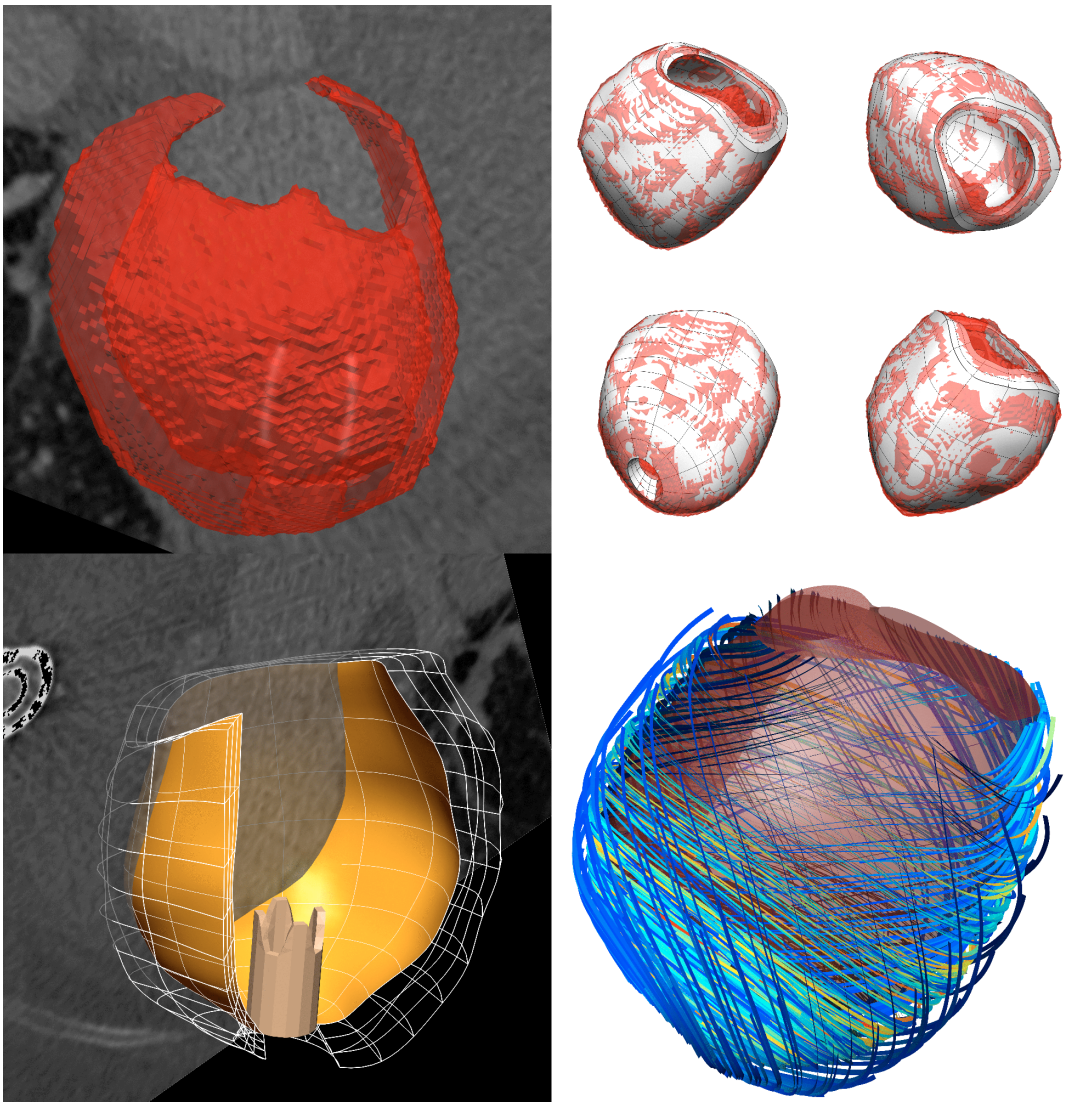

FIGURE 6.1. *Myocardial geometry fitting to patient image data. Top left, digitised binary myocardial map superimposed against a CT slice, LVAD cannula visible; top right, the fitted myocardial geometry compared with the binary myocardial map; bottom left, the fitted myocardial geometry superimposed against a CT slice; bottom right, visualisation of the* $\pm 60^\circ$ *fibre geometry.*

digitised data. The technique is a two stage process whereby, firstly, a binary representation of the template geometry is registered to the segmented data, before secondly, the warping field, resulting from the registration process, is applied to deform the template mesh. For the LVAD supported LV case an ellipsoidal topology was used as the mesh template. This was fitted, using an automated meshing tool[90], to the segmented binary data with a mean error (with respect to the normal distance between binary data and the fitted mesh) of $0.72mm$ $\pm 1.05mm$.

The final fitted cubic Lagrange mesh was interpolated from the warped cubic Hermite geometry. The resulting HEX(3,3,2,3) mesh consisted of 324 elements, with a through wall thickness of 3 elements. As before, an idealised fibre geometry, $\pm 60^\circ$ on the endo/epicardial surfaces, was defined within the myocardial geometry.

Within the ventricular cavity formed by the fitted myocardial geometry, a linear tetrahedral fluid mesh, consisting of $\approx 3.2 \times 10^4$ elements, was constructed using the software package CUBIT[65], with a characteristic mesh length of $3.2mm$. The linear mesh was modified to provide a curvilinear description (TET(2cr,2cr,1dc)) of the cavity by projecting surface nodes onto the endocardial surface. Internal nodes were unchanged maintaining the linear spatial description of non–boundary fluid elements. The LVAD cannula was prescribed as a FD and the geometry, provided by Berlin Heart, was as defined previously in this thesis. Using this geometry, the FD mesh was constructed, with a characteristic length equivalent to that of the fluid mesh, from 544 TRI(1,0) elements

6.1.2 Passive Myocardial Parameters

To incorporate the residual strain, present in the myocardium at end diastole, an estimate of the zero–stress, or reference state of the myocardium is required. Using the method outlined in section 4.2.2, the passive myocardial parameters were fitted to the Klotz pressure volume relationship[83] defined by the end diastolic volume of $240.95ml$ and pressure of $13.13mmHg$. Since patient specific pressure data was not available, the pressure value was taken from equivalent LVAD supported patient data in Klotz *et al.*[82].

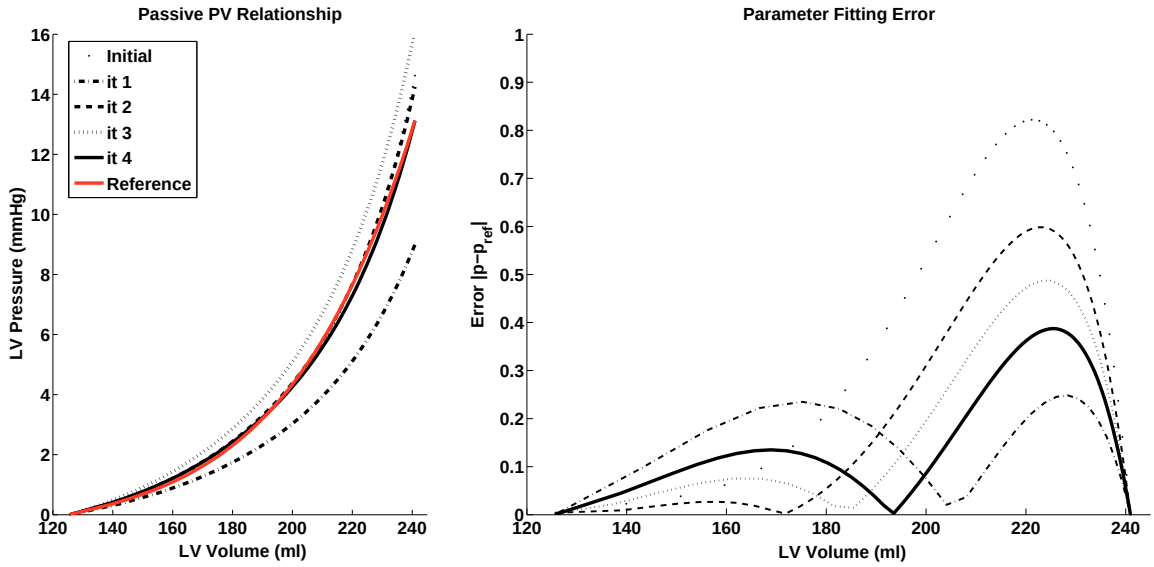

FIGURE 6.2. *Fitting of patient passive myocardial parameters. Left, iterative updates of the passive PV relationship (it 1 to 4); right pressure error ($|p-p_{ref}|$) with respect to cavity volume, scaled so that end diastolic pressure was equivalent for all iterations. p_{ref} is the reference pressure from the reference curve calculated from Klotz* et al.[83] *for an end diastolic volume and pressure of* $240.95ml$ *and* $13.13mmHg$ *respectively.*

Starting with the fitted parameters from the normal LV mesh (section 4.2.2), a bisection method was used to iteratively minimise the cost function (equation 4.17) of the error between the model pressure volume relationship and the estimated Klotz relationship. The iterative updates of the model pressure volume relationship, as well as the error compared with the Klotz relationship, are provided in figure 6.2 and table 1. The final, fitted, parameter values are given in table 2, while a visualisation of reference mesh, along with the

Iteration	0	1	2	3	4
Error $\|p - p_{ref}\|$	6.77	4.52	3.21	3.09	2.11

TABLE 1

Total error for each iteration of the passive myocardial fitting procedure.

$C(KPa)$	$C_2(KPa)$	b_1	b_2	b_3	b_4	b_5	b_6	K	C_Ψ
380.05	380.05	33.41	6.45	3.61	14.68	10.92	4.83	33.41	3000

TABLE 2

Fitted Costa law parameters for the patient myocardial model.

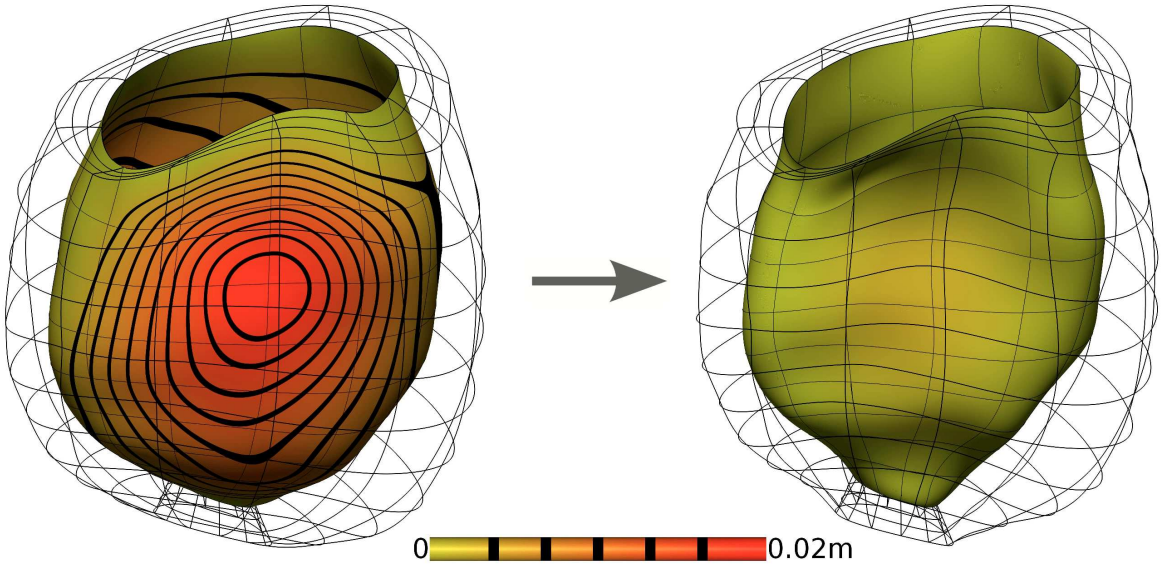

FIGURE 6.3. *Left, initial end diastolic configuration, right, estimated zero stress state. Scale shows the Euclidean displacement, from the zero stress state, in the geometry at end diastole.*

residual deformation at end diastole, is shown in figure 6.3.

6.1.3 Active Myocardial Parameters

One of the primary challenges in fitting biophysically based contraction models to patient data is overcoming the disconnect between tension generation observed in myocytes and the cavity pressures observed on the organ scale. This can be seen in the results presented in chapter 5, where the tension generation in the contraction model was largely symmetric through the contractile phases (figure 5.4), yet the duration of isovolumetric contraction was relatively short, while the duration of isovolumetric relaxation was overly long (figure 5.18). This observation has also been made in other studies, including Niederer *et al.*[129] and Nickerson *et al.*[126].

To resolve this issue, simpler functional models have been developed[74, 128] that can be fitted to patient data

by tuning gross parameters such as the model length dependence and the rate of tension development. Since clinical measurements can only be made of these gross metrics, these relatively simplified models provide the ability to determine a unique parameter fit to available data. Specifically, for this patient study the Niederer contraction model[128] was implemented (section 6.1.3.1). The parameters for this model were then fitted to available data (section 6.1.3.2).

6.1.3.1 Niederer Contraction Model

The Niederer contraction model is based on a previous model by Kerckoffs *et al.*[74]. To reduce the number of parameters that were required to be fitted, and to improve the uniqueness of the parameter fit, the contraction model was developed with a focus on tension development and systole, while providing a limited representation of relaxation. The resulting 6 parameters capture the length dependent rates of tension development, along with peak tension. In the model, active tension, T_a, is defined as,

$$\phi = \tanh(a_1(\lambda - a_2)), \tag{6.1a}$$

$$t_r = t_{r0} + a_3(1 - \phi), \tag{6.1b}$$

$$T_a = \begin{cases} T_0\,\phi \tanh\left(\frac{t}{t_r}\right)^2 \tanh\left(\frac{t_{max}-t}{t_d}\right)^2 & 0 < t < t_{max} \\ 0 & \text{else} \end{cases}, \tag{6.1c}$$

where $\lambda = \sqrt{2\mathbf{E}_{F,ff} + 1}$ is the strain in the fibre direction, a_1 corresponds to the degree of length dependence, a_2 is the length at which no tension is generated, a_3 is a scalar of length dependent activation, t_{r0} is the baseline activation time constant, t_d is the relaxation time constant, t_{max} is the duration of tension generation and T_0 is the peak isometric tension. The function t_r regulates the rise time of the tension transient, while ϕ is a nonlinear length dependent function.

6.1.3.2 Parameter Fitting

The contraction parameters were tuned so that LV stroke volume was $\approx 50ml$ and peak systolic pressure was between 100 and $120mmHg$ when the LVAD was switched off, consistent with observations in Klotz *et al.*[82]. Additionally, due to the slow rate of myocardial relaxation typically observed in cardiomyopic heart failure patients[62], the desired durations of isovolumetric contraction and relaxation were $0.1s$ and $0.2s$, with a systolic period of $0.2s$. Fitting of myocardial constitutive parameters was performed as a solid only problem, coupled to the Windkessel model using the volume constraint Lagrange multiplier.

To enable the Windkessel model to provide adequate feedback to changes in the active contraction model, it was tuned, by varying the pulmonary and systemic resistances, along with the total volume of fluid in the system, to match the desired patient gross metrics. The modified Windkessel parameters are provided in table 3.

The myocardial model was coupled to the fitted Windkessel model and the values from Niederer *et al.*[128] (fitted to a cardiac resynchronisation therapy patient, pre–operation) were used as an initial configuration

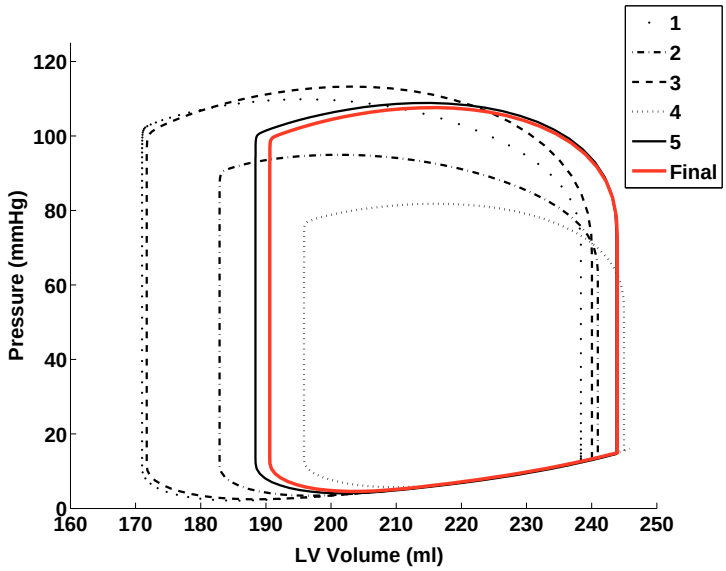

FIGURE 6.4. *A sample of PV loops from the fitting of the active tension and Windkessel models. The models were fitted for a stroke volume of* $\approx 50ml \cdot s^{-1}$ *and peak LV pressure during systole of between* 100 *and* $120mmHg$*. The final fitted relationship is in red.*

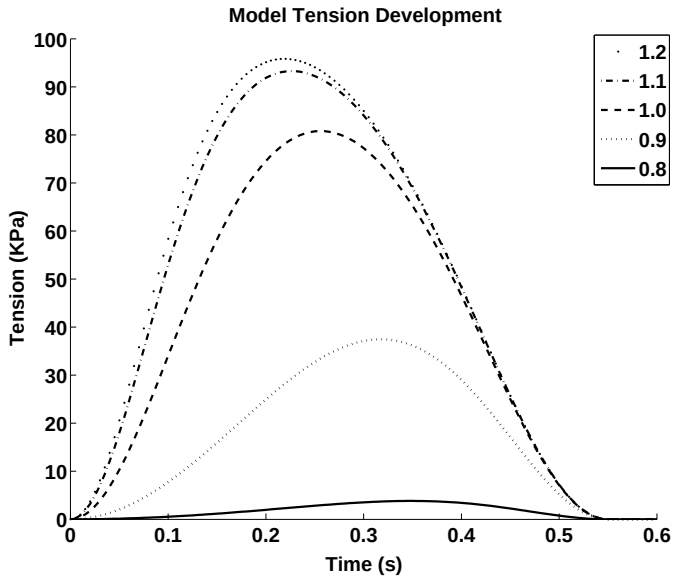

FIGURE 6.5. *Model tension development over time for different fibre strains* ($\lambda = \sqrt{2\mathbf{E}_{F,ff} + 1}$).

R_{scp} $(mmHg\,s\,ml^{-1})$	R_{pcp} $(mmHg\,s\,ml^{-1})$	V_{lv} (ml)
0.70	0.45	905

TABLE 3

The tuned Windkessel model parameters. The values were varied so that the Windkessel PV relationship matched that desired from the myocardial model. See appendix D for the other parameter values.

T_0	t_{r0}	t_d	a_1	a_2	a_3
$120KPa$	$0.11s$	$0.199s$	2.0	0.7	3.2

TABLE 4

Fitted Parameters for the Niederer contraction model.

for the fitting of the active tension parameters. Holding the constants a_2 and a_3 fixed, a parameter sweep was performed to determine the optimal values of the time constants, t_{r0} and t_d, as well as the a_1 length dependence constant, with respect to the desired gross ventricular metrics. Peak isometric tension (T_0) was scaled so that peak systolic pressure fell within the desired region. A sampling of PV relationships from this sweep is provided in figure 6.4. The final, fitted parameter values are given in table 4, while the strain/tension generation relationship for the fitted model is shown in figure 6.5.

6.1.4 Experimental Protocol

Simulations on the patient model were performed using a variety of LVAD flow protocols, ranging from the LVAD switched off to an LVAD flow rate of $100ml \cdot s^{-1}$. The protocols are defined in table 5 and were selected to test the impact of various constant flow rates, as well as the effect of transient flow profiles either increasing, or decreasing during systole, and vice versa during diastole.

Simulation	Flow rate $(ml \cdot s^{-1})$	Description
L_0	$Q_{LVAD} = 0$	LVAD switched off
L_{60}	$Q_{LVAD} = 60$	Constant flow rate
L_{80}	$Q_{LVAD} = 80$	Constant flow rate
L_{100}	$Q_{LVAD} = 100$	Constant flow rate
L_{s60+}	$Q_{LVAD} = 60 + 45sin(2\pi t)$	Sinusoidal flow rate, in sync
L_{s60-}	$Q_{LVAD} = 60 - 45sin(2\pi t)$	Sinusoidal flow rate, counter sync
L_{s80+}	$Q_{LVAD} = 80 + 60sin(2\pi t)$	Sinusoidal flow rate, in sync
L_{s80-}	$Q_{LVAD} = 80 - 60sin(2\pi t)$	Sinusoidal flow rate, counter sync

TABLE 5

LVAD flow protocols for the patient study. Time $t = 0$ was taken with respect to the start of isovolumetric contraction, while in sync refers to increasing LVAD flow during systole and, conversely, counter sync refers to decreasing flow. Total flow rate through one cardiac cycle in the sinusoidal LVAD protocols was the same as for their equivalent constant flow rate cases.

For each flow protocol, simulations were performed for two heart beats, each of one second, consisting of 2500 time steps per beat, with a time step of $0.00025s$ during the contractile phases and $0.001s$ during diastole. A linear activation sequence, endocardium to epicardium, was defined with a period of $0.05s$.

Model boundary conditions were the same as in chapter 5, however the initial configuration varied depending on the flow protocol. Solid only simulations were performed to converge the myocardial and Windkessel models on repeating pressure volume loops for each of the flow protocols. The solutions from each of these simulations were used as the initial conditions in each case. In the L_{100} case, a converged solid only pressure volume loop (defined as less than 0.5% difference between heart beats) was not reached and the initial configuration was taken as the solution after 10 heart beats. The relevant LV and Windkessel model initial conditions are provided in table 6. Note that due to continuous flow through the LVAD, increased LVAD flow rates led to increased aortic pressures.

	LV Parameters		Windkessel Parameters		
	V_{LV}	P_{LV}	P_{LA}	V_{LA}	P_{Ao}
L_0	247.24	16.09	13.62	59.24	75.07
L_{60}	232.37	10.60	9.79	42.49	107.49
L_{80}	225.55	8.75	8.35	36.19	120.18
L_{100}	179.07	2.00	2.60	11.01	150.47
L_{s60+}	234.38	11.21	10.23	44.41	101.74
L_{s60-}	230.01	9.92	9.30	40.33	113.56
L_{s80+}	227.79	9.32	8.74	37.90	114.22
L_{s80-}	222.35	7.99	7.82	33.87	126.80

TABLE 6

Initial LV pressures and volumes, as well as the Windkessel model initial values for the left atria (LA) and aorta (Ao). The values were taken from the solid only models at end diastole, after convergence on a repeating pressure volume loop (For the L_{100} case the values are from the 10^{th} heart beat as convergence was not reached). Pressures (P) are given in $mmHg$, while volumes (V) are in ml. All initial flow rates across the mitral and aortic valves, as well as the LVAD cannula, were zero.

The resulting problems, initiated from end diastole, consisted of $\approx 5.5 \times 10^5$ fluid and $\approx 3.4 \times 10^4$ solid degrees of freedom. The same external model parameters (*i.e.* Windkessel and contraction models) were used in all cases. The results, including particle tracking and energy analyses, are provided in section 6.2.

6.2 Results

The results from simulations performed on the model described above are presented in this section. A description of the gross metrics describing simulation behaviour through the second simulated heart beat is provided in section 6.2.1. Section 6.2.2 presents a visualisation of the flow and pressure features observed in the simulations, while section 6.2.3 discusses the impact on these features of LVAD flow synchrony with the cardiac cycle. Finally, energy and particle tracking analyses of the results are provided in sections 6.2.4 and 6.2.5 respectively.

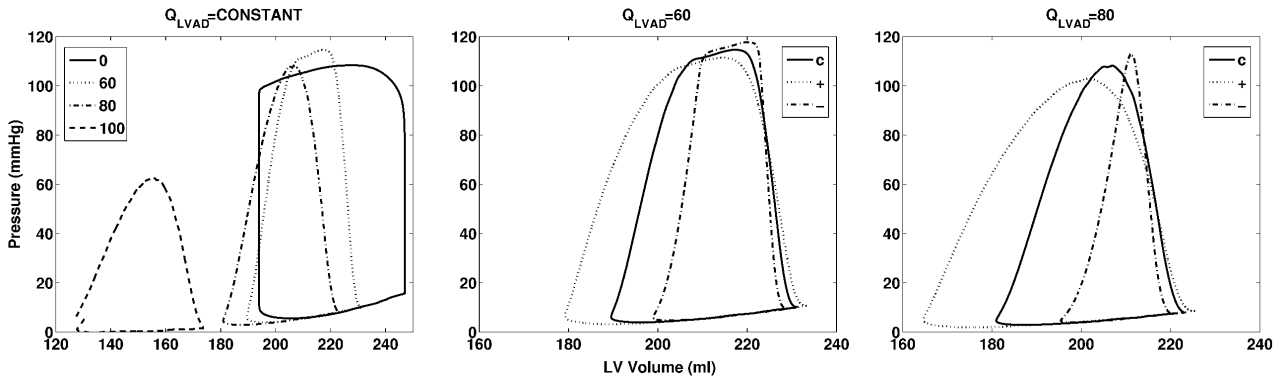

FIGURE 6.6. *LV pressure volume loops from the second simulated heart beat of the patient simulations. Left, the PV loops from the constant flow rate cases; centre, the PV loops from the L_{60} cases; and right, the PV loops from the L_{80} cases. c, $+$ and $-$ refer to the L_X, L_{sX+} and L_{sX-} cases respectively, where X is the LVAD flow rate through one cardiac cycle.*

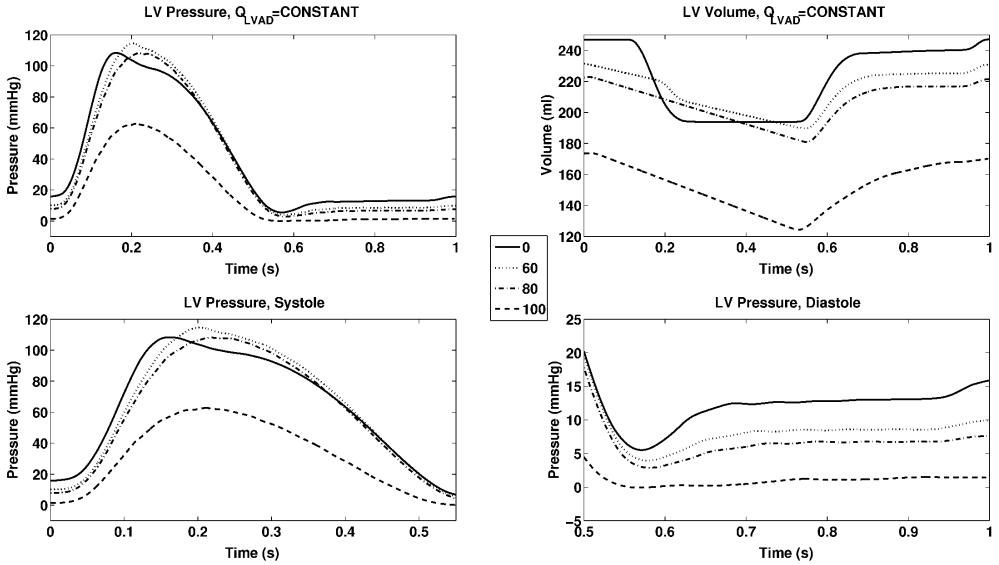

FIGURE 6.7. *A comparison of LV pressures and volumes through the second simulated heart beat for the four constant flow rate simulations. Pressure, through the entire heart beat, top left, is divided into the contractile phases, bottom left, and diastole, bottom right.*

6.2.1 LV Pressure Volume Relationships

The gross LV pressure volume metrics enable an understanding of overall model behaviour. With the exception of the L_{100} case, a repeating pressure volume loop was achieved in all simulations over the second heart beat. A visualisation of these relationships is provided in figure 6.6, while a comparison of their relationships through time, *i.e.* over the duration of the second simulated heart beat, is given in figures 6.7 (constant LVAD flow rates) and 6.8 (the sinusoidal LVAD flow protocols). Finally, to compare how the $0D$ Windkessel model applies boundary conditions on the mitral and aortic valves, a comparison of valve flow rates from the second simulated beat is presented in figure 6.9.

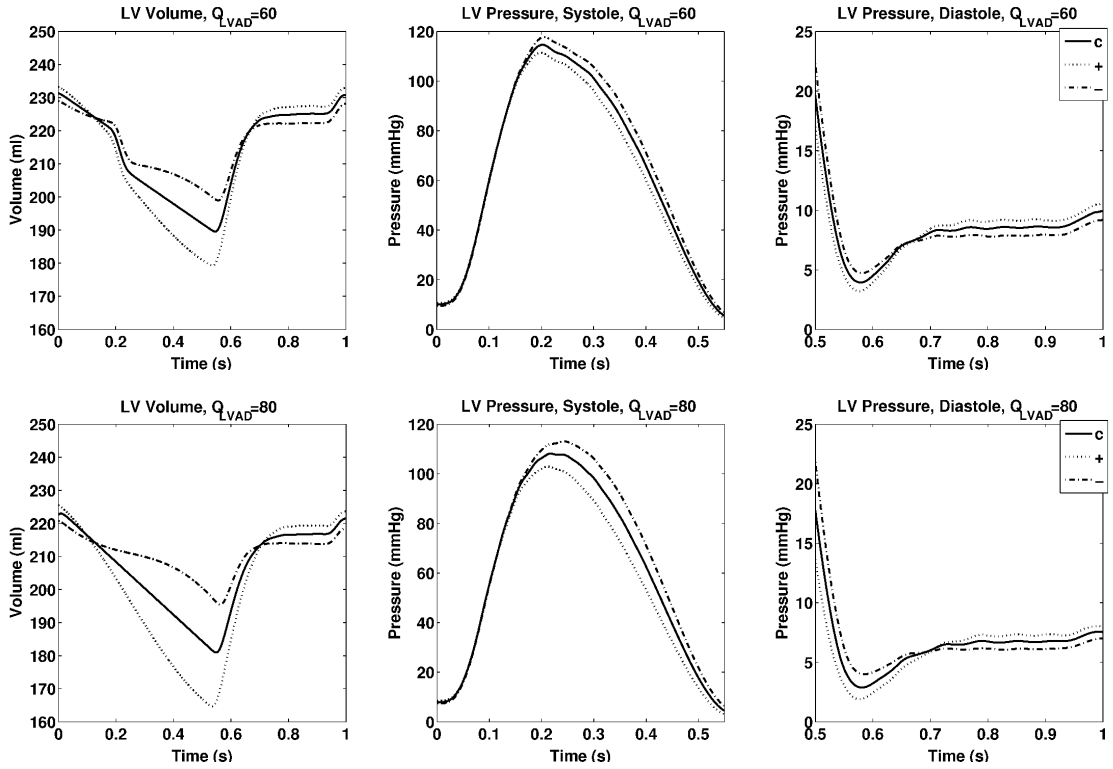

FIGURE 6.8. *A comparison of LV pressures and volumes through the second simulated heart beat for the L_{60} cases, top row, and L_{80} cases, bottom row. Pressure is divided into the contractile phases, centre, and diastole, right. c, + and − refer to the L_X, L_{sX+} and L_{sX-} cases respectively, where X is the LVAD flow rate through one cardiac cycle.*

The first notable feature of the LV pressure volume relationships, was that significant volume unloading occurred in response to increased LVAD flow. Unloading ranged from $\approx 15ml$ for the L_{60} case, to $\approx 74ml$ for the L_{100} case. The second main feature was the impact of LVAD flow synchrony on the PV loops. Increasing LVAD outflow during the contractile phases (L_{s60+} and L_{s80+}) increased the operational volume range of the LV and decreased peak systolic pressure. Interestingly, peak LV volume was also higher in these cases. The opposite trend was observed in the L_{s60-} and L_{s80-} cases.

The pressure relationship was more complicated, with peak systolic pressure increasing, compared with the L_0 case, in the L_{60} case, before decreasing in the L_{80} and L_{100} cases. The reason for this is apparent in the transient LV volume plot, figure 6.7. On the opening of the aortic valve in the L_0 case, LV volume decreased at a faster rate than in any of the other cases. Towards the end of systole, this resulted in a temporarily lower LV volume, compared with the L_{60} and L_{80} cases, in the L_0 case. Due to the force length relationship, this led to higher pressures in the L_{60} and L_{80} cases through this period. Note that due to the combination of lower ventricular and higher aortic pressures, systolic duration reduced with increasing LVAD flow rates and the aortic valve did not open at all in the L_{80} and L_{100} cases.

Significant variations in mitral flow rates, and profiles, were observed in the simulation results. A lower LVAD flow rate coincided with increased early diastolic flow (note that through diastole the L_{s+} cases had lower LVAD outflow than the L_{s-} cases), while higher LVAD flow led to increased flow during diastasis. Late diastolic flow was similar in all cases except L_{100}. The increased early diastolic flow can be explained from the transient

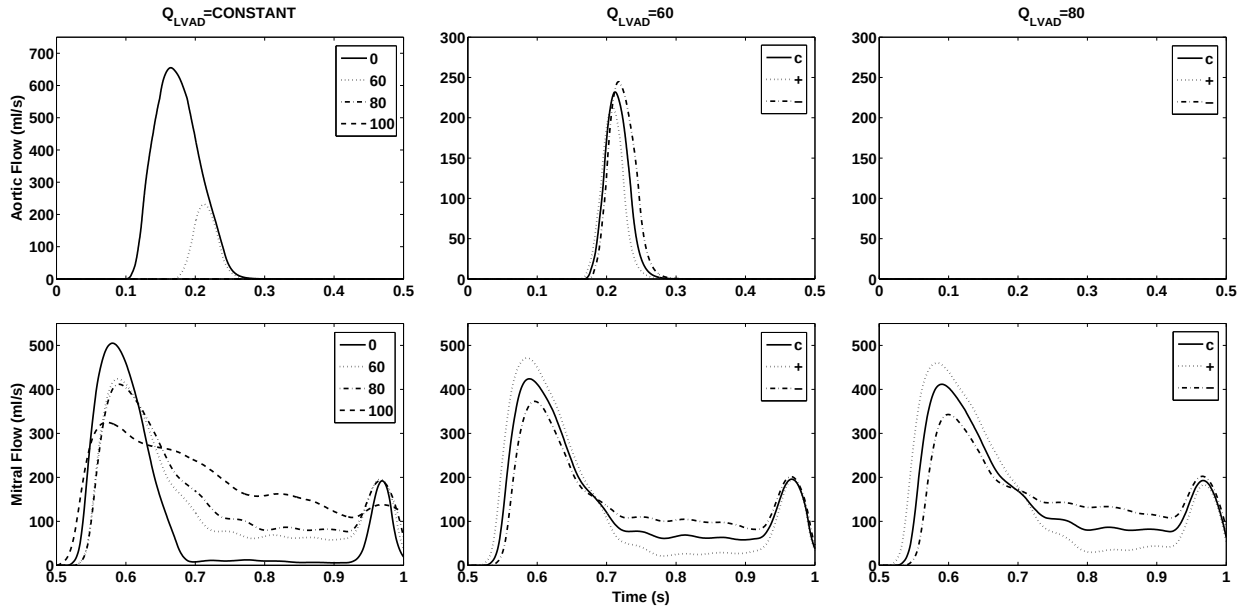

FIGURE 6.9. *A comparison of flow across the aortic, top row, and mitral, bottom row, valves in the second simulated heart beat. The left column shows the results of the constant LVAD flow simulations, the central column shows the L_{60} cases, and the right column the L_{80} cases. Note that no aortic flow occurred in any of the L_{80} cases, or in the L_{100} case. c, + and − refer to the L_X, L_{sX+} and L_{sX-} cases respectively, where X is the LVAD flow rate through one cardiac cycle.*

diastolic pressure plots (figures 6.7 and 6.8) which exhibited a greater rate of pressure decrease during early diastole. This resulted in a greater force of suction, caused by the relaxing myocardium, increasing mitral inflow through this period. With respect to the higher flow observed during diastasis in the cases with higher LVAD outflow, increased LVAD flow reduced ventricular pressure, resulting in increased mitral flow.

6.2.2 Ventricular Flow with Constant LVAD Outflow

Myocardial deformation and ventricular hemodynamics vary significantly through the cardiac phases. It is convenient, particularly given that systole does not necessarily occur at high LVAD flow rates, to consider two broad periods of cardiac behaviour, the contractile phases (*i.e.* IVC, systole and IVR) and diastole. Using this distinction to divide the results, the blood flow streamlines and myocardial displacements from the second heart beat from the constant LVAD flow simulations are presented in figures 6.10 (contractile phases) and 6.12 (diastole). Additionally, ventricular cavity pressures from the constant LVAD flow simulations are provided in figures 6.11 (contractile phases) and 6.13 (diastole).

6.2.2.1 Contractile Phases

During the early contractile phases (the $0.0065s$ and $0.12s$ sub–figures in figure 6.10) the flow features in the L_{60} and L_{80} cases were similar, with a dominant central flow feature drawing fluid towards the apex, driven

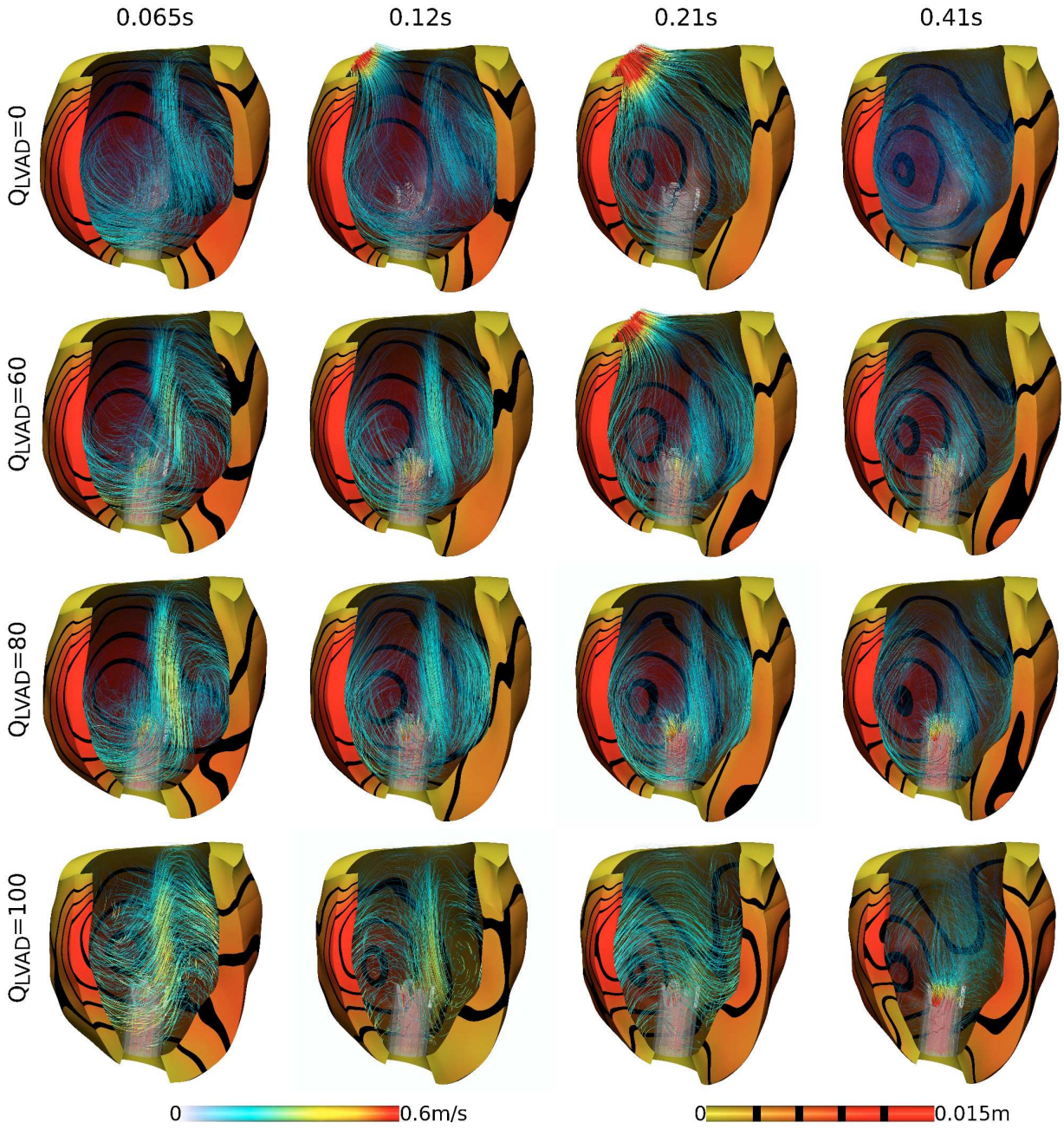

FIGURE 6.10. *Flow streamlines and myocardial displacements from the constant LVAD flow cases during the contractile cardiac phases in the second simulated heart beat. The columns correspond to time instances during the simulations, where,* 0.0065*s was isovolumetric contraction;* 0.12*s and* 0.21*s systole (with respect to the* L_0 *case); and* 0.41*s was isovolumetric relaxation. The rows show the results from each constant LVAD flow simulation.*

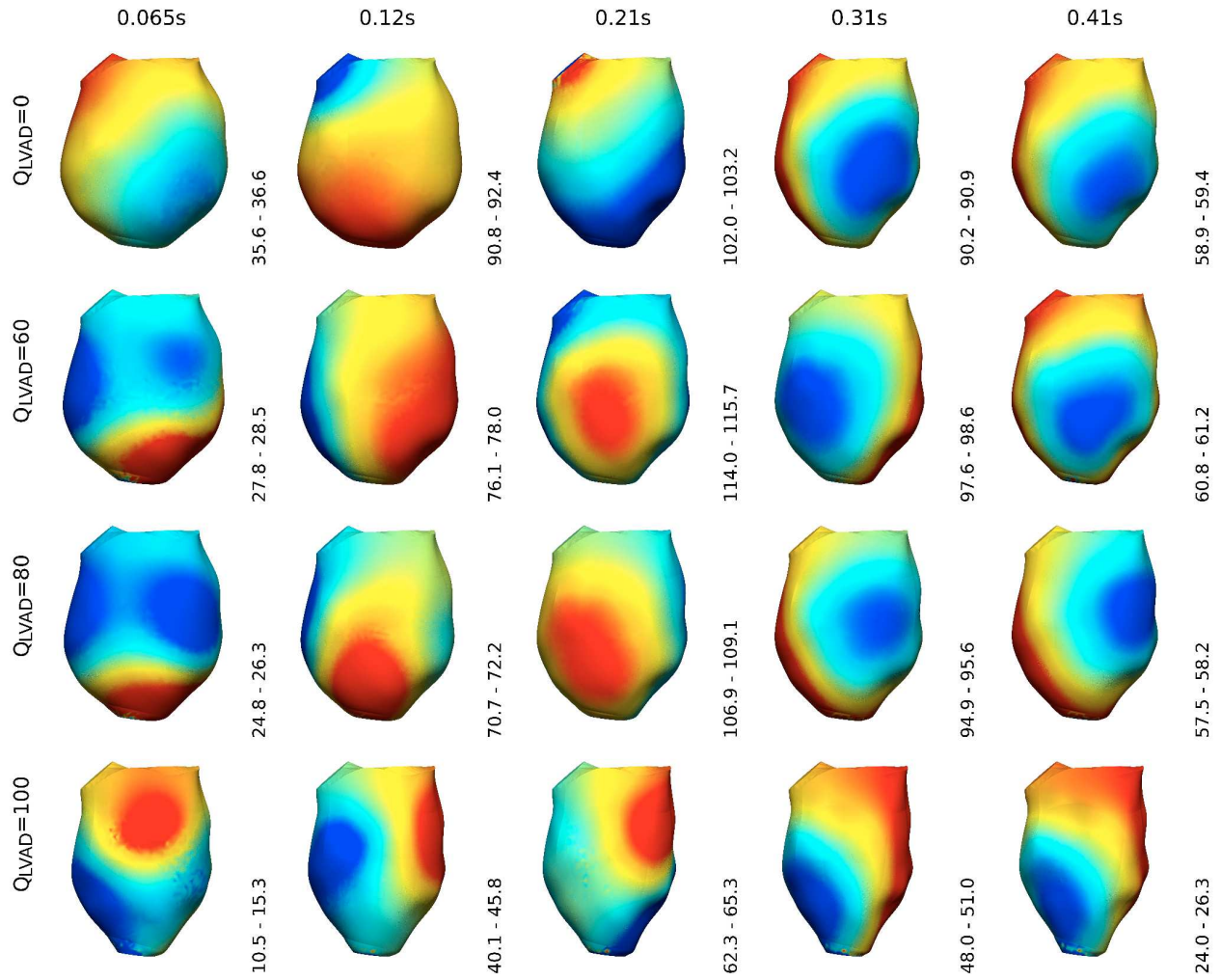

FIGURE 6.11. *Endocardial fluid cavity pressures from the constant LVAD flow cases during the contractile cardiac phases in the second simulated heart beat. The columns correspond to time instances during the simulations, where,* $0.0065s$ *was isovolumetric contraction;* $0.12s$ *and* $0.21s$ *systole (with respect to the* L_0 *case); and* $0.31s$ *and* $0.41s$ *were isovolumetric relaxation. The rows show the results from each constant LVAD flow simulation. The pressure scale in* $mmHg$*, blue to red, is provided on the bottom right of each sub–figure.*

by the LVAD cannula and the remnants of late diastolic inflow. Due to the greater LVAD flow rate in the L_{80} case, the velocity of this feature was greater. A similar feature was observed in the L_{100} case, however, due to greater end diastolic deformation (see figures 6.11 and 6.13), boundary velocities were greater, disrupting the vortical flow features remaining from diastole. In the L_0 case the remnants of diastole acted to maintain vortical flow features that draw fluid away from the apex.

During systole, in the L_0 case, outflow initially acted to draw fluid directly from the apex, leaving vortex remnants opposite to the aortic valve. However, uniaxial outflow rapidly developed, which can be seen at $0.21s$. In the L_{60} case, strong uniaxial outflow never formed as the continual suction of fluid from the apex prevented this from occurring. Systolic outflow did not occur in either the L_{80} or L_{100} cases. Due to this, the dominant flow features in the L_{80} case remained in place throughout the contractile phases, gradually diminishing in

intensity. In contrast, unstructured flow behaviour was a feature of the L_{100} simulation throughout this period.

Prior to systolic outflow the pressure distribution in the L_{60} case was broadly similar to that observed in the L_{80} case. Systolic outflow significantly affected this distribution, pushing it more towards that observed in the L_0 case, however delayed due to the later aortic valve opening time. Post systole this similarity with the L_0 case continued as pressure waves, resulting from valve closure, spread through the LV. In both the cases where systole did not occur, pressure during the contractile phases was characterised by momentum shifts within the fluid. Due to the greater extremes of deformation in the L_{100} case, this was amplified and the range in cavity pressures was greater. This largely explains the more unstructured flow patterns observed in this case. For the other constant LVAD flow cases, no trend in the range of cavity pressure was observed during the contractile phases.

6.2.2.2 Diastole

The predominant flow feature during diastole was the formation of a large vortex during diastole, which enlarged to fill the LV cavity during diastasis. The late diastolic flow peak marginally reduced the size of this feature. A clear correlation was observed between vortex formation and LVAD flow rate. Increased LVAD outflow led to greater disruption of vortex formation, reducing the strength of these flow features. This is seen clearly in figure 6.12, where a vortex fills the entire LV cavity during diastasis in the L_0 case, yet is almost absent from the L_{100} case. Additionally, the greater inflow during diastasis in the higher LVAD flow cases resulted in a strong, jet like, feature in the apical direction, emanating from the mitral valve. The interaction between this feature, the apical myocardial wall, and the LVAD cannula outflow was largely responsible for the weaker vortex formation. As with the contractile flow results, flow, in the L_{100} was observed to be more unstable. This can largely be accounted for by the greater deformation of the LV cavity, compared with the other cases. This can be seen in figure 6.13.

The distribution of pressure in the LV cavity was comparable between the L_{60} and L_{80} cases. The significant exception was during diastasis, $0.70s$, which can be accounted for by variations in the pressure waves between the two cases. The L_0 case showed similar behaviour with respect to the formation and spread of pressure waves. However, the pattern and distribution was different, apart from during early diastole where the wave was formed in conjunction with increasing mitral flow. As with the contractile results, the range of pressure values in the L_{100} case was greater compared with the other constant LVAD flow simulations. As before this can be accounted for by greater myocardial deformation.

6.2.3 The Impact of LVAD Synchrony on LV Blood Flow

The results in the previous section detailed significant variations in flow features observed in the model at different constant LVAD flow rates. Of interest, particularly with regard to optimising LVAD flow to individual patients, is how varying flow rate over the cardiac cycle impacts these features. This section presents the results visualising LV hemodynamics and myocardial displacements, along with LV cavity pressures, for the L_{60}, L_{s60+} and L_{s60-} cases. The blood flow streamlines and myocardial displacements from the second heart beat of these

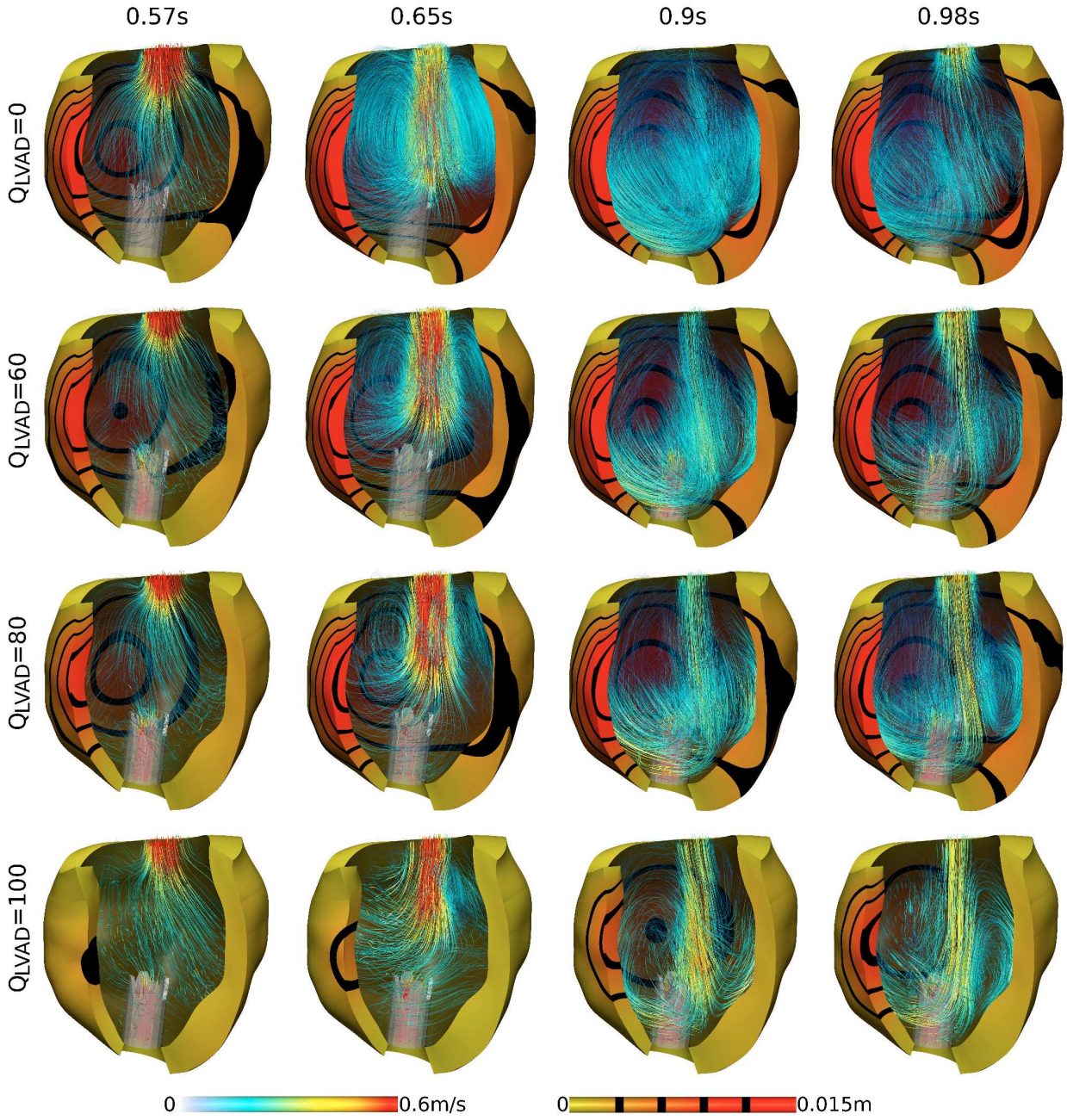

FIGURE 6.12. *Flow streamlines and myocardial displacements from the constant LVAD flow cases during diastole in the second simulated heart beat. The columns correspond to time instances during the simulations, where,* 0.57*s and* 0.65*s were early diastole;* 0.9*s, diastasis; and* 98*s was late diastole. The rows show the results from each constant LVAD flow simulation.*

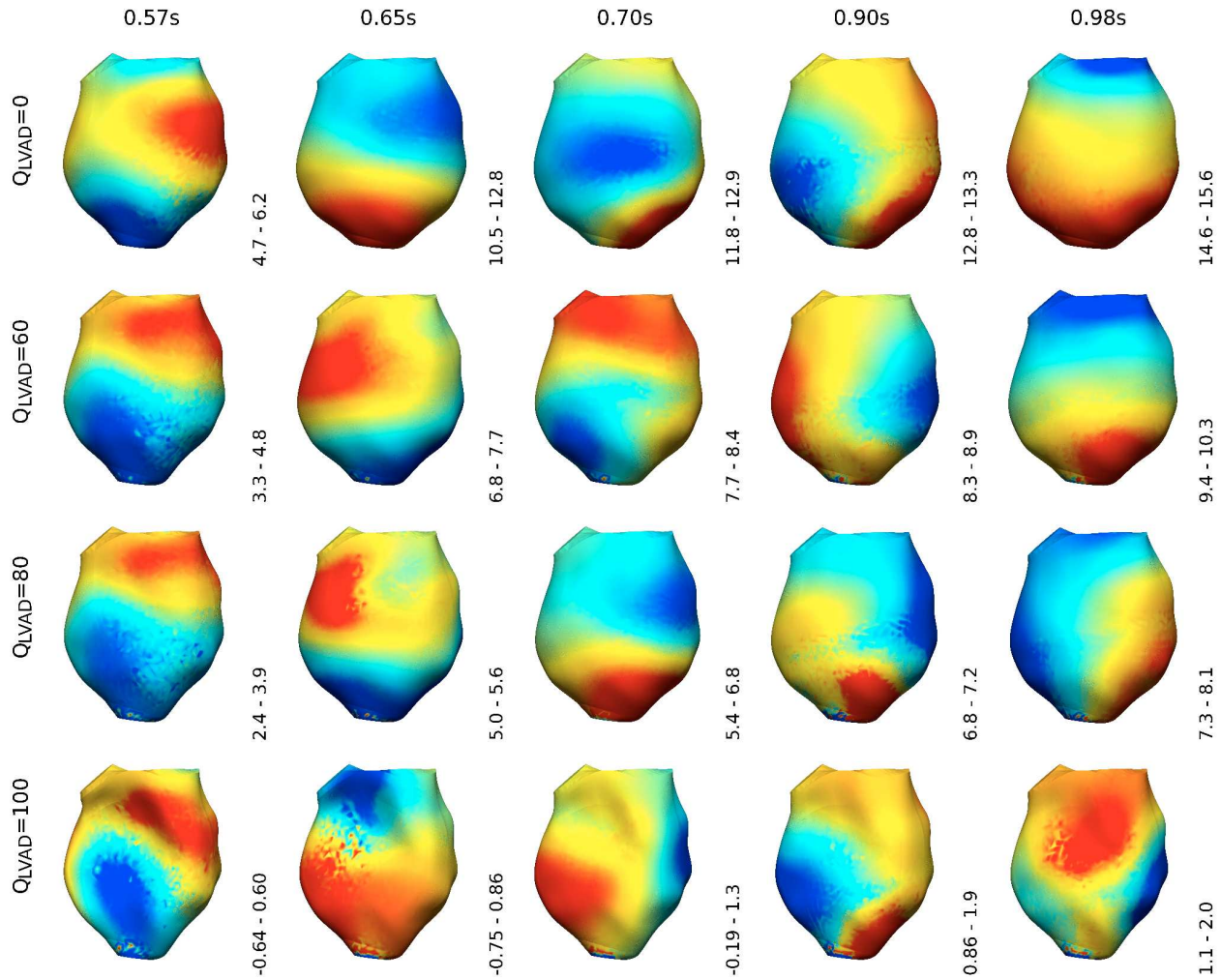

FIGURE 6.13. *Endocardial Fluid cavity pressures from the constant LVAD flow cases during diastole in the second simulated heart beat. The columns correspond to time instances during the simulations, where,* 0.57*s and* 0.65*s were early diastole;* 0.7*s and* 0.9*s diastasis; and* 0.98*s was late diastole. The rows show the results from each constant LVAD flow simulation. The pressure scale in mmHg, blue to red, is provided on the bottom right of each sub–figure.*

cases are presented in figures 6.14 (contractile phases) and 6.16 (diastole). Additionally, ventricular cavity pressures, again from the second heart beat, are provided in figures 6.15 (contractile phases) and 6.17 (diastole). The results observed in the equivalent L_{80} showed similar trends and can be found in appendix E.

6.2.3.1 Contractile Phases

The flow behaviour in the constant and sinusoidal LVAD flow cases was similar throughout the cardiac phases. Of note, however, was the consistently higher intensity of vortical flow features in the L_{s60-} case, *i.e.* when LVAD flow was reduced. This indicates that LVAD flow acts to dissipate vortices in the LV. This result provides a better comparison of this effect than the constant flow results, as in this case the intensity of late diastolic filling, along with the duration and intensity of systolic outflow, was comparable between the three simulations.

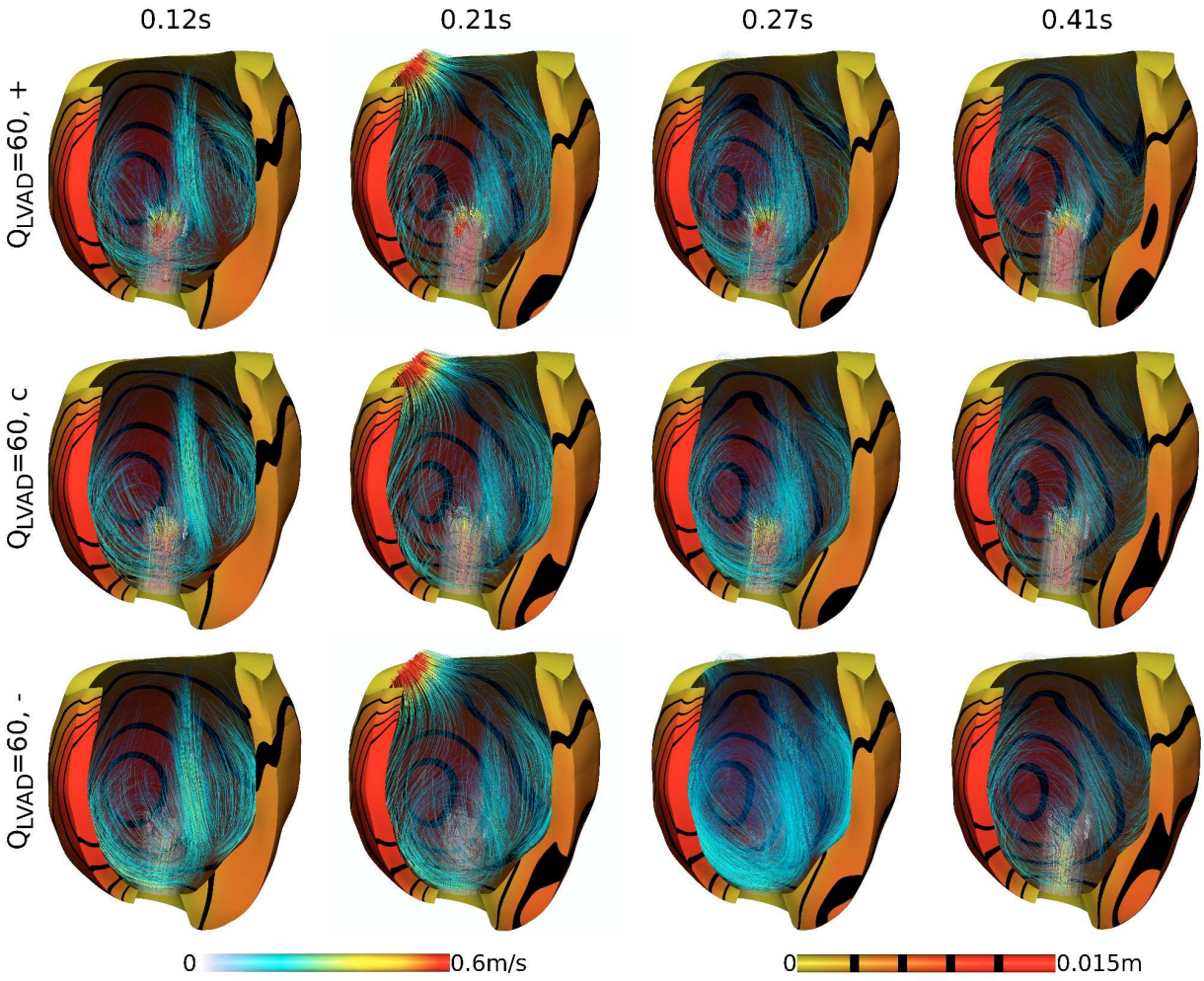

FIGURE 6.14. *Fluid streamlines and myocardial displacements from the second simulated heart beat of the L_{60} LVAD flow regime cases during the contractile phases: top row, L_{s60+}, centre row, L_{s60+}, and bottom row L_{s60-}. The results are visualised at IVC (0.12s), systole (0.21s) and IVR (0.27s and 0.41s). Note that due to LVAD outflow the isovolumetric phases were not strictly isovolumetric. Additionally, systole was still ongoing at 0.27s in the L_{s60-} case.*

With regard to the cavity pressure results, a general trend was observed, whereby the range in ventricular pressures (evidenced by colour intensity in figure 6.15) increased with lower LVAD flow rates. This can be partly explained by the increase in peak LV pressures due to reduced LVAD flow. The distribution of pressure across the LV was comparable throughout the cardiac cycle in the three cases. This is consistent with the similarity of flow features observed.

6.2.3.2 Diastole

During diastole a similar relationship between LVAD flow and vortex formation to that seen in the contractile phases was observed. During this phase, vortices formed with increasing intensity in correlation with decreasing LVAD flow (in this phase reduced LVAD outflow occurred in the L_{s60+} case). Again this indicates the

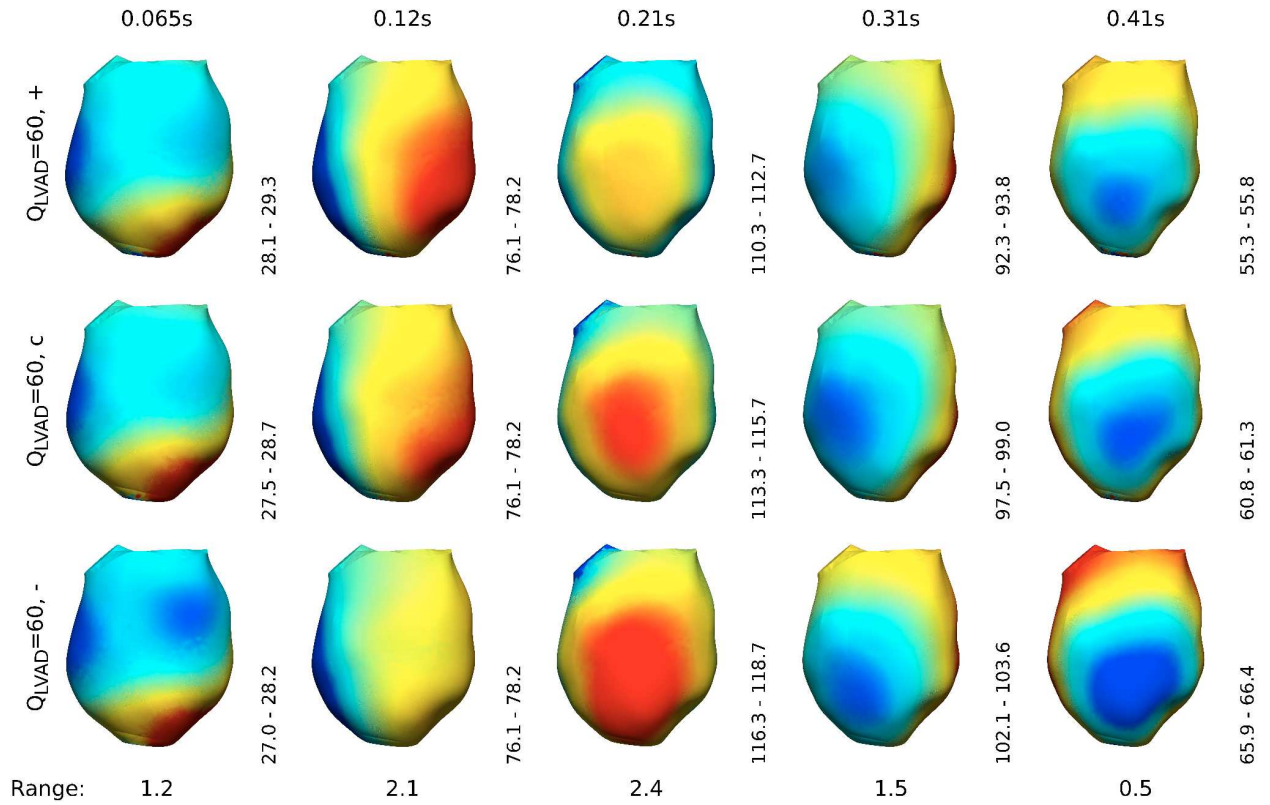

FIGURE 6.15. *LV cavity pressure from the second simulated heart beat of the L_{60} LVAD flow regime cases during the contractile phases: top row, L_{s60+}, centre row, L_{s60+}, and bottom row L_{s60-}. The results are visualised at IVC (0.065s and 0.12s), systole (0.21s) and IVR (0.31s and 0.41s). The pressure scale in mmHg, blue to red, is provided on the bottom right of each sub–figure. The range in pressure values was constant across each column of sub–figures and is provided at the bottom of each column.*

destructive effect of LVAD outflow on the formation of vortices in the LV.

The pressure results also show a similar trend to those from the contractile phases. While the distribution of pressure through the LV was similar in the three cases, the range in pressure (evidenced by colour intensity in figure 6.17) increased in conjunction with decreasing LVAD outflow, particularly during diastasis and early diastole. This can be accounted for by two primary reasons. The rate of myocardial relaxation was greater in the L_{s60+} case (equivalently it was lower in the L_{s60-} case). This resulted in greater early diastolic inflow, increasing the pressure range during this phase. Additionally, mitral inflow during diastasis was lower in cases with reduced LVAD outflow. This increased the drop in mitral inflow between the early diastolic peak and the diastatic minimum. As a result, the pressure wave caused by this drop was stronger, increasing the range in cavity pressures observed during this phase. Since the late diastolic inflow peak was comparable between the three cases, no significant variation in pressure range was observed during this phase.

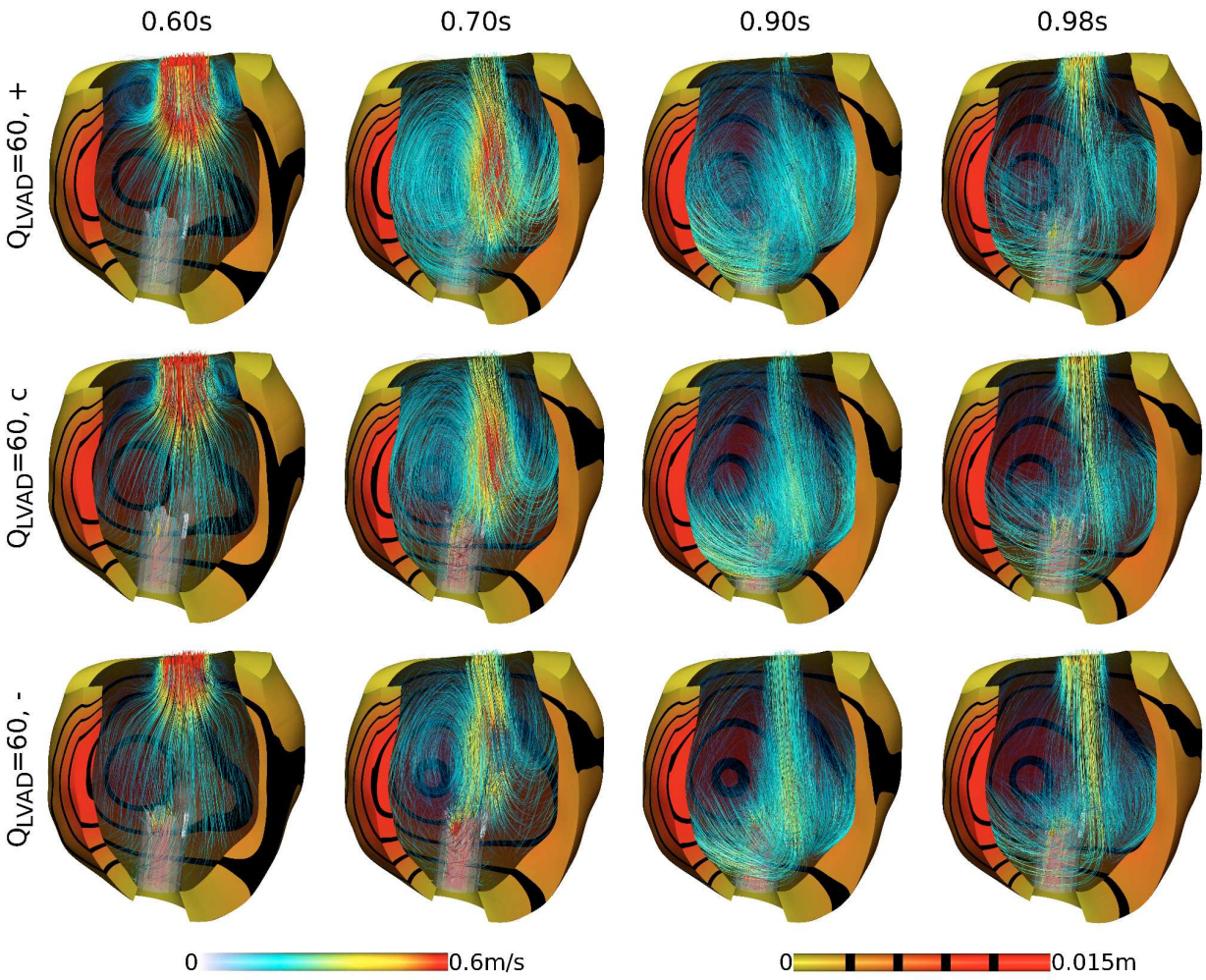

FIGURE 6.16. *Fluid streamlines and myocardial displacements from the second simulated heart beat of the L_{60} LVAD flow regime cases during diastole: top row, L_{s60+}, centre row, L_{s60+}, and bottom row L_{s60-}. The results are visualised at early diastole (0.60s), diastasis (0.70s and 0.90s) and late diastole (0.98s).*

6.2.4 Myocardial Energetics under different Flow Protocols

The behaviour of myocardial energetics varies significantly through the cardiac cycle. Changes in potential energy and work depend on a multitude of factors including timing within the cardiac cycle, myocardial strain (correlated to LV cavity volume), flow across the inflow/outflow valves and the LVAD cannula, as well as momentum shifts within the fluid. The energy sources and sinks in the model were the contraction model (which performed work), the LVAD outflow boundary, and the aortic and mitral valve boundaries. Additionally energy could be lost advectively over the inflow/outflow boundaries or via viscous dissipation. By continually removing energy from the system, LVAD support significantly impacted the transfer of energy in the heart. A summary of energy transfer during the second heart beat under the different simulated LVAD flow protocols is provided in table 7.

Over the second heart beat, with the exception of the L_{100} case, the total change in stored energy was small,

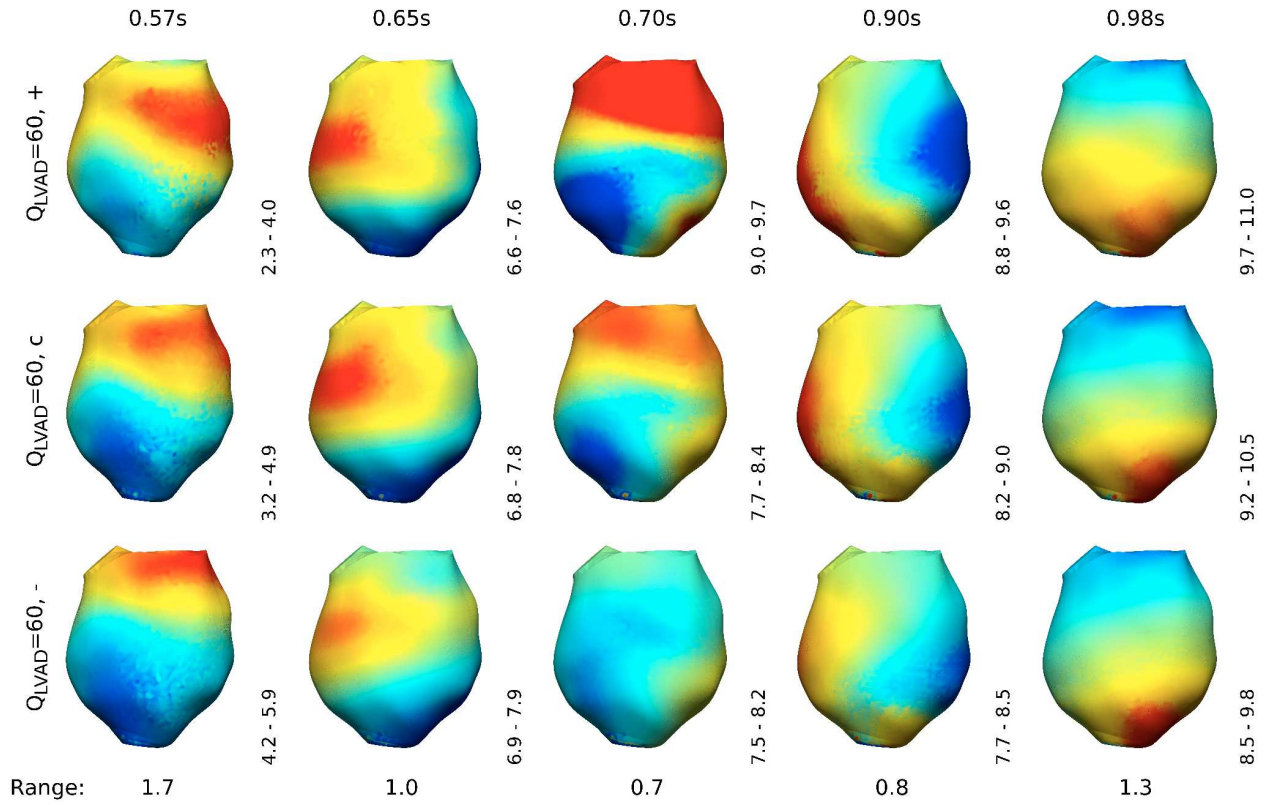

FIGURE 6.17. *LV cavity pressure from the second simulated heart beat of the L_{60} LVAD flow regime cases during diastole: top row, L_{s60+}, centre row, L_{s60+}, and bottom row L_{s60-}. The results are visualised at early diastole (0.57s and 0.65s), diastasis (0.70s and 0.90s) and late diastole (0.98s). The pressure scale in mmHg, blue to red, is provided on the bottom right of each sub–figure. The range in pressure values was constant across each column of sub–figures and is provided at the bottom of each column.*

$< 5\%$ of the total energy present (fluid kinetic and solid potential) at the start and end points of the cardiac cycle. The discrepancies can be accounted by minor variations in the LV pressure–volume relationship between the first and second beats. In the L_{100} case, a larger change in potential energy was observed as this simulation did not converge on a pressure–volume loop within two beats.

As expected, increased LVAD outflow reduced the work performed by the myocardium. This was particularly evident in the cases where LVAD outflow reduced during the contractile phases. Similarly, total energy outputted over the model boundaries decreased with LVAD flow rate, see figure 6.18. In general it was noted that in cases where flow output during the contractile phases was higher, either due to aortic valve opening or increased LVAD outflow in this phase, the greater the energy outputted from the system. This was due to elevated boundary tractions caused by higher contractile cavity pressures. Finally, the total energy lost over the cardiac cycle was dominated by advective losses, which were greatest in simulations with higher peak outflows, *i.e.* the L_0, L_{sX+}, L_{sX-} and L_{100} cases. Greater peak outflow also increased the rate of viscous energy dissipation, further amplifying this effect.

Of particular interest with respect to determining the optimal degree of LV unloading under LVAD support are the energetics of the myocardium. The remainder of this section focuses on energy transfer within the

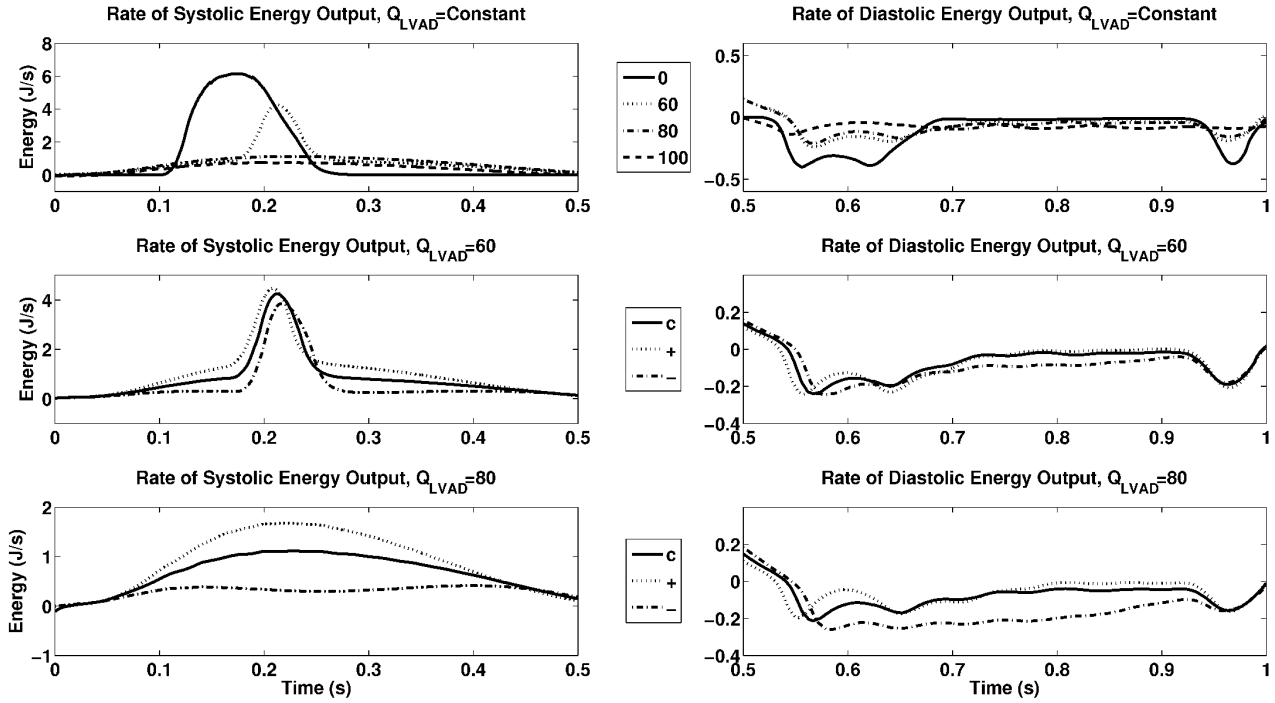

FIGURE 6.18. *Rates of energy output from the contractile phases (left) and diastole (right). Top row, results from the constant LVAD flow simulations, middle row, the L_{60} cases, bottom row, the L_{80} cases. c, + and − refer to the L_X, L_{sX+} and L_{sX-} cases respectively, where X is the LVAD flow rate through one cardiac cycle.*

myocardium, focusing initially on whole organ metrics (section 6.2.4.1), before investigating the spatial variation of work during contraction (section 6.2.4.2). For completeness, the energetics of fluid flow (*i.e.* kinetic and viscous energies) from the patient model are discussed in appendix E.

6.2.4.1 Gross Myocardial Energetics

The results from the patient study enable an analysis to be performed on how variations in LVAD flow rate effect myocardial potential energy and work. Considering whole organ myocardial energies, a visualisation of myocardial rates of potential energy and work during the contractile phases is provided in figure 6.19, while the rates of potential energy during diastole are shown in figure 6.20.

The behaviour myocardial energetics during the contractile phases depended on whether or not the aortic valve opened. Following the initial increase in potential energy and work during the early part of contraction, the opening of the aortic valve resulted in a rapid decrease in the rates of myocardial potential energy and a corresponding increase in the rates of work. If the aortic valve did not open, the rates of potential energy and work peaked around $0.1s$ before declining slowly as myocardial tension first plateaued, then declined in the latter part of the contractile phases. Oscillations in these rates were observed and corresponded to momentum shifts in the fluid. Greater oscillations were seen in the L_{100} case and this explains the greater range in LV

	$\triangle$ KE (J)	$\triangle$ PE (J)	Work (J)	Energy Output (J)	Energy Loss (J)
L_0	-1.06×10^{-4}	2.51×10^{-3}	0.681	0.546	0.137
L_{60}	-1.21×10^{-4}	7.71×10^{-4}	0.402	0.390	1.30×10^{-2}
L_{s60+}	-1.34×10^{-4}	1.08×10^{-3}	0.518	0.496	2.32×10^{-2}
L_{s60-}	-8.57×10^{-5}	4.54×10^{-4}	0.279	0.253	2.64×10^{-2}
L_{80}	2.60×10^{-4}	4.36×10^{-4}	0.338	0.311	2.71×10^{-2}
L_{s80+}	-1.31×10^{-4}	-3.86×10^{-4}	0.500	0.448	5.15×10^{-2}
L_{s80-}	-6.70×10^{-5}	-4.53×10^{-4}	0.149	9.35×10^{-2}	5.44×10^{-2}
L_{100}	-2.19×10^{-4}	5.20×10^{-3}	0.243	0.185	6.23×10^{-2}

TABLE 7

Summary of energy transfer during the second simulated heart beat under different LVAD flow protocols. $\triangle$ KE is the total change in kinetic energy, $\triangle$ PE is the total change in potential energy, work refers to total work performed through the cardiac cycle, energy output represents the total energy outputted over the boundaries (mitral, aortic and LVAD), while energy loss is the total energy lost via either boundary advection or viscous energy dissipation. All energies are in Joules.

cavity pressures observed for this problem (see figure 6.11). As time averaged myocardial stress and strain were lower in the L_{100} case, the tissue was more pliant to deformation. Hence it was possible for greater fluid momentum shifts to occur. The rates of potential energy were similar between all L_{60}, and also between all L_{80}, cases. However, observed rates of work were lower in cases where LVAD flow decreased during the contractile phases (L_{s60-} and L_{s80-}) and greater when LVAD outflow increased (L_{s60+} and L_{s80+}). This was because the reduced change in LV cavity volume, due to lower LVAD outflow, placed more constraint on the performance of mechanical work. It should be noted that tension generation was similar across all L_{60} and L_{80} cases. This indicates that mechanical work is not necessarily a good metric for comparing myocardial loading. This issue is discussed further in the following section.

The early part of diastole was dominated by the relaxing myocardium drawing fluid into the ventricular cavity. As LV volume began to increase, this suction effect diminished and the rates of potential energy shifted from negative to positive. As early diastolic inflow continued, the rate of increase in myocardial potential energy peaked, before declining during diastasis. The magnitude of this peak was correlated to LVAD flow rate, with lower LVAD outflow corresponding to greater rates of potential energy and vice versa. This trend was also observed in the sinusoidal flow profile cases. The rates of potential energy were minimal during diastasis, as LV cavity volume only increased slowly. Oscillations were observed as fluid momentum shifted in the cavity. The magnitude of the late peak in potential energy rates, corresponding to late diastole, was also correlated to LVAD flow rate. Again, lower LVAD outflow resulted in an increased peak in the rate of potential energy. Due to the contraction model used, active tension was no longer generated in the model after $0.6s$ from initiation. As a result, minimal mechanical work was performed during diastole.

6.2.4.2 Work Asynchrony

As shown in section 5.3.5, gross myocardial metrics only provide a partial picture of myocardial energetics. How work is spatially distributed, in particular between regions of positive and negative work, enables a better

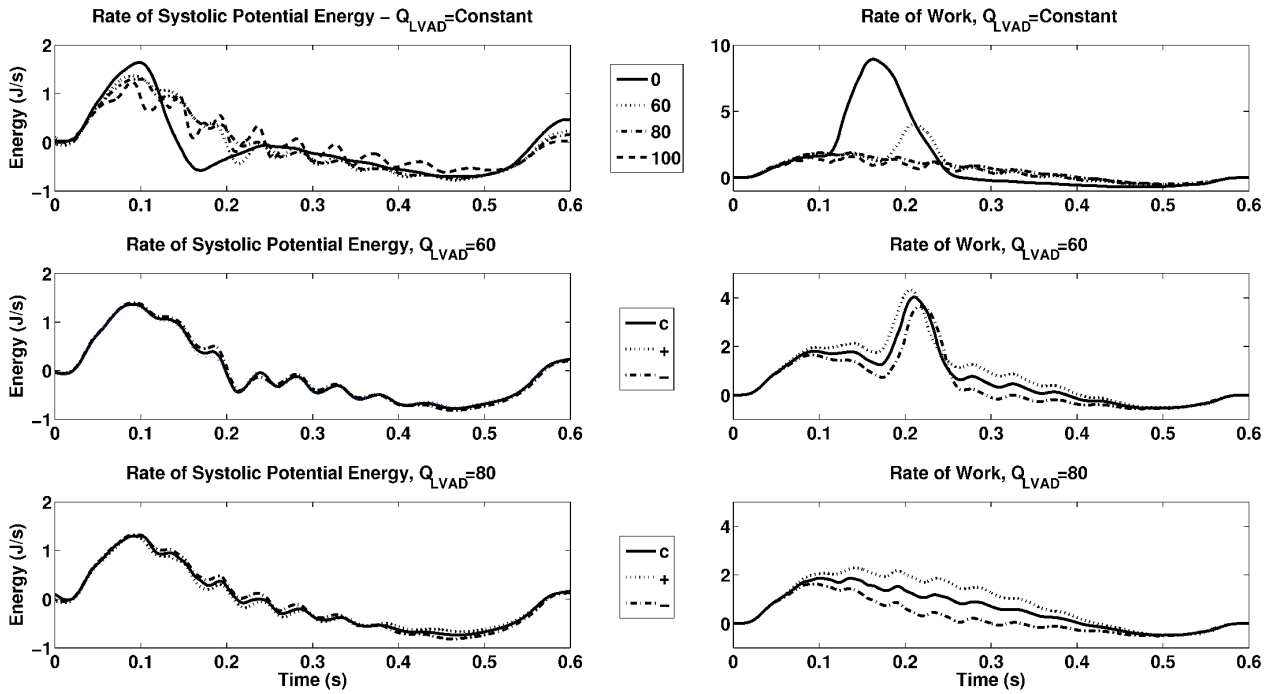

FIGURE 6.19. *Rates of potential energy and work during the contractile phases. Top row, results from the constant LVAD flow simulations, middle row, the L_{60} cases, bottom row, the L_{80} cases. c, $+$ and $-$ refer to the L_X, L_{sX+} and L_{sX-} cases respectively, where X is the LVAD flow rate through one cardiac cycle.*

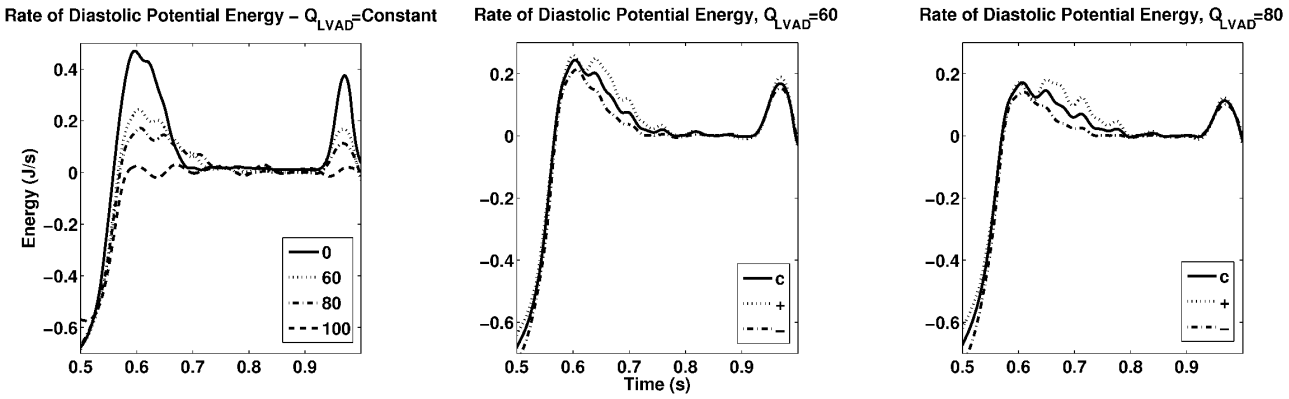

FIGURE 6.20. *Rates of potential energy during diastole. Left, results from the constant LVAD flow simulations, middle the L_{60} cases, right, the L_{80} cases. c, $+$ and $-$ refer to the L_X, L_{sX+} and L_{sX-} cases respectively, where X is the LVAD flow rate through one cardiac cycle.*

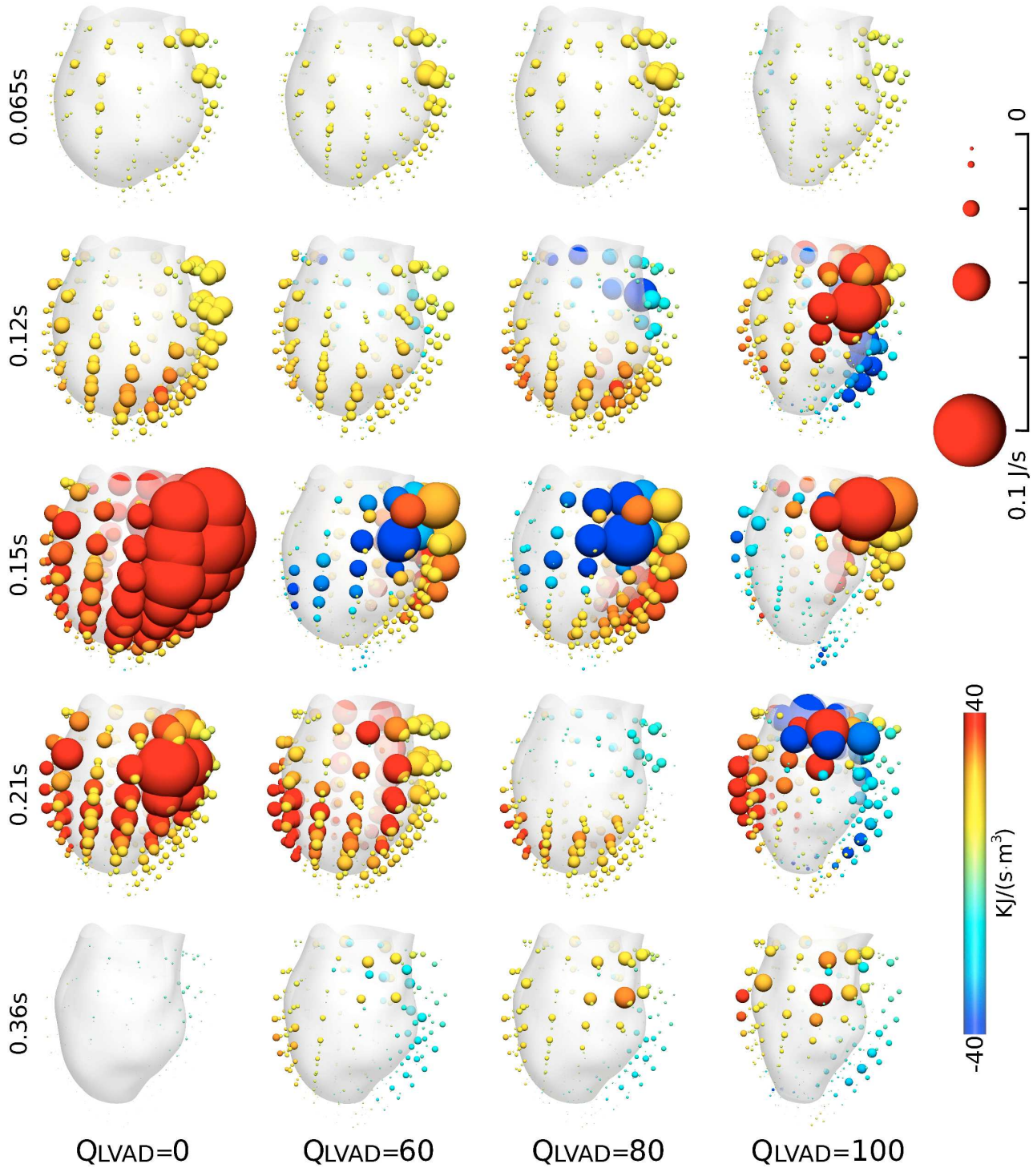

FIGURE 6.21. *Spatial distribution of work during the contractile phases from the simulations of constant LVAD flow, left to right,* L_0, L_60, L_80 *and* L_100. *The visualised results are from the second simulated heart beat in each simulation. Spheres are located at myocardial element centrepoints and are scaled by the magnitude of elemental rate of work* ($J \cdot s^{-1}$). *Sphere colour, blue to red, is the mean intensity of work* ($J \cdot s^{-1} \cdot m^{-3}$) *within the element. Total rates of work* ($J \cdot s^{-1}$) *for each simulation at each visualised time point (in sequential order) were:* $L_0 = [1.19, 2.61, 7.99, 4.29, -0.339]$, $L_{60} = [1.30, 1.71, 1.61, 4.02, 0.369]$, $L_{80} = [1.27, 1.71, 1.74, 1.21, 0.555]$, *and* $L_{100} = [1.12, 1.34, 1.31, 0.747, 0.329]$.

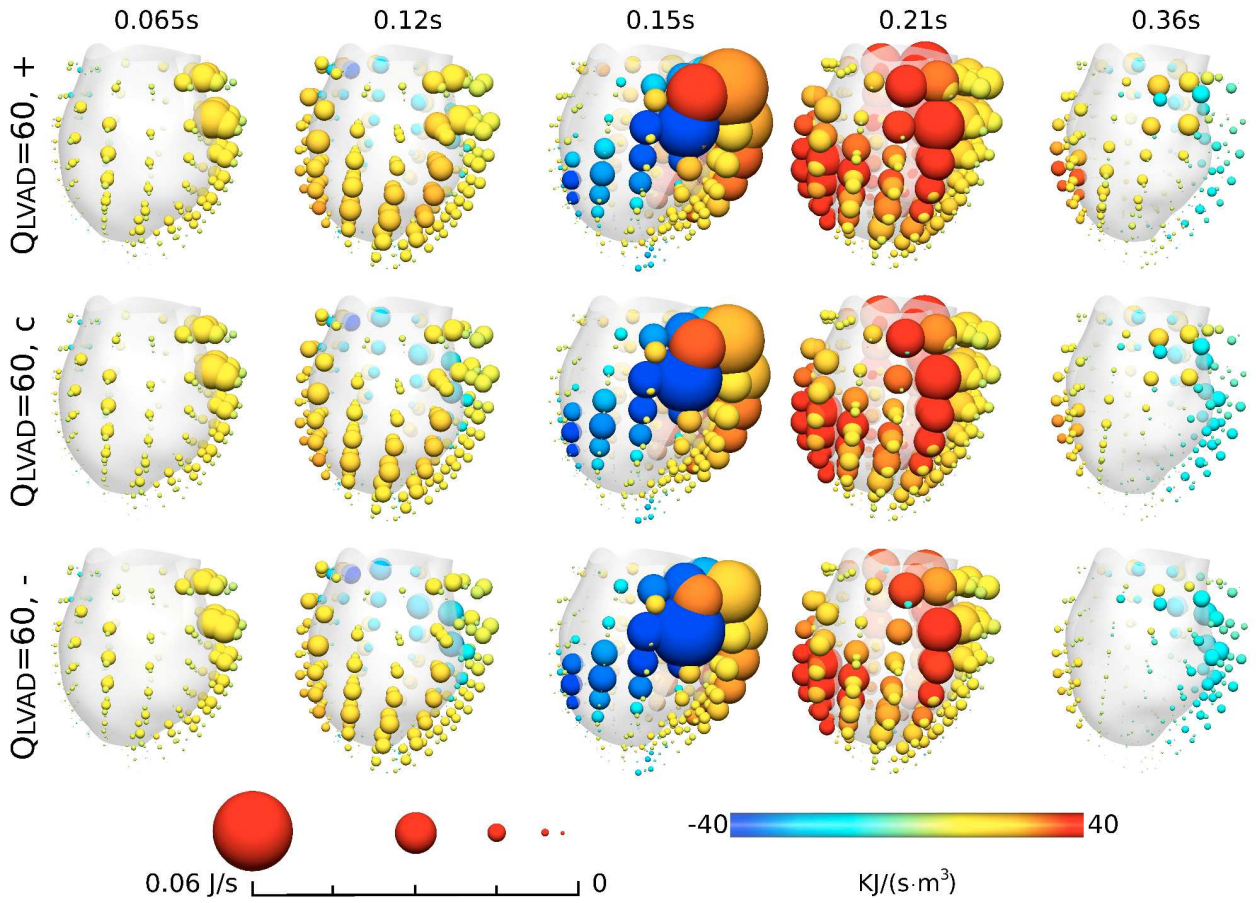

FIGURE 6.22. *Spatial distribution of work during the contractile phases from the L_{s60+}, top, L_{60}, centre, and L_{s60-} bottom simulations. The visualised results are from the second simulated heart beat in each simulation. Spheres are located at myocardial element centrepoints and are scaled by the magnitude of elemental rate of work ($J \cdot s^{-1}$). Sphere colour, blue to red, is the mean intensity of work ($J \cdot s^{-1} \cdot m^{-3}$) within the element. Total rates of work ($J \cdot s^{-1}$) for each simulation at each visualised time point (in sequential order) were:* $L_{60} = [1.30, 1.71, 1.61, 4.02, 0.369]$, $L_{s60+} = [1.36, 1.99, 2.01, 4.27, 0.747]$, *and* $L_{s60-} = \left[1.23, 1.43, 1.20, 3.45, 7.27 \times 10^{-2}\right]$.

comparison to be made of the impact of LVAD support. To this end, a visualisation of the spatial distribution of work during the contractile phases of the constant LVAD flow simulations is provided in figure 6.21, while a comparison between the L_{60} cases is shown in figure 6.22 and L_{80} cases in figure 6.23.

Immediately obvious, with respect to the constant flow simulations, was the relationship between LVAD outflow and the spatial dyssynchrony of work. This was particularly apparent during periods of peak tension, *i.e.* $0.12s$, $0.15s$ and $0.21s$. It was also evident that during aortic ejection ($0.12s$, $0.15s$ and $0.21s$ in the L_0 case and $0.21s$ in the L_{60} case) work was stronger and more homogeneous. This can be explained by the relationship, observed in the previous section, between outflow and work. Not only did the rate of myocardial work increase during systole, but volume change was connected to cavity pressure, and by extension myocardial energetics. As a result, increases in local work no longer acted to shift fluid around the ventricular chamber altering myocardial work in another region. Instead, work acted to eject more fluid from the LV cavity. Therefore, the net result of systolic ejection was to increase the spatial homogeneity of work in the myocardium. Outflow via the LVAD

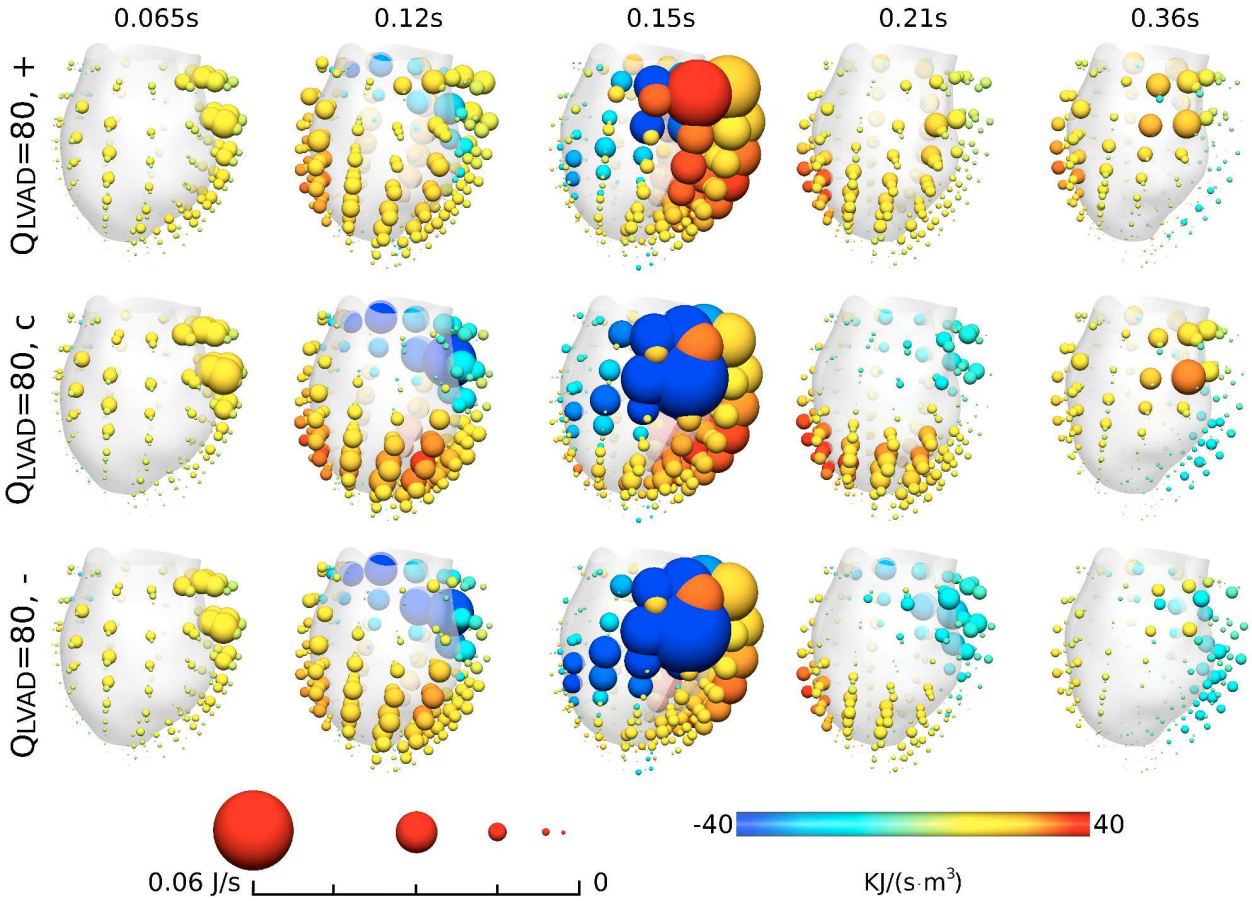

FIGURE 6.23. *Spatial distribution of work during the contractile phases from the L_{s80+}, top, L_{80}, centre, and L_{s80-} bottom simulations. The visualised results are from the second simulated heart beat in each simulation. Spheres are located at myocardial element centrepoints and are scaled by the magnitude of elemental rate of work ($J \cdot s^{-1}$). Sphere colour, blue to red, is the mean intensity of work ($J \cdot s^{-1} \cdot m^{-3}$) within the element. Total rates of work ($J \cdot s^{-1}$) for each simulation at each visualised time point (in sequential order) were:* $L_{80} = [1.27, 1.71, 1.74, 1.21, 0.555]$, $L_{s80+} = [1.32, 2.03, 2.24, 1.88, 1.00]$, *and* $L_{s80-} = \left[1.20, 1.40, 1.21, 0.450, 5.38 \times 10^{-3}\right]$.

cannula, as it was unconnected to ventricular behaviour, did not have the same effect.

The effect of systolic outflow, with respect to different LVAD flow protocols, can be seen when comparing figures 6.22 and 6.23. In the L_{80} cases, where the aortic valve did not open, heterogeneity of work increased as LVAD outflow decreased – as expected since similar tensions were generated in all three cases, yet work was lower in the L_{s80-} case. However, this effect was substantially reduced in the L_{60} cases, due to the homogenising effect of systolic outflow.

6.2.4.3 Discussion of Myocardial Energetics

The analysis of myocardial energetics demonstrates that different LVAD flow rates significantly alter the dynamics of the myocardium. With respect to the constant flow simulations, increased LVAD outflow reduced

the loading on the myocardium, reducing both potential energy and mechanical work during both the contractile phases and diastole. Regarding the sinusoidal flow simulations, the predominant effect was observed in myocardial work where greater outflow corresponded to greater mechanical work performed. During diastole, large variations in rates of potential energy were observed. However due to low cavity pressures during this phase, the significance of this on overall myocardial unloading is questionable.

The observed homogenising effect of systolic outflow on the spatial variation work enables an interesting hypothesis to be developed regarding the importance of aortic valve opening and the choice of LVAD flow protocol. If the aortic valve does not open, these simulations indicate that more homogeneous (and in comparison with the L_0 case, normal) myocardial behaviour can be achieved by synchronising increases in LVAD outflow with the contractile phases. However, if the aortic valve does open, the importance of LVAD flow synchrony on myocardial energetics is less important and the choice of flow protocol can be weighted more towards its impact on fluid residence times, discussed in the following section.

6.2.5 Residence Times under different Flow Protocols

To provide an analysis of the recirculation of blood within the simulated ventricular cavity, the particle tracking algorithm from section 4.3 was used. Particles were seeded at regular, $0.046s$, intervals during the first simulated diastolic period and were tracked for two cardiac beats. Since this period extends beyond the simulated duration, the tracking algorithm looped over the second heart beat. This section presents the results from this study, with visualisations of the movement of particles provided in figures 6.24 (constant LVAD flow simulations) and 6.26 (the L_{60} cases). Figure 6.25 details the percentage of particles, grouped according to diastolic periods, remaining in the LV cavity over time, while a summary of the composition of ejected fluid is given in table 8. Note that since the results from the L_{80} cases were similar to those from the L_{60}, visualisation of these results is shown in appendix E.3.

	S.V. (ml)	E.F. (%)	% S.V. Beat 1	% S.V. Beat 2	E.F. Old Cavity Vol. (%)
L_0	53.05	21.47	8.03	33.74	20.96
L_{60}	69.69	26.64	23.41	30.72	22.99
L_{s60+}	68.22	27.38	22.24	23.63	28.78
L_{s60-}	71.39	26.10	15.74	28.88	27.74
L_{80}	80.00	30.31	27.89	26.10	28.26
L_{s80+}	80.00	32.43	32.14	22.52	31.01
L_{s80-}	80.00	28.54	20.74	24.51	31.25
L_{100}	100.00	44.40	44.12	18.79	47.31

Table 8

Table summarising the constitution of ejected blood from the LV cavity. S.V. is the stroke volume (defined as volume of fluid outputted by the ventricle per beat) of the LV; E.F. is the ejection fraction of the ventricle (defined as the ratio S.V. over end diastolic volume); % S.V. Beat 1 is the percentage of the S.V. made up of fluid that entered the chamber during the current cardiac cycle; % S.V. Beat 2 is the percentage of the S.V. made up of fluid that entered the chamber during the previous cardiac cycle; E.F. Old Cavity Vol. (%) is the fraction of fluid that has been in the cavity greater than two heart beats exiting the LV per beat.

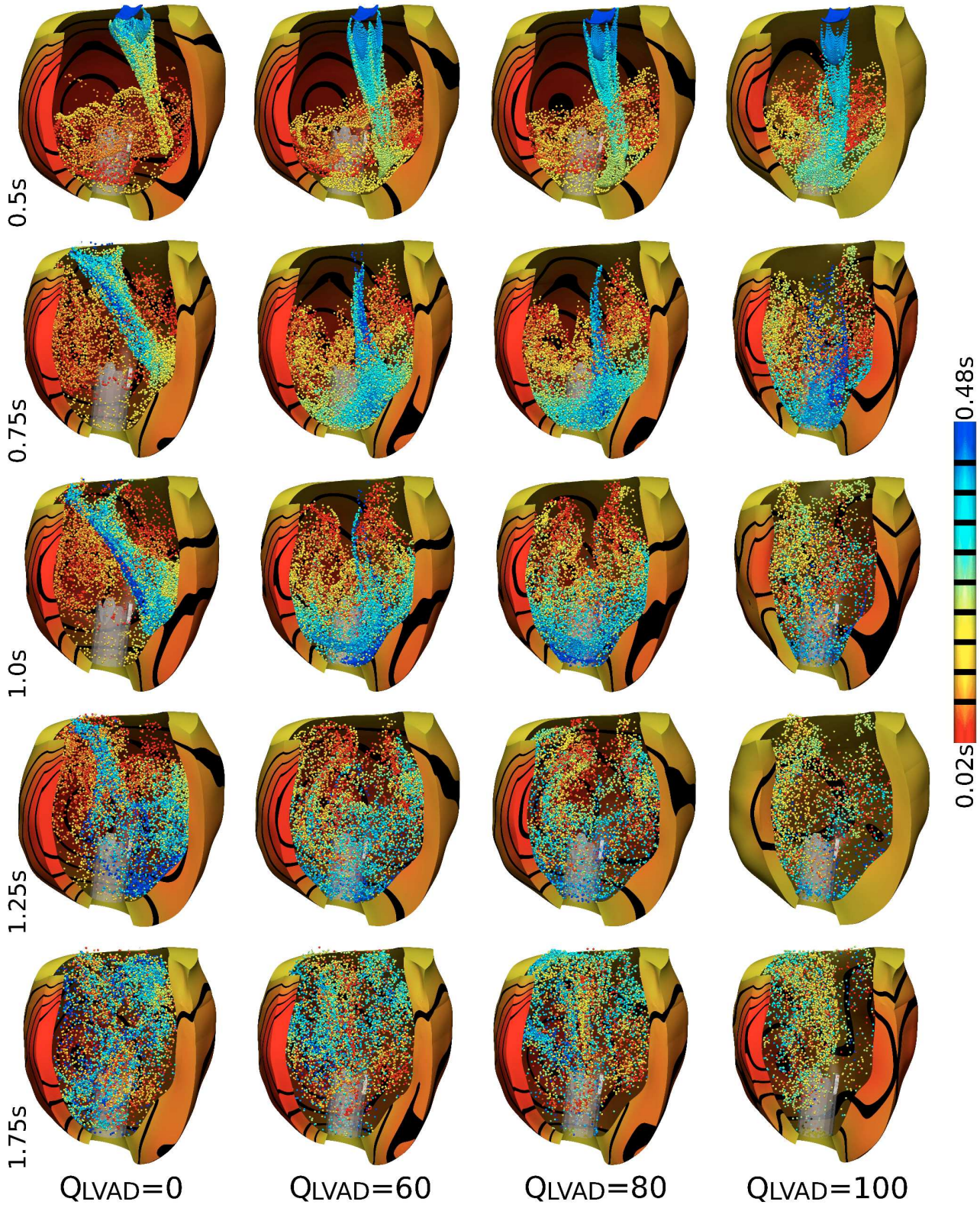

FIGURE 6.24. *Seeded particles from the constant LVAD flow simulations, coloured by their seed time with respect to the first set of seeded points. Particles were seeded at intervals of* 0.046*s with an initial seed time of* 0.02*s into the first diastolic period (*i.e. 0.52*s into the simulation). Two complete beats were tracked by looping over the second heart beat. Particle locations are shown at selected time points through the two tracked heart beats. Note* $t = 0$ *is equivalent to the commencement of diastole.*

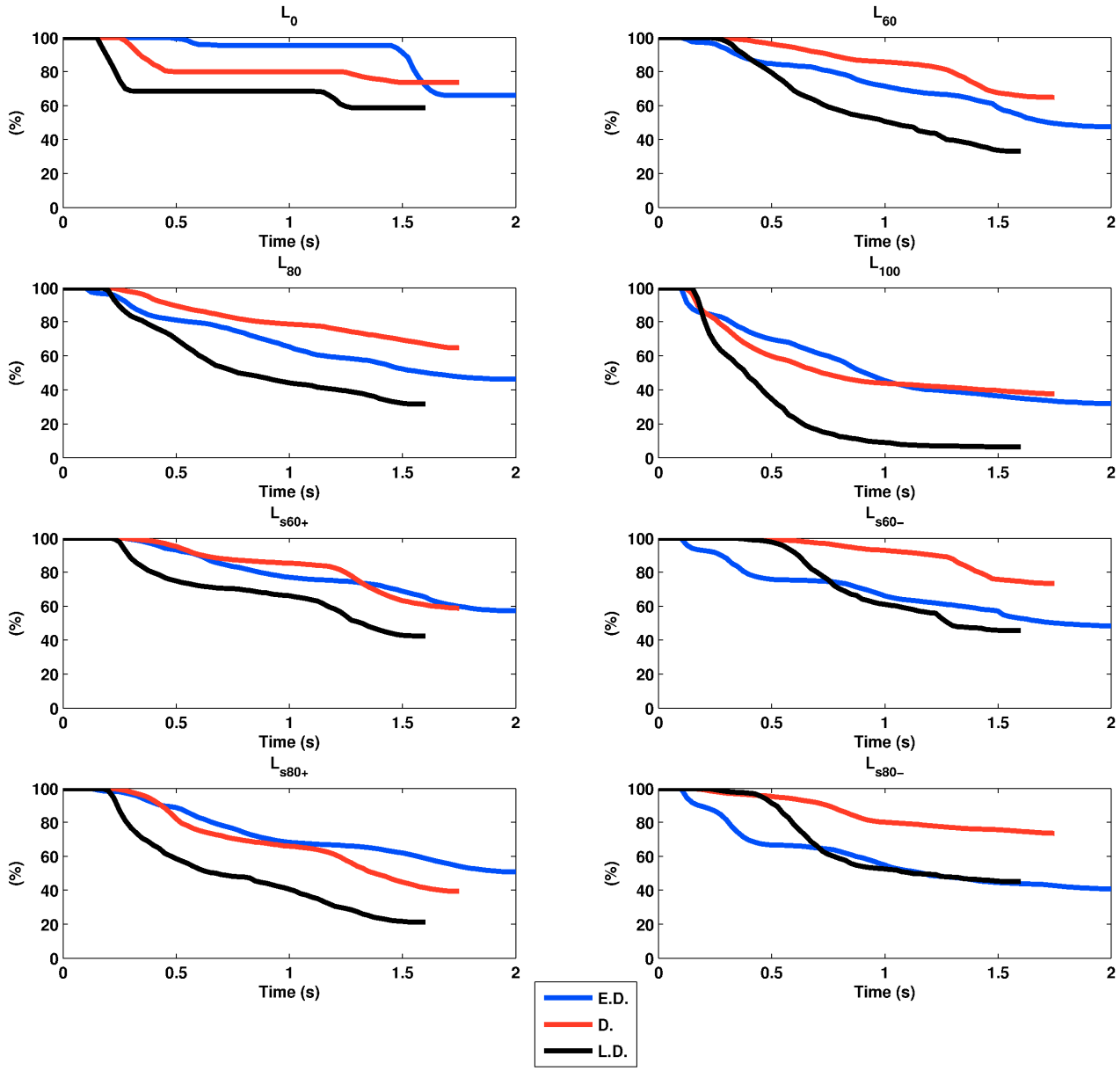

FIGURE 6.25. *The percentage of seeded particles remaining in the ventricle over time since seeding from the patient LV simulations. Results are summarised by the period of diastole within which they were seeded* – i.e. *early diastole (E.D.)* 0.0*s to* 0.18*s, diastasis (D.)* 0.18*s to* 0.41*s and late diastole (L.D.)* 0.41*s to* 0.50*s. Plots are shown for each simulation, top two rows the constant LVAD flow simulations, bottom two rows, the sinusoidal LVAD flow results.*

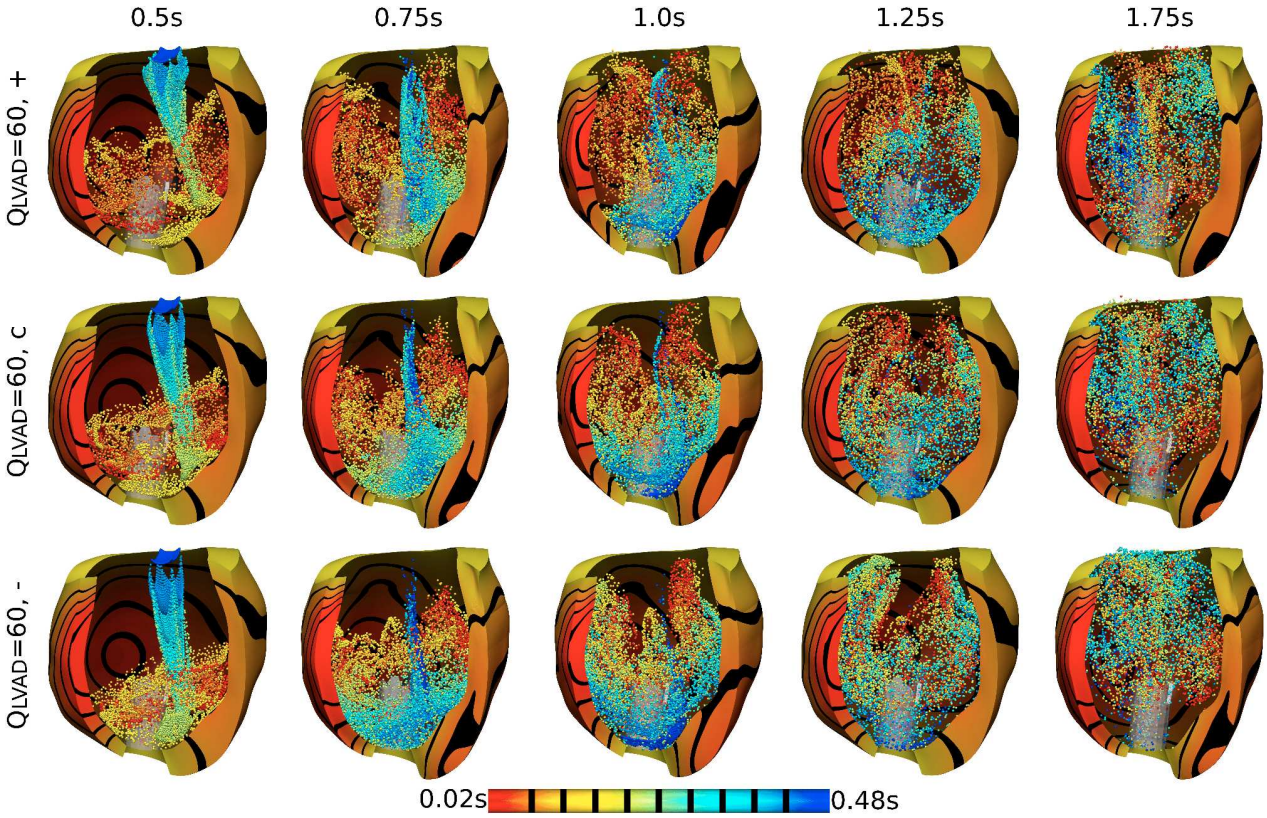

FIGURE 6.26. *Seeded particles from the L_{s60+}, top, L_{60}, centre, and L_{s60-} bottom simulations, coloured by their seed time with respect to the first set of seeded points. Particles were seeded at intervals of* 0.046*s with an initial seed time of* 0.02*s into the first diastolic period (*i.e. 0.52*s into the simulation). Two complete beats were tracked by looping over the second heart beat. Particle locations are shown at selected time points through the two tracked heart beats. Note $t = 0$ is equivalent to the commencement of diastole.*

The pattern of particle motion in the constant LVAD flow simulations was similar between the L_{60} and L_{80} cases. In the L_{60} case, aortic outflow was clearly insufficient to significantly impact the dispersal pattern of particles through the LV. The primary difference between these two cases was the accumulation of particles around the aortic mouth in the L_{80} case (see 1.75*s* in figure 6.24, this was also visible in the additional results provided in appendix E.3). The ejection distribution, with respect to diastolic period, was also similar between these cases. Differences with the L_{100} case can be explained by the less structured flow patterns observed in this simulation. Of note was the angle of the incoming stream of particles during diastole, which veers towards the cannula mouth as LVAD outflow increases. Additionally, possibly due to the large cavity volume, good recirculation of particles was observed at the cannula base.

In contrast to the LVAD results, the much stronger aortic valve outflow in the L_0 case had a significant impact on observed ventricular hemodynamics, breaking up the central, base to apex flow feature, predominant in the LVAD flow cases, and replacing it with a uniaxial drive towards the aortic valve. Due to the dilated size of the LV cavity, the main vortex that forms during diastole did not have sufficient time to draw diastolic inflow up from the apex to the basal region prior to systole. As a result, in the L_0 case, only a small fraction of diastolic inflow (in particular regarding early diastole) was ejected during the first systolic period. By the

second diastolic period, see $1.25s$ in figure 6.24, a significant volume of the early diastolic inflow volume was situated around the aortic mouth, explaining the high ratio of particles exiting the cavity during the second instance of systole.

Varying the synchrony of LVAD outflow dramatically altered the ejection pattern of particles from the cavity. Immediately obvious when examining the particle motion is the correlation between LVAD flow rate during diastole and the basal motion of particles due to vortices in the LV chamber. The greater LVAD diastolic outflow, the slower this motion. This was consistent with the weaker vortices observed in the L_{s60-} case in section 6.2.3. It is also apparent that the equivalent weaker vortices in the L_{s60+} case during systole did not substantially impact this improved circulation of particles. Overall, the higher rate of circulation in the L_{s60+} case improved mixing of the fluid, visible at $1.0s$, $1.25s$ and $1.75s$ in figure 6.26. Further evidence for this improved mixing can be seen in the traces in figure 6.25 where the percentage of ejected particles form a narrower grouping in the L_{s60+} case than either the L_{60} or L_{s60-} cases. This trend was less apparent in the L_{80} cases. However, the different rates of particle ejection between early diastole, diastasis and late diastole observed in the L_{s60-} and L_{s80-} cases highlight this poorer mixing of fluid.

The general metrics provided in table 8 provide a more quantitative basis for comparing the observed behaviour. By associating particles with diastolic inflow volumes, an estimate of the volume ratios of systolic and LVAD outflow could be made. Given the volume and low ejection fraction of the patient LV, higher rates of ejection of older fluid (*i.e.* fluid that has resided in the cavity for multiple cardiac beats) is important. Surprisingly, using this metric, both the positive and negative sinusoidal cases performed strongly, while the constant LVAD flow simulations did not. A possible explanation is that the improved mixing in the L_{s60+} and L_{s80+} cases resulted in a more even composition of systolic outflow, while the poorer mixing in the L_{s60-} and L_{s80-} cases led to periods when the predominance of outflow was from preexisting fluid (or vice versa). Both instances would result in improved ejection rates for older particles. The poor ratios observed from the negative sinusoidal cases in the % S.V. beat 1 column in table 8 provide evidence for this explanation. This result does not, however, rule out the possibility that while a high percentage of older fluid was ejected in the negative sinusoidal cases, this was only true in an averaged sense and certain regions may have exhibited poor recirculation due to the lower levels of mixing.

6.2.5.1 Discussion of Particle Tracking Results

A significant observation from these results was that the rate of fluid mixing was correlated with lower LVAD outflow during diastole. A possible explanation for this result relates to the increase in mitral inflow during diastasis in cases where LVAD outflow was higher. During diastole, incoming fluid displaces pre–existing fluid at the LV apex, forcing this volume towards the LV base. At lower diastolic LVAD flow rates, this displacement induced the formation of vortices that grew to fill the LV cavity during diastasis. As has been observed in both the preceding and current chapters, these vortices play an important role in circulating fluid through the cavity. The increase in mitral inflow, particularly during diastasis, when LVAD outflow was higher acted to block vortex formation, resulting in two layers of fluid, a basal layer of older fluid and an apical layer consisting of fluid from the current diastolic interval. Mixing between these layers was observed to be slow. This displacement of fluid can be clearly seen at $1.75s$ in the L_{s60-} case in figure 6.26.

Additionally, the importance of greater LVAD flow rates during the contractile phases can also be extrapolated from these results. If LVAD outflow decreases during this period, and limited/no outflow occurs via the aortic valve, overall flow in the ventricle will also decrease. This will have the effect of reducing mixing during this phase. This, in part, explains the varied ejection ratios between incoming diastolic groups observed in the L_0 case. Aortic outflow, weak due to tuning to heart failure parameters, was insufficient to drive adequate mixing of ventricular fluid. This hypothesis highlights the importance of aortic outflow in the mixing of blood in the ventricle. Furthermore, since increasing LVAD outflow during the contractile phases acts as a pseudo–systolic event, this theory can also explain why the weaker vortices observed during the contractile phases in the positive sinusoidal cases did not have observable negative impacts on particle mixing.

6.3 Summary and Limitations

The results presented in this chapter provide a detailed analysis of model performance under different LVAD flow regimes on a patient LV geometry. Significant variations in hemodynamic and myocardial dynamics were observed across the range of loading conditions investigated and these results provide an insight into how LVAD support impacts gross LV function. This section discusses the conclusions that can be drawn from these simulations, taking into account the impact of model limitations on these conclusions.

The most significant prediction emerging from the patient study relates to the importance of aortic valve opening on myocardial work. It was noted that the opening of the aortic valve tended to homogenise the spatial variation of work. This observation provides a rational for the current common practice of tuning LVAD flow so that the aortic valve opens on a semi–regular basis, as it indicates that this assists in enhancing the synchrony of work performed by the myocardium.

The primary conclusion from the particle tracking results, that greater fluid mixing occurs when LVAD outflow is lower during diastole, fits well with the spatial variation of work results. Given that work was more spatially homogeneous in the L_{s80+} case when the aortic valve did not open, and that improved mixing was observed in both that case and the L_{s60+} case, these results indicate that increasing LVAD outflow during systole and decreasing it during diastole improves both the spatial distribution of work and the mixing of fluid in the ventricular chamber.

Of fundamental importance with regard to using the predictions resulting from this study in a clinical setting, is the effect of model assumptions on the observed results and predictions. As noted in section 5.4, one of the primary model limitations is the boundary conditions used to constrain myocardial movement. By fixing the basal plane of the myocardium, physiological deformation is restricted. The impact of this on both myocardial deformation and the hemodynamics of blood within the ventricle is unknown. Additional considerations, such as the models lack of trabeculae, valves, the smoothness of the endocardial surface and the fluid inflow/outflow boundary conditions will also all have an impact on model behaviour.

With respect to overall simulation behaviour under different LVAD flow regimes, certain aspects, in particular peak systolic pressure and early diastolic inflow, were dependent on the contraction parameters chosen. Furthermore, the Windkessel model parameters were unchanged in each case, resulting in the simulations possibly underestimating the degree of unloading due to LVAD support. This is because greater ventricular

output leads to reduced preload and afterload, reducing the stress on the system. By maintaining the Windkessel parameters constant across all simulations, the extent of these changes was not fully captured in the model. However, in spite of these model limitations, the model provides a useful platform for investigating the impact of LVAD support on ventricular hemodynamics, myocardial stress and myocardial work.

Due to the lack of experimental and patient data, it was not possible to correlate predicted results with physical observations. As a result, further studies are required. However, the predictions made in this chapter all have simple, intuitive explanations. These results provide an indication of the impact of LVAD support on LV function under different flow regimes. The hypotheses resulting from them provide avenues and directions for future research on the subject.

7 Discussion and Future Work

In this thesis a model was developed to study the myocardial behaviour and blood hemodynamics of an LVAD supported LV. Several studies were performed using the model, including investigations into passive diastolic ventricular behaviour, LV function through the full cardiac cycle under LVAD support, as well as a patient study on the impact of varying LVAD flow rates on ventricular function. Overall, the contribution of this thesis can be divided into two categories, firstly, model development and verification, and secondly, LV simulations and results.

Building on the work of Nordsletten *et al.*[134, 136], novel contributions to the numerical scheme were made, including implementing a FD method within a fluid–solid coupled ALE framework, Newton–Raphson/line search modifications and the development of 0D/3D coupling methods. Using a series of canonical test problems, a thorough analysis of their numerical performance and convergence properties was undertaken. This provided confidence that the numerical scheme was both convergent and stable. Additionally, these test problems highlighted the importance of representing discontinuous pressures for capturing pressure gradients in FD problems. Similar studies were performed investigating the choice of element type for both FD problems and for coupling with high tension solids. These results assisted in the development of the larger LV simulations presented later in the thesis.

Alongside these major developmental contributions, additional models, constitutive laws and techniques were developed and implemented to facilitate the simulation of LV behaviour. These included various active and passive constitutive models, parameter fitting techniques, results analysis algorithms and lumped parameter models. In each case either numerical verification, or a demonstration of the schemes behaviour was presented to enhance understanding of how they impacted the overall behaviour of the system.

This model development formed the foundation on which the LV simulations were built. By combining the implemented methods and techniques, it was possible to extend the model to simulate LV function through the full cardiac cycle, converging on a repeating pressure volume loop. Additionally, this thesis presented the first, to our knowledge, patient customised study of fluid–solid mechanics in an LVAD supported LV. The simulation results outlined in the preceding chapters extend beyond merely enhancing understanding of how LVAD support affects LV function. The predictions and hypotheses relate to both aspects of patient treatment and the importance of fluid mechanics in cardiac modelling. Crucially, the results outlined in chapters 5 and 6 indicate that without blood being incorporated into the model, local analysis of myocardial behaviour is limited. This result is of wider interest to the field of cardiac modelling.

With regard to predictions relating to the impact of LVAD support on LV function, the full cardiac cycle results provide insights into both blood hemodynamics and myocardial behaviour. The importance of diastolic vortices in ventricular function was hinted at in both the normal geometry and patient results. Additionally, examining the spatial variation of work in the myocardium, the patient model provides predictions relating to the homogenising effect of aortic valve opening on the distribution of work across the LV. These results led to

the development of two main hypotheses. Firstly, that greater fluid mixing occurs when LVAD outflow is lower during diastole, and secondly, due to the homogenising effect of aortic valve opening, it is less important for LVAD outflow to be in sync with the cardiac cycle if the valve opens, than it is when the valve remains shut. These predictions provide interesting avenues for future research.

As with all biological models, various assumptions and simplifications were incorporated to facilitate the simulation of LV function. The remainder of this chapter outlines these limitations and their impact on the predictions made in this thesis. Additionally, the future direction, with respect to both incorporating greater physiological realism into the model and further investigations into LV behaviour under LVAD support, is discussed.

7.1 Model Limitations

Primary model limitations centre on two areas, simulation techniques (*i.e.* boundary conditions and other model features) and the numerical scheme itself. These limitations impact both solution refinement and accuracy, as well as the physiological realism of the model.

7.1.1 Numerical Limitations

One of the most obvious limitations of the numerical scheme was the imperfect boundary formed when using FD, leading to leakage across the FD surface. With respect to the LV simulations, this limited the capacity to investigate blood pooling around the cannula base in the full cycle results. Greater fluid refinement would reduce leakage over the FD boundary (shown in the convergence studies in chapter 3), however this was not possible due to constraints on overall problem size.

For practical purposes, the large transient fluid–solid coupled simulations performed during this thesis were limited to $\approx 8 \times 10^5$ degrees of freedom. This was due to two principle factors, firstly inverting large matrices with high bandwidth (typical in saddle point problems) is computationally costly and often involves unfeasible memory requirements. Secondly, aspects of the numerical scheme were not optimised for parallelisation and, as a result, larger simulations involved impractical time step durations. Considering the first factor, work was performed in this thesis on the choice of direct matrix solver. This resulted in the choice of SuperLU[29], due to its reduced memory requirements, for the large simulations presented in this thesis. However, all direct solvers are ultimately limited by memory requirements. With regard to the second limitation, improved parallelisation of the core routines in cHeart should improve scalability, increasing the practical range of problem sizes.

Along with improving the accuracy of the FD method, an increased capacity for problem refinement would address several other model limitations, particularly relating to the proximity of the 0D/3D interface to regions of interest. Additionally, it would enable the incorporation into the model (as well as investigation into their respective importance) of the various physiological features currently lacking from the model.

7.1.2 Physiological Limitations

The primary physiological limitations of the LV model centre on the boundary conditions applied to the system. Constraining both the apex and the base of the LV, restricted the deformation of the myocardium. Additionally, the proximity of the 0D/3D interface to the LV cavity potentially impacted the fluid solution. Incorporating either a model of basal motion, or a left atrial model would free the myocardium to behave in a more physiologically realistic manner. A left atrial model would also remove the issue regarding 0D/3D coupling on the mitral valve plane. With respect to the aortic valve, incorporation of an outflow cannula, currently not feasible due to restrictions on problem size, would improve the behaviour of the aortic 0D/3D interface.

Aside from boundary conditions, certain features of cardiac physiology are currently absent from the model. These include physiological representations of valves, trabeculae, anatomically accurate endocardial surfaces and a description of external forces, for example due to the presence of the right heart and the pericardium. The impact of these features on myocardial function and blood hemodynamics remains a subject for further research.

Other features incorporated in the model currently have idealised representations. For example the fibre orientations and choice of contraction model. These representations were primarily selected due to limited patient data. Paucity of data is an inherent limitation in biological modelling. However, recent progression in DTMRI[167] has facilitated greater insight into the laminar structure of the human heart. Additionally, within the developed framework, implementing novel contraction models is trivial. This will enable more biophysically based models to be implemented, within the existing framework, as techniques and methods improve.

Additional physiological limitations hinge on physical properties absent from the constitutive equations. These primarily revolve around the quasi–static assumption for the solid mechanics equations. By neglecting both momentum coefficients and viscous energy dissipation, the solid model can be subject to instantaneous accelerations and acts as a loss–less energy store. This approximation is valid if it is assumed that myocardial momentum effects are insignificant compared with those of the blood, and that the primary causes of ventricular energy loss are advection across the inflow/outflow valves and viscous fluid energy dissipation. Whitely *et al.*[203] found that the impact of momentum effects on the behaviour of cardiac solid mechanics models was minor. However, the effect of visco–elastic energy dissipation in myocardial tissue remains to be investigated.

7.2 Future Directions

This thesis has encompassed a broad range of focus and subjects. As a result, there are several clear directions in which the work can be extended and predictions explored. In general, these can be placed into the same two broad categories outlined in the introduction to this chapter – model development and physiological investigations. However, many of the aspects of the second category depend on the first before they can be realised.

7.2.1 Model Development – Towards a Model of the Left Heart

As discussed in the model limitations section, there are several areas that need to be addressed before the physiological realism of simulations can be extended. Of principle importance is an improved description of the basal boundary conditions. To accomplish this, the most logical extension is the incorporation of a left atrial model – creating a model of the left heart. For this to occur, several other current limitations need to be addressed, primarily relating to problem size, but also encompassing valve behaviour and descriptions of external forces. Of note regarding the development of a left heart model, is that due to the generality of the methods outlined in this thesis, the challenges relate to problem size and model peripherals, rather than the basic fluid and solid descriptions of the left atrial geometry and their coupling to the LV model.

The current numerical scheme is solved as a monolithic system using a direct matrix solver. While this ensures numerical stability, it places limitations on problem size, as discussed in section 7.1.1. Existing alternatives include partitioned schemes and iterative solvers. Due to the number of constraints applied to the model, developing a suitable pre–conditioner is inherently complex. As a result, the development of a robust, stable, partitioned numerical scheme for the finite element model presented in this thesis would be challenging. In contrast, the incorporation of an iterative matrix solver provides a clear avenue for increasing problem size. Additionally, improving the scalability of the code by increasing the parallelisation of some of the core routines in cHeart, would further assist the solving of large problems.

A simple description of valve behaviour was used to define the opening and closing of the aortic and mitral valves in this thesis. However, for a left atrial model to be coupled to the LV, an improved valve model is required to encompass the 3D motion of the valve plane *in situ*. Similar extensions would be required for the aortic valve if the 0D/3D outflow boundary is to be separated from the LV cavity. With respect to the external forces applied to the model, for a left heart model to be both stable and physiologically plausible, descriptions of these forces need to incorporated. In this regard, much work has been performed in aortic modelling, which could be directly applied to a model of the left heart.

Aside from the left atria, additional developments are required before investigations into some of the other model limitations discussed above can be performed. To investigate the impact of valves and trabeculae on the hemodynamics of blood in the LV, extension of the FD scheme to cope with deformation would be preferable in comparison to holding these features fixed. In addition, investigations into solid momentum and visco–elastic effects obviously require an extension to the current solid mechanics formulation.

7.2.2 Physiological Investigations

One of the most significant contributions of the LV simulation results presented in this thesis is to provide direction for future investigations into the impact of LVAD support on LV function. The predictions and hypotheses outlined here provide areas of investigation not only for further modelling, but also for experimental research. In conjunction with that, model validation should be attempted, requiring both greater patient data, as well as reference solutions.

Investigations into the hypotheses outlined in this thesis require a combination of both greater patient data

(*i.e.* comprehensive experimental results) and improved understanding into the impact of model limitations on simulation results. Validation of these hypotheses will represent an important advancement in the customisation of LVAD support to individual patients.

Due to the nature of the LVAD pump, obtaining in vivo patient information is challenging. Therefore direct validation of the LVAD supported LV model against patient data is not feasible. However, the model outlined in this thesis can also be used to study normal ventricular function. Therefore a two stage validation process is proposed, firstly focusing on normal LV function validating against comprehensive clinical data, before secondly using available patient metrics to compare with model behaviour under LVAD support. As *in vivo* data is limited, further physical validation of the computational model can be performed against ventricular phantoms.

A final area of physiological investigation is the application of the model to patient studies. The model has the potential to act as a tool for the customisation of LVAD support to individual patients or patient groups. In doing so, it would represent a significant advance in our ability to assist and treat heart failure patients.

7.3 Conclusions

The methods and results outlined in this thesis provide important contributions to both the methodology for developing fluid–solid coupled models of cardiac function, and the understanding of left ventricular behaviour under LVAD support. Additionally, they provide a foundation for further research in the field. While validation is required to confirm the results, the predictions made by the ventricular simulations have the potential to impact LVAD treatment protocols in patients. The broad applicability of the methodology means the results can be extended to cases beyond LVAD support. As a result, this thesis represents a significant step towards the application and customisation of patient specific fluid–solid coupled cardiac models. Such models have the potential to enhance both the understanding and treatment of heart failure.

Appendices

A Basis Functions

A.1 Basis Function to Reference Element Map

It is convenient to define the basis functions, ψ, with respect to a reference element, $\hat{e}(\boldsymbol{\phi})$, on which local basis functions, $\varphi(\boldsymbol{\phi})$, are defined ($\boldsymbol{\phi}$ represents the local coordinates on $\hat{e}$). For the element types used in this thesis (Taylor–Hood/Crouzeix–Raviart), $\hat{e}$ is constructed from n nodes, where φ is defined on $\hat{e}$ by n m^{th}–order polynomial functions. Considering the Nodal Lagrange basis definition, $\varphi_i = 1$ on node j if $i = j$ and $\varphi_i = 0$ on node j if $i \neq j$. Summing the basis set, φ, at the local coordinate, $\boldsymbol{\phi}$,

$$\sum_{i=1}^{n} \varphi_i(\boldsymbol{\phi}) = 1, \tag{1.1}$$

where, depending on element type, $\boldsymbol{\phi}$ is restricted to,

$$\begin{aligned} \boldsymbol{\phi} = [\phi_1, \cdots, \phi_d],\ 0 \leq \phi_j \leq 1, & \qquad \text{Hexahedral and Quadrilateral Elements,} \\ \boldsymbol{\phi} = [\phi_1, \cdots, \phi_d],\ 0 \leq \phi_j \leq 1 \text{ and } \textstyle\sum_{j=1}^{d} \phi_j \leq 1, & \qquad \text{Tetrahedral and Triangular Elements.} \end{aligned}$$

From this definition, the basis functions, $\varphi(\boldsymbol{\phi})$, can be used to interpolate a field, defined at each node in $\hat{e}$ by the parameters a_k, at any point $\boldsymbol{\phi}$. The interpolated value, $\bar{a}(\phi)$, is calculated as,

$$\bar{a}(\boldsymbol{\phi}) = \sum_{i=1}^{n} \varphi_i(\boldsymbol{\phi}) a_i. \tag{1.2}$$

Considering the nodal basis function ψ^i, where $i = T(j,k)$ is a node in the mesh $\mathcal{T}_h(\Lambda)$ and $T(j,k)$ represents a nodal map mapping the global node i to the k^{th} node in e_j. For the purposes of this section, the ordering of nodes within e_j and $\hat{e}$ is considered to be the same. Therefore, i is mapped to the k^{th} node in $\hat{e}$. Note, however, that i is not necessarily unique to element j. Therefore, $\psi^i = \varphi_k$ only on element j. In other elements, with which node i is shared, ψ^i will be mapped to a potentially different component of the basis set φ.

Using these definitions, the reference element to global element mapping, $\mathcal{P}_{\hat{e}}^{e_j}$, is equivalent to,

$$\mathcal{P}_{\hat{e}}^{e_j} := \varphi_i(\boldsymbol{\phi}) X_i = \mathbf{x}^h(\boldsymbol{\phi}). \tag{1.3}$$

Gradients performed on $\hat{e}$ with respect to $\boldsymbol{\eta}$ are defined as,

$$\nabla_{\boldsymbol{\eta}} = \hat{F}^{-T} \nabla_{\boldsymbol{\phi}},\ \ \hat{F} = \nabla_{\boldsymbol{\phi}} \mathcal{P}_{\hat{e}}^{e_j} = (\nabla_{\boldsymbol{\phi}} \varphi_i(\boldsymbol{\phi})) X_i, \tag{1.4}$$

where $\hat{F}$ is the reference element to domain deformation gradient tensor. Integrals over e_j are therefore defined as,

$$\int_{e_j} 1 \ \mathbf{dx} = \int_{\hat{e}} \hat{\jmath}_{e_j} \ \mathbf{d}\boldsymbol{\phi},\ \ \hat{\jmath}_{e_j} = det|\hat{F}|. \tag{1.5}$$

Practically, integrals performed over Ω/Λ are performed as a sum of integrals over each element $e_j \in \mathcal{T}_h(\Lambda)$. These integrals are performed using a Gaussian quadrature scheme, where the integral is approximated by a weighted sum of function values at points within $\hat{e}$.

A.2 Gaussian Quadrature

The reference element facilitates the integration of the nodal fields $\mathcal{V}_j$ on each element $e_j \in \mathcal{T}_h(\Lambda)$. Numerical integration is performed using quadrature schemes that approximate the definite integral of a function as a weighted sum of function values at specified points within the domain of integration. Gaussian quadrature is an n^{th} order quadrature scheme constructed to yield an exact result for polynomials of order $2n-1$. Given that fields on $\mathcal{T}_h(\Lambda)$ are approximated by polynomial functions, a Gaussian quadrature scheme enables an accurate approximation of the discrete weak equations over e_j[1]. Defining the set of n Gauss points and weights as,

$$Gp = \begin{pmatrix} Gp(1,\cdots,d) \\ \vdots \\ Gp(n,\cdots,d) \end{pmatrix}, \quad Gw = \begin{pmatrix} Gw(1) \\ \vdots \\ Gw(n) \end{pmatrix}, \quad \sum_{i=1}^{n} Gw(i) = 1. \tag{1.6}$$

The Gauss points and weights are defined with respect to a reference shape, for example triangular, hexahedral, tetrahedral etc. The i^{th} points on the reference shape are restricted to,

$$\begin{array}{cc} 0 \leq Gp(i,j) \leq 1, & \text{Hexahedral and Quadrilateral} \\ 0 \leq Gp(i,j) \leq 1, \text{ and } \sum_{j=1}^{d} Gp(i,j) \leq 1, & \text{Tetrahedral and Triangular} \end{array}, \quad j = (1,\cdots,d). \tag{1.7}$$

Choosing the correct scheme corresponding to the shape of $\hat{e}$, the integral of the local basis function, φ_k, over the reference element, $\hat{e}$, can be defined,

$$\int_{e_j} \varphi_k d\phi = \sum_{i=1}^{n} \varphi_k(Gp(i,1,\cdots,d))Gw(i). \tag{1.8}$$

Extending this, an integral, over the an element e_i, of a variable $a^h \in \mathcal{V}_a$, is approximated by,

$$\int_{e_i} a^h d\mathbf{x} = \sum_{j=1}^{np} \sum_{k=1}^{n} a^{T_a(i,j)} \varphi_j(Gp(k,1,\cdots,d))Gw(k)\hat{j}_\Omega, \tag{1.9}$$

where $T_a(i,j)$ is the nodal map for the variable a^h and np is the number of nodes in $\hat{e}$.

[1] Note that due to non–linear terms within the governing equations, the n^{th}–order Gaussian quadrature scheme will not exactly integrate the weak equations on e_j for any computationally realistic value of n.

A.3 Basis Function Coefficients

In this thesis many different basis functions were used on four different element types - 3D hexahedrals and tetrahedrons, as well as 2D quadrilaterals and triangles. This appendix contains the α and β coefficients from equation 2.77 for the basis functions used in this thesis along with the local ϕ coordinates of the nodes on the reference element. Note that the i^{th} order basis functions for any quadrilateral or hexahedron (by extension any n–dimensional hyper–quadrilateral) can be defined by the tensor product of the $1D$ i^{th} order basis functions for a line segment, *i.e.*

$$\varphi_k(\phi_a, \phi_b) = \hat{\varphi}_a(\phi_a) \cdot \hat{\varphi}_b(\phi_b), \;\; a, b \in [1, \cdots, i+1], \;\; k \in \left[1, \cdots, (i+1)^d\right],$$

where d is the dimension of the element and $\hat{\varphi}$ are the basis functions of the $1D$ line segment. Due to this simplification, only the $1D$ α and β coefficients and ϕ coordinates for these element types will be given.

A.4 Triangular Basis

Order 0: n-basis=1, n-power=1,

$$\alpha = [1], \quad \beta = \begin{bmatrix} 0 \\ 0 \end{bmatrix}, \quad \phi = \begin{bmatrix} 1/3 & 1/3 \end{bmatrix}.$$

Order 1: n-basis=3, n-power=3,

$$\alpha = \begin{bmatrix} 1 & -1 & -1 \\ 0 & 1 & 0 \\ 0 & 0 & 1 \end{bmatrix}, \quad \beta = \begin{bmatrix} 0 & 1 & 0 \\ 0 & 0 & 1 \end{bmatrix}, \quad \phi = \begin{bmatrix} 0 & 0 \\ 1 & 0 \\ 0 & 1 \end{bmatrix}.$$

Order 2: n-basis=6, n-power=6,

$$\alpha = \begin{bmatrix} 1 & -3 & -3 & 2 & 4 & 2 \\ 0 & -1 & 0 & 2 & 0 & 0 \\ 0 & 0 & -1 & 0 & 0 & 2 \\ 0 & 4 & 0 & -4 & -4 & 0 \\ 0 & 0 & 4 & 0 & -4 & -4 \\ 0 & 0 & 0 & 0 & 4 & 0 \end{bmatrix}, \quad \beta = \begin{bmatrix} 0 & 1 & 0 & 2 & 1 & 0 \\ 0 & 0 & 1 & 0 & 1 & 2 \end{bmatrix}, \quad \phi = \begin{bmatrix} 0 & 0 \\ 1 & 0 \\ 0 & 1 \\ 0.5 & 0 \\ 0 & 0.5 \\ 0.5 & 0.5 \end{bmatrix}.$$

ORDER 2CR: n-basis=7, n-power=8,

$$\alpha = \begin{bmatrix} 1 & -3 & -3 & 2 & 2 & 7 & -3 & -3 \\ 0 & -1 & 0 & 2 & 0 & 3 & -3 & -3 \\ 0 & 0 & -1 & 0 & 2 & 3 & -3 & -3 \\ 0 & 4 & 0 & -4 & 0 & -16 & 12 & 12 \\ 0 & 0 & 0 & 0 & 0 & -8 & 12 & 12 \\ 0 & 0 & 4 & 0 & -4 & -16 & 12 & 12 \\ 0 & 0 & 0 & 0 & 0 & 27 & -27 & -27 \end{bmatrix}, \quad \beta = \begin{bmatrix} 0 & 1 & 0 & 2 & 0 & 1 & 2 & 1 \\ 0 & 0 & 1 & 0 & 2 & 1 & 1 & 2 \end{bmatrix},$$

$$\phi = \begin{bmatrix} 0 & 0 \\ 1 & 0 \\ 0 & 1 \\ 0.5 & 0 \\ 0.5 & 0.5 \\ 0 & 0.5 \\ 1/3 & 1/3 \end{bmatrix}.$$

A.5 Tetrahedral Basis

ORDER 1: n-basis=4, n-power=4,

$$\alpha = \begin{bmatrix} 1 & -1 & -1 & -1 \\ 0 & 1 & 0 & 0 \\ 0 & 0 & 1 & 0 \\ 0 & 0 & 0 & 1 \end{bmatrix}, \quad \beta = \begin{bmatrix} 0 & 1 & 0 & 0 \\ 0 & 0 & 1 & 0 \\ 0 & 0 & 0 & 1 \end{bmatrix}, \quad \phi = \begin{bmatrix} 0 & 0 & 0 \\ 1 & 0 & 0 \\ 0 & 1 & 0 \\ 0 & 0 & 1 \end{bmatrix}.$$

ORDER 2: n-basis=10, n-power=10,

$$\alpha = \begin{bmatrix} 1 & -3 & -3 & -3 & 2 & 4 & 4 & 2 & 4 & 2 \\ 0 & -1 & 0 & 0 & 2 & 0 & 0 & 0 & 0 & 0 \\ 0 & 0 & -1 & 0 & 0 & 0 & 0 & 2 & 0 & 0 \\ 0 & 0 & 0 & -1 & 0 & 0 & 0 & 0 & 0 & 2 \\ 0 & 4 & 0 & 0 & -4 & -4 & -4 & 0 & 0 & 0 \\ 0 & 0 & 4 & 0 & 0 & -4 & 0 & -4 & -4 & 0 \\ 0 & 0 & 0 & 4 & 0 & 0 & -4 & 0 & -4 & -4 \\ 0 & 0 & 0 & 0 & 0 & 4 & 0 & 0 & 0 & 0 \\ 0 & 0 & 0 & 0 & 0 & 0 & 4 & 0 & 0 & 0 \\ 0 & 0 & 0 & 0 & 0 & 0 & 0 & 0 & 4 & 0 \end{bmatrix}, \quad \beta = \begin{bmatrix} 0 & 1 & 0 & 0 & 2 & 1 & 1 & 0 & 0 & 0 \\ 0 & 0 & 1 & 0 & 0 & 1 & 0 & 2 & 1 & 0 \\ 0 & 0 & 0 & 1 & 0 & 0 & 1 & 0 & 1 & 2 \end{bmatrix},$$

$$\phi = \begin{bmatrix} 0 & 0 & 0 \\ 1 & 0 & 0 \\ 0 & 1 & 0 \\ 0 & 0 & 1 \\ 0.5 & 0 & 0 \\ 0 & 0.5 & 0 \\ 0 & 0 & 0.5 \\ 0.5 & 0.5 & 0 \\ 0.5 & 0 & 0.5 \\ 0 & 0.5 & 0.5 \end{bmatrix}.$$

ORDER 2CR: n-basis=15, n-power=20,

$$\alpha =$$

$$\begin{bmatrix} 1 & -3 & -3 & -3 & 2 & 2 & 2 & -13 & 4 & 4 & 4 & 7 & -3 & -3 & 7 & -3 & -3 \\ 0 & -1 & 0 & 0 & 2 & 0 & 0 & -7 & 4 & 4 & 4 & 0 & 0 & 0 & 3 & -3 & -3 \\ 0 & 0 & -1 & 0 & 0 & 2 & 0 & -7 & 4 & 4 & 4 & 3 & -3 & -3 & 0 & 0 & 0 \\ 0 & 0 & 0 & -1 & 0 & 0 & 2 & -7 & 4 & 4 & 4 & 3 & -3 & -3 & 3 & -3 & -3 \\ 0 & 4 & 0 & 0 & -4 & 0 & 0 & 56 & -32 & -32 & -32 & 0 & 0 & 0 & -16 & 12 & 12 \\ 0 & 0 & 0 & 0 & 0 & 0 & 0 & 32 & -32 & -32 & -32 & 0 & 0 & 0 & 0 & 0 & 0 \\ 0 & 0 & 4 & 0 & 0 & -4 & 0 & 56 & -32 & -32 & -32 & -16 & 12 & 12 & 0 & 0 & 0 \\ 0 & 0 & 0 & 4 & 0 & 0 & -4 & 56 & -32 & -32 & -32 & -16 & 12 & 12 & -16 & 12 & 12 \\ 0 & 0 & 0 & 0 & 0 & 0 & 0 & 32 & -32 & -32 & -32 & 0 & 0 & 0 & -8 & 12 & 12 \\ 0 & 0 & 0 & 0 & 0 & 0 & 0 & 32 & -32 & -32 & -32 & -8 & 12 & 12 & 0 & 0 & 0 \\ 0 & 0 & 0 & 0 & 0 & 0 & 0 & -135 & 108 & 108 & 108 & 0 & 0 & 0 & 0 & 0 & 0 \\ 0 & 0 & 0 & 0 & 0 & 0 & 0 & -135 & 108 & 108 & 108 & 0 & 0 & 0 & 27 & -27 & -27 \\ 0 & 0 & 0 & 0 & 0 & 0 & 0 & -135 & 108 & 108 & 108 & 27 & -27 & -27 & 0 & 0 & 0 \\ 0 & 0 & 0 & 0 & 0 & 0 & 0 & -81 & 108 & 108 & 108 & 0 & 0 & 0 & 0 & 0 & 0 \\ 0 & 0 & 0 & 0 & 0 & 0 & 0 & 256 & -256 & -256 & -256 & 0 & 0 & 0 & 0 & 0 & 0 \end{bmatrix} \cdots$$

$$\begin{bmatrix} 7 & -3 & -3 \\ 3 & -3 & -3 \\ 3 & -3 & -3 \\ 0 & 0 & 0 \\ -16 & 12 & 12 \\ -8 & 12 & 12 \\ -16 & 12 & 12 \\ 0 & 0 & 0 \\ 0 & 0 & 0 \\ 0 & 0 & 0 \\ 27 & -27 & -27 \\ 0 & 0 & 0 \\ 0 & 0 & 0 \\ 0 & 0 & 0 \\ 0 & 0 & 0 \end{bmatrix}, \quad \beta = \begin{bmatrix} 0 & 1 & 0 & 0 & 2 & 0 & 0 & 1 & 2 & 1 & 1 & 0 & 0 & 0 & 1 & 2 & 1 & 1 & 2 & 1 \\ 0 & 0 & 1 & 0 & 0 & 2 & 0 & 1 & 1 & 2 & 1 & 1 & 2 & 1 & 0 & 0 & 0 & 1 & 1 & 2 \\ 0 & 0 & 0 & 1 & 0 & 0 & 2 & 1 & 1 & 1 & 2 & 1 & 1 & 2 & 1 & 1 & 2 & 0 & 0 & 0 \end{bmatrix},$$

$$\phi = \begin{bmatrix} 0 & 0 & 0 \\ 1 & 0 & 0 \\ 0 & 1 & 0 \\ 0 & 0 & 1 \\ 0.5 & 0 & 0 \\ 0.5 & 0.5 & 0 \\ 0 & 0.5 & 0 \\ 0 & 0 & 0.5 \\ 0.5 & 0 & 0.5 \\ 0 & 0.5 & 0.5 \\ 1/3 & 1/3 & 0 \\ 1/3 & 0 & 1/3 \\ 0 & 1/3 & 1/3 \\ 1/3 & 1/3 & 1/3 \\ 0.25 & 0.25 & 0.25 \end{bmatrix}.$$

A.6 Quadrilateral/Hexahedral Basis

ORDER 1: n-basis=2, n-power=2,

$$\alpha = \begin{bmatrix} 1 & -1 \\ 0 & 1 \end{bmatrix}, \quad \beta = \begin{bmatrix} 0 & 1 \end{bmatrix}, \quad \phi = \begin{bmatrix} 0 \\ 1 \end{bmatrix}.$$

ORDER 2: n-basis=3, n-power=3,

$$\alpha = \begin{bmatrix} 1 & -3 & 2 \\ 0 & 4 & -4 \\ 0 & -1 & 2 \end{bmatrix}, \quad \beta = \begin{bmatrix} 0 & 1 & 2 \end{bmatrix}, \quad \phi = \begin{bmatrix} 0 \\ 0.5 \\ 1 \end{bmatrix}.$$

ORDER 3: n-basis=4, n-power=4,

$$\alpha = \begin{bmatrix} 1 & -5.5 & 9 & -4.5 \\ 0 & 9 & -22.5 & 13.5 \\ 0 & -4.5 & 18 & -13.5 \\ 0 & 1 & -4.5 & 4.5 \end{bmatrix}, \quad \beta = \begin{bmatrix} 0 & 1 & 2 & 3 \end{bmatrix}, \quad \phi = \begin{bmatrix} 0 \\ 1/3 \\ 2/3 \\ 1.0 \end{bmatrix}.$$

B Calculating Rates of Work and Energy

Energy analysis was performed on the ventricular simulations performed in this thesis. This appendix outlines the equations used to calculate the transfer of energy into and out of the system, as well as between the fluid and solid domains. For a full analysis of the energy conservation properties of the coupled system presented in chapter 2 see Nordsletten[134].

From Taber[187], under isothermal conditions, the rate of kinetic, $\partial_t \mathcal{K}$, potential, $\partial_t \mathcal{U}$, and source/sink, $\partial_t \mathcal{L}$, energies are equal to the power input, $\mathcal{F}$, into a system, *i.e.*

$$\partial_t \mathcal{K} + \partial_t \mathcal{U} + \partial_t \mathcal{L} = \mathcal{F}. \tag{2.1}$$

Kinetic energy represents the internal energy due to motion, potential energy is a bodies stored elastic energy, while a source or sink of energy represents the transfer of energy into or out of the mechanical system. Finally, the power imparted to a mechanical system is the sum of any power induced by internal body forces, $\mathcal{B}$, power supplied on the domain boundaries, $\mathcal{T}$, and any energy advected into the system, $\mathcal{A}$, *i.e.*

$$\mathcal{F} = \mathcal{B} + \mathcal{T} + \mathcal{A}. \tag{2.2}$$

The energy equations, at time $t \in I$, $I = [0, T]$, for the fluid model are given in equations 2.3. Due to the Navier–Poisson constitutive law, the fluid does not store potential energy, therefore in this case $\mathcal{U}_f = 0$.

$$\mathcal{K}_f(t) = \frac{\rho}{2} \int_{\Omega_f} \mathbf{v}(t) \cdot \mathbf{v}(t) \; d\mathbf{x}, \quad \text{(Fluid Kinetic Energy)}, \tag{2.3a}$$

$$\partial_t \mathcal{L}_f(t) = \mu \int_{\Omega_f} \nabla_{\mathbf{x}} \mathbf{v}(t) : \nabla_{\mathbf{x}} \mathbf{v}(t) \; d\mathbf{x}, \quad \text{(Fluid Viscous Energy)}, \tag{2.3b}$$

$$\mathcal{B}_f(t) = \int_{\Omega_f} \mathbf{f}(t) \cdot \mathbf{v}(t) \; d\mathbf{x}, \quad \text{(Fluid Internal Power)}, \tag{2.3c}$$

$$\mathcal{T}_f(t) = \int_{\Gamma_f} \mathbf{t}_f(t) \cdot \mathbf{v}(t) \; d\mathbf{x}, \quad \text{(Boundary Power)}, \tag{2.3d}$$

$$\mathcal{A}_f(t) = \frac{\rho}{2} \int_{\Gamma_f} |\mathbf{v}(t)|^2 \mathbf{v}(t) \cdot \mathbf{n} \; d\mathbf{x}, \quad \text{(Advected Energy)}. \tag{2.3e}$$

For the solid model, due to the quasi–static assumption, Lagrangian reference frame and the hyperelastic constitutive laws used, kinetic energy, energy advection and energy sources/sinks are all negligible (*i.e.* $\mathcal{K}_s$, $\mathcal{L}_s$ and $\mathcal{A}_s \approx 0$). Considering this, the solid energy equations are defined as,

$$\partial_t \mathcal{U}_s(t) = \int_{\Lambda_s} \boldsymbol{\sigma}(t) : \nabla_x \partial_t \mathbf{u}(t)\ d\boldsymbol{\eta}, \quad \text{Solid Potential Energy,} \tag{2.4a}$$

$$\mathcal{B}_s(t) = \int_{\Lambda_s} \mathbf{f}_s(t) \cdot \partial_t \mathbf{u}(t)\ d\boldsymbol{\eta}, \quad \text{Solid Internal Power,} \tag{2.4b}$$

$$\mathcal{T}_s(t) = \int_{\Upsilon_s} \mathbf{t}_s(t) \cdot \mathbf{u}(t)\ d\boldsymbol{\eta}, \quad \text{(Boundary Power),} \tag{2.4c}$$

where $\boldsymbol{\sigma}$ is defined using the relevant constitutive law[1].

Using these definitions, the system can be defined as an energy balance where,

$$\int_I \partial_t \mathcal{K}_f + \partial_t \mathcal{L}_f + \partial_t \mathcal{U}_s\ dt = \int_I \mathcal{F}_f + \mathcal{F}_s\ dt. \tag{2.5}$$

Considering the coupled problem, on the interface between the fluid and solid domains the boundary tractions, $\mathbf{t}_f$ and $\mathbf{t}_s$, are weakly equal and opposite to each other. Additionally, since mesh velocity is weakly equal to fluid velocity on the fluid interface boundary, advective energy on the interface is negligible. Therefore, for a coupled fluid–solid problem with no external energy sources $\mathcal{F}_f = -\mathcal{F}_s$, and

$$\int_I \partial_t \mathcal{K}_f + \partial_t \mathcal{L}_f\ dt = -\int_I \partial_t \mathcal{U}_s\ dt. \tag{2.6}$$

In the LV problem, energy is advected into the system via the heart valves and the LVAD cannula outflow. Additionally, energy is provided from active tension within the myocardium. Effectively, this tension is a component of the stress tensor (see section 5.1). Therefore, to determine myocardial work, the stress tensor $\boldsymbol{\sigma}$ is broken up into its active ($\boldsymbol{\sigma}_a$) and passive ($\boldsymbol{\sigma}_p$) components. Using this division, potential energy can be redefined, and myocardial work ($\mathcal{W}$) defined, as,

$$\partial_t \mathcal{U}_s(t) = \int_{\Lambda_s} \boldsymbol{\sigma}_p(t) : \nabla_x \partial_t \mathbf{u}(t)\ d\boldsymbol{\eta}, \quad \text{Solid Potential Energy,} \tag{2.7a}$$

$$\partial_t \mathcal{W}(t) = \int_{\Lambda_s} \boldsymbol{\sigma}_a(t) : \nabla_x \partial_t \mathbf{u}(t)\ d\boldsymbol{\eta}, \quad \text{Solid Work.} \tag{2.7b}$$

[1] Note by equation 2.40, $\int_{\Upsilon_s} 1\, d\boldsymbol{\eta} = \int_{\Omega_s} 1\, d\mathbf{x}$ due to the incompressibility constraint.

C Derivation of the Myocardial Contraction Model

The contraction model[137] was derived based on the reactions that bind and unbind myosin from actin during the cross–bridge cycle. Assuming myocytes in the cell are at periodic steady state with heavily buffered concentrations of $[ADP]$, $[ATP]$ and $[Pi]$, myofilament kinetics were simplified to three principle reactions,

$$MYO_u + nA \xrightarrow{k_1} MYO_w, \tag{3.1a}$$

$$MYO_w \xrightarrow{k_2} MYO_s, \tag{3.1b}$$

$$MYO_s \xrightarrow{k_3} MYO_u + nA, \tag{3.1c}$$

where MYO_u is unbound myosin, A is exposed actin, MYO_w represents the weakly bound myosin–actin complex and the parameter n denotes the average number of exposed actin subunits required for unsterically hindered myosin binding. MYO_s is the strongly bound myosin–actin complex, which results in force generation. $k_{1:3}$ are the rate constants. Using these equations, the differential system for the concentrations of $[MYO_u]$, $[MYO_w]$ and $[MYO_s]$ is,

$$\frac{\partial}{\partial t}[MYO_u] = k_3[MYO_s] - k_1[MYO_u][A]^n, \tag{3.2a}$$

$$\frac{\partial}{\partial t}[MYO_w] = k_1[MYO_u][A]^n - k_2[MYO_w], \tag{3.2b}$$

$$\frac{\partial}{\partial t}[MYO_s] = k_2[MYO_w] - k_3[MYO_s]. \tag{3.2c}$$

Summing equations 3.2 and integrating, the sum of myosin concentrations is equal to the constant $[MYO_T]$,

$$[MYO_u] + [MYO_w] + [MYO_s] = [MYO_T]. \tag{3.3}$$

Using this, equations 3.2 can be reduced to two equations where $z = [MYO_s]/[MYO_T]$ and $x = [MYO_w]/[MYO_T]$,

$$\frac{\partial x}{\partial t} = k_1(1-z)[A]^n - (k_1[A]^n + k_2)x \tag{3.4a}$$

$$\frac{\partial z}{\partial t} = k_2 x - k_3 z. \tag{3.4b}$$

Since the strongly bound myosin–actin complex is the principle source of force generation, equations 3.4 can be further reduced into a single ODE describing the fraction of strongly bound myosin–actin,

$$\frac{d^2 z}{dt^2} + (k_2 + k_3 + k_1[A]^n)\frac{dz}{dt} + (k_2 k_3 + k_1(k_2 + k_3)[A]^n)z = k_1 k_2 [A]^n, \tag{3.5}$$

assuming that the rate of change of the reaction rates, $k_{1:3}$, is negligible relative to the reaction kinetics. Finally, since actin monomers form a regulatory subunit with troponin C and tropomyosin, it is assumed that $[A] \approx K[Ca]^{2+}$ (which is absorbed into k_1), allowing the substitution of $[Ca]^{2+}$ into the single ODE model.

D Shi–Korakianitis Windkessel Model

The Shi–Korakianitis[86, 85, 178] Windkessel model consists of ordinary differential equations (ODEs) describing the flow of blood through the systemic and pulmonary circulatory networks as well as the four cardiac chambers. This appendix details the model equations (section D.1), including the derivation of the valve resistance modification (section D.1.3), as well as the model parameters (section D.2).

D.1 Windkessel Equations

This section details the equations used in the modified Shi–Korakianitis Windkessel model implemented for this thesis. Variables are shown bold.

D.1.1 Heart Chambers

A variable elastance model was used to describe the pressure–volume relationship in the four heart chambers. In the LV, volume change was defined as,

$$\frac{d\mathbf{V}_{lv}}{dt} = \mathbf{Q}_m i - \mathbf{Q}_{ao} - \mathbf{Q}_{LVAD}, \tag{4.1}$$

and LV pressure as,

$$\mathbf{P}_{lv} = P_{lv,0} + e_{lv}(V_{lv} - V_{lv,0}), \tag{4.2}$$

where e_{lv} is a time varying elastance function of characteristic elastance $E_{lv,s}$ and $E_{lv,d}$, as well as an activation function, $e(t)$. e_{lv} was given as,

$$e_{lv}(t) = E_{lv,d} + \frac{E_{lv,s} - E_{lv,d}}{2} e(t). \tag{4.3}$$

Activation was defined using cosine functions as,

$$e(t) = \begin{cases} cos\left(\frac{t}{T_{s1}}\pi\right), & 0 \leq t < T_{s1}, \\ cos\left(\frac{t+T_{s2}-T_{s1}}{T_{s1}}\pi\right), & T_{s1} \leq t < T_{s1}, \\ 0 & T_{s2} \leq t < T. \end{cases} \tag{4.4}$$

The RV was modeled using the same equations, with detailed parameters changed.

The left and right atria were modeled using similar equations (again with different parameter values), however the activation function was redefined as,

$$e(t) = \begin{cases} 0, & 0 \leq t < T_{pb}, \\ 1 - cos\left(\frac{t - T_{pb}}{T_{pw}} 2\pi\right), & T_{pb} \leq t < T_{pb} + T_{pw}, \\ 0 & T_{pb} + T_{pw} \leq t < T. \end{cases} \tag{4.5}$$

D.1.2 Systemic/Pulmonary Networks

The systemic and pulmonary networks were described using a series of inductors, capacitors and resistors, with pressure equivalent to voltage and flow rate equivalent to current. Considering the systemic network, the the pressure and current variables were defined using the following equations,

Aortic sinus:

$$\frac{d\mathbf{P}_{sas}}{dt} = \frac{\mathbf{Q}_{ao} + \mathbf{Q}_{LVAD} - \mathbf{Q_{sas}}}{C_{sas}} \tag{4.6a}$$

$$\frac{d\mathbf{Q}_{sas}}{dt} = \frac{\mathbf{P}_{sas} - \mathbf{P}_{sat} - R_{sas}\mathbf{Q_{sas}}}{L_{sas}} \tag{4.6b}$$

Systemic Arterial Network:

$$\frac{d\mathbf{P}_{sat}}{dt} = \frac{\mathbf{Q}_{sas} - \mathbf{Q_{sat}}}{C_{sat}} \tag{4.7a}$$

$$\frac{d\mathbf{Q}_{sat}}{dt} = \frac{\mathbf{P}_{sas} - \mathbf{P}_{svn} - (R_{sat} + R_{sar} + R_{scp})\mathbf{Q_{sat}}}{L_{sat}} \tag{4.7b}$$

Systemic Venous Network:

$$\frac{d\mathbf{P}_{svn}}{dt} = \frac{\mathbf{Q}_{sat} - \mathbf{Q_{svn}}}{C_{svn}} \tag{4.8a}$$

$$\frac{d\mathbf{Q}_{svn}}{dt} = \frac{\mathbf{P}_{svn} - \mathbf{P}_{ra}}{R_{svn}} \tag{4.8b}$$

The model of the pulmonary loop was similar to that of the systemic loop, with different system parameters.

D.1.3 Valve Resistance

The modified valve resistance functions were derived, assuming laminar flow and no gravity, by considering Bernoulli's equation relating the conservation of energy between two points on the same streamline,

$$\mathbf{P}_1 + \frac{1}{2}\rho\mathbf{V}_1^2 = \mathbf{P}_2 + \frac{1}{2}\rho\mathbf{V}_2^2, \tag{4.9}$$

where $\mathbf{P}_1$ and $\mathbf{V}_1$ are the upstream pressure and velocity, while $\mathbf{P}_2$ and $\mathbf{V}_2$ are the downstream equivalents. Considering conservation of mass, the flow rate, $\mathbf{Q}$, is defined as,

$$\mathbf{Q} = A_1\mathbf{V}_1 = A_2\mathbf{V}_2, \tag{4.10}$$

where A_i is the cross–sectional area of the cavity at point $i = [1, 2]$. Equation 4.9 becomes,

$$\mathbf{P}_1 - \mathbf{P}_2 = \frac{1}{2}\rho\left(\frac{\mathbf{Q}}{A_2}\right)^2 - \frac{1}{2}\rho\left(\frac{\mathbf{Q}}{A_1}\right)^2, \tag{4.11}$$

solving for $\mathbf{Q}$,

$$\mathbf{Q} = A_2\left(\frac{2(\mathbf{P}_1 - \mathbf{P}_2)/\rho}{1 - (A_2/A_1)^2}\right)^{0.5}. \tag{4.12}$$

Breaking equation 4.12 down into constant and variable components,

$$\mathbf{Q} = CQ(\mathbf{P}_1 - \mathbf{P}_2)^{0.5}, \tag{4.13}$$

where,

$$CQ = A_2\left(\frac{2}{\rho(1 - (A_2/A_1)^2)}\right)^{0.5}. \tag{4.14}$$

Considering the mitral valve, $A_{mi,b}$ was defined as the area of the valve boundary, including both open and closed regions, and $A_{mi,o}$ was the open valve area. The resistance, CQ_{mi}, was defined as,

$$CQ_{mi} = A_{mi,o}\left(\frac{2}{\rho(1 - (A_{mi,o}/A_{mi,b})^2)}\right)^{0.5}, \tag{4.15}$$

and $\mathbf{Q}_{mi}$, incorporating the inductance parameter, as,

$$\mathbf{Q}_{mi} = \begin{cases} CQ_{mi}(\mathbf{P}_{la} - \mathbf{P}_{lv})^{0.5} - L_{mi}\frac{d\mathbf{Q}_{mi}}{dt}, & \text{if } \mathbf{P}_{lv} < \mathbf{P}_{la} \\ -L_{mi}\frac{d\mathbf{Q}_{mi}}{dt}, & \text{else} \end{cases} \tag{4.16}$$

If $\mathbf{P}_{lv} > \mathbf{P}_{la}$, L_{mi} was scaled by $(\mathbf{P}_{la}/\mathbf{P}_{lv})^2$. The other valve flow rates, $\mathbf{Q}_{ao}$, $\mathbf{Q}_{ti}$ and $\mathbf{Q}_{po}$ were defined similarly. For valves not coupled to fluid boundaries, CQ_{valve} was considered to be a constant.

D.2 Windkessel Parameters

The model parameters for the modified Shi–Korakianitis are outlined in this section. Most of the parameters are as defined in Korakianitis and Shi[86], however, for tuning the model to desired LV pressure–volume systemic arterial resistance, R_{sat}, pulmonary arterial resistance, R_{pat}, as well as total system blood volume (see table 4) were varied. This section defines the heart parameters, table 1, circulation parameters, table 2, additional constants, table 3, as well as the initial conditions from the Windkessel only simulations (section 5.2.1.1). For the other simulations, the initial conditions were calculated by first solving the Windkessel model until steady state was reached, then solving a solid only ventricular model coupled to the Windkessel, again until steady state, before using the resulting Windkessel variable values as initial conditions for the fluid–solid coupled LV simulations.

Part	Parameter	Value	Units
Left Heart	CQ^*_{ao}	120	$ml\,(s\,mmHg^{0.5})^{-1}$
	CQ^*_{mi}	140	$ml\,(s\,mmHg^{0.5})^{-1}$
	L_{mi}	0.01	$mmHg\,s^2\,ml^{-1}$
	L_{ao}	0.01	$mmHg\,s^2\,ml^{-1}$
	E_{lvs}	2.5	$mmHg\,ml^{-1}$
	E_{lvd}	0.1	$mmHg\,ml^{-1}$
	$P_{lv,0}$	1	$mmHg$
	$V_{lv,0}$	5	ml
	E_{las}	0.25	$mmHg\,ml^{-1}$
	E_{lad}	0.15	$mmHg\,ml^{-1}$
	$P_{la,0}$	1	$mmHg$
	$V_{la,0}$	5	ml
Right Heart	CQ^*_{po}	120	$ml\,(s\,mmHg^{0.5})^{-1}$
	CQ^*_{ti}	140	$ml\,(s\,mmHg^{0.5})^{-1}$
	L_{po}	0	$mmHg\,s^2\,ml^{-1}$
	L_{ti}	0	$mmHg\,s^2\,ml^{-1}$
	E_{rvs}	1.15	$mmHg\,ml^{-1}$
	E_{rvd}	0.1	$mmHg\,ml^{-1}$
	$P_{rv,0}$	1	$mmHg$
	$V_{rv,0}$	10	ml
	E_{ras}	0.25	$mmHg\,ml^{-1}$
	E_{rad}	0.15	$mmHg\,ml^{-1}$
	$P_{ra,0}$	1	$mmHg$
	$V_{ra,0}$	4	ml

TABLE 1

*Parameter values for the four heart chambers. * parameters are the valve resistances which are not used when the model is coupled to a fluid boundary.*

Part	Parameter	Value	Units
Systemic Network	C_{sas}	0.08	$ml\,mmHg^{-1}$
	R_{sas}	0.003	$mmHg\,s\,ml^{-1}$
	L_{sas}	0.000062	$mmHg\,s^2\,ml^{-1}$
	C_{sat}	1.6	$ml\,mmHg^{-1}$
	R^*_{sat}	0.05	$mmHg\,s\,ml^{-1}$
	L_{sat}	0.0017	$mmHg\,s^2\,ml^{-1}$
	R_{sar}	0.5	$mmHg\,s\,ml^{-1}$
	R_{scp}	0.52	$mmHg\,s\,ml^{-1}$
	R_{svn}	0.075	$mmHg\,s\,ml^{-1}$
	C_{svn}	20.5	$ml\,mmHg^{-1}$
	C_{svc}	1.5	$ml\,mmHg^{-1}$
Pulmonary Network	C_{pas}	0.18	$ml\,mmHg^{-1}$
	R_{pas}	0.002	$mmHg\,s\,ml^{-1}$
	L_{pas}	0.000052	$mmHg\,s^2\,ml^{-1}$
	C_{pat}	3.8	$ml\,mmHg^{-1}$
	R^*_{pat}	0.01	$mmHg\,s\,ml^{-1}$
	L_{pat}	0.0017	$mmHg\,s^2\,ml^{-1}$
	R_{par}	0.05	$mmHg\,s\,ml^{-1}$
	R_{pcp}	0.25	$mmHg\,s\,ml^{-1}$
	R_{pvn}	0.006	$mmHg\,s\,ml^{-1}$
	C_{pvn}	20.5	$ml\,mmHg^{-1}$
	C_{pvc}	1.5	$ml\,mmHg^{-1}$

TABLE 2

*Parameter values for the systemic and pulmonary circulation networks. * parameters were varied when tuning the Windkessel model.*

Parameter	Value	Units
T	1	s
T_{s1}	0.3	s
T_{s2}	0.45	s
T_{pb}	0.87	s
T_{pw}	0.13	s

TABLE 3

Time parameter values.

Parameter	Value	Units
$\mathbf{V}^*_{lv,0}$	800	ml
$\mathbf{V}_{rv,0}$	500	ml
$\mathbf{V}_{la,0}$	60	ml
$\mathbf{V}_{ra,0}$	45	ml

TABLE 4

*Initial conditions, note all variables not listed had an initial condition of 0. * parameter was varied when tuning the Windkessel model.*

E Additional Patient Results

This appendix provides supplementary results from the customised patient LVAD study. Visualisation of flow features, myocardial displacements and LV cavity pressures from the L_{80} simulations is provided in section E.1, an analysis of the energetics of blood flow in the patient simulations is presented in section E.2, while further visualisation of the particle tracking results from the patient model are shown in section E.3.

E.1 Additional LV Flow and Pressure Features

The results in section 6.2.3 only showed streamlines and pressures from the L_{60} constant and sinusoidal flow regime results. The trends observed in those results were similar to those seen in the L_{80} cases (apart from during systole), which are presented in this section. Figures E.1 and E.3 show the streamlines and myocardial displacements from the contractile and diastolic phases respectively. The corresponding pressure plots are provided in figures E.2 and E.4.

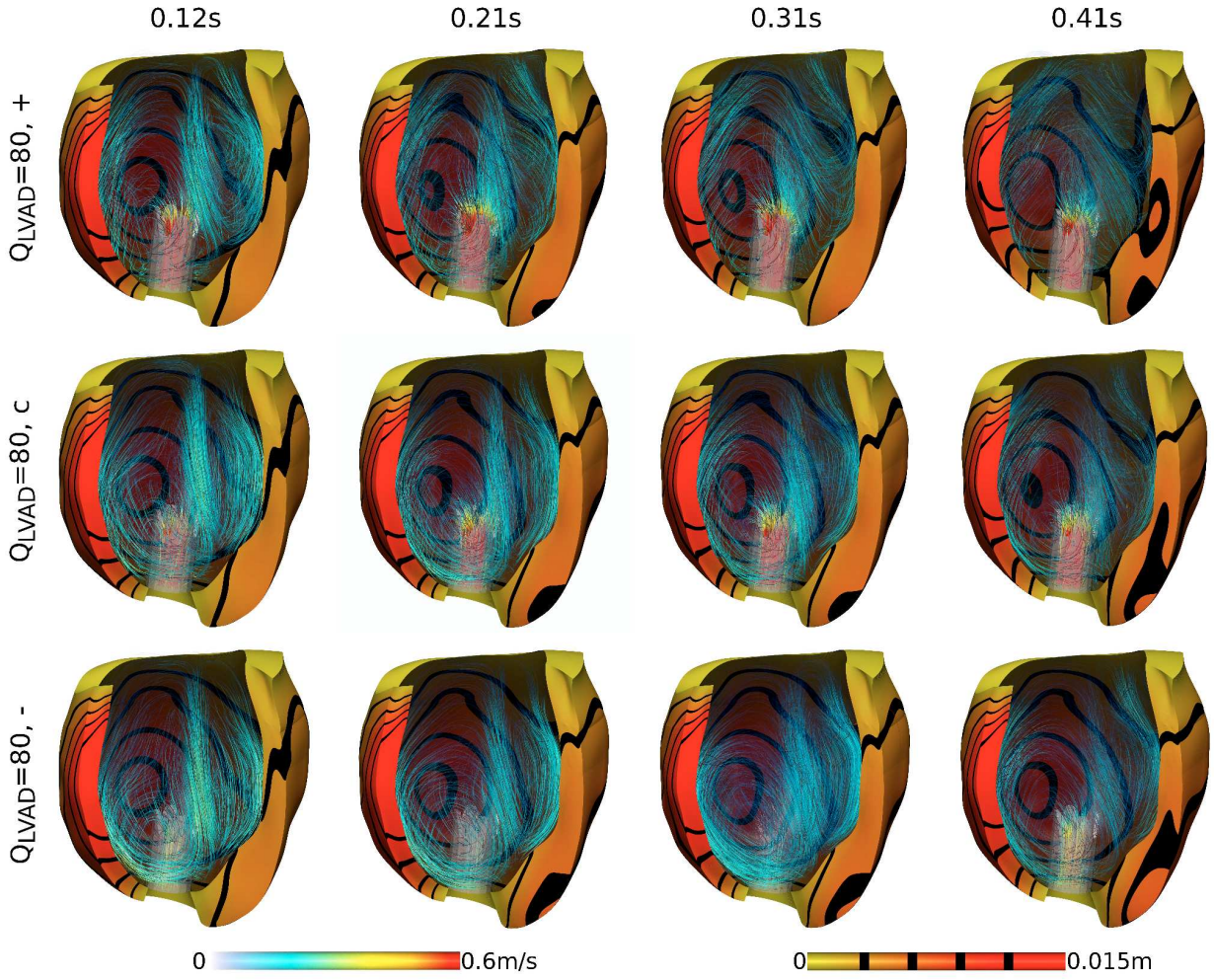

FIGURE E.1. *Fluid streamlines and myocardial displacements from the second simulated heart beat from the L_{80} LVAD flow regime cases during the contractile phases: top row, L_{s80+}, centre row, L_{s80+}, and bottom row L_{s80-}. The results are visualised at $0.12s$, $0.21s$, $0.27s$ and $0.41s$. Note that since the aortic valve never opened, a distinction between IVC, systole and IVR cannot be made.*

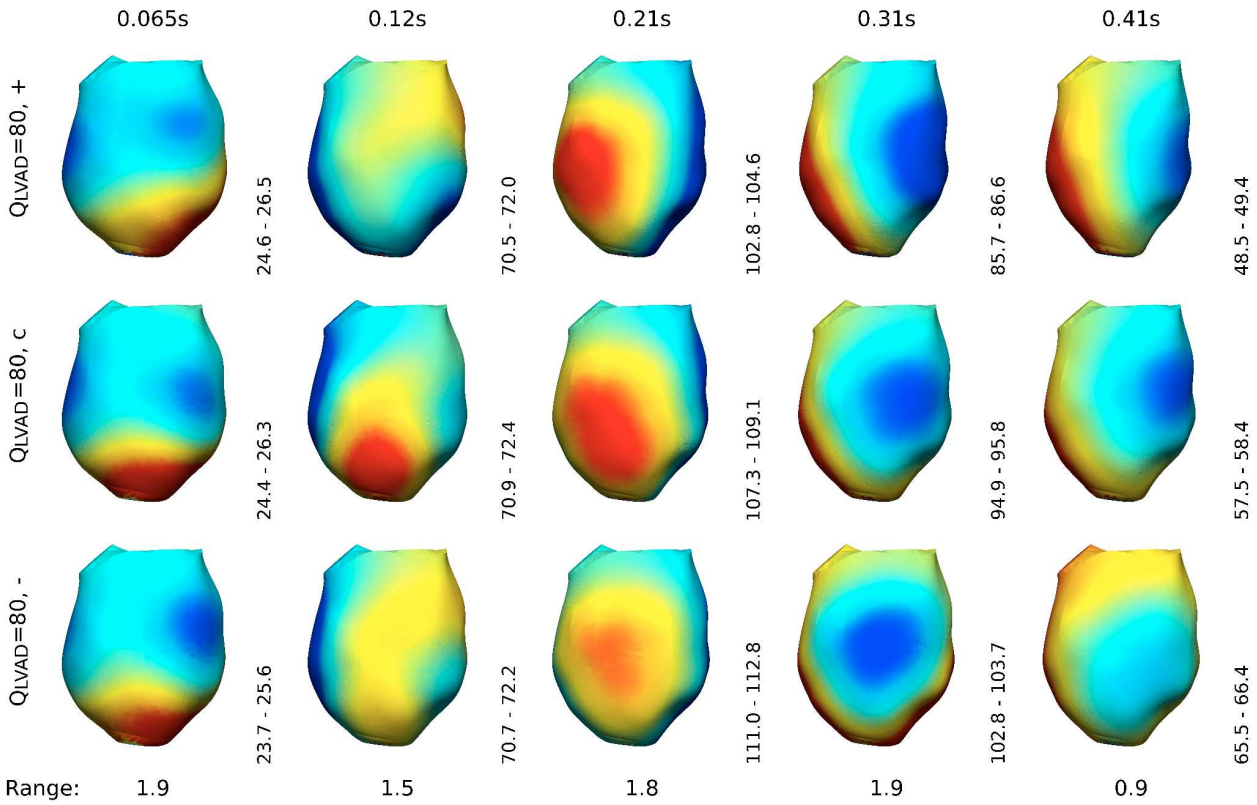

FIGURE E.2. *LV cavity pressure from the second simulated heart beat of the L_{80} LVAD flow regime cases during the contractile phases: top row, L_{s80+}, centre row, L_{s80+}, and bottom row L_{s80-}. The results are visualised at* $0.065s$, $0.12s$, $0.21s$, $0.31s$ *and* $0.41s$. *Note that since the aortic valve never opened, a distinction between IVC, systole and IVR cannot be made. The pressure scale in $mmHg$, blue to red, is provided on the bottom right of each sub–figure. The range in pressure values was constant across each column of sub–figures and is provided at the bottom of each column.*

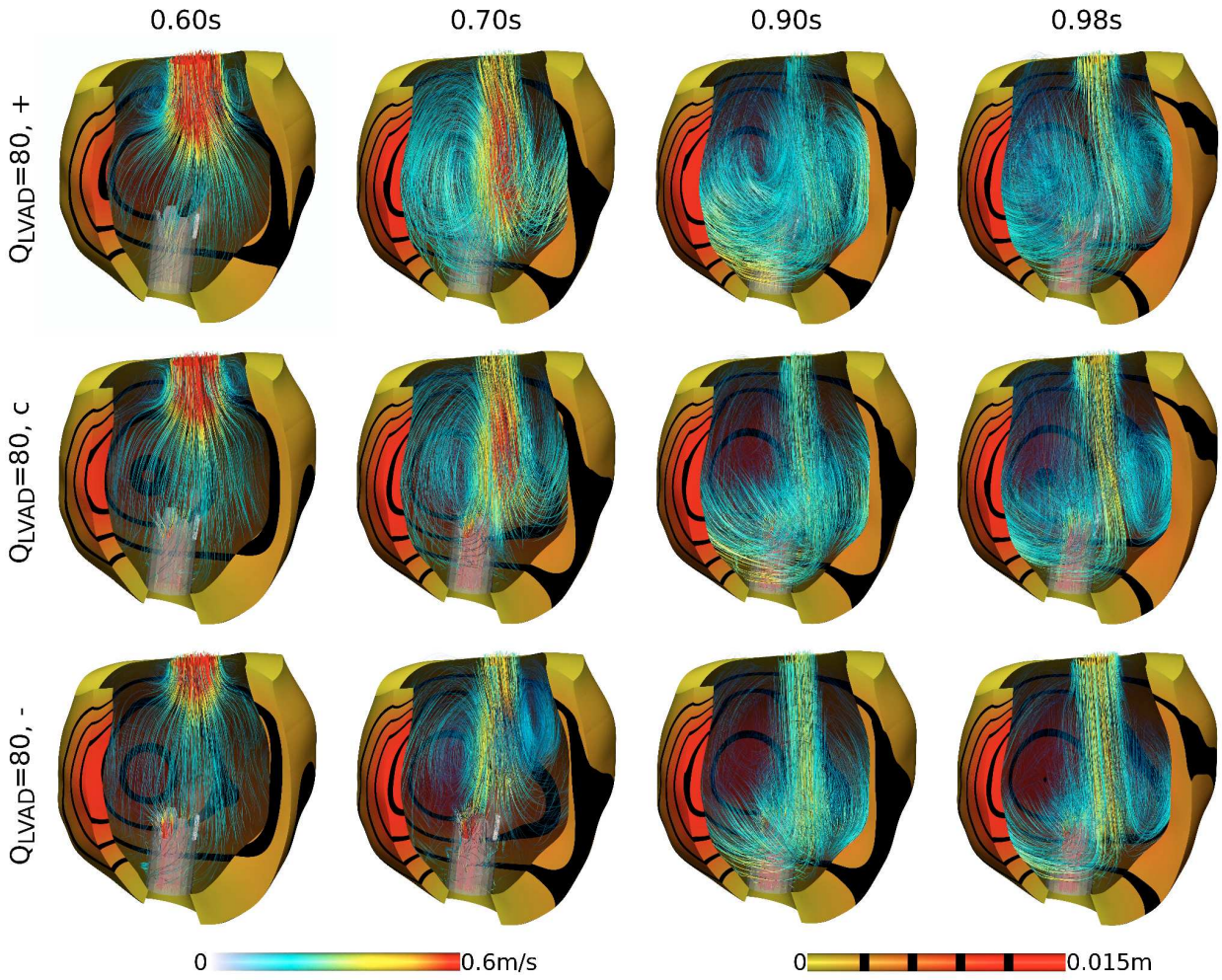

FIGURE E.3. *Fluid streamlines and myocardial displacements from the second simulated heart beat from the L_{80} LVAD flow regime cases during diastole: top row, L_{s80+}, centre row, L_{s80+}, and bottom row L_{s80-}. The results are visualised at early diastole (0.60s), diastasis (0.70s and 0.90s) and late diastole (0.98s).*

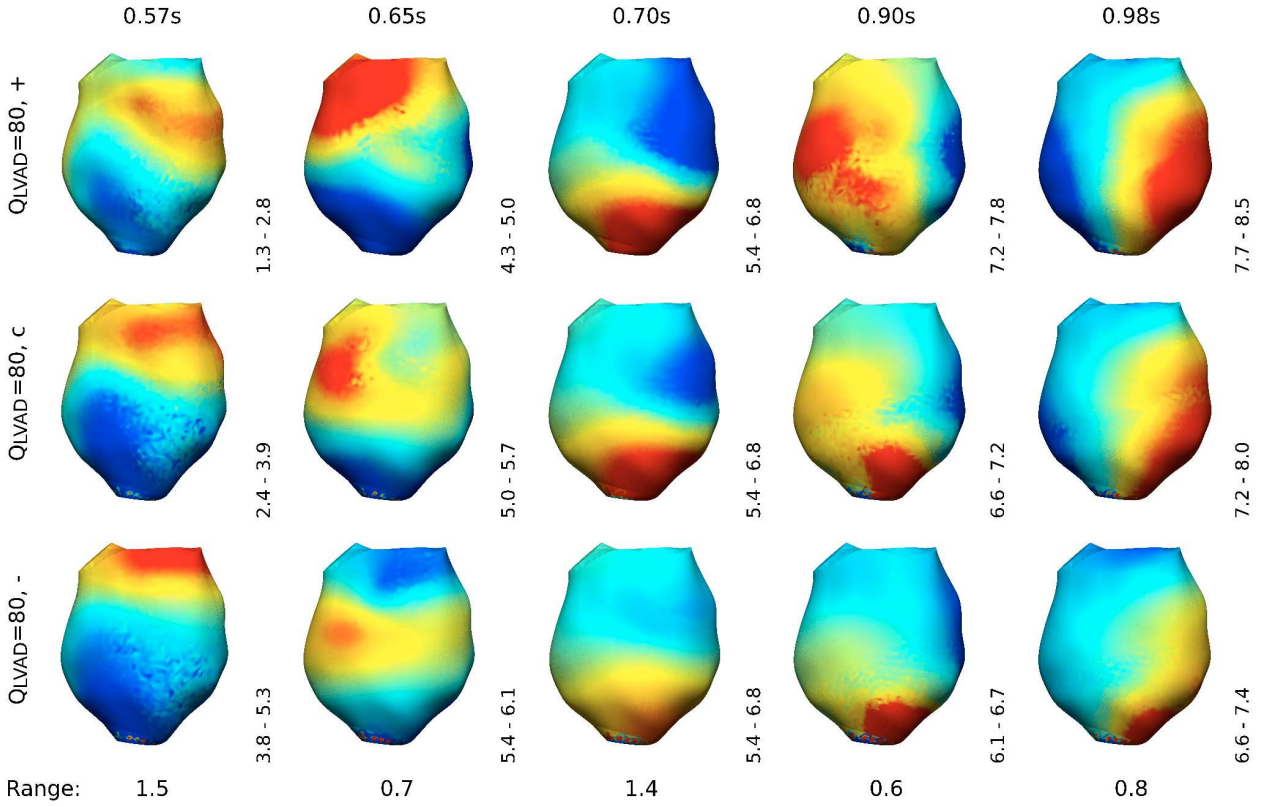

FIGURE E.4. *LV cavity pressure from the second simulated heart beat of the L_{80} LVAD flow regime cases during diastole: top row, L_{s80+}, centre row, L_{s80+}, and bottom row L_{s80-}. The results are visualised at early diastole (0.57s and 0.65s), diastasis (0.70s and 0.90s) and late diastole (0.98s). The pressure scale in mmHg, blue to red, is provided on the bottom right of each sub–figure. The range in pressure values was constant across each column of sub–figures and is provided at the bottom of each column.*

E.2 Energetics of Blood flow in the Patient Model

An analysis of myocardial energy transfer in the patient simulations is provided in section 6.2.4. For completeness, this section presents the fluid energetics from the same simulations. A comparison of rates of kinetic energy and viscous loss between the various LVAD flow regimes is provide in figures E.5 (contractile phases) and E.6 (diastole).

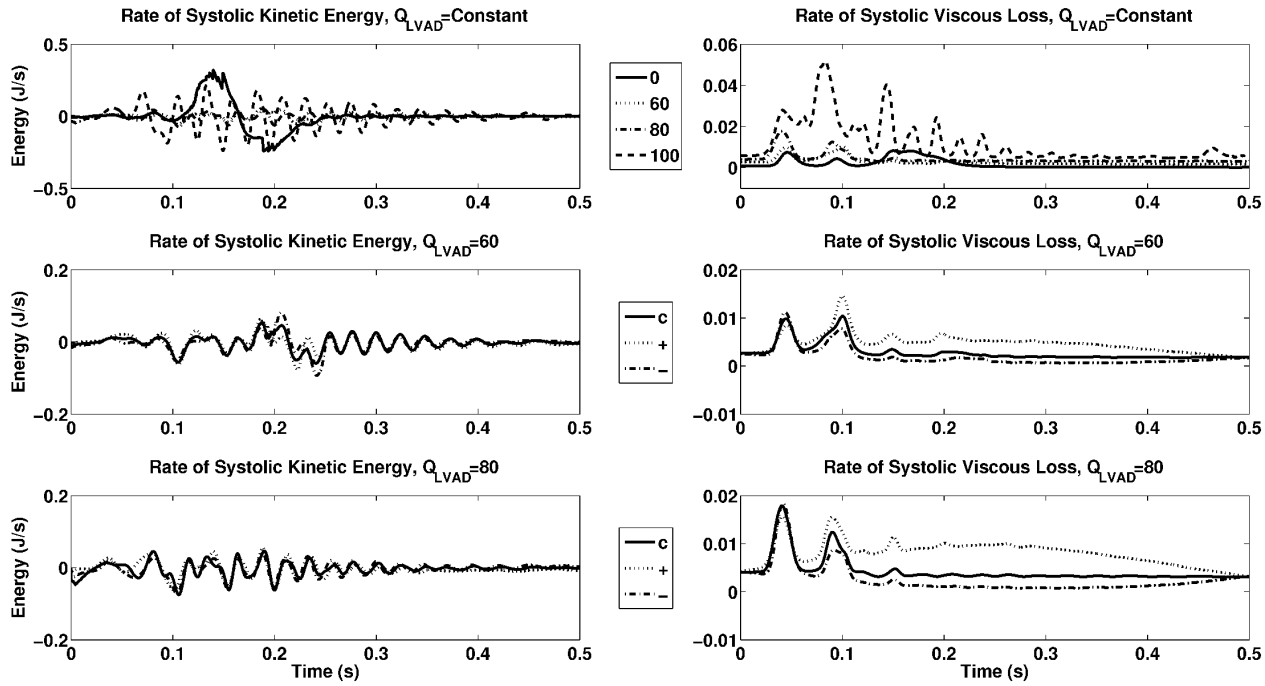

FIGURE E.5. *Rates of kinetic energy and viscous energy dissipation during the contractile phases. Top row, results from the constant LVAD flow simulations, middle row, the L_{60} cases, bottom row, the L_{80} cases. c, + and − refer to the L_X, L_{sX+} and L_{sX-} cases respectively, where X is the LVAD flow rate through one cardiac cycle.*

Of note is the correlation between higher LVAD outflow and viscous energy dissipation. This is particularly evident from the sinusoidal simulations, where, when LVAD outflow was higher, viscous loss was greater – this occurred during the contractile phases for the in sync sinusoidal simulations and during diastole for the counter sync cases. Additionally, significant oscillations in kinetic energy were observed in the L_{100} case. This was the manifestation of the greater range in systolic LV cavity pressure seen in this case (see figure 6.11). LV volume, and as a result myocardial potential energy, was significantly lower in this problem. Therefore, due to the non–linear constitutive law, the myocardium was less resistant to strain, enabling greater momentum shifts to occur. This led to the observed oscillations in the rate of kinetic energy. Similar oscillations in kinetic energy were observed during the contractile phases in the L_{60} and L_{80} cases. These were also caused by energy transfer between the fluid and solid domains, leading to momentum shifts in the fluid.

Other fluid energy features correlate with peaks in aortic or mitral valve flow. For example, the peak observed in kinetic energy in the L_0 case corresponds to peak aortic outflow. Similarly, also due to aortic outflow, a

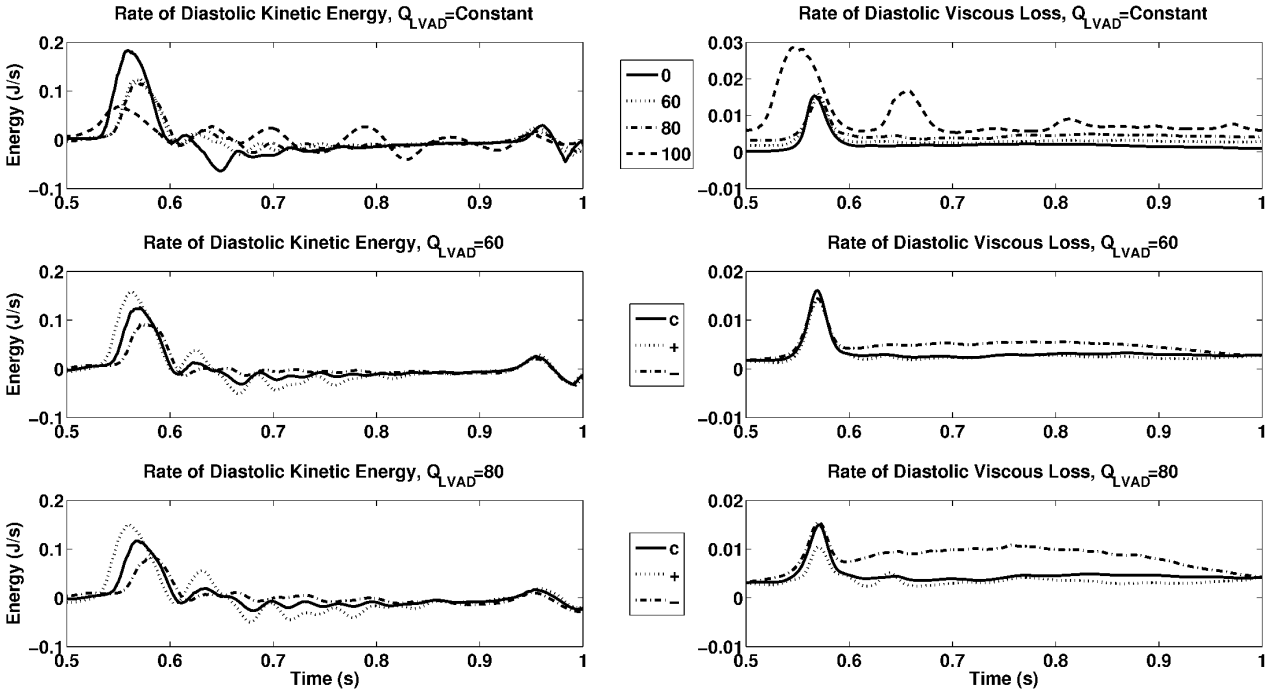

FIGURE E.6. *Rates of kinetic energy and viscous energy dissipation during diastole. Top row, results from the constant LVAD flow simulations, middle row, the L_{60} cases, bottom row, the L_{80} cases. c, + and − refer to the L_X, L_{sX+} and L_{sX-} cases respectively, where X is the LVAD flow rate through one cardiac cycle.*

minor peak was observed around $0.2s$ in the L_{60} cases. The peaks in diastolic kinetic energy in figure E.6 were caused by peaks in mitral inflow (see figure 6.9).

E.3 Residence Times in the Patient Model

Section 6.2.5 presented the results from the particle tracking analysis of the patient LV simulations. Figures visualising the movement of the seeded particles were shown for both the constant LVAD smulations and the L_{60} constant and sinusoidal results. Figure E.7 provides the L_{80} constant and sinusoidal results which show the same general trends as the L_{60} cases presented in the main thesis body.

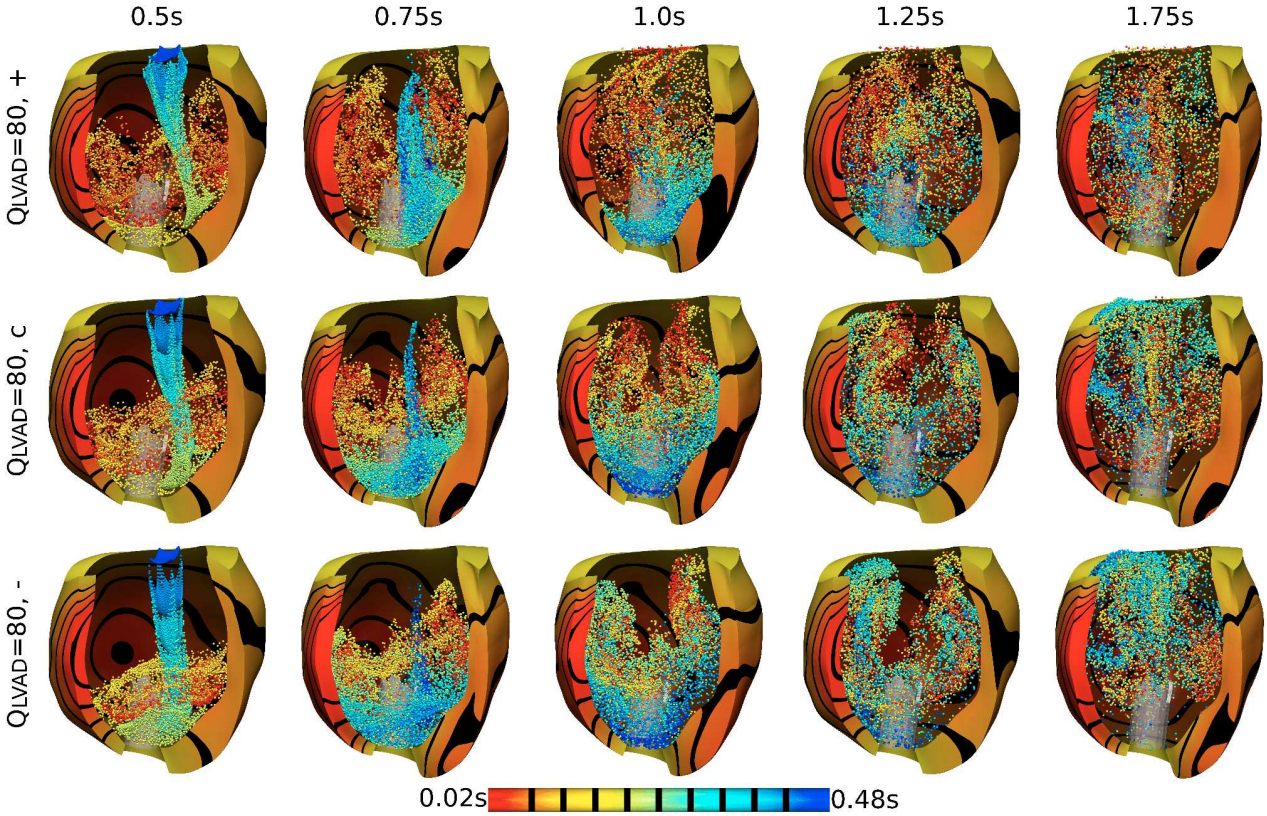

FIGURE E.7. *Seeded particles from the L_{s80+}, top, L_{80}, centre, and L_{s80-} bottom simulations, coloured by their seed time with respect to the first set of seeded points. Particles were seeded at intervals of* 0.046*s with an initial seed time of* 0.02*s into the first diastolic period (*i.e. 0.52*s into the simulation). Two complete beats were tracked by looping over the second heart beat. Particle locations are shown at selected time points through the two tracked heart beats. Note $t = 0$ is equivalent to the commencement of diastole.*

References

1. F. Arabia, R. Smith, D. Rose, D. Arzouman, G. Sethi, and J. Copeland. Success rates of long-term circulatory assist devices used currently for bridge to heart transplantation. *ASAIO Journal*, 42:M542–M546, 1996.
2. I. Babuska, E. Podnos, and G. Rodin. New ficititious domain methods: Formulation and analysis. *Mathematical Models and Methods in Applied Science*, 15:1575–1594, 2005.
3. B. Baccani, F. Domenichini, G. Pedrizzetti, and G. Tonti. Fluid dynamics of the left ventricular filling in dilated cardiomyopathy. *Journal of Biomechanics*, 35:665–671, 2002.
4. G. Batchelor. On steady laminar flow with closed streamlines at large reynolds number. *Journal of Fluid Mechanics*, 1:177–190, 1956.
5. K Bathe and G. Ledezma. Benchmark problems for incompressible fluid flows with structural interactions. *Computers and Structures*, 85:628–644, 2007.
6. Y. Bazilevs, J. Gohean, T. Hughes, R. Moser, and Y. Zhang. Patient-specific isogeometric fluid-structure interaction analysis of thoracic aortic blood flow due to implantation of the jarvik 2000 left ventricular assist device. *Computer Methods in Applied Mechanics and Engineering*, 198(45-46):3534 – 3550, 2009.
7. Y. Bazilevs, M. Hsu, Y. Zhang, W. Wang, X. Liang, T. Kvamsdal, R. Brekken, and J. Isaksen. A fully-coupled fluid-structure interaction simulation of cerebral aneurysms. *Computational Mechanics*, 46:3–16, 2010. 10.1007/s00466-009-0421-4.
8. A. Benim, A. Nahavandi, A. Assmann, D. Schubert, P. Feindt, and S. Suh. Simulation of blood flow in human aorta with emphasis on outlet boundary conditions. *Applied Mathematical Modelling*, 35:3175–3188, 2011.
9. F. Bertrand, M. Gadbois, and P. Tanguy. Tetrahedral elements for fluid flow. *International Journal of Numerical Methods in Engineering*, 33:1251–1267, 1992.
10. E. Birks, M. Yacoub, N. Banner, and A. Khaghani. The role of bridge to transplantation: should LVAD patients be transplanted. *Current Opinion in Cardiology*, 19:148–153, 2004.
11. J. Bischoff, E. Arruda, and K. Grosh. A microstructurally based orthotropic hyperelastic constitutive law. *Journal of Biomechanical Engineering*, 69:570–579, 2002.
12. P. Blanco, R. Feijoo, and S. Urquiza. A unified variational approach for coupling 3d–1d models and its blood flow applications. *Computational methods in Applied Mechanical Engineering*, 196:4391–4410, 2007.
13. J. Boland and R. Nicolaides. Stability of finite elements under divergence constraints. *SIAM Journal of Numerical Analysis*, 20:722–731, 1983.
14. D. Bradley, E. Bradley, and K. Baughman. Cardiac resynchronization and death from progressive heart failure: a meta-analysis of randomized controlled trials. *Journal of the American Medical Association*, 289:730–740, 2003.
15. D. Braess. *Finite Elements*. Cambridge, 2 edition, 2001.
16. F. Brezzi, J. Douglas, R. Duran, and M. Fortin. Mixed finite elements for second order elliptic problems in three variables. *Numerical Mathematics*, 51:237–250, 1987.
17. F. Brezzi and R. Falk. Stability of higher-order hood-taylor methods. *SIAM Journal of Numerical Analysis*, 28:581–590, 1991.
18. A. Brown, Y. Shi, A. Arndt, J. Muller, P. Lawford, and D. Hose. Importance of realistic LVAD profiles for assisted aortic simulations: evaluation of optimal outflow anastomosis locations. *Computer Methods in Biomechanics and Biomedical Engineering*, page DOI: 10.1080/10255842.2011.556628, 2011.
19. B. Bruckner, S. Stetson, A. Perez-Verdia, K. Youker, B. Radovancevic, and J. Connelly. Regression of fibrosis and hypertrophy in failing myocardium following mechanical circulatory support. *Journal of Heart and Lung Transplant*, 20:457–64, 2001.
20. A. Bundkirchen and R. Schwinger. Epidemiology and economic burden of chronic heart failure. *European Society of Cardiology*, 6:D57–D60, 2004.
21. D. Burkhoff, S. Klotz, and D. Mancini. LVAD induced reverse remodeling: basic and clinical implications for myocardial recovery. *Journal of Caridac Failure*, 12:227–239, 2006.

22. V. Calo, N. Brasher, Y. Bazilevs, and T. Hughes. Multiphysics model for blood flow and drug transport with application to patient specific coronary artery flow. *Computational Mechanics*, 43:161–177, 2008.
23. P. Castelland, M. Fatemi, V. Bertault-Valls, Y. Etienne, and J. Blanc. Cardiac resynchronisation therapy: "nonresponders" and "hyperresponders". *Heart Rhythm*, 5:193–197, 2008.
24. Y. Cheng, H. Oertel, and T. Schenkel. Fluid-structure coupled CFD simulation of the left ventricular flow during filling phase. *Annals of Biomedical Engineering*, 8:567–576, 2005.
25. J. Cleland, J. Daubert, and E. Erdmann. The effect of cardiac resynchronization on morbidity and mortality in heart failure. *New England Journal of Medicine*, 352:1539–1549, 2005.
26. W. Colucci, R. Wright, and E. Braunwald. New positive inotropic agents in the treatment of congestive heart failure. mechanisms of action and recent clinical developments. *New England Journal of Medicine*, 314:290–299, 1986.
27. K. Costa, J. Holmes, and A. McCulloch. Modeling cardiac mechanical properties in three dimensions. *Philisophical Transactions of the Royal Society*, 359:1233–1250, 2001.
28. M. Courtois, S. Kovacs, and P. Ludbrook. Transmitral pressure–flow velocity relaton. importance of regional pressure gradients in the left ventricle during diastole. *Circulation*, 78:661–671, 1988.
29. crd.lbl.gov/ xiaoye/SuperLU/, 2011.
30. M. Crouzeix and P. Raviart. Conforming and nonconforming finite element methods for solving the stationary stokes equations. *RAIRO*, 7:33–76, 1973.
31. A. de Boer, A. van Zuijlen, and H. Bijl. Review of coupling methods for non-matching meshes. *Computer Methods in Applied Mechanics and Engineering*, 196:1515–1525, 2007.
32. I. Demirdžić and M. Perić. Space conservation law in finite volume calculations of fluid flow. *International Journal for Numerical Methods in Fluids*, 8:1037–1050, 1988.
33. I. Demirdžić and M. Perić. Finite volume method for prediction of fluid flow in arbitrarily shaped domains with moving boundaries. *International Journal for Numerical Methods in Fluids*, 10:771–790, 1990.
34. S. Dennis and G. Chang. Numerical solutions for steady flow past a circular cylinder at Reynolds numbers up to 100. *Journal of Fluid Mechanics*, 42:471–489, 1970.
35. S. Deparis, M. Fernandez, and L. Formaggia. Acceleration of a fixed point algorithm for fluid-structure interaction using transpiration conditions. *ESAIM: M2AN*, 37:601–616, 2003.
36. S. Dokos, B. Smaill, A. Young, and I. LeGrice. Shear properties of passive ventricular myocardium. *American Journal of Physiology and Heart Circulation Physiology*, 283, 2002.
37. J. Donea. An arbitrary lagrangian–eulerian finite element method for transient dynamic fluid–structure interactions. *Computational Methods in Applied Mechanical Engineering*, 33:689–723, 1982.
38. G. Faber and Y. Rudy. Action potential and contractility changes in $[na^+]_i$ overloaded cardiac myocytes: a simulation study. *Biophysical Journal*, 78:2392–2404, 2000.
39. C. Farhat, M. Lesoinne, and N. Maman. Explicit/implicit time integration of coupled aeroelastic problems: three-field formulation, geometric conservation and distributed solution. *International Journal of Numerical Methods in Fluids*, 21:807–835, 1994.
40. S. Faure. Stability of colocated finite volume scheme for the Navier-Stokes equations. *Numerical Methods for Partial Differential Equations*, 157:242–271, 2005.
41. J. Fernandez, P. Mithraratne, S. Thrupp, M. Tawhai, and P. Hunter. Anatomically based geometric modeling of the musculo–skeletal system and other organs. *Biomechanics and Modeling in Mechanobiology*, 2:139–155, 2003.
42. C. Figueroa, I. Vignon-Clementel, K. Jansen, T. Hughes, and C. Taylor. A coupled momentum method for modeling blood flow in three-dimensional deformable arteries. *Computational Methods in Applied Mechanical Engineering*, 195:5685–5706, 2006.
43. L. Formaggia, , J. Gerbeau, F. Nobile, and A. Quarteroni. On the coupling of 3d and 1d navier–stokes equations for flow problems in compliant vessels. *Computational Methods in Applied Mechanical Engineering*, 191:561–582, 2001.
44. L. Formaggia, A. Moura, and F. Nobile. On the stability of the coupling of 3d and 1d fluid structure interaction models for blood flow simulations. *Mathematical Models in Numerical Analysis*, 41:743–769, 2007.
45. B. Fornberg. A numerical study of steady viscous flow past a circular cylinder. *Journal of Fluid Mechanics*, 98:819–855,

1980.

46. C. Fox and G. Hutchins. The architecture of the human ventricular myocardium. *Johns Hopkins Medical Journal*, 130:289–299, 1972.
47. C. Fox and G. Hutchins. Left ventricular fiber architecture in man. *British Heart Journal*, 45:248–263, 1981.
48. A. Gambaruto, J. Janela, A. Moura, and A. Sequeira. Sensitivity of hemodynamics in a patient specific cerebral aneurysm to vascular geometry and blood rheology. *Mathematical Biosciences and Engineering*, 8:409–423, 2011.
49. D. Ghista, K. Patil, P. Gould, and K. Woo. Computerized left ventricular mechanics and control system analyes models relevant for cardiac diagnosis. *Computers in Biology and Medicine*, 3:27–4, 1973.
50. D. Ghista and H. Sandler. An analytic elastic–visco–elastic model for the shape and forces of the left ventricle. *Journal of Biomechanics*, 2:35–47, 1969.
51. V. Girault, R. Glowinski, H. Lopez, and J. Vila. A boundary multiplier/fictitious domain method for the steady incompressible navier-stokes equations. *Numerical Mathematics*, 48:75–103, 2001.
52. V. Girault and P. Raviart. *Finite element methods for navier-stokes equations.* Springer-Verlag, 1986.
53. D. Goldstein, M. Oz, and E. Rose. Implantable left ventricular assist devices. *The New England Journal of Medicine*, 339:1522–1533, 1998.
54. S. Goldstein, A. Ali, and H. Sabbah. Ventricular remodelling: mechanisms and prevention. *Cardiology Clinics*, 16:623–632, 1998.
55. P. Gould, D. Ghista, L. Bormbolich, and I. Mirsky. In vivo stresses in the human left ventricular wall: analysis accounting for the irregular three-dimensional geometry and comparison with idealised geometry analyses. *Journal of Biomechanics*, 5:521–539, 1972.
56. graal.ens lyon.fr/MUMPS/, 2011.
57. P. Gresho and R. Sani. *Incompressible flow and the finite element method II, isothermal laminar flow.* John Wiley and Sons, Ltd., 1998.
58. J. Guccione, A. McCulloch, and L. Waldmann. Mechanics of active contraction in cardiac muscle: part i – constitutive relations for fibre stress that describe deactivation.. *Journal of Biomechanical Engineering*, 115:72–81, 1991.
59. J. Gwathmey and R. Hajjar. Relation between steady–state force and intracellular $[ca^{2+}]$ in intact human myocardium. *Circulation*, 82:1266–1278, 1990.
60. J. De Hart, G. Peters, P. Schreuers, and F. Baaijens. A three-dimensional computational analysis of fluid-structure interaction in the aortic valve. *Journal of Biomechanics*, 36:103–112, 2003.
61. M. Heil, A. Hazel, and J. Boyle. Solvers for large–displacement fluid–structure interaction problems. *Computational Mechanics*, 43:91–101, 2008.
62. Y. Hirota. A clinical study of left ventricular relaxation. *Circulation*, 62:756–763, 1980.
63. C. Hirt, A. Amsden, and J. Cook. An arbitrary Lagrangian-Eulerian computing method for all flow speeds. *Journal of Computational Physics*, 14:227–253, 1974.
64. H. Ho, G. Sands, H. Schmid, K. Mithraratne, G. Mallinson, and P. Hunter. A hybrid 1d and 3d approach to hemodynamics modelling for a patient–specific cerebral vasculature and aneurysm. *MICCAI*, 2:323–330, 2009.
65. http://cubit.sandia.gov, 2008.
66. T. Hughes, W. Liu, and T. Zimmermann. Lagrangian-Eulerian finite element formulation for incompressible viscous flows. *Computational Methods in Applied Mechanical Engineering*, 29:329–349, 1981.
67. P. Hunter. *Finite element analysis of cardiac muscle mechanics.* University of Oxford, 1975.
68. P. Hunter, A. McCulloch, and H. ter Keurs. Modeling the mechanical properties of cardiac muscle. *Progress in Biophysics and Molecular Biology*, 69:289–331, 1998.
69. P. Hunter and B. Smaill. The analysis of cardiac function: A continuum approach. *Progress in Biophysics and Molecular Biology*, 52:101–164, 1988.
70. J. Janicki and K. Weber. Ejection pressure and the diastolic left ventricular pressure-volume relation. *American Journal of Physiology.*, 6:H545–H552, 1977.
71. R. Janz, B. Kubert, T. Moriarty, and A. Grimm. Deformation of the diastolic left ventricle II nonlinear geometric effects. *Journal of Biomechanics*, 7:509–516, 1974.

72. A. Jeays, P. Lawford, R. Gillott, P. Spencer, D. Barber, K. Bardhan, and D. Hose. Characterisation of the haemodynamics of the superior mesenteric artery. *Journal of Biomechanics*, 40:1916–1926, 2007.
73. B. Kar, R. Delgardo, O. Frazier, I. Gregoric, M. Harting, Y. Wadia, T. Myers, R. Moser, and J. Freund. The effect of LVAD aortic outflow-graft placement on hemodynamics and flow. *Tex Heart Inst J.*, 32:294–298, 2005.
74. R. Kerckhoffs, P. Bovendeerd, F. Prinzen, K. Smits, and T. Arts. Intra– and interventricular asynchrony of electromechanics in the ventricularly paced heart. *Journal of Engineering Mathematics.*, 47:201–216, 2003.
75. T. Khan, R. Delgado, B. Radovancevic, G. Torre-Amione, J. Abrams, K. Miller, T. Myers, K. Okerberg, S. Stetson, I. Gregoric, A. Hernandez, and O. Frazier. Dobutamine stress echocardiography predicts myocardial improvement in patients supported by left ventricular assist devices. *Journal of Heart and Lung Transplantation.*, 22:137–46, 2003.
76. P. Kilner, M. Henein, and D. Gibson. Our tortuous heart in dynamic mode: an echocardiographic study of mitral flow and movement in exercising subjects. *Heart Vessels*, 12:103–110, 1997.
77. P. Kilner, G. Yang, R. Mohiaddin, D. Firmin, and D. Longmore. Helical and retrograde secondary flow patterns in the aortic arch studied by three-directional magnetic resonance velocity mapping. *Circulation*, 88:2235–2247, 1993.
78. P. Kilner, G. Yang, A. Wilkes, R. Mohiaddin, D. Firmin, and M. Yacoub. Asymmetric redirection of flow through the heart. *Nature*, 404:759–761, 2000.
79. H. Kim, C. Figueroa, T. Hughes, K. Jansen, and C. Taylor. Augmented lagrangian method for constraining the shape of velocity profiles at outlet boundaries for three–dimensional finite element simulations of blood flow. *Computational Methods in Applied Mechanical Engineering*, 198:3551–3566, 2009.
80. H. Kim, I. Vignon-Clementel, C. Figueroa, J. LaDisa, K. Jansen, J. Feinstein, and C. Taylor. On coupling a lumped parameter heart model and a three dimensional finite element aorta model. *Annals of Biomedical Engineering*, 37:2153–2169, 2009.
81. W. Kim, P. Walker, E. Pedersen, J. Poulsen, S. Oyre, K. Houlind, and A. Yoganathan. Left ventricular blood flow patterns in normal subjects: a quantitative analysis by three-dimensional magnetic resonance velocity mapping. *JACC*, 26:224–238, 1995.
82. S. Klotz, M. Deng, and J. Stypmann. Left ventricular pressure and volume unloading during pulsatile versus nonpulsatile left ventricular assist device support. *Annals of Thoracic Surgery*, 77:143–149, 2004.
83. S. Klotz, S. Dickstein, and M. Burkhoff. A computational method of prediction of the end-diastolic pressure volume relationship by single beat. *Nature Protocol*, 2:2152–2158, 2007.
84. S. Klotz, J. Stypmann, H. Welp, C. Schmid, G. Drees, A. Rukosujew, and H. Scheld. Does continuous flow LVAD technology have a positive impact on outcome pretransplant and posttransplant? *Annals of Thoracic Surgery*, 82:1774–1778, 2006.
85. T. Korakianitis and Y. Shi. A concentrated parameter model for the human cardiovascular system including heart valve dynamics and atrioventricular interaction. *Medical Engineering and Physics*, 28:613–628, 2006.
86. T. Korakianitis and Y. Shi. Numerical simulation of cardiovascular dynamics with healthy and diseased heart valves. *Journal of Biomechanics*, 39:1964–1982, 2006.
87. M. Krafczyk, M. Cerrolaza, M. Schulz, and E. Rank. Analysis of 3d transient blood flow passing through an artificial aortic valve by latticeboltzmann methods. *Journal of Biomechanics*, 31:453–462, 1998.
88. S. Krittian, U. Janoske, H. Oertel, and T. Bhlke. Partitioned fluid–solid coupling for cardiovascular blood flow: Left ventricular fluid mechanics. *Annals of Biomedical Engineering*, 38:1426–1441, 2010.
89. S. Krittian, U. Janoske, H. Oertel, and T. Bhlke. Partitioned fluid–solid coupling for cardiovascular blood flow: Validation study of pressure driven fluid–domain deformation. *Annals of Biomedical Engineering*, 38:2676–2689, 2010.
90. P. Lamata, S. Niederer, D. Barber, D. Nordsletten, J. Lee, D. Hose, and N. Smith. Personalization of cubic hermite meshes for efficient biomechanical simulations. *Lecture Notes in Computer Science*, 6362:380–387, 2010.
91. P. Lamata, S. Niederer, D. Nordsletten, D. Barber, I. Ray, D. Hose, and N. Smith. An accurate, fast and robust method to generate patient–specific cubic hermite meshes. *Medical Image Analysis*, DOI:10.1016/j.media.2011.06.010, 2011.
92. W. Layton. *Introduction to the Numerical Analysis of Incompressible Viscous Flows.* SIAM, 2008.
93. I. LeGrice. *A finite element model of myocardial structure: Implications for electrical activation in the heart. Ph.D. Thesis.* University of Auckland, 1992.
94. I. LeGrice, P. Hunter, A. Young, and B. Smaill. The architecture of the heart: A data-based model. *Philisophical*

Transactions of the Royal Society, 359:1217–1232, 2001.

95. I. LeGrice, G. Sands, D. Hooks, D. Gerneke, and B. Smaill. Microscopic imaging of extended tissue volumes. *Clinical and Experimental Pharmacology and Physiology*, 31(12):902–905, 2004.
96. I. LeGrice, B. Smaill, L. Chai, S. Edgar, J. Gavin, and P. Hunter. Laminar structure of the heart: ventricular myocyte arrangement and connective tissue architecture in the dog. *American Journal of Physiology*, 269:H571–H582, 1995.
97. J. Lemmon and A. Yoganathan. Computational modeling of left heart diastolic function: examination of ventricular dysfunction. *Journal of Elasticity*, 122:297–303, 2000.
98. H. Levin, M. Oz, K. Catanese, E. Rose, and D. Burkhoff. Transient normalisation of systolic and diastolic function after support with a left ventricular assist device in a patient with dilated cardiomyopathy. *Journal of Heart and Lung Transplantation*, 15:840–842, 1996.
99. Z. Li and C. Kleinstreuer. Analysis of biomechanical factors affecting stent-graft migration in an abdominal aortic aneurysm model. *Journal of Biomechanics*, 39(12):2264 – 2273, 2006.
100. M. Loebe, A. Koster, and S. Sanger. Inflammatory response after implantation of a left ventricular assist device: comparison between the axial flow micromed vad and the pulsatile novacor device. *ASAIO Journal*, 47:272–274, 2001.
101. I. Lomtev, R. Kirby, and G. Karniadakis. A second–order time–accurate finite volume method for unsteady incompressible flow on hybrid unstructured grids. *Journal of Computational Physics*, 162:411–428, 2000.
102. J. Maccallum. On the muscular architecture and growth of the ventricles of the heart. *Johns Hopkins Hospital Reports*, 9:307–335, 1900.
103. J. Madigan, A. Barbone, A. Choudhri, D. Morales, B. Cai, and M. Oz. Time course of reverse remodeling of the left ventricle during support with a left ventricular assist device. *Journal of Thoracic Cardiovascular Surgery*, 121:902–8, 2001.
104. K. Mahesh. A family of high order finite difference schemes with good spectral resolution. *Journal of Computational Physics*, 145:332–358, 1998.
105. F. Mall. On the muscular architecture of the ventricles of the human heart. *American Journal of Anatomy*, 11:211–266, 1911.
106. L. Malvern. *Introduction to the mechanics of continuous medium.* Prentice-Hall, 1969.
107. D. Mancini, A. Beniaminovits, and H. Levin. Low incidence of myocardial recovery after left ventricular assist device implantation in patients with chronic heart failure. *Circulation*, 98:2383–2389, 1998.
108. K. Margulies. Reversal mechanisms of left ventricular remodeling: Lessons from left ventricular assist device experiments. *Journal of Cardiac Failure*, 8:s500–s505, 2002.
109. E. Di Martino, G. Guadagni, A. Fumero, G. Ballerini, R. Spirito, P. Biglioli, and A. Redaelli. Fluid-structure interaction within realistic three-dimensional models of the aneurysmatic aorta as a guidance to assess the risk of rupture of the aneurysm. *Medical Engineering and Physics*, 23:647 – 655, 2001.
110. K. May-Newman, B. Hillen, C. Sironda, and W. Dembitsky. Effect of LVAD outflow conduit insertion angle on flow through the native aorta. *Journal of Medical Engineering and Technology*, 28:105–109, 2004.
111. P. McCarthy, R. Savage, C. Fraser, R. Vargo, K. James, and M. Goormastic. Haemodynamic and physiologic changes during support with an implantable left ventricular assist device. *Journal of Thoracic Cardiovascular Surgery*, 109:409–17, 1995.
112. M. McCormick, D. Nordsletten, A. de Vecchi, D. Kay, and N. Smith. Fluid–mechanics simulations of ventricular function under LVAD support. *Conference: Medical Physics and Biomedical Engineering, Munich*, 2009.
113. M. McCormick, D. Nordsletten, D. Kay, and N. Smith. Modelling left ventricular function under assist device support. *International Journal for Numerical Methods in Biomedical Engineering*, DOI: 10.1002/cnm.1428, 2011.
114. M. McCormick, D. Nordsletten, D. Kay, and N. Smith. Simulating left ventricular function through the full cardiac cycle under LVAD support. *Journal of Computational Physics*, Submitted, In Review, 2012.
115. A. McCulloch. *Deformation and stress in the passive heart.* University of Auckland, 1987.
116. A. McCulloch, B. Smaill, and P. Hunter. Left ventricular epicardial deformation in the isolated arrested dog heart. *American Journal of Physiology*, 252:233–241, 1988.
117. D. McQueen and C. Peskin. A 3d computational method for blood flow in the heart. II contractile fibers. *Journal of Computational Physics*, 82:289, 1989.
118. D. McQueen and C. Peskin. A three-dimensional computer model of the human heart for studying cardiac fluid dynamics.

Computers and Graphics, 34:56 – 60, 2000.

119. V Mihalef, R Ionasec, P Sharma, B Georgescu, I Voigt, M Suehling, and D. Comaniciu. Patient–specific modelling of whole heart anatomy, dynamics and haemodynamics from four–dimensional cardiac CT images. *Interface Focus*, 1:286–296, 2011.
120. I. Mirsky. Left ventricular stresses in the intact human heart. *Biophysical Journal*, 9:189–208, 1969.
121. I. Mirsky. Ventricular and arterial wall stresses based on large deformations analyses. *Biophysical Journal*, 13:1141–1159, 1973.
122. M. Nash. *Mechanics and Material Properties of the Heart using an Anatomically Accurate Mathematical Model. Ph.D. Thesis.* University of Auckland, 1998.
123. M. Nash and P. Hunter. Computational mechanics of the heart. *Journal of Elasticity*, 61:113–141, 2000.
124. J. Nazareth. Conjugate gradient method. *Wiley Interdisciplinary Reviews: Computational Statistics*, 1:348–353, 2009.
125. D. Nickerson, N. Smith, and P. Hunter. A model of cardiac cellular electromechanics. *Philisophical Transactions of the Royal Society*, 359:1159–1172, 2001.
126. D. Nickerson, N. Smith, and P. Hunter. New developments in a strongly coupled cardiac electromechanical model. *Europace*, 7:S118–S127, 2005.
127. F. Nicoud, H. Vernhet, and M. Dauzat. A numerical assessment of wall shear stress changes after endovascular stenting. *Journal of Biomechanics*, 38(10):2019 – 2027, 2005.
128. S. Niederer, G. Plank, P. Chinchapatnam, M. Ginks, P. Lamata, K. Rhode, C. Rinaldi, R. Razavi, and N. Smith. Length-dependent tension in the failing heart and the efficacy of cardiac resynchronization therapy. *Cardiovascular Research*, 89:336–343, 2011.
129. S. Niederer, K. Rhode, R. Razavi, and N. Smith. The importance of model parameters and boundary conditions in whole organ models of cardiac contraction. *Lecture Notes in Computer Science.*, 5528:348–356, 2009.
130. S. Niederer and N. Smith. An improved numerical method for strong coupling of excitation and contration models in the heart. *Progress in Biophysics and Molecular Biology.*, 96:90–111, 2008.
131. P. Nielsen, I. LeGrice, B. Smaill, and P. Hunter. Mathematical model of geometry and fibrous structure of the heart. *American Heart Journal*, 260:1365 1378, 1991.
132. F. Nobile. *Numerical approximation of fluid-structure interaction problems with application to haemodynamics. Ph.D. Thesis.* Ecole Polytechnique Federale de Lausanne, 2001.
133. C. Norberg. Fluctuating lift on a circular cylinder: review and new measurements. *Journal of Fluids and Structures*, 17:57–96, 2003.
134. D. Nordsletten. *Fluid–Solid Coupling for the Simulation of Left Ventricular Mechanics. PhD Thesis.* University of Oxford, 2009.
135. D. Nordsletten, P. Hunter, and N. Smith. Conservative and non-conservative arbitrary Lagrangian-Eulerian forms for ventricular flows. *International Journal for Numerical Methods in Biomedical Engineering*, 56:1457–1463, 2008.
136. D. Nordsletten, D. Kay, and N. Smith. A non–conforming monolithic finite element method for problems of coupled mechanics. *Journal of Computational Physics*, 20:7571–7593, 2010.
137. D. Nordsletten, M. McCormick, P. Kilner, D. Kay, and N. Smith. Fluid-solid coupling for the investigation of diastolic and systolic human left ventricular function. *International Journal for Numerical Methods in Biomedical Engineering*, 27:1017–1039, 2011.
138. D. Nordsletten, S. Niederer, M. Nash, P. Hunter, and N. Smith. Coupling multi–physics models to cardiac mechanics. *Progress in Biophysics and Molecular Biology*, 104:77–88, 2009.
139. D. Nordsletten and N. Smith. Triangulation of p-order parametric surfaces. *Journal of Scientific Computing*, 34:308–335, 2007.
140. H. Oertel, K. Spiegel, and S. Donisi. *Modelling the Human Cardiac Fluid Mechanics.* Universitatsverlag karlsruhe, 2006.
141. L. Opie. *Heart Physiology.* Lippincott Williams and Wilkins, 4 edition, 2004.
142. M. Oshima, R. Torii, T. Kobayashi, N. Taniguchi, and K. Takagi. Finite element simulation of blood flow in the cerebral artery. *Computational Methods in Applied Mechanics and Engineering*, 191:661–671, 2001.
143. J. Ottesen and M. Danielsen. Modelling ventricular contraction with heart rate changes. *Journal of Theoretical Biology*, 222:337–346, 2003.

144. S. Panda and R. Natarajan. Finite element analysis of laminated shells of revolution. *Computers and Structures*, 6:61–64, 1976.
145. S. Panda and R. Natarajan. Finite element method of stress analysis in the human left ventricular layered wall structure. *Medical and Biological Engineering and Computing*, 15:67–71, 1977.
146. J. Parameshwar and J. Wallwork. Left ventricular assist devices: current status and future applications. *International Journal of Cardiology*, 62:s23–s27, 1997.
147. R. De Paulis, G. De Matteis, P. Nardi, R. Scaffa, M. Buratta, and L. Chiariello. Opening and closing characteristics of the aortic valve after valve sparing procedures using a new aortic root conduit. *Annals of Thoracic Surgery*, 72:487–494, 2001.
148. G. Pennati, M. Bellotti, and R. Fumerco. A mathematical model of circulation in the presence of the bidirectional cavopulmonary anastomosis in children with a univentricular heart. *Medical Engineering and Physics*, 19:223–234, 1997.
149. K. Perktold and G. Rappitsch. Computer simulation of local blood flow and vessel mechanics in a compliant carotid artery bifurcation model. *Journal of Biomechanics*, 28:845–856, 1995.
150. C. Peskin. Flow patterns around heart valves: A numerical method. *Journal of Computational Physics*, 10:252–271, 1972.
151. C. Peskin. Numerical analysis of blood flow in the heart. *Journal of Computational Physics*, 25:220–252, 1977.
152. C. Peskin. Fiber architecture of the left ventricular wall: An asymptotic analysis. *Communications on Pure and Applied Mathematics*, 42:79–113, 1989.
153. C. Peskin. The immersed boundary method. *Acta Numerica*, 11:479–517, 2002.
154. C. Peskin and D. McQueen. *Fluid Dynamics of the Heart and its Valves. in Case Studies in Mathematical Modeling.* Prentice–Hall, 1997.
155. E. Potapov, M. Loebe, and H. bdul Khaliq. Postoperative course of s-100b protein and neuron specific enolase in patients after implantation of continuous and pulsatile flow LVADs. *Journal of Heart and Lung Transplant*, 20:1310–1316, 2001.
156. W. Press, S. Teukolsky, W. Vetterling, and B. Flannery. *Numerical Recipes in Fortran.* Cambridge University Press, 3^{rd} edition, 2007.
157. A. Pries, D. Neuhaus, and P. Gaehtgens. Blood viscosity in tube flow: dependence on diameter and hematocrit. *American Journal of Physiology*, 32:H1770–H1778, 1992.
158. A. Quarteroni, S. Ragni, and A. Veneziani. Coupling between lumped and distributed models for blood flow problems. *Computing and Visualisation in Science*, 4:111–124, 2001.
159. A. Quarteroni and A. Valli. *Numerical Approximation of Partial Differential Equations.* Springer–Verlag, 1994.
160. R., Kerckhoffs, O. Faris, P. Bovendeerd, F. Prinzen, K. Smits, E. McVeigh, and T. Arts. Electromechanics of paced left ventricle simulated by straightforward mathematical model: comparison with experiments. *American Journal of Physiology*, 289:H1889–H1897, 2005.
161. B. Radovancevic, B. Vrtovec, and O. Frazier. Left ventricular assist devices: an alternative to medical therapy for end stage heart failure. *Current Opinion in Cardiology*, 18:210–214, 2003.
162. M. Rajagopal, J. Chung, D. Bullivant, P. Nielsen, and M. Nash. Determining the finite elasticity reference state from a loaded configuration. *International Journal of Numerical Methods in Engineering*, 72:1434–1451, 2007.
163. K. Reesink, A. Dekker, T. Van der Nagel, C. Beghi, F. Leonardi, P. Botti, G. De Cicco, R. Lorusso, F. Van der Veen, and J. Maessen. Suction due to left ventricular assist: implications for device control and management. *Artificial Organs*, 31:542–549, 2007.
164. E. Remme, A. Opdahl, and O. Smiseth. Mechanics of left ventricular relaxation, early diastolic lengthening and suction investigated in a mathematical model. *American Journal of Physiology*, doi: 10.1152/ajpheart.00165.2010, 2011.
165. L. Richardson. On the approximate arithmetical solution by finite differences of physical problems involving differential equations, with an application to the stresses in a masonry dam. *Proceedings of the Royal Society*, 83:335–336, 1910.
166. J. Robb and R. Robb. The normal heart. anatomy and physiology of the structural units. *American Heart Journal*, 23:455–467, 1942.
167. D. Rohmer, A. Sitek, and G. Gullberg. Reconstruction and visualization of fiber and laminar structure in the normal human heart from ex vivo diffusion tensor magnetic resonance imaging (DTMRI) data. *Investigative Radiology*, 42:777–789, 2007.
168. L. Rosado and J. Copeland. Orthotopic heart transplantation: Recent advances. *Primary Cardiology*, 16:33–47, 1990.
169. N. Saber, A. Gosman, N. Wood, P. Kilner, C. Charrier, and D. Firmin. Computational flow modeling of the left ventricle

based on *In Vivo* MRI data: Initial experience. *Annals of Biomedical Engineering*, 29:275–283, 2001.

170. N. Saber, N. Wood, A. Gosman, R. Merrifield, G. Yang, C. Charrier, P. Gatehouse, and D. Firmin. Progress towards patient-specific computational flow modeling of the left heart via combination of MRI with computational fluid dynamics. *Annals of Biomedical Engineering*, 31:42–52, 2003.
171. G. Sands, D. Gerneke, D. Hooks, C. Green, B. Smaill, and I. LeGrice. Automated imaging of extended tissue volumes using confocal microscopy. *Microscopy Research and Technique*, 67(5):227–239, 2005.
172. T. Schenkel, M. Malve, M. Reik, M. Markl, B. Jung, and H. Oertel. MRI–based CFD analysis of flow in a human left ventricle: Methodology and application to a healthy heart. *Annals of Biomedical Engineering*, 37, 2009.
173. C. Schmid, T. Tjan, C. Etz, C. Schmidt, F. Wenzelburger, M. Wilhelm, M. Rothenburger, G. Drees, and H. Scheld. First clinical experience with the Incor left ventricular assist device. *The Journal of Heart and Lung Transplantation*, 24:1188–1194, 2005.
174. H. Schmid. *Passive myocardial mechanics: constitutive laws and material parameter estimation. PhD Thesis.* University of Auckland, 2006.
175. H. Schmid, P. O'Callaghan, M. Nash, W. Lin, I. LeGrice, B. Smaill, A. Young, and P. Hunter. Myocardial material parameter estimation - a non–homogeneous finite element study from simple shear tests. *Biomechanics and Modelling in Mechanobiology*, 7:161–173, 2008.
176. M. Sermesant, H. Delingette, and N. Ayache. An electromechanical model of the heart for image analysis and simulation. *IEEE Trans. Med. Imaging*, 25:612–62, 2006.
177. M. Sermessant, P. Moireau, O. Camara, J. Sainte-Marie, R. Andriantsimiavona, R. Cimrman, D. Hill, D. Chapelle, and R. Razavi. Cardiac function estimation from MRI using a heart model and data assimilation: Advances and difficulties. *Medical Image Analysis*, 4:642–656, 2006.
178. Y. Shi and T. Korakianitis. Numerical simulation of cardiovascular dynamics with left heart failure and in–series pulatile ventricular assist device. *Artificial Organs*, 30:929–948, 2006.
179. O. Smiseth and M. Tendera, editors. *Diastolic Versus Systolic Heart Failure*. Springer London, 2008.
180. X. Song, A. Throckmorton, H. Wood, J. Antaki, and D. Olsen. Quantitative evaluation of blood damage in a centrifugal vad by computational fluid dynamics. *Journal of Fluids Engineering*, 126(3):410–418, 2004.
181. C. Stevens. *An anatomically-based computational study of cardiac mechanics and myocardial infarction. Ph.D. Thesis.* University of Auckland, 2002.
182. C. Stevens, E. Remme, I. LeGrice, and P. Hunter. Ventricular mechanics in diastole: Material parameter sensitivity. *Journal of Biomechanics*, 36:737–748, 2003.
183. J. Stijnen, J. De Hart, P. Bovendeerd, and F. van de Vosse. Evaluation of a fictitious domain method for predicting dynamic response of mechanical heart valves. *Journal of Fluids and Structures*, 19:835–850, 2004.
184. D. Streeter and D. Bassett. An engineering analysis of myocardial fiber orientation in pigs left ventricle in systole. *Anatomy Record*, 155:503–511, 1966.
185. D. Streeter, H. Spotnitz, D. Patel, J. Ross, and E. Sonnenblick. Fiber orientation in the canine left ventricle during diastole and systole. *Circulation Research*, 24:339–347, 1969.
186. H. Suga, K. Sagawa, and A. Shoukas. Load independence of the instantaneous pressure-volume ratio of the canine left ventricle and effects of epinephrine and heart rate on the ratio. *Circulation Research*, 32:314–322, 1973.
187. L. Taber. *Nonlinear Theory of Elasticity Applications in Biomechanics.* World Scientific Publishing Co. Pte. Ltd., 2004.
188. D. Taylor, L. Edwards, and P. Mohacsi. The registry of the international society for heart and lung transplant report. *The Journal of Heart and Lung Transplantation*, 22:616–624, 2003.
189. T. Taylor, H. Suga, Y. Goto, H. Okino, and T. Yamaguchi. The effects of cardiac infarction on realistic three–dimensional left ventricular blood ejection. *Journal of Biomechanical Engineering*, 118:106–110, 1996.
190. R. Temam. *Navier–Stokes equations and non–linear functional analyses.* SIAM, 1983.
191. R. Temam. *Navier–Stokes equations. Theory and numerical analysis.* North–Holland, 1984.
192. S. Thackray, J. Easthaugh, N. Freemantle, and J. Gleland. The effectiveness and relative effectiveness of intravenous inotropic drugs acting through the adrenergic pathway in patients with heart failure. *European Journal of Heart Failure*, 4:515–529, 2002.

193. A. Throckmorton, A. Untaroiu, P. Allaire, H. Wood, G. Matherne, D. Lim, B. Peeler, and D. Olsen. Computational analysis of an axial flow pediatric ventricular assist device. *Artificial Organs*, 28(10):881–891, 2004.
194. R. Unger, M. Haupt, and P. Horst. Application of lagrange multipliers for coupled problems in fluid and structural interactions. *Computers and Structures*, 85:796–809, 2007.
195. C. Vahl, T. Timek, A Bonz, H. Fuchs, R. Dillman, and S. Hagl. Length dependence of calcium and force transients in the normal and failing human myocardium. *Journal of Molecular and Cellular Cardiology*, 30:957–966, 1998.
196. J. van der Velden, J. de Jong, V. Owen, P. Burton, and G. Stienen. Effect of protein kinase on calcium sensitivity of force and its sarcomere length dependence in human cariomyocytes. *Cardiovascular Research*, 46:487–495, 1988.
197. R. van Loon, P. Anderson, and F. van de Vosse. A fluid–structure interaction method with solid–rigid contact for heart valve dynamics. *Journal of Computational Physics*, 217:806–823, 2006.
198. I. Vignon-Clementel, C. Alberto Figueroa, K. Jansen, and C. Taylor. Outflow boundary conditions for three–dimensional finite element modelling of blood flow and pressure in arteries. *Computer Methods in Applied Mechanics and Engineering*, 195, 2006.
199. M. Vollkron, H. Shima, L. Huber, and G. Wieselthaler. Interaction of the cardiovascular system with an implanted rotary assist device: simulation study with a refined computer model. *Artificial Organs*, 26:349–359, 2002.
200. Z Wang and Y. Liu. Spectral (finite) volume method for conservation laws on unstructured grids v: extension to three-dimensional systems. *Journal of Computational Physics*, 2005.
201. H. Watanabe, T. Hisada, S. Sugiura, J. Okada, and H. Fukunari. Computer simulation of blood flow, left ventricular wall motion and their interrelationship by fluid-structure interation finite element method. *JSME International Journal*, 45:1003–1012, 2002.
202. H. Watanabe, S. Sugiura, H. Kafuku, and T. Hisada. Multiphysics simulation of left ventricular filling dynamics using fluid-structure interaction finite element method. *Biophysical Journal*, 87:2074–2085, 2004.
203. J. Whiteley, M. Bishop, and D. Gavaghan. Soft tissue modelling of cardiac fibres for use in coupled mechano-electric simulations. *Bulletin of Mathematical Biology*, 69:2199–2225, 2007.
204. R. Whitmore. The flow behavior of blood in the circulation. *Nature*, 215:126–123, 1967.
205. M. Williams and M. Oz. Indications and patient selection for mechanical ventricular assistance. *Annals of Thoracic Surgery*, 71:S86–S91, 2001.
206. R. Winslow, D. Scollan, A. Holmes, C. Yung, J. Zhang, and M. Jafri. Electrophysiological modelling of cardiac ventricular function: from cell to organ. *Annual Review in Biomedical Engineering*, 2:119–155, 2000.
207. J. Wohlschlaeger, K. Schmitz, C. Schmid, K. Schmid, P. Keul, A. Takeda, S. Weis, B. Levkau, and H. Baba. Reverse remodelling following insertion of left ventricular assist devices: A review of morphological and molecular changes. *Cardiovascular Research*, 68:376–386, 2005.
208. R. Woods. A few applications of a physical theorem to membranes in the human body in a state of tension. *Journal of Anatomy and Physiology*, 26:362–370, 1892.
209. www.berlinheart.de, 2011.
210. www.cmiss.org, 2008.
211. www.euheart.eu, 2011.
212. www.oerc.ox.ac.uk, 2011.
213. www.research.philips.com, 2011.
214. J. Xi, P. Lamata, W. Shi, S. Niederer, S. Land, D. Rueckert, S. Duckett, A. Shetty, C. Rinaldi, R. Razavi, and N. Smith. An automatic data assimilation framework for patient–specific myocardial mechanical parameter estimation. *Functional Imaging and Modelling of the Heart*, 6666:392–400, 2011.
215. E. Yellin, C. Peskin, C. Yoran, M. Koenigsberg, M. Matsumoto, S. Laniado, D. McQueen, D. Shore, and R. Frater. Mechanisms of mitral valve motion during diastole. *American Journal of Physiology*, 241:H389–H400, 1981.
216. A. Yoganathan, J. Lemmon, Y. Kim, P. Walker, R. Levine, and C. Vesier. A computational study of a thin–walled three–dimensional left ventricle during early systole. *Journal of Biomechanical Engineering*, 116:307–314, 1994.
217. S. Zhao, X. Xu, A. Hughes, S. Thom, A. Stanton, B. Ariff, and Q. Long. Blood flow and vessel mechanics in a physiologically realistic model of a human carotid arterial bifurcation. *Journal of Biomechanics*, 33:975–984, 2000.

218. O. Zienkiewicz and R. Taylor. *The Finite Element Method*. Elsevier, 2000.
219. W. Zoghbi, K. Farmer, J. Soto, J. Nelson, and M. Quinones. Accurate noninvasive quantification of stenotic aortic valve area by doppler echocardiography. *Circulation*, 73:452–459, 1986.